ISBN 0-315-61826-4

FATIGUE LIFE PREDICTION OF OFFSHORE TUBULAR T-JOINTS USING FRACTURE MECHANICS APPROACH

CENTRE FOR NEWFOUNDLAND STUDIES

TOTAL OF 10 PAGES ONLY
MAY BE XEROXED

(Without Author's Permission)

GOURI SHANKAR BHUYAN

001311

CENTRE FOR NFLD. STUDIES
MEMORIAL UNIVERSITY
OF NEWFOUNDLAND

National Library of Canada
Bibliothèque nationale du Canada

Canadian Theses Service
Service des thèses canadiennes

Ottawa, Canada
K1A 0N4

NOTICE

The quality of this microform is heavily dependent upon the quality of the original thesis submitted for microfilming. Every effort has been made to ensure the highest quality of reproduction possible.

If pages are missing, contact the university which granted the degree.

Some pages may have indistinct print especially if the original pages were typed with a poor typewriter ribbon or if the university sent us an inferior photocopy.

Reproduction in full or in part of this microform is governed by the Canadian Copyright Act, R.S.C. 1970, c. C-30, and subsequent amendments.

AVIS

La qualité de cette microforme dépend grandement de la qualité de la thèse soumise au microfilmage. Nous avons tout fait pour assurer une qualité supérieure de reproduction.

S'il manque des pages, veuillez communiquer avec l'université qui a conféré le grade.

La qualité d'impression de certaines pages peut laisser à désirer, surtout si les pages originales ont été dactylographiées à l'aide d'un ruban usé ou si l'université nous a fait parvenir une photocopie de qualité inférieure.

La reproduction, même partielle, de cette microforme est soumise à la Loi canadienne sur le droit d'auteur, SRC 1970, c. C-30, et ses amendements subséquents.

NL-339 (r. 88/04) c

Canada

FATIGUE LIFE PREDICTION OF OFFSHORE TUBULAR T-JOINTS USING FRACTURE MECHANICS APPROACH

BY

Gouri Shankar Bhuyan, B.E.(Civil), M.Tech.(Ocean)

© A thesis submitted to the School of Graduate Studies in partial fulfillment of the requirements for the degree of Doctor of Philosophy

Faculty of Engineering & Applied Science
Memorial University of Newfoundland
June 1986

St.John's Canada

National Library of Canada
Bibliothèque nationale du Canada

Canadian Theses Service
Service des thèses canadiennes

Ottawa, Canada
K1A 0N4

The author has granted an irrevocable non-exclusive licence allowing the National Library of Canada to reproduce, loan, distribute or sell copies of his/her thesis by any means and in any form or format, making this thesis available to interested persons.

L'auteur a accordé une licence irrévocable et non exclusive permettant à la Bibliothèque nationale du Canada de reproduire, prêter, distribuer ou vendre des copies de sa thèse de quelque manière et sous quelque forme que ce soit pour mettre des exemplaires de cette thèse à la disposition des personnes intéressées.

The author retains ownership of the copyright in his/her thesis. Neither the thesis nor substantial extracts from it may be printed or otherwise reproduced without his/her permission.

L'auteur conserve la propriété du droit d'auteur qui protège sa thèse. Ni la thèse ni des extraits substantiels de celle-ci ne doivent être imprimés ou autrement reproduits sans son autorisation.

ISBN 0-315-61826-4

Canada

To my parents

ABSTRACT

The thesis presents the results of an analytical and experimental investigation of the fatigue behaviour of tubular T-joints, using a linear fracture mechanics approach. The analytical study includes the development of a finite element computer program to analyse tubular joints with/without weld toe cracks. The experimental investigation consists of quantifying the effects of sea water, temperature, frequency, load ratio and wave form on fatigue crack-growth-rates in CSA G40.21 M 350 WT steel, which has been proposed for the Canadian Offshore.

The actual curved surface and the brace/chord intersection are approximated by the assemblage of flat quadrilateral and triangular plate elements for two dimensional analysis. The analysis uses a plane stress element to account for membrane stiffness and a plate bending element to account for flexural stiffness. For three dimensional analyses, chord/brace/weld regions are modelled using incompatible brick and prism elements. In order to reduce the computer storage requirements as well as the solution costs, the region of high stress gradient is analysed using the rezone technique. Hot spot stress and stress concentration factors obtained from these analyses are compared with the experimental values available in the literature.

To study the effect of a shallow weld toe crack on through-thickness and surface stress redistribution, the region at the vicinity of the crack is modelled using special elements which produce singular stress fields at the crack front. The crack-

tip stress intensity factors are determined by comparing the crack-tip stresses, obtained from the analyses, with the available theoretical solutions.

Fatigue crack-growth-rate data and material coefficients, C and m, for various temperature, load ratio and frequency ranges are obtained from compact tension specimen tests in air as well as in sea water. Knowing the crack-growth behaviour in the base metal, the through-thickness-cracking lives of tubular T-joints are predicted analytically using the modified Paris' equation and the estimated lives are compared with reported experimental results. The accuracy of the computer program and the validity of the proposed method for predicting fatigue life of tubular joints are checked by testing a prototype tubular T-joint.

ACKNOWLEDGEMENT

I have great pleasure in expressing sincere gratitude to my supervisor Dr. A.S.J. Swamidas for his guidance and encouragement. Grateful acknowledgements are due to Dr. M. Arockiasamy, who suggested the topic of the thesis and supervised most of the work during his stay at Memorial University. Special thanks also go to Drs. D.B. Muggeridge and M. Hinchey, members of the supervisory committee, for their criticisms and helpful suggestions while reading the manuscript.

I acknowledge gratefully the help given by Dr. K. Munaswamy during the development of the computer software. Grateful acknowledgement is due to Dr. O. Vosikovsky, for his constructive criticisms in the preparation of the final report of CANMET Contract No. OSU83-00033, which has been freely used in preparation of this thesis and for donating steel plate for CT specimens.

Thanks are due to Dr. F.A. Aldrich, Dean of Graduate Studies, for the award of a Memorial University Fellowship during the entire period of this research. Additional financial assistance by Drs. A.S.J. Swamidas and M. Arockiasamy from their grants is acknowledged. Sincere appreciations are due to Dr. G.R. Peters, Dean, and Dr. T.R. Chari, Associate Dean, Faculty of Engineering and Applied Science, for providing research facilities.

The generous support from computing services at Memorial University is very much appreciated. I express my appreciation to ETV photography and Mr. T. Dyer of the drafting section, for the preparation of photographs and figures of my

illustrations. I would also like to acknowledge Mr. T. Durate, Mr. A. Bursey, Mr. P. Robinson, for their cooperation in the fabrication and testing of the CT specimens. Special thanks to Mr. R. Burrows, for reading the final manuscript. Finally, I express my thanks to my wife Jocelyn for the understanding and moral support she has shown during the course of this study.

CONTENTS

DEDICATION			ii
ABSTRACT			iii
ACKNOWLEDGEMENT			v
CONTENTS			vii
LIST OF RELATED PUBLICATIONS			x
LIST OF TABLES			xi
LIST OF ILLUSTRATIONS			xii
NOMENCLATURE			xix
CHAPTER	1	INTRODUCTION	1
	1.1	Background	1
	1.2	Purpose of this Research	3
	1.3	Scope of the Investigation	6
CHAPTER	2	LITERATURE REVIEW	10
	2.1	Introduction	10
	2.2	Analytical Investigation	11
		2.2.1 Mesh generation	12
		2.2.2 Finite element stress analysis	13
		2.2.3 Parametric formulae	18
		2.2.4 Analysis of crack problems	22
	2.3	Experimental Investigation	27
		2.3.1 Standard specimens	27
		2.3.2 Plated joints	32
		2.3.3 Tubular joints	34
	2.4	Summary	39
CHAPTER	3	TWO DIMENSIONAL ANALYSIS	41
	3.1	Introduction	41
	3.2	Discretization	42

	3.3	Element Stiffness Formulation	46
		3.3.1 Plate bending element	46
		3.3.2 Membrane element	51
		3.3.3 Assembly of six degrees of freedom	53
	3.4	Results and Discussion	56
		3.4.1 Chord stresses	62
		3.4.2 Brace stresses	75
CHAPTER	4	THREE DIMENSIONAL ANALYSIS	82
	4.1	Introduction	82
	4.2	Modelling of Entire Joint	82
		4.2.1 Element stiffness formulation	84
	4.3	Modelling of Hot Spot Region Using Rezone Technique	91
		4.3.1 Rezone section	92
		4.3.2 Displacement transformation	96
		4.3.3 Force transformation	99
		4.3.4 Boundary conditions	103
	4.4	Results and Discussion	104
		4.4.1 Entire joint analysis	106
		4.4.2 Rezoned analysis	115
CHAPTER	5	ANALYSIS OF WELD TOE CRACKS	122
	5.1	Introduction	122
	5.2	Modelling of the Joint	123
	5.3	Finite Element Idealization	124
	5.4	Determination of Stress Intensity Factor	127
	5.5	Results and Discussion	132
CHAPTER	6	FATIGUE CRACK PROPAGATION IN BASE METAL	142
	6.1	Introduction	142
	6.2	Experimental Procedure	143
	6.3	Data Analysis Procedures	146
		6.3.1 Computation of ΔK	146
		6.3.2 Crack-growth-rate evaluation	150
	6.4	Results and Discussion	151
		6.4.1 Crack-growth-rates in air	161
		6.4.2 Crack-growth-rates in sea water	161
		6.4.3 Influence of sea water	168
		6.4.4 Comparison with published results	177

CHAPTER	7	FATIGUE LIFE ESTIMATION	181
	7.1	Introduction	181
	7.2	Linear Elastic Fracture Mechanics(LEFM) Approach	182
		7.2.1 Initial defect size and failure depth	183
		7.2.2 Fatigue life	184
	7.3	Results and Discussion	185
CHAPTER	8	EXPERIMENTAL VERIFICATION	190
	8.1	Introduction	190
	8.2	Instrumentation	190
	8.3	Data Acquisition	193
	8.4	Test Procedure	196
	8.5	Results and Discussion	196
CHAPTER	9	GENERAL DISCUSSION AND CONCLUSIONS	204
	9.1	Contribution to the Field of Research	204
	9.2	Conclusions	205
	9.3	Scope for Further Research	208
BIBLIOGRAPHY AND LIST OF REFERENCES			209

LIST OF RELATED PUBLICATIONS

1. Bhuyan, G.S., Arockiasamy, M. and Munaswamy, K., (1985), Analysis of Tubular Joint with Weld Toe Crack by Finite Element Methods. Communications in Applied Numerical Methods, Vol. 1, 325-331.

2. Bhuyan, G.S., Arockiasamy, M., Munaswamy, K. and Vosikovsky, O., (1986), Finite Element Analysis of Cracked and Uncracked Tubular T-joint. Canadian Journal of Civil Engg., Vol. 13, No.3, 261-269.

3. Bhuyan, G.S., Munaswamy, K. and Arockiasamy, M., (1986), Three Dimensional Stress Analysis of Tubular Joint Using Rezone Technique. Canadian Journal of Civil Engg., Vol. 13, No.3, 382-385.

4. Bhuyan, G.S., Swamidas, A.S.J. and Vosikovsky, O., Effects of Frequency, Temperature, Load Ratio and Environment on Crack Growth Rate in Offshore Steel. Submitted for possible publication in the Int. Journal of Fatigue of Engg. Materials and Structures.

5. Bhuyan, G.S., Arockiasamy, M. and Munaswamy, K., (1985), 3-D Stress Analysis of Welded Tubular T-joint with Weld Toe Crack. Proc. of Conf. on Effects of Fabrication Related Stresses on Product Manufacture and Performance, Cambridge, England, 4.1-4.9.

6. Bhuyan, G.S., Munaswamy, K. and Arockiasamy, M., (1985), Through Thickness and Surface Stress Distribution for Welded Tubular T-joint Using Finite Element Analysis. Proc. of Fourth Int. Conf. on Engg. Software, London, England, 10.75-10.86.

7. Arockiasamy, M., Vosikovsky, O., Bhuyan, G.S. and Munaswamy, K., (1984), Stress Concentration Factors for Welded Tubular T-joints Using Finite Element Analysis with Automatic Mesh Generation. Proc. of the Second Int. Conf. on Welding of Tubular Structures, Boston, U.S.A., 401-410.

8. Munaswamy, K., Bhuyan, G.S. and Arockiasamy, M., (1984), Finite Element Mesh Generation with Interactive Graphics for Tubular T-joints. Proc. of the Int. Conf. on Accuracy Estimates and Adaptive Refinements in Finite Element Computations(ARFEC), Lisbon, Portugal, 7p.

9. Munaswamy, K., Bhuyan, G.S., Swamidas, A.S.J. and Arockiasamy, M., (1986), Experimental and Analytical Studies on Fatigue of Stiffened and Unstiffened Tubular T-Joints. Proc. of Offshore Tech. Conf., OTC 5308, Vol. 4, Houston, 153-162.

LIST OF TABLES

Table No.	Title	Page No.
3.1	Joint parameters.	57
3.2	Stress concentration factor.	63
4.1	Hot spot stress concentration factor	107
6.1	Chemical composition and mechanical properties of CSA G40.21 M 350 WT steel.	144
6.2	Schedule of variables for crack-growth-rate data generation.	147
6.3	Initial and final crack-growth-rates and stress intensity factor ranges for CT specimens.	152
6.4	Coefficients C and m for CT specimens.	162
7.1	Estimated fatigue life of tubular T-joint in air due to axial load.	186
7.2	Estimated fatigue life of tubular T-joint in air due to in-plane bending load.	186
7.3	Estimated fatigue life of tubular T-joint in sea water due to axial load.	187
7.4	Estimated fatigue life of tubular T-joint in sea water due to in-plane bending load.	187
8.1	Joint parameters of the specimen tested.	191

LIST OF ILLUSTRATIONS

Figure No.	Title	Page No.
1.1	Schematic representation of fatigue-crack-growth.	4
2.1	Non-dimensional parameters of tubular joint.	20
2.2	Three modes of cracking	20
2.3	Small scale specimens used for fatigue-crack-growth-rate determination.	29
3.1	Regions of T-joint model for mesh generation.	43
3.2	Node numbering sequences.	45
3.3	Rotation of coordinate system axes for mesh generation.	45
3.4	Triangular area coordinate.	48
3.5	Bending element.	48
3.6	Membrane element.	52
3.7	Assembly of six degrees-of-freedom.	52
3.8	Assembly of triangular element to form quadri-lateral element.	58
3.9	Schematic of T-joint model.	59
3.10	Finite element mesh for different region.	60
3.11	Finite element mesh for the joint.	61
3.12	Deformed joint due to axial compressive load.	64
3.13	Deformed joint due to in-plane bending load.	65
3.14	Characteristic lines of the joint.	66

Figure No.	Title	Page No.
3.15	Principal stress distribution: brace, line 1 - axial load.	67
3.16	Principal stress distribution: brace, line 1 - in-plane bending.	68
3.17	Principal stress distribution: brace, line 2 - axial load.	69
3.18	Principal stress distribution: brace, line 2 - in-plane bending.	70
3.19	Principal stress distribution: chord, line 3 - axial load.	71
3.20	Principal stress distribution: chord, line 3 - in-plane bending.	72
3.21	Principal stress distribution: chord, line 4 - axial load.	73
3.22	Principal stress distribution: chord, line 4 - in-plane bending.	74
3.23	Schematic of displacements on the plane of symmetry(Irvine 1980).	76
3.24	Modified principal stress distribution after axial shifting: brace, line 1 - in-plane bending.	78
3.25	Modified principal stress distribution after axial shifting: brace, line 1 - axial load.	79
3.26	Modified principal stress distribution after axial shifting: brace, line 2 - axial load.	80
3.27	Modified principal stress distribution after axial shifting: brace, line 2 - in-plane bending.	81
4.1	Modelling of weld at chord/brace intersection.	83
4.2	Three dimensional finite element mesh for the joint.	85

Figure No.	Title	Page No.
4.3	Three dimensional 8-noded element.	86
4.4	Six-noded prism element.	86
4.5	Rezone section at saddle point.	93
4.6	Rezone section at crown point.	93
4.7	Plate-to-solid element transition.	94
4.8	Expanded view of plate-to-solid element transition.	95
4.9	Shell surface local coordinate system definition.	95
4.10	Translation of surface node due to rotation of plate node about Y-axis.	97
4.11	Translation of surface node due to rotation of plate node about Z-axis.	97
4.12	Forces transformed to local shell surface coordinate system.	101
4.13	Use of spherical trigonometry to solve for azimuth angle b.	101
4.14	Three dimensional finite element mesh for rezoned section of the joint at saddle point.	105
4.15a	Maximum surface stress variation at saddle point due to axial compressive load.	108
4.15b	Stresses along line-4 (Parkhouse 1981).	109
4.15c	Stresses along line-2 (Parkhouse 1981)	110
4.15d	Transverse midsection strain levels for the TEXGAP-3D solutions (Morgan 1979).	111
4.15e	Stress distribution along line-4 due to axial load.	112

Figure No.	Title	Page No.
4.15f	Stress distribution along line-2 due to axial load.	113
4.16	Stress distribution across the weld and brace wall at saddle point due to axial compressive load.	114
4.17	Maximum surface stress variation at crown point due to axial compressive load.	116
4.18	Stress distribution across the weld and brace wall at crown point due to axial compressive load.	117
4.19	Maximum surface stress variation at crown point due to in-plane bending load.	118
4.20	Stress distribution across the weld and brace wall at crown point due to in-plane bending load.	119
4.21	Comparison of entire joint model and rezoned section analyses results along line-4.	120
4.22	Comparison of entire joint model and rezoned section analyses results along line-2.	121
5.1	Singular wedge element.	125
5.2	Various singular elements developed to model crack front region.	128
5.3	Schematic arrangement of three types of element around crack front.	129
5.4	Three-dimensional discretization of the crack region.	130
5.5	Fracture modes.	131
5.6	Stress variation along chord surface at saddle point in presence of weld toe crack due to axial load.	133

Figure No.	Title	Page No.
5.7	Stress variation along chord surface at crown point in presence of weld toe crack due to in-plane bending load.	135
5.8	Stress variation along brace surface at saddle point in presence of weld toe crack due to axial load.	136
5.9	Stress variation along brace surface at crown point in presence of weld toe crack due to in-plane bending load.	137
5.10	Through-thickness stress variation in front of weld toe crack at saddle point due to axial load.	138
5.11	Through-thickness stress variation in front of weld toe crack at crown point due to in-plane bending load.	139
5.12	Comparison of computed Y_σ with reported experimental variation.	141
6.1	Compact tension specimen (ASTM E647-81).	145
6.2	CT specimen test set-up.	148
6.3	Schematic diagram of CT specimen under test with recirculation system.	149
6.4	Fractured CT specimens.	153
6.5	Crack growth data in air: R = 0.1, f = 0.2 Hz and T = -15 to 4°C.	154
6.6	Crack growth data in air: T = 4°C, R = 0.1 and f = 0.05 to 2.0 Hz.	155
6.7	Crack growth data in air: T = 4°C, f = 0.2 Hz and R = 0.05 to 0.3.	156
6.8	Crack growth data in sea water: T = 0°C, f = 0.2 Hz and R = 0.05 to 0.3.	157

Figure No.	Title	Page No.
6.9	Crack growth data in sea water: T = 0°C, R = 0.1 and f = 0.05 to 0.2 Hz.	158
6.10	Crack growth data in sea water: T = 0 and 21°C, R = 0.1 and f = 0.2 Hz.	159
6.11	Crack growth data in sea water under sinusoidal and saw tooth loading: T = 0°C, R = 0.1 and f = 0.1 Hz.	160
6.12	Effect of temperature on fatigue crack-growth-rates in air: R = 0.1, f = 0.2 Hz and T = -15 to 4°C.	163
6.13	Effect of frequency on fatigue crack-growth-rates in air: T = 4°C, R = 0.1 and f = 0.05 to 2.0 Hz.	164
6.14	Effect of load ratio on fatigue crack-growth-rates in air: T = 4°C, f = 0.2 Hz and R = 0.05 to 0.3.	165
6.15	Effect of temperature on fatigue crack-growth-rates in sea water: T = 0 and 21°C, R = 0.1 and f = 0.2 Hz.	166
6.16	Effect of frequency on fatigue crack-growth-rates in sea water: T = 0°C, R = 0.1 and f = 0.05 to 0.5 Hz.	167
6.17	Effect of load ratio on fatigue crack-growth-rates in sea water: T = 0°C, f = 0.2 Hz and R = 0.1 to 0.3.	169
6.18	Effect of loading wave form on fatigue crack-growth-rates in sea water: T = 0°C, R = 0.1 and f = 0.1 Hz.	170
6.19	Fatigue crack-growth-rates in air and sea water: R = 0.1 and f = 0.05 Hz.	171
6.20	Fatigue crack-growth-rates in air and sea water: R = 0.1 and f = 0.1 Hz.	172

Figure No.	Title	Page No.
6.21	Fatigue crack-growth-rates in air and sea water: R = 0.1 and f = 0.2 Hz.	173
6.22	Fatigue crack-growth-rates in air and sea water: R = 0.1 and f = 0. 5 Hz.	174
6.23	Fatigue crack-growth-rates in air and sea water: R = 0.2 and f = 0.2 Hz.	175
6.24	Fatigue crack-growth-rates in air and sea water: R = 0.3 and f = 0.2 Hz.	176
6.25	Comparison of fatigue crack-growth-rate in air with other published results.	178
6.26	Comparison of fatigue crack-growth-rate in sea water with other published results.	179
6.27	Variation of m versus C.	180
7.1	Comparison of estimated fatigue life of tubular T-joint with reported experimental S-N data.	189
8.1	Test frame.	192
8.2	Schematic arrangement of strain gauges on outer and inner surfaces of chord.	194
8.3	Schematic arrangement of ACPD probes on the specimen.	195
8.4	Block diagram for data acquisition system.	197
8.5	Variation of uniaxial strain and brace wall thickness.	198
8.6	Variation of hot spot stress concentration factor along the intersection.	200
8.7	Variation of stress concentration factor along chord/brace surface at saddle point.	201

NOMENCLATURE

a	Crack length
a_i	Initial crack depth, instantaneous crack length
a_f	Critical crack depth
$\{a_1\}$	Element nodal displacement vector
$\{a_2\}$	Element generalized coordinate vector
B	Compact tension specimen thickness
b	Azimuth angle
C	Coefficient in Paris' equation
D	Diameter of chord
d	Diameter of brace
E	Young's modulus of elasticity
F_x, F_y, F_z	Forces at plate nodes at transition
F_{xi}, F_{yi}, F_{zi}	Forces at inner surface nodes of solid elements at transition
F_{xo}, F_{yo}, F_{zo}	Forces at outer surface nodes of solid element at transition
$\{F_1\}$	Element nodal load vector
$\{F_2\}$	Element load vector corresponding to generalized coordinates
$\{f\}$	Force vector
$\{f_b\}$	Flexural force vector
$\{f_m\}$	Membrane force vector

g_j	Incompatible shape function
[J]	Jacobian matrix
K	Stress intensity factor
K_I, K_{II}, K_{III}	Stress intensity factors for modes I, II, III, respectively
[K],[k]	Stiffness matrices for solid and plate elements, respectively
$[k_b]$	Flexural element stiffness matrix
$[k_m]$	Membrane element stiffness matrix
L	Length of chord
L_i, L_j, L_k	Triangular area coordinates
M_x, M_y, M_z	Moments about x, y and z axes
m	Coefficient in Paris' equation
N	Number of loading cycles
N_i	Shape function, instantaneous number of loading cycles
$\hat{n}_y, \hat{n}_z$	Projections of position vector onto x-z and x-y planes, respectively
p	Small positive correction factor
q	Small positive correction factor for weld profile
r	Radial distance from the crack front
S	Hot spot stress range
T	Chord wall thickness
t	Shell thickness, brace wall thickness

u,v,w	Displacements in x, y and z directions
u_I	Inner surface node's displacement in x-direction
u_O	Outer surface node's displacement in x-direction
$u_O(\theta_y)$	Displacement component of solid element node due to y-rotation of plate element node
$u_O(\theta_z)$	Displacement componentof solid element node due to z-rotation of plate element node
V	Element volume
W	Compact specimen's net width
x_i,y_i,z_i	Coordinates of inner solid element's node
x_o,y_o,z_o	Coordinates of outer solid element's node
α,β,γ	Angles made by position vector with x, y and z axes; joint non-dimensional parameters; angles through which x, y and z axes are rotated for mesh generation
$\alpha_j,\beta_j,\gamma_j$	Generalized displacement coordinates
Δ	Area of triangle, shift in brace stresses
ν	Poisson's ratio
$\{\epsilon\}$	Strain vector
$\{\sigma\}$	Stress vector
$\theta_x,\theta_y,\theta_z$	Rotations about x, y and z axes
$\{\delta\}$	Displacement vector
ΔK	Stress intensity factor range
da/dN	Crack-growth-rate

ΔP	Load range
λ_{yx}	Inclination made by $\hat{n}_y$ with z-axis
λ_{zx}	Inclination made by $\hat{n}_z$ with y-axis
SCF	Stress concentration factor
SNCF	Strain concentration factor

CHAPTER 1

INTRODUCTION

1.1 Background

The offshore exploration for oil has confronted the designers of fixed and floating structures with more complex fatigue problems. These offshore structures are subjected to alternating wave loads. In particular, the joints (intersections of tubular members) experience very high stresses due to geometric discontinuities in welded connections, and the local stress concentration at brace-chord intersections plays a major role in determining the fatigue life of the joints. The current procedure for the design of steel offshore structures against fatigue requires an accurate knowledge of the stress distribution in tubular joints whereas the traditional design based on the S-N curves required only the calculation of maximum hot spot stress or strain. Moreover the method currently employed for fatigue life estimation assumes that no defects or flaws are present in the structure prior to service and then makes allowance for both crack initiation and propagation. But this method proves to be inefficient owing to the following reasons. The nature of offshore structures is such that the regions of high stress concentration and residual stresses coincide with the areas where flaws are most likely to be present. In addition, the stress required for fatigue crack initiation is much higher than that necessary for crack propagation. Consequently, if a flaw is present prior to service, crack growth will be rapid which will give a much shorter fatigue life than

that given by the currently employed methods.

In view of the above, it would be more appropriate to assume that incipient surface cracks are always present in welded tubular joints. These incipient surface cracks will grow during service, eventually causing failure of the member. Computations based on this assumption could be used to estimate the life of the structure or the inspection interval before repair is necessary. The linear fracture mechanics approach based on the stress concentration existing near the crack tip and the use of a suitable fatigue crack growth expression provides a more realistic method for fatigue life determination. The investigation of crack propagation at the chord-brace intersection, in the weld toe region of tubular joints, is a complex three-dimensional problem because the crack propagates rapidly along the weld, while the penetration into the thickness direction is relatively slow.

The theoretical stress analyses produced so far have shown that the stresses in front of the crack can be characterized by a term known as the stress intensity factor K. The uncertainty in predicting the stresses (at the intersection) and the fatigue life, due to the extremely complex geometry near the intersection, has prompted initiation of extensive research programmes. As a result of the difficulties experienced in obtaining a closed-form solution for the stress intensity factors of various structural configurations, several approximate three dimensional methods such as direct potential and finite element methods have been used for the stress analysis of finite-thickness fracture specimens containing through-thickness cracks. These results cannot directly be used by the designer

since the results vary for different specimen configurations, and a separate analysis has to be carried out for the specimen configuration under consideration.

The stress distribution close to the crack front is dominated by the presence of the stress-free crack surfaces at the crack tip. The square root singularity is present in the existing solutions, regardless of the other features of the geometry of the member. The magnitude of each component of the crack tip stresses is directly proportional to the stress intensity factor K.

Observation of fatigue crack growth indicates that a certain amount of growth occurs in each cycle. The fracture of small ligaments ahead of the crack tip can be thought of as a minute brittle fracture occuring on each tensile load application. The crack growth rate process can be broken into three states (Fig. 1.1): (i) threshhold - below a certain stress intensity level cracks will not grow (this is analogous to crack initiation in the fatigue process description), (ii) stable crack propagation, and (iii) rapid or unstable crack propagation (analogous to the failure portion of the fatigue process). The stable crack propagation stage is of most interest to the designer carrying out an analysis to determine the fatigue life of a joint.

1.2 Purpose of this Research

The earlier S-N curves used in the design of offshore structures were developed from onshore welded fabrication design curves and used a nominal member stress which enabled the fatigue life to be quickly assessed. With time, it was necessary

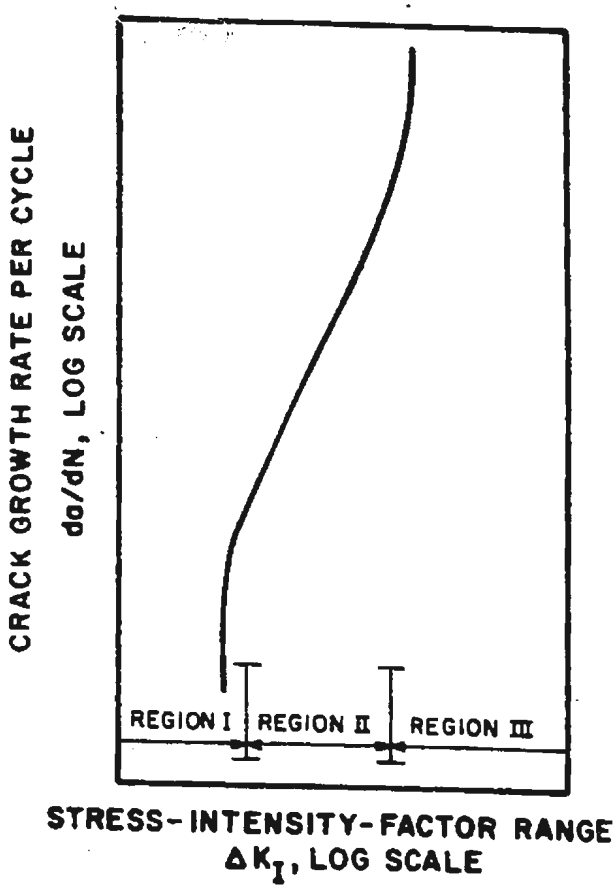

Fig. 1.1 Schematic representation of fatigue-crack-growth.

to include in the design stress such effects as weld toe stress concentration and the high stresses produced by the local bending of the chord and the brace at the intersection. To date many long term tests on full scale steel joints have been completed, and further tests are underway to produce S-N curves for the design of tubular joints. Factors being studied include thickness, internal/external stiffeners, environment and post-weld heat treatment.

Fracture mechanics can be used effectively to establish the criteria for the design, inspection and repair of offshore platforms. The fracture mechanics design methodology assumes that a crack-like defect exists at the intersection of the brace and the chord. The rates of extension of this crack along the surface and through the thickness are dependent on the initial crack shape, the mean stress, the type of loading and the stress concentration factors at the weld toe. The application of linear elastic fracture mechanics for fatigue life prediction is based on the assumption of linear elastic material behaviour near the crack tip. While the stress and strain distributions around the crack tip control the crack initiation and propagation and remote boundaries, the nature of applied loading and environment affect only the intensity of the local stress field. The initial defect size a_i, is normally considered as a surface imperfection due to welding, and its value significantly influences the accurate determination of fatigue life.

The fracture mechanics approach to fatigue life estimation considers many parameters compared to the traditional S-N curve and the PM cumulative damage rule methods, viz.,

(a) the initial depth of defect, a_i

(b) the critical crack depth defining the failure of the joint, a_f

(c) the stress intensity factor, K, for the crack

(d) the fatigue crack growth data for the material subjected to actual environmental service loading.

The main goal of a fracture mechanics approach (to assess the strength of structures containing crack-like defects) is to determine the so-called stress intensity factor, which is a function of the structure's geometry and the load character. This quantity has been evaluated for a number of idealized situations by analytical techniques, and these values provide useful guidance for designers. Unfortunately, the welded tubular joints are of such complex shapes that the determination of the stress intensity factor necessitates recourse to some approximate numerical approach, and the finite element method is very appropriate for this task. To make use of the stress intensity factor in the fatigue life prediction of tubular joints, a knowledge of crack-growth data for the material is essential. The objective of the present investigation is to predict the fatigue life of tubular joints analytically, knowing the crack growth characteristics of the base metal in various environmental conditions.

1.3 Scope of the Investigation

As will be shown in Chapter 2 there is a need to develop a generalized finite element method to study the stress fields in the hot spot area of tubular joints, considering the through-thickness variation and the effect of shallow weld toe crack

on stress redistribution, and to determine the stress intensity factors; this study seeks to fill this need. The analytical study includes the development of computer software for a two-dimensional analysis of uncracked tubular joints and for a three-dimensional analysis of cracked and uncracked tubular joints. To study the effect of weld toe cracks on the stress redistribution and to determine the corresponding stress intensity factors, the joint is modelled using special singular elements along with solid incompatible elements. The crack growth characteristics of the base metal G40.21 M 350 WT, which has been proposed for the Canadian East Coast offshore region, is determined experimentally (using CT Specimens), and this data is used to predict the fatigue life of tubular joints analytically. The analytically predicted fatigue life is verified experimentally by testing a prototype tubular joint. In order to achieve this goal, a physical problem is selected, and the above-mentioned procedures are carried out sequentially.

In Chapter 3, a two-dimensional finite element analysis of a tubular T-joint is discussed. The joint is discretized using an automatic mesh generation technique. Triangular and quadrilateral elements are used for the analysis of the joint. Plane stress elements are used to account for membrane stiffness while plate bending elements are used to account for flexural stiffness. The distribution of surface stresses along the critical sections and the stress concentration factors are investigated.

Chapter 4 describes a three-dimensional analysis of the joint which accounts for the through-thickness variation of stresses. The joint is modelled using 8-noded

and 6-noded incompatible elements to improve flexural characteristics. In order to reduce computer storage requirements as well as solution costs (due to the large number of degrees-of-freedom associated with the entire joint analysis) the rezone technique is used to analyse the hot spot region. The region of high stress gradient and the weld zone are reanalysed using force and displacement methods. The boundary force/displacement values at the plate-to-solid-element transition zone, obtained from the two-dimensional analysis, are distributed between the outer and inner surface nodes of the solid elements in such a way as to maintain the boundary force equilibrium and the displacement compatibility. The results obtained from both the entire and the rezoned analyses are compared with the two dimensional analysis.

The effect of a weld toe crack on the stress distribution in the tubular joint is discussed in Chapter 5. The joint is discretized using special singular elements around the crack front. The singular elements are surrounded by solid incompatible elements. By comparing the stresses at the crack tip obtained from this analysis with the theoretical solutions available, the stress intensity factors are determined.

To make use of the stress intensity factor in the fatigue life prediction a knowledge of the crack growth data for the material is essential. The compact tension specimens (CTS) are tested both in air and in sea water to evaluate the effect of colder sea water on the fatigue crack propagation. The effects of load ratio, frequency and temperature on the crack growth rate under constant ampli-

tude loading are discussed in Chapter 6.

Based on the fatigue crack growth rate pattern in the base metal for different environmental conditions and the stress intensity factor obtained from the finite element analysis, the fatigue life of the joint is predicted using linear fracture mechanics approach in Chapter 7.

In order to verify the proposed model, a prototype test is carried out on a large scale tubular T-joint. The results of this test and the comparison with numerically computed values are given in Chapter 8. The contribution to the field of research, the general conclusions and the scope for the further research are outlined in Chapter 9.

CHAPTER 2

LITERATURE REVIEW

2.1 Introduction

In offshore structures, which are generally of tubular construction, the intersection of the chord and the brace induces high local stresses adjacent to the connecting weld, and it is here that fatigue damage will generally occur. Therefore, the fatigue analysis is highly dependent on the accuracy with which this high local stress at the hot spot can be calculated. During the past decade there has been considerable development in the method used for the assessment of the fatigue of offshore structures. Extensive research programmes have been carried out in the United Kingdom and Europe to determine the appropriate S-N curve to be used in design and on the definition of stress and life. To understand the effect of thickness and environment on fatigue life, many researchers have increasingly used fracture mechanics concepts to explain the crack growth behaviour of tubular joints.

The study of fatigue crack growth around the weld toe region of a tubular joint is an extremely complex problem, and the experimental and analytical investigations of this problem are both costly and time consuming. For this reason, much of the work to date has been concerned with the testing and analysis of welded plate specimens. Much more analytical and experimental work needs to be carried

out before the fracture mechanics procedures for tubular joints can be formalized into a final design methodology. The available literature related to the present research has been reviewed under two distinct categories, e.g., analytical and experimental investigation.

2.2 Analytical Investigation

Because of the relative complexity of the geometrical configuration of tubular intersections as well as the thin-shell theory governing their behaviour, reliable prediction of the stresses in such joints by analytical techniques has proven to be difficult. The finite element method seems to offer the best natural solution for modelling complex geometries and boundary conditions. Early attempts to apply finite element methods to the stress analysis of tubular intersections were somewhat hindered by the computational demands generated by too many elements. This difficulty was overcome by third-generation computers with their larger central memory and faster computing speed.

The finite element method would at first appear to be ideal for studying the elastic behaviour of structures containing crack-like defects. However, problems arise when one tries to model the near crack tip stress field using finite elements. This is due to the singularity at the crack tip, which in practice has a small plastic region at its tip. Finite elements in their basic form are unable to represent this crack tip singularity and thus produce poor results when applied to fracture problems, unless extremely fine meshes are used. Many attempts have been made to overcome the inability of finite elements to represent the crack tip singularity

by developing special elements which incorporate the required stress singularity in their formulation.

The analytical investigation can be reviewed in four separate subsections i.e., (a) mesh generation technique - (through which the input data for any finite element analysis are generated), (b) analysis of shell structures without crack and the related finite element procedure, (c) semi-empirical parametric equation - (used to determine the hot spot stress concentration in tubular joints), (d) analysis of elastic continua with cracks and the related finite element procedure.

2.2.1 Mesh generation

Computer-oriented mesh generators, which serve as pre-processors to finite element programs, have been developed by several investigators to reduce the amount of time involved in the subdivision of a complex structure into finite elements. 'Mesh generation' refers to the automatic generation of nodal coordinates and nodal and element numbers based on a minimal amount of user-supplied data. Automation reduces errors, and the solution accuracy may increase because a computer-generated mesh is more regular than one manually prepared by a user. Such codes are generally not available to an engineer in a small or medium size firm or to a researcher in view of the proprietary nature of most of the codes.

Felippa(1972) developed a Fortran subroutine to generate the alphanumeric image of an arbitrary two-dimensional finite element mesh on a line printer. The plotting can be used for fast on-line display of nodal points, elements, boundary

conditions and loads during the input data processing stage of a finite element analysis. A code was devised by Adamek(1973) for automatic mesh generation schemes, utilizing the techniques of mapping from a local non-dimensional system of reference into the global cartesian system of reference. An interactive graphic system was developed by Bousquet and Yates(1973) for use with the finite element programs in a production analysis environment.

A relatively straight forward mesh generation program based on the isoparametric mapping concept was developed by Durocher(1979). The program generated node numbers, coordinates, and element connectivity information for five commonly used 2-D elements. User-defined superelements were subdivided into 3-node/6-node triangular or into 4-node/8-node isoparametric quadrilateral elements. A procedure for the interactive modelling of two and three dimensional finite element grids was presented by Hoffman(1983). The grids were generated by specifying the key points, boundary or intersection lines, surfaces and regions. The general process of displaying a two dimensional representation of a three dimensional model was discussed. Based on the maximum model dimension, the dimensions of the displayed area and the position on the screen at which the object is to be placed, an initial screen/object orientation ratio was determined.

2.2.2 Finite element stress analysis

Finite element concepts for the representation of generally curved thin shells can be classified into three groups, i.e., the faceted form using flat elements, curved shell elements formulated directly from appropriate thin shell theories and

isoparametric solid elements specialized to tackle thin shells. The generally better performance of the higher-order elements cannot always be exploited and often is outweighed by their complexity in use. Clough and Tocher(1965) studied the relative accuracy provided by seven different types of finite elements in the approximate analysis of plate bending. The stiffness matrices for three rectangular and four triangular elements were considered. Analyses were made with each of these elements for the central deflection in eight different rectangular plate systems using five different mesh sizes. The twelve-term polynomial rectangular element and the compatible triangular element were found to give results which converged towards the correct answer as the mesh size was refined; but the compatible triangular elements gave relatively poor results for very coarse mesh systems, being too stiff. Clough and Johnson(1968) presented an approximate numerical analysis procedure for solving thin shells. The shell was idealized as an assemblage of triangular flat plate finite elements having both membrane and flexural stiffness properties. Five examples were presented demonstrating the versatility of the procedure for analyzing different shell configurations. Ahmad et al(1970) presented a general formulation for curved, arbitrarily shaped, thick shell finite elements.

Five typical joints were modelled by Greimann et al(1973) using finite elements: three by manually laying out the mesh and two using an automatic mesh generation program. The finite element idealizations were then used as input in the computer program STARDYNE. The results were compared with experimental stress analysis results of scale models and were found to agree to within 20

percent. Miller and Trammell(1974) developed a computer program, as a design tool, for analyzing a ring-stiffened tubular joint with multiple non-intersecting branch members.

Acceptable triangular membrane element formulations were given for various degrees of higher-order elements, using either the displacement function itself or the displacement function and various orders of its derivatives. One could employ a simple formulation based on a complete cubic polynomial (Thomas and Gallagher 1974) or a highly accurate but computationally expensive formulation such as that based on a 21-term polynomial (Dawe 1975). Irons(1976) developed semiloof curved shell elements which have three translational degrees of freedom at corner and mid-side nodes and one normal rotation at the two Gauss points along each side.

There are a number of general purpose programs available for shell analysis, e.g. ASAS, ASKA, NASTRAN, STRUDL. The ASAS (Atkins Stress Analysis System) has flat faceted, quintic shell and semiloof curved shell elements. The flat facet element combines the constant strain triangle and the conforming linear bending strain triangle. It has six degrees of freedom at each vertex. The quintic shell element is a higher-order curved shell element formulated directly from thin shell theories. A total of 54 geometric parameters are required to describe each element. The semiloof elements are general curved triangles and quadrilaterals developed by Irons(1976). The ASKA (Automatic System for Kinematic Analysis) library has three shell elements, e.g., three noded flat shell element, six noded and

three noded curved shell elements. For the displacement the six-noded element uses a complete fifth-order polynomial whereas the three-noded curved element uses an incomplete fifth-order polynomial. The NASTRAN (NAsa STRuctural ANalysis) program has facet type flat, triangular and quadrilateral shell elements. The STRUDL (STRUctural Design Language) library has two shallow shell elements, e.g. three and four node elements. These elements have three translational and two rotational degrees of freedom at each node.

Liaw et al(1976) described the application of 3-D isoparametric elements to the analysis of welded tubular connections. It was concluded that the three-dimensional isoparametric elements, when implemented in an efficient and versatile computer program, could provide more accurate values of stress concentration factors than would be possible using flat plate finite elements. A new procedure using curved thick shell finite element was developed overcoming the approximation of the geometry of the structure and the neglect of shear deformation. Several illustrated examples ranging from thin to thick shell applications were given to assess the accuracy of the solution attainable (Zienkiewicz 1977). Radenkovic(1981) obtained the stresses for a T-joint in tension using thin/thick shell and brick elements. The magnitudes of stress were almost the same for all three element cases. Several large codes, i.e., ASAS, SESAM 69, SATE and TITUS were used for the stress analysis during the course of the research on tubular/shell structures. But little direct comparison was established between the codes.

Two types of three-dimensional isoparametric elements were used by Hoffman and Sharifi (1980) for tubular joint analysis. Various incompatible modes were introduced into the stiffness formulations of these elements to improve their flexural behaviour. Three and one incompatible even shape functions were incorporated into the 8-noded brick and the 16-noded thick shell elements, respectively. In the irregular mesh, the incompatible brick element was more satisfactory than the basic element. Parkhouse(1981) suggested an improved modelling of tube wall intersections using brick elements. The joints away from the intersection were modelled using an 8-noded quadrilateral curved shell element whereas the intersection area was modelled using a 20-noded brick element. Structural continuity between the two types of element was achieved by the sharing of the translational degrees of freedom at common nodes and by additional constraints imposed on certain degrees of freedom for effective flexural continuity. The results were compared with thin-shell analysis.

Dijkstra(1981) compared the results of strain measurements and finite element calculations of X-joints. The SATE (Structural Analysis using Thin shell finite Elements) and ASKA programs were used for the analysis of the joints. For joints with thickness ratio 0.5, all results were close together, and the maximum difference at the initiation point was 15 percent. But for joints with equal thickness, the calculated values were overestimated by 30 percent. Gibstein and Moe(1981) compared numerical and experimental stress analysis results for T, Y and K-joints. The analysis was carried out by means of 'NV332', which is a thick/thin shell program using 8-node superparametric quadrilateral shell

elements. It was observed that the stress distribution and stress concentration factor (SCF) values for the Y and K-joints were sensitive to the boundary and load conditions in the analysis. The calculated SCF values for the chord side, based on the maximum stress values at the nearest Gaussian point to the intersection, were in good agreement with the experimental data. But for the brace the difference was found to be 20 percent.

Shiyekar et al(1982) used the degenerate 20-node isoparametric brick element for the stress analysis of a T-joint. The ill-conditioned stiffness matrix due to the higher stiffness properties in the thickness direction in comparison to the other two directions was eliminated. The stiffness properties of the joint were determined ignoring the strain energy of the stresses normal to the midsurface of the shell.

2.2.3 Parametric formulae

The fatigue performance of tubular joints is a function of the stress range to which the joint is subjected. The highest stress range will occur at the point around the brace/chord intersection where the largest stress concentration factor (SCF) occurs. Therefore the determination of these geometric SCFs, which are themselves a function of the joint stiffness and the applied loading, has occupied the increasing attention of many investigators. These geometric stress concentration factors are estimated from parametric equations that are based on either extensive finite element stress analyses or experimental data from acrylic model tests. Existing SCF parametric formulae cover only single plane simple joint

types, and there are no such formulae for complex joints or loading.

Based on the results of experimental and numerical analyses, parametric formulae were determined and presented in the familiar form (Fig. 2.1)

$$SCF = C\,\alpha^{n1}\,\beta^{n2}\,\gamma^{n3}\,\tau^{n4}\,\varsigma^{n5}\,(\sin\theta)^{n6} \qquad (2.1)$$

where α, β, γ, τ, ς are non-dimensional joint parameters (defined in Fig. 2.1), C, n1, n2, n3, n4, n4, n6 are constants and θ is the intersection angle between the members. Many investigators presented an empirical equation for the determination of the SCFs e.g. Beale and Toprac(1967), Visser(1974). But the most significant contribution was made after this. Kuang et al(1977) developed the most complete collection of formulae applicable to (i) T and Y-joints under axial loading, (ii) K and KT-joints under balanced axial loading and (iii) K-joints with in-plane bending applied to one brace. These formulae were based on finite element analysis results and gave the SCFs at the location adjacent to the intersection line of the mid-surface of the brace and chord. Wordsworth and Smedly(1978) produced parametric formulae covering T, Y and X-joints based on acrylic model test results. Based on their finite element analyses, Gibstein(1978) also produced parametric formulae, which are applicable to T-joints.

Irvine(1981) compared the performance of two semi-empirical parametric equations for the stress concentration factors. It was concluded that the SCFs obtained using Smedley's equation were more conservative than those of Kuang. Both sets of equations could underpredict SCF values for axial and out-of-plane

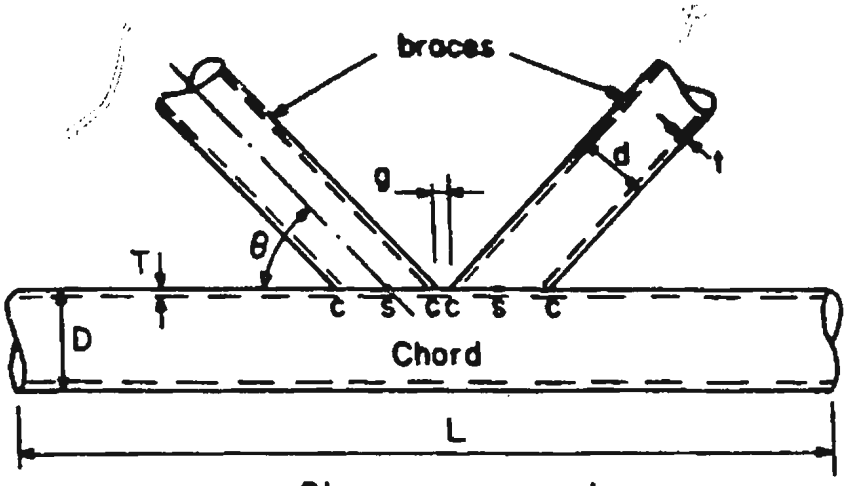

$$\alpha = \frac{2L}{D} \qquad \tau = \frac{t}{T}$$

$$\beta = \frac{d}{D} \qquad \zeta = \frac{g}{D}$$

$$\gamma = \frac{D}{2T}$$

c and s are crown and saddle positions respectively

Fig. 2.1 Non-dimensional parameters of tubular joint.

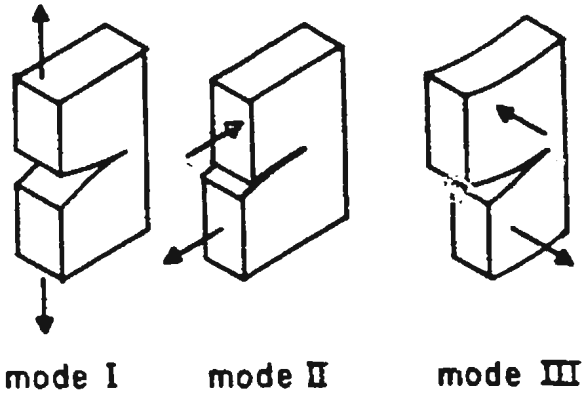

Fig. 2.2 Three modes of cracking

bending load cases in joints with equal wall thickness. Generally, Kuang's equation underpredicted SCF values in X-joints. For complex joints, the designers have to use the simple joint formulae as best as they can. Factors are applied to terms within the formulae to account in some way for the geometrical complexity of the joints with no real justification for the actual factors used. Existing parametric formulae suitably factored are utilized for complex joints, e.g., ring-stiffened joints (Lloyd's Register 1983). For an out-of-plane bending load the effective thickness of the chord wall (which will give equivalent area of chord and stiffener) is substituted in the existing parametric formulae, whereas for in-plane and axial load cases, individual consideration is required. For overlapped joints, the lower limit for the separation between the braces is substituted into the existing formulae.

Dharmavasan and Dover(1984) presented a new set of stress distribution formulae for predicting the stresses in simple joints under multi-mode loading. Their formulae overpredicted the SCFs by as much as 20 percent. Efthymiou and Durkin(1985) developed parametric equations for estimating the SCFs in overlapped tubular T, Y and K-joints under all relevant load cases, based on finite element stress analysis results. Significant reduction in chord SCFs for overlapped K-joints under balanced axial loading was observed. The benefit of overlapping was more pronounced in joints with 90°/45° brace inclinations than for 45°/45° inclinations. No beneficial effect was observed in overlapped K-joints under in-plane bending loads. Edwards and Fessler(1985) presented parametric equations for cast tubular T and Y-joints, based on the strain-gauged and photo-elastic model tests,

of the form

$$SCF = C\ f(\alpha)\ f(\beta)\ f(\theta)\ \gamma^{n1}\ \rho^{n2}\ \tau^{n3} \tag{2.2}$$

for several positions around the braces due to axial, in-plane and out-of plane bending load cases. In Eqn. 2.2, α, β, γ, ρ, τ are non-dimensional joint parameters, C, n1, n2, n3 are constants, and θ is the angle between the members. The SCFs of these joints were 40-60 percent of the predicted values for similar welded joints.

2.2.4 Analysis of crack problems

A crack in a solid can be stressed in three different modes (Fig. 2.2). Normal stresses give rise to the 'opening mode' denoted as mode I; the displacements of the crack surfaces are perpendicular to the plane of the crack. In-plane shear results in mode II or the 'sliding mode'; the displacements of the crack surfaces are in the plane of the crack and perpendicular to the leading edge of the crack. The 'tearing mode' or mode III is caused by out-of-plane shear; crack surface displacements are in the plane of the crack and parallel to the leading edge of the crack. The quantitative measure of the severity of a crack is given by the stress intensity factor, K, which characterizes the intensity of the stress field in a small region surrounding the leading edge of the crack.

Finding the stress intensity factor in front of a crack is a very heavy numerical task. Even with the best algorithms, the accuracy of the calculation is not always satisfactory. It should also be noted that the stress intensity factor depends

heavily on the boundary conditions fairly distant from the crack front, so that for a complex geometry it would be necessary to take into account the whole structure of the joint. For a three-dimensional elastic continua with cracks, Kassir and Sih(1966) obtained the stress field near the crack front by solving Navier's equations of equilibrium subjected to appropriate boundary conditions. Due to the complexity of the problem, stress fields around the crack front in a three-dimensional continua were available for only a few restricted classes of problems such as penny-shaped and elliptic cracks in an infinite solid. Hartranft and Sih(1969) showed that the stresses σ_{xx} , σ_{yy} and σ_{xy} had a square-root singularity at the crack front, and σ_{zz} and the two transverse shear stresses σ_{yz} and σ_{xz} were finite throughout the plate. For specimens of finite thickness with through-thickness cracks, some attempts were made by Sih(1971) to obtain the stress distribution close to the crack front, but the solutions have been found to be intractable in closed-form.

Using triangular singular elements, Tracey(1971) obtained, for two typical cracked configurations, stress intensity factors which were within 5 percent of the accepted values. Blackburn(1973) proposed a six-node triangular element which had terms in its displacement shape functions which were proportional to the square root of the distance along lines emanating from a singular vertex. Tracey(1974) formulated a finite element model for the three-dimensional analysis of an elastic continua with a crack front state in combined opening and sliding modes. Special elements which embed the inverse square-root singularity along the crack front were suggested. The singular element used was a six-node wedge

focused onto the front. The crack front was taken as rectilinear, and a group of singular elements were used about each segment. Adjacent to the singular elements, eight node brick elements were used. A compact tension plate specimen was analyzed based on the above formulation.

Bergan and Aamodt(1974) obtained the stress intensity factor for a semi-elliptical surface crack in a plate by computing the strain energy release rate for the crack. They used a 20-node isoparametric solid element in modelling the plate. Barsoum(1976) proposed a general curved element of arbitrary shape for the crack analysis of both thick and thin shells. The singularity in these elements was achieved by placing the mid-side nodes near the crack tip at the quarter point. A simply supported rectangular cracked plate in bending was solved for the stress intensity factor, and the error was 5 percent.

Raju and Newman(1977) calculated the stress intensity factors for most of the commonly used notched specimens using a three-dimensional finite element formulation. A three-dimensional singular element in the shape of a pentahedron, similar to that developed earlier by Tracey, was used at the crack front. A nodal force method was developed and used to evaluate the opening mode stress intensity factors along the crack front. The effects of specimen thickness and length on the stress intensity distributions were investigated. Blackburn and Hellen(1977) calculated the stress intensity factors for an edge-cracked plate containing penny-shaped and semi-circular surface cracks and subjected to opening and tearing mode loadings. Computed displacements at the vertex and mid-side nodes

around the crack tip by the finite element analysis were compared with the classical solution. Special elements were used at the tip to represent the variation of the displacements with respect to the square root of the distance from the tip. These were compatible with the surrounding quadratic elements. The calculated stress intensity factors were accurate to within 4 percent of known solutions.

Albrecht and Yamada(1977) reviewed an alternate approach for rapid calculation of stress intensity factors. The procedure required the finite element computation of stresses for uncracked body. Then the geometry correction factors for crack and finite width correction were considered for final calculation of stress intensity factors. Without sacrificing the advantage of simplicity and conformability of Blackburn's six-node element for modelling the crack tip, a minor adjustment in the interpolation field was proposed by Morris and Becker(1978), which permitted a quadratic variation in the singular part of displacement. Using a convenient co-ordinate system, the integrations were done exactly in the radial direction. The shape functions provided both constant strain capability and conformability with the quadratic isoparametric elements.

Gifford and Hilton(1978) extended the finite element method to direct calculation of combined opening and sliding modes' stress intensity factors for axisymmetric and planar structures. The 12-node isoparametric quadrilateral element was made into a special crack-tip element, with one corner corresponding to the crack-tip. In addition to nodal displacements, the opening and the sliding modes' stress intensity factors were the basic unknowns in this element and were calculated

directly. The results varied from approximately 3 percent less than to 7 percent more than the reference value. The accuracy of the results was not highly sensitive to changes in the finite element mesh.

Alwar and Ramachandran(1983) investigated the variation of the stress intensity factors for finite plates across the plate thickness using finite element techniques. The crack tip region was represented by degenerate triangular quarter-point prism elements, having the required square root singularity for all normal stresses and in-plane shear stress at the crack tip. A convergence study for the variation of the stress intensity factors was made by using two, three and four layers of elements across half the thickness of the plate and also by reducing the crack tip element size and increasing the degrees-of-freedom for a single layer. For a thin plate, the variation was found to be linear. However, for thicker plates, the variation was nonlinear.

A finite element method, utilizing quadrilateral elements, was developed by Kuo-Kuang et al(1983) to determine the opening mode stress intensity factor for a single-edge notched beam. Hermitian interpolation functions were used to describe the displacements in the regular elements, and William's stress function was used to develop the singular element. Bell et al(1984) analysed a welded plate joint for a series of crack shapes and crack depth. The crack tip regions were modelled using the degenerate isoparametric element developed by Barsoum(1976). The effects of crack shape, crack depth and weld angle on the stress intensity factors were investigated and the results presented.

2.3 Experimental Investigation

Determination of the fatigue crack propagation curve is an integral part of the fracture mechanics design approach. To predict the minimum fatigue life of structural components and to establish the safe inspection intervals, an understanding of the fatigue-crack propagation rate is required. Most fatigue crack growth tests are conducted by subjecting a cracked specimen to constant-amplitude cyclic-load. The incremental increase of crack length is measured, and the corresponding number of elapsed load cycles is recorded. The data are presented as a plot of crack length, 'a' vs. total number of elapsed load cycles, 'N'. An increase in the magnitude of cyclic-load results in a decrease of the fatigue life of specimens having identical geometry. Furthermore, the fatigue life of a specimen subjected to a fixed constant-amplitude cyclic load decreases as the length of the initial crack is increased. The influence of load ratio (minimum load/ maximum load) on the fatigue crack growth rate cannot be easily assessed because the functional dependence of crack growth rate da/dN on load ratio R varies greatly with the growth region. This indicates that several underlying phenomena control the observed R-effect. Crack closure is known to occur during fatigue crack growth and undoubtedly influences the R-dependence particularly at low growth rate. The experimental investigation can be classified into three sub-sections, i.e. standard specimens, plated joints, tubular joints.

2.3.1 Standard specimens

To generate fatigue crack growth data for a particular material, arbitrarily

shaped small scale specimens may be employed. Realistically, however, a limited number of specimen types are preferred (Fig. 2.3). Alternative specimen geometries can be used for the test method, provided that well established stress intensity calibrations for the specimens are known. The various investigations conducted so far using standard specimens are discussed below.

The effects of salt and distilled water environments on the fatigue crack growth rate of a pin-loaded single-edge notch specimen were evaluated by Vosikovsky(1975) for a X-65 pipe-line steel. Tests were conducted under cathodic and free corrosion potential conditions, and a distinct pattern in the functional dependence of growth rates on stress intensity factor range, ΔK, and frequency was found. At free corrosion, the growth rates in distilled water were identical to those in salt water. Using a consistent technique, Kikukswa et al(1976) obtained extensive data indicating that compressive loading at $R = -1$ could either increase, decrease or have no effect on fatigue crack growth rates compared to data at $R = 0$. Sasski et al(1977) found the fatigue crack growth rate for $R < 0$ to be mixed. A comparison of these data with others is complicated by the fact that the procedure used to compute ΔK for $R < 0$ is not always specified, i.e., whether or not the compressive portion of the loading cycle was included in the computation of ΔK.

Using compact tension specimens, Hudak et al(1978) examined the influence of load ratio over a wide range of fatigue crack growth rates. Tests were conducted on 2219-T851 aluminium at R values of -1, 0.1, 0.3, 0.5 and 0.8 in air at a room

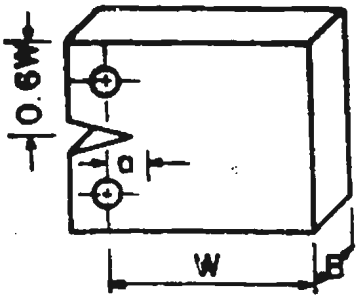

Compact tension specimen
(CT)

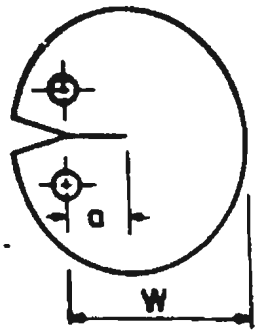

Disk-shaped compact tension specimen
(DCT)

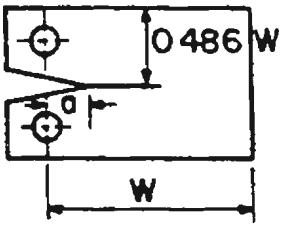

Wedge opening loaded specimen
(WOL)

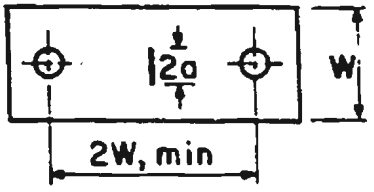

Center-cracked tension specimen
(CCT)

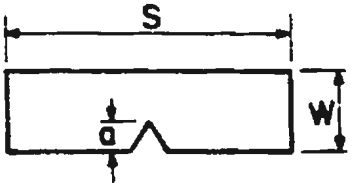

Single edge-notched bend specimen
(SEB)

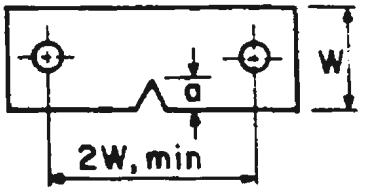

Single edge-notched tension specimen
(SET)

Fig. 2.3 Small scale specimens used for fatigue-crack-growth-rate determination.

temperature of 24°C. Low da/dN values were strongly sensitive to the applied stress intensity factor range and became diminishingly small as the threshold stress intensity range, ΔK_{th}, was approached. In this growth rate region, both da/dN and ΔK_{th} were stongly R-dependent. At intermediate growth rates, da/dN was much less dependent on both ΔK and R. At high growth rates, da/dN was again strongly dependent on both ΔK and R. The influences of temperature and frequency on crack growth rate were studied for both aluminium and 10Ni steel in laboratory air. Tests were carried out for a temperature and frequency ranges of -73°C to 121°C and 0.01 Hz to 200 Hz, respectively. The temperature dependence varied with test frequency. Tests at lower frequencies were less sensitive to changes in temperature. The results suggested that, for a given test frequency, changes in temperature caused a parallel shift of data along the da/dN axis.

Claude et al(1980) carried out experimental work on E36-Z steel specimens for various crack widths using compact tension specimens fabricated from both parent material and heat affected zone. The rate of propagation of a crack recorded in the heat affected zone, for a given level of stress intensity factor, was much slower than in the parent material. The propagation of the surface crack in the direction perpendicular to a curved fronted crack seemed to depend not on the shape of the front but on the local value of the stress intensity factor. Stephens et al(1980) reviewed the low temperature fatigue behavior of steels. Many steels showed increased fatigue crack growth resistance in stable and unstable growth regions as the temperature was lowered. The effects of

temperature, frequency, mean stress and intermittent immersion on fatigue crack growth were studied by Morgan et al(1981) on structural steel compact tension specimens with through-thickness cracks. The crack growth rates were measured at two sea water temperatures, i.e. 5° and 20°C. Crack growth rates of freely corroding structural steel in sea water were described by an upper bound of six times the growth rates observed in air. Load ratio had no effect on crack growth rates in air, but ratios greater than 0.7 resulted in the maximum observed growth rates in sea water. Intermittent immersion, temperature and load wave form had a relatively small effect on crack growth. Haagensen et al(1981) studied the delay effects caused by single peak overloads on BS4360 grade D steel using multiple single edge specimen (MSEN) with six parallel cracks. The crack propagation rate was observed to be higher in sea water than in air.

Scholte and Wildschut(1981) studied the crack propagation in normalized C-Mn steel under constant amplitude loading using single edge notched specimens loaded in four point bending. In sea water the crack growth rate was about three times higher than in air. As the crack growth rate increased, the magnitude of the influence of sea water decreased and finally vanished. The crack propagation rate in sea water at $R = 0.5$ appeared to be only slightly higher than that at $R = 0.1$. Austen et al(1981) observed the crack growth rates in aqueous environments to be faster in the intermediate region due to localized hydrogen embrittlement. There was also an additional environmental effect due to crack tip blunting by metal dissolution on the growth rate behaviour, most noticeably in the initial region. In sea water, crack tip blunting provided increased resistance to

initiation in comparison to air for all type of steels. Without crack tip blunting, the effect of the presence of sea water was to promote even greater rates of growth.

Using pin-loaded single-edge notched specimens, Vosikovsky et al(1983) studied the effect of cold artificial sea water on fatigue crack growth in structural steel at constant load amplitude. At the free corrosion potential, room temperature growth rates in sea water and in salt water (3.5 percent NaCl solution) were comparable. In the intermediate ΔK range, the growth rates in both solutions were about four times higher than those in air. A drop in sea water temperature to 0°C resulted in a reduction of the intermediate ΔK range growth rate by a factor of two at stress ratios slightly less than 0.5. The fatigue crack growth rates in cold sea water (0°C) under free corrosion potential were only marginally higher than the growth rates in air at room temperature.

2.3.2 Plated joints

Clear evidence of a tendency for fatigue strength to decrease with increasing plate thickness was obtained by Gurney(1979). Somewhat in contrast to this, Wildschut et al(1978) showed virtually no effect of plate thickness between 40 and 70 mm. Indeed, the thicker specimens gave a slightly higher strength. On the other hand, Booth(1978) showed a significant decrease in strength with thickness, from 111 to 97 MN/m^2 at 2×10^6 cycles, in his tests on 25 mm thick and 38 mm thick transverse load-carrying fillet welds subjected to bending. To study the plate thickness effect, Berge and Engesvik(1981) carried out fatigue tests on non-

load carrying fillet welds in structural steel subjected to axial tension. At a stress range of 150 MPa and zero load ratio, the fatigue endurance was found to decrease significantly with increasing plate thickness.

Holmes and Booth(1981) carried out fatigue tests on a transverse load-carrying joint and a longitudinal non-load-carrying joint under environmental and random loading conditions. The joints were manufactured from 38mm steel plate conforming to BS4360 grad 50 D specification. It was observed that a free corrosion environment reduced the fatigue lives of welded joints by a maximum amount of 40 percent. This influence was not increased by alternate immersion/exposure conditions. Zwaans et al(1981) performed fatigue tests on welded T-shaped specimens subjected to bending loads. Two load spectra were used, e.g., Gaussian and Rayleigh distributions. For both spectra it was observed that the fatigue lives in sea water were smaller than the lives in air by a factor of 2.2.

Walker(1981) reviewed the results of the U.K. Offshore Steels Research Project (UKOSRP). It was concluded that the fatigue life of a welded plate joint under freely corroding conditions in sea water was only 50 percent of the life in air. The rate of fatigue crack propagation in sea water at high stress ratios was seen to be considerably greater than that in air. Gurney(1983) summarised the revised fatigue design rules. The influences of plate thickness, weld shape, stress relief and environment were taken into account in the design of welded joints. Vosikovsky and Rivard(1984) reported crack growth rate results for eight 26 and 52 mm thick T-plated joints. A crack depth of 0.5 mm was taken as the initiation value.

The initiation periods were observed to be about 22-31 percent of the total life. After initiation, the fatigue crack growth curves were almost linear up to 85 percent of the total life.

Berge(1985) investigated the effect of plate thickness on the fatigue strength of transverse non-load carrying fillet welds subjected to axial loading. The thickness effect was found to follow a power law with a decrease in fatigue strength of 40 percent when the plate thickness was increased from 12.5 mm to 80 mm. Fatigue lives and crack growth were measured on 16, 26, 52, 78 and 103 mm thick T-plated joints, loaded in three-point bending under constant load amplitude (Vosikovsky et al 1985). The effect of plate thickness was reflected in both the initiation and the propagation lives. The dependence of the number of starting cracks and their subsequent rate of coalescence on the stress range and the plate thickness was also observed.

2.3.3 Tubular joints

Due to the increased use of circular hollow sections in offshore applications in the U.S.A. during the sixties, a number of investigations were carried out regarding the joint strength under fatigue loading e.g. by Bouwkamp(1966), Natarajan and Toprac(1968) and Marshall(1974). At about the same time Kurobane(1969) started fatigue tests on tubular joints in Japan. From these tests, codes and design curves such as the API and AWS design curves were derived based on the punching shear method or the hot spot strain concepts.

The exploitation of natural gas and oil under deeper and rougher areas, such as the North Sea, required very large structures and the use of thick plate steels. The lack of data regarding the fatigue behaviour of larger tubular joints made it apparent that a complete test program would be needed to provide knowledge which could be used by designers. With the already existing program of the UKOSRP as a basis, a large European research program was set up and executed. This program was sponsored by the European Coal and Steel Community (ECSC). The fatigue behaviour of the tubular joints investigated by the various researchers is discussed below.

Hibbered and Dover(1977) conducted fatigue tests on tubular T-joints under random in-plane bending. The crack growth was analysed, and a satisfactory life estimation was made using the fracture mechanics approach. Dover et al(1978) concluded from tests on tubular joints under out-of-plane bending that the fatigue crack growth propagation life forms the major part of the fatigue life of joints. Dover and Holdbrook(1979) observed the crack-depth growth rate to be nearly constant for much of the total life of welded tubular T-joints. Iwasaki et al(1979) reported increase in both fatigue crack initiation and propagation lives for TY-joints with overlapped braces. Ring stiffeners were not effective in improving the crack initiation life but were found to be more effective in increasing the crack propagation life. An increase in the chord dimension produced a reduction in fatigue performance (Wylde and McDonald 1979). Specimens with 457 mm chord diameter and 16 mm wall thickness showed a reduction in fatigue strength of 40 percent at an endurance level of 10^6 cycles, compared to the results

obtained from specimens with chord diameter and wall thickness of 168 mm and 6 mm, respectively.

Dijkstra and de Back(1980) performed fatigue tests on 40 tubular T and X-joints. It was found that, after initiation, crack propagates along the weld toe and, at a later stage, branches away from the weld toe into the chord wall. When a surface crack length exceeded 1/4 of the brace diameter, a through crack usually occurred. The life time of the tests in artificial sea water was about 0.4 times the life time of the tests in air. There was no difference in the fatigue life time between cathodically protected and unprotected specimens. But there was a difference in initiation and crack growth. The initiation of a visible crack occurred at about 25 percent of the life time of the specimens. Gibstein(1981) presented fatigue test results carried out at Det Norske Veritas. It was found that both the depth and the length of cracks in tubular joints were approximately linear functions of the number of cycles.

Donald et al(1981) presented the results of T-joint tests in air carried out at NEL. It was observed that there was a decrease in fatigue life with an increase in the size of the joint. Constant compressive chord loading with cyclic axial and in-plane bending brace loads could increase the fatigue life by a factor of 5.7. Brandi(1981) presented fatigue test results for 12 stiffened and unstiffened Y-joints, carried out in Italy. The joints were stiffened by means of three internal rings. It was observed that the stiffened joints could sustain a load which was 4 times higher than the load the unstiffened joints could sustain, and they could

still have almost the same or even longer life. The crack propagation time was also very high in the stiffened joints.

Wylde(1981) presented fatigue test results for K and KT-joints under axial and out-of-plane bending. Specimens were tested with and without overlapping braces. The brace overlap was observed to be beneficial under axial loading but had no effect in the out-of-plane bending case. Damilano et al(1981) presented fatigue test results for twelve stiffened and unstiffened Y-joints, conducted in Italy. It was observed, in case of stiffened joints with three internal rings, that the difference between the through-crack life and the complete failure life was comparable with the life till through-crack.

Fatigue crack depth was monitored during tests on tubular Y-joints (Dover and Dharmavasan 1982). No rapid acceleration in crack-depth growth rate was observed. Gowda(1983) investigated the fatigue behaviour of monopod tubular joints in air and seawater environments. The joints, having 318.7 mm chord diameter, were fabricated from ASTM A36 steel. Two out of seven joints were tested under pseudo-random loading, and the others were tested under constant amplitude loading. The visible crack initiation period was observed to be in the range of 38-64 percent of the joint lives. The measured fatigue lives were shorter than those of T or Y-joints of comparable dimensions.

Mitsui et al(1984) tested six types of stiffened and unstiffened tubular K-joints under axial loading. All specimens were fabricated from STK 41 grade steel, and the chord outer diameter for all specimens was 457.2 mm. It was observed that

either a pad plate on the chord or wing plates stiffened by ring and rib plates had beneficial effects in the improvement of the fatigue resistance. Ryan et al(1984) proposed new design recommendations for the fatigue life of tubular joints from thickness effect considerations, based on 73 tests conducted in France. The range of joint thickness was from 5 mm to 80 mm. A size effect was evident in the results. The effect was indicated as mainly due to thickness. The resulting fatigue design curve was expressed as

$$\text{Log } N = 12.29 - 3.00 \text{ Log } S_r \tag{2.3}$$

The thickness effect was represented as

$$S_r = S_r^* \, (T/18)^{0.29} \qquad MN/m^2 \tag{2.4}$$

where S_r is the stress range on the reference design curve and S_r^* is the stress range of a joint with thickness T mm. Wylde(1984) reviewed the results of fatigue tests carried out in the UK. It was concluded that fatigue cracks, typically about 5 mm in length, could be detected visually at less than 10 percent of the total fatigue life in many of the specimens. Initially fatigue cracks propagated more rapidly along the surface of the specimens than in the through-thickness direction. The tubular joints tested retained their stiffness until the final 10 percent of total life. Van Delft et al(1985) evaluated European fatigue test data on about 200 large-size welded T, K and KT tubular joints with/without overlaps. The diameter of the chord of the joints tested varied from 168 to 1830 mm. Investigations were pursued into the effects of sea water, cathodic protection lev-

els, material thickness, stress history and fatigue life improvement techniques on fatigue life. The scale factor was found to be a dominating factor. The fatigue life in sea water was found to be only 1/3 of the life in air.

2.4 Summary

In the literature reviewed above, most of the finite element analyses of tubular joints are based on two dimensional plate/shell elements, which neglect the displacement variation across the shell thickness (Kuang et al 1977, Clayton & Martin 1980, Dijkstra 1981, Gibstein and Moe 1981). The stress concentration factor is underestimated on the chord side and is overestimated on the brace side due to the lack of three dimensional representation of the chord/brace intersection. Several general purpose programs, such as ASAS, ASKA, NASTRAN, STRUDL, SATE are available for shell analysis; but these package programs cannot be used to analyse the crack front region which has square root singularity in the stress field. The stress intensity factors already available in the literature are obtained from finite element analyses for a number of idealized cases such as plates, CT specimens and notched beams (Tracey 1974, Bergan and Aamodt 1974, Raju and Newman 1977, Blackburn and Hellen 1977, Alwar and Ramchandran 1983, Kuo-Kuang et al 1983). To the author's best knowledge, no finite element analysis exists in the literature for the stress intensity factor of a crack situated in a three-dimensional field of external stress concentration (e.g., presence of weld toe cracks at the high stress concentration regions of the tubular joints).

A knowledge of crack growth data for the material is essential for the fatigue life

prediction, based on LEFM approach. Most of the studies reported are for the steel plates Fe 510 DD, according to Euronorm 25-72 or to the equivalent national standard of the individual European country (Claude et al 1980, Walker 1981, Holmes and Booth 1981). Since the chemical composition of each steel differs from one another, the crack growth data from the above tests cannot be used in our study which used CSA G40.21 M 350 WT steel; no study has reported the crack growth data for the same.

In addition, very few studies have examined the crack growth in the prototype tubular joints analytically and experimentally (Hibbered and Dover 1977, Dover and Dharamavasan 1982). But in these studies, the stress intensity factors are determined approximately in terms of factors dependent on crack shape, loading, joint geometry and hot spot stress without analytically modelling the crack.

Hence there is a need for carrying out an analysis for the stress intensity factors of an embedded weld toe crack in a tubular specimen. The crack growth characteristics of the base metal (CSA G 40.21 M 350 WT) are required for the fatigue life estimation of the tubular T-joints. Finally the predicted fatigue life must be checked with the experimental value obtained from the test on a prototype specimen. The present study seeks to meet this need.

CHAPTER 3

TWO DIMENSIONAL ANALYSIS

3.1 Introduction

Three stress levels i.e. nominal stress, geometric stress and local stress can be distinguished according to the analytical approach used for a tubular joint. A global analysis of the joint, viewing it as a network of beams, yields the forces and the bending moments in the members. Using the conventional strength of materials calculations, the nominal stresses in the straight tubular section can be deduced. An analysis of the joint in terms of the intersection of thin shells, where each component is represented by its mean surface, yields the forces in the walls necessary to ensure the compatibility of the displacements along the line of the intersection. The stresses in the walls, obtained from the theory of thin shells, are termed as the geometric stresses since they correspond to an ideal joint geometry. A numerical approach based on the theory of thin shells gives the geometric stresses and therefore direct access to geometric stress concentration factor, K_G. The finite element method has the advantage of giving not only the value of peak geometric stress but also its precise position as well as a pattern of the stress distribution in the entire zone of shell intersection.

This chapter deals with a variant of the automatic discretization procedure (developed specifically for this study) and the subsequent analysis of a tubular

T-joint using plate bending and membrane elements.

3.2 Discretization

Automation in the data preparation reduces errors, and the solution accuracy may increase because a computer-generated mesh is more regular than one manually prepared by the user. Hence a computer software is developed for discretizing the tubular T-joint using an automatic mesh generation technique. For the present investigation, the loads acting on the T-joint are restricted to axial load and in-plane bending. Because of this, the advantage of symmetry is taken into consideration in discretization and only half of the T-joint is considered for modelling. The following procedures are adopted for the mesh generation:

(a) A fine mesh is utilized near the intersection between the chord and brace, where the stress gradient is sharp.

(b) A coarser mesh is used at the ends of both the chord and the brace where the stresses are small.

(c) The nodes are numbered in such a way as to minimize the incidence of elements and thereby reduce the band width of the global stiffness matrix.

The stuctural model considered is shown in Fig. 3.1. An oxyz coordinate system is defined at the left of the model. The model consists of seven sections. For each section some key points are defined by setting either a cartesian coordinate or an

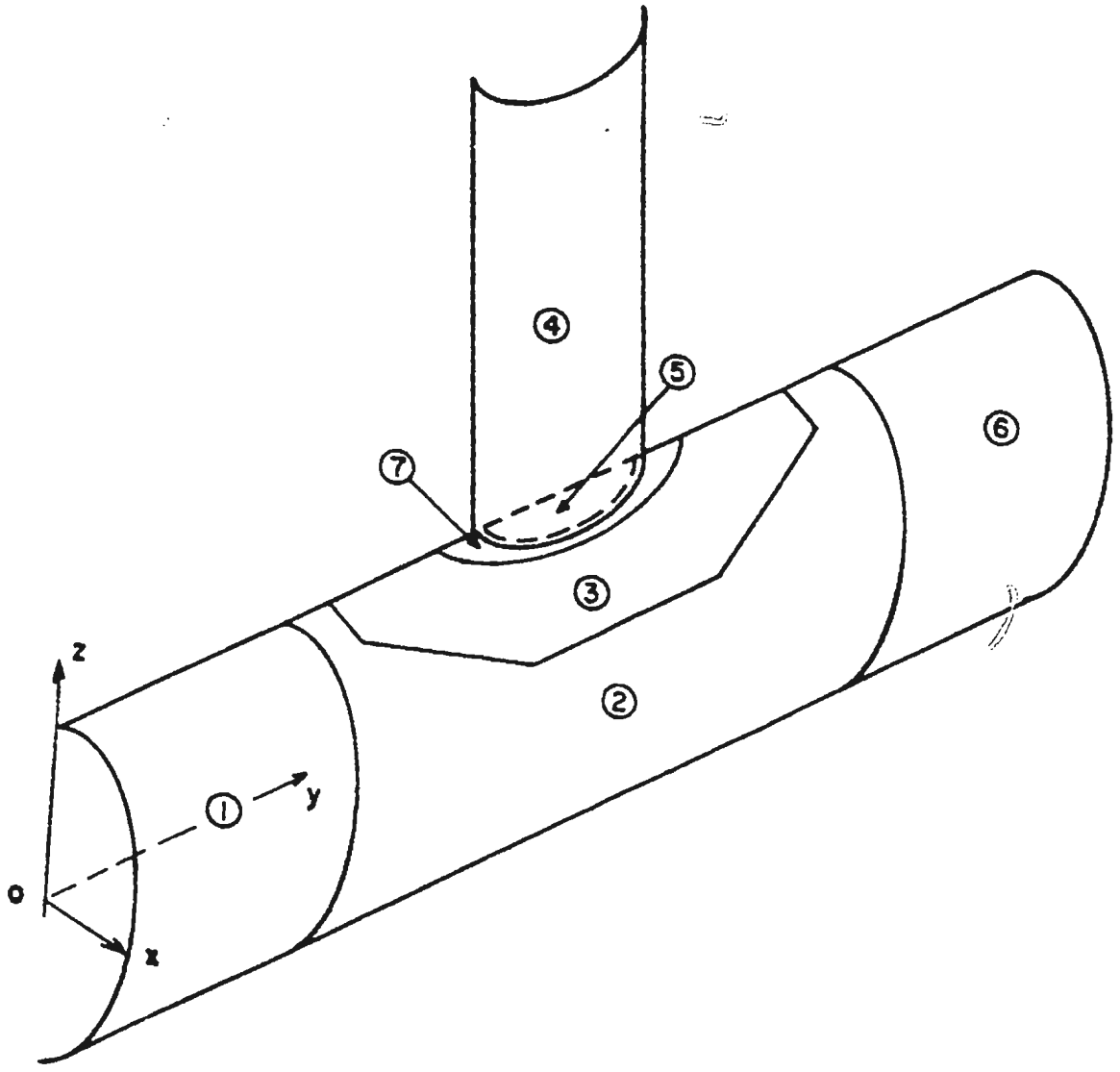

Fig. 3.1 Regions of T-joint model for mesh generation.

angle. For example, the y-coordinates of the bottom nodes of sections 1, 2 and 6 and the lower curve nodes of section 3 are specified. For section 4, the z coordinates of the side nodes are specified. The coordinates of the nodes at the intersection of the brace and the chord are generated. The nodal coordinates are generated section-wise, and the node numbers are generated by assigning the proper indices corresponding to a particular section. All sections are combined together using the common node matching technique between the sections. Then the node numbers are rearranged for the complete model in a way so as to have the minimum band width. For the nodal connectivity of the elements, the node numbering sequences are defined in an anti-clockwise direction (Fig.3.2).

In order to plot the generated mesh for the model, the x, y and z axes are rotated through angles α , β and γ in three stages to attain the new axis systems $ox'y'z'$, $ox''y''z''$ and $o\bar{x}\,\bar{y}\,\bar{z}$ respectively (Fig. 3.3). The relation between oxyz and $o\bar{x}\,\bar{y}\,\bar{z}$ coordinates can be written as

$$\begin{Bmatrix} x \\ y \\ z \end{Bmatrix} = [A][B][C] \begin{Bmatrix} \bar{x} \\ \bar{y} \\ \bar{z} \end{Bmatrix} \tag{3.1}$$

where

$$[A] = \begin{bmatrix} 1 & 0 & 0 \\ 0 & \cos\alpha & -\sin\alpha \\ 0 & \sin\alpha & \cos\alpha \end{bmatrix} \tag{3.2}$$

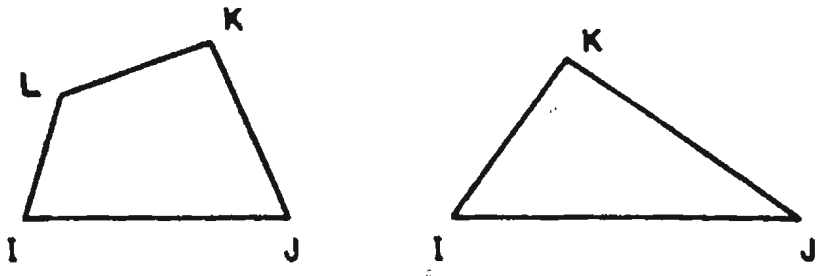

Fig. 3.2 Node numbering sequences.

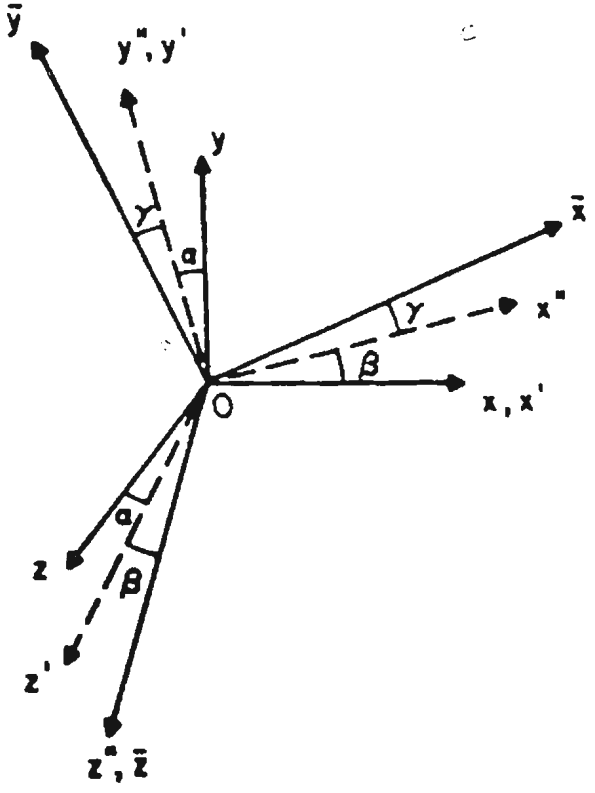

Fig. 3.3 Rotation of coordinate system axes for mesh generation.

$$[B] = \begin{bmatrix} \cos\beta & 0 & \sin\beta \\ 0 & 1 & 0 \\ -\sin\beta & 0 & \cos\beta \end{bmatrix} \tag{3.3}$$

$$[C] = \begin{bmatrix} \cos\gamma & -\sin\gamma & 0 \\ \sin\gamma & \cos\gamma & 0 \\ 0 & 0 & 1 \end{bmatrix} \tag{3.4}$$

Using Eqn.(3.1), the coordinates of the nodal points are transformed into a new oxyz coordinate system, which are then used in plotting the discretized model of the tubular T-joint.

3.3 Element Stiffness Formulation

The most critical step in two-dimensional stress analysis is the evaluation of the stiffness properties of an individual element. It is assumed that the elements are interconnected only at their corner points. Two types of elements stiffnesses are considered in this analysis: membrane stiffness which relates forces and displacements in the plane of the elements, and the plate bending stiffness which takes account of displacements for out-of-plane deformations. The membrane and flexural stiffnesses are represented without coupling using plane stress and plate bending elements; this idealization is justified since only small deformations are assumed to occur under the applied loads.

3.3.1 Plate bending element

The triangular element stiffness matrix is derived using area coordinates. The area coordinates L_i , L_j , L_k of any point P in the triangle are defined as the ratio

of the area, Δ_i, of the subtriangles subtended at that point, to the total area, Δ, of the triangle i.e. $L_i = \Delta_i / \Delta$ (Fig.3.4). The linear relation between the set of area coordinates and the cartesian system is given by

$$\begin{Bmatrix} 1 \\ x \\ y \end{Bmatrix} = \begin{bmatrix} 1 & 1 & 1 \\ x_i & x_j & x_k \\ y_i & y_j & y_k \end{bmatrix} \begin{Bmatrix} L_i \\ L_j \\ L_k \end{Bmatrix} \tag{3.5}$$

Inversion of Eqn.(3.5) gives the area coordinates as

$$\begin{Bmatrix} L_i \\ L_j \\ L_k \end{Bmatrix} = \frac{1}{2\Delta} \begin{bmatrix} a_i & b_i & c_i \\ a_j & b_j & c_j \\ a_k & b_k & c_k \end{bmatrix} \begin{Bmatrix} 1 \\ x \\ y \end{Bmatrix} \tag{3.6}$$

where

$$\begin{aligned} a_i &= x_j y_k - x_k y_j \\ b_i &= y_j - y_k \\ c_i &= x_k - x_j \\ \Delta &= \frac{1}{2} \begin{vmatrix} 1 & x_i & y_i \\ 1 & x_j & y_j \\ 1 & x_k & y_k \end{vmatrix} \end{aligned} \tag{3.7}$$

The transverse displacement, w_i, and the rotations, θ_{xi} and θ_{yi}, at each corner node about the x and y axes of an element are taken as the nodal degrees of freedom in the flexural element stiffness derivation (Fig.3.5). The displacement within the element can be described in the form (Bazeley et al 1965)

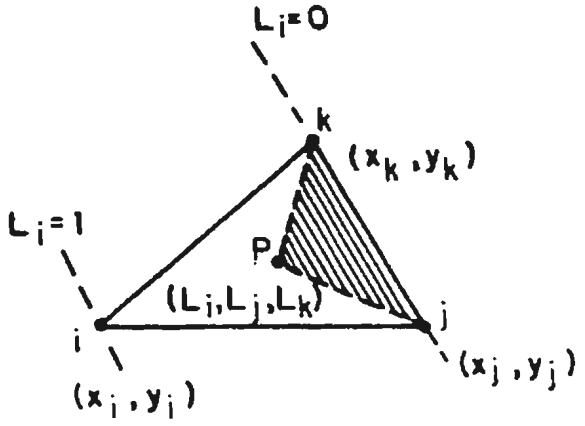

Fig. 3.4 Triangular area coordinate.

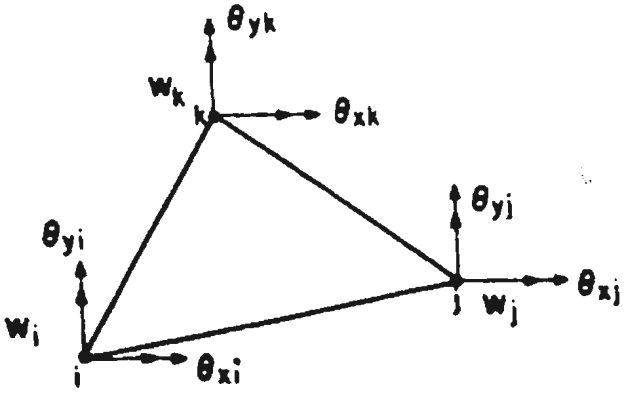

Degrees - of - Freedom

Fig. 3.5 Bending element.

$$w = \beta_1 L_i + \beta_2 L_j + \beta_3 L_k + \beta_4 (L_i^2 L_j + \frac{1}{2} L_i L_j L_k)$$
$$+ \beta_5(L_i L_j^2 + \frac{1}{2} L_i L_j L_k) + \beta_6(L_j^2 L_k + \frac{1}{2} L_i L_j L_k)$$
$$+ \beta_7(L_j L_k^2 + \frac{1}{2} L_i L_j L_k) + \beta_8 (L_k^2 L_i + \frac{1}{2} L_i L_j L_k)$$
$$+ \beta_9(L_k L_i^2 + \frac{1}{2} L_i L_j L_k) \qquad (3.8)$$

Substituting the nodal values of

$$w_i , \theta_{xi} = - \left(\frac{\partial w}{\partial y} \right)_i \quad \text{and} \quad \theta_{yi} = \left(\frac{\partial w}{\partial x} \right)_i$$
$$w_j , \theta_{xj} = - \left(\frac{\partial w}{\partial y} \right)_j \quad \text{and} \quad \theta_{yj} = \left(\frac{\partial w}{\partial x} \right)_j \qquad (3.9)$$
$$w_k , \theta_{xk} = - \left(\frac{\partial w}{\partial y} \right)_k \quad \text{and} \quad \theta_{yk} = \left(\frac{\partial w}{\partial x} \right)_k$$

for the i, j and k nodes, the constants β_1, β_2,....β_9 and hence the shape functions, N_i, N_j, N_k are determined. For node i, the shape function, N_i can be written as

$$\left[N_i \right]^T = \begin{Bmatrix} L_i + L_i^2 L_j + L_i^2 L_k - L_i L_j^2 - L_i L_k^2 \\ b_k (L_i^2 L_j + \frac{1}{2} L_i L_j L_k) - b_j (L_k L_i^2 + \frac{1}{2} L_i L_j L_k) \\ c_k (L_i^2 L_j + \frac{1}{2} L_i L_j L_k) - c_j (L_k L_i^2 + \frac{1}{2} L_i L_j L_k) \end{Bmatrix} \qquad (3.10)$$

The strain displacement relation for the element is written in terms of nodal displacements as

$$\left\{ \epsilon \right\} = \begin{Bmatrix} -\frac{\partial^2 w}{\partial x^2} \\ -\frac{\partial^2 w}{\partial y^2} \\ 2 \frac{\partial^2 w}{\partial x \partial y} \end{Bmatrix} = \left[B_i \; B_j \; B_k \right] \begin{Bmatrix} a_{bi} \\ a_{bj} \\ a_{bk} \end{Bmatrix} \qquad (3.11)$$

where

$$\left\{ B_i \right\} = \begin{Bmatrix} -\dfrac{\partial^2 N_i}{\partial x^2} \\ -\dfrac{\partial^2 N_i}{\partial y^2} \\ 2\dfrac{\partial^2 N_i}{\partial x \partial y} \end{Bmatrix}$$

$$\left\{ a_{bi} \right\} = \begin{Bmatrix} w_i \\ \theta_{xi} \\ \theta_{yi} \end{Bmatrix} = \begin{Bmatrix} w_i \\ -(\dfrac{\partial w}{\partial y})_i \\ (\dfrac{\partial w}{\partial x})_i \end{Bmatrix} \qquad (3.12)$$

As the shape function, N_i, is a polynomial in the area coordinates, the differentiation with respect to x, y is performed as

$$\frac{\partial N_i}{\partial x} = \sum_{j=1}^{3} \frac{\partial N_i}{\partial L_j} \frac{\partial L_j}{\partial x} = \frac{1}{2\Delta} \left(b_i \frac{\partial N_i}{\partial L_1} + b_j \frac{\partial N_i}{\partial L_2} + b_k \frac{\partial N_i}{\partial L_3} \right)$$

$$\frac{\partial N_i}{\partial y} = \sum_{j=1}^{3} \frac{\partial N_i}{\partial L_j} \frac{\partial L_j}{\partial y} = \frac{1}{2\Delta} \left(c_i \frac{\partial N_i}{\partial L_1} + c_j \frac{\partial N_i}{\partial L_2} + c_k \frac{\partial N_i}{\partial L_3} \right) \qquad (3.13)$$

The terms in the [B] matrix remain as polynomials in the area coordinates. The flexural element stiffness matrix is obtained using the general expression

$$\left[k_b \right] = t \int\int_A [B]^T [D] [B] \, dA \qquad (3.14)$$

where t = the thickness of the element and [D] = the elasticity matrix.

For an isotropic plate, [D] is given by

$$[\,D\,] = \frac{Et^3}{12\,(\,1-\nu^2)} \begin{bmatrix} 1 & \nu & 0 \\ \nu & 1 & 0 \\ 0 & 0 & \frac{1-\nu}{2} \end{bmatrix} \tag{3.15}$$

Equation 3.14 is a polynomial in the area coordinates and is integrated here using the relation

$$\int\int_A L_i^{\alpha}\, L_j^{\beta}\, L_k^{\gamma}\; dA = \frac{\alpha!\;\beta!\;\gamma!}{(\,\alpha+\beta+\gamma+2\,)!}\; 2A \tag{3.16}$$

3.3.2 Membrane element

The nodal displacements u and v along the x and y axes of an element are taken as the nodal degrees of freedom (Fig.3.6). The displacements within an element are expressed in terms of nodal values as

$$\begin{aligned} u &= L_i u_i + L_j u_j + L_k u_k \\ v &= L_i v_i + L_j v_j + L_k v_k \end{aligned} \tag{3.17}$$

in which shape functions are

$$\begin{aligned} N_i &= L_i \\ N_j &= L_j \\ N_k &= L_k \end{aligned} \tag{3.18}$$

The strain-displacement relations are

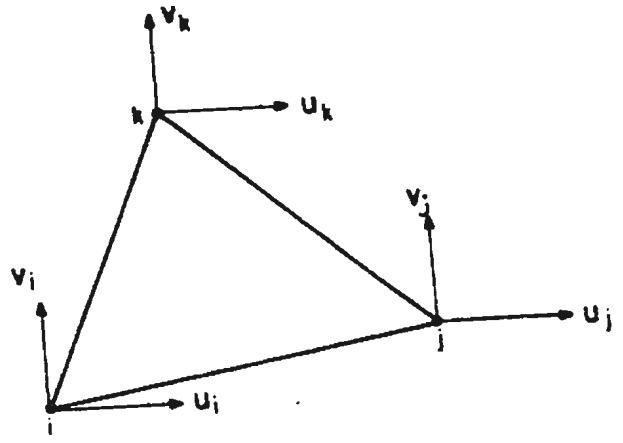

Fig. 3.6 Membrane element.

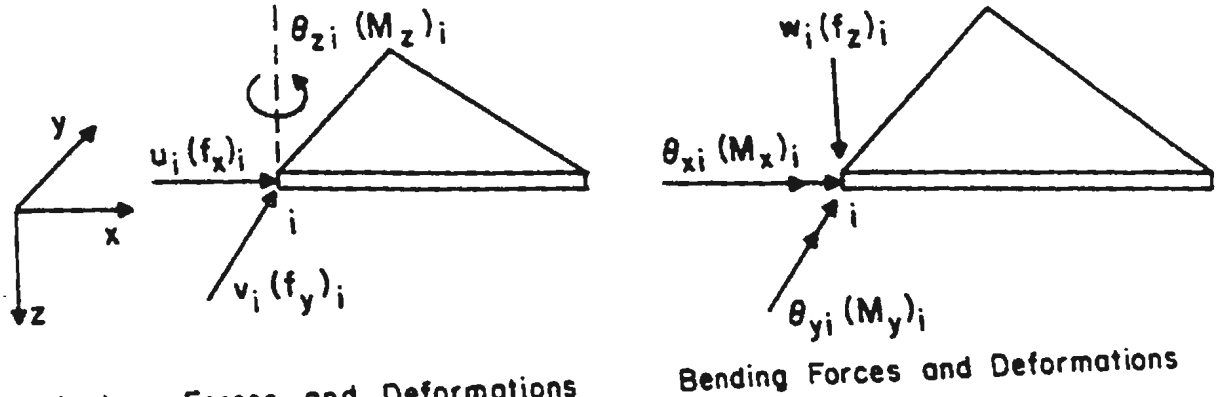

Fig. 3.7 Assembly of six degrees-of-freedom.

$$\left\{ \epsilon \right\} = \begin{Bmatrix} \dfrac{\partial u}{\partial x} \\ \dfrac{\partial v}{\partial y} \\ \dfrac{\partial u}{\partial y} + \dfrac{\partial v}{\partial x} \end{Bmatrix} = \left[B_i \;\; B_j \;\; B_k \right] \begin{Bmatrix} a_{mi} \\ a_{mj} \\ a_{mk} \end{Bmatrix} \tag{3.19}$$

where

$$\left[B_i \right] = \begin{bmatrix} \dfrac{\partial N_i}{\partial x} & 0 \\ 0 & \dfrac{\partial N_i}{\partial y} \\ \dfrac{\partial N_i}{\partial y} & \dfrac{\partial N_i}{\partial x} \end{bmatrix}$$

$$\left\{ a_{mi} \right\} = \begin{Bmatrix} u_i \\ v_i \end{Bmatrix} \tag{3.20}$$

The membrane element stiffness matrix is determined using the expression

$$\left[k_m \right] = t \iint_A \left[B \right]^T \left[D \right] \left[B \right] dA \tag{3.21}$$

where [D] is the elasticity matrix, which is given by

$$\left[D \right] = \frac{E}{(1-\nu^2)} \begin{bmatrix} 1 & \nu & 0 \\ \nu & 1 & 0 \\ 0 & 0 & \dfrac{(1-\nu)}{2} \end{bmatrix} \tag{3.22}$$

3.3.3 Assembly of six degrees of freedom

For in-plane action, the state of strain at each node i is uniquely described in

terms of the u and v displacements at the node by stiffness matrices of the type

$$\left\{ f_m \right\} = \left[k_m \right] \left\{ a_m \right\} \tag{3.23}$$

where

$$\left\{ a_{mi} \right\} = \left\{ \begin{matrix} u_i \\ v_i \end{matrix} \right\}$$

$$\left\{ f_{mi} \right\} = \left\{ \begin{matrix} f_{xi} \\ f_{yi} \end{matrix} \right\} \tag{3.24}$$

For bending, the state of strain is expressed in terms of the nodal displacement in the z-direction, w, and the two rotations, θ_x and θ_y (Fig.3.7). The stiffness matrix is of the form

$$\left\{ f_b \right\} = \left[k_b \right] \left\{ a_b \right\} \tag{3.25}$$

where

$$\left\{ a_{bi} \right\} = \left\{ \begin{matrix} w_i \\ \theta_{xi} \\ \theta_{yi} \end{matrix} \right\}$$

$$\left\{ f_{bi} \right\} = \left\{ \begin{matrix} f_{zi} \\ M_{xi} \\ M_{yi} \end{matrix} \right\} \tag{3.26}$$

The flexural and membrane effects are combined using the relation

$$\left\{ f \right\} = \left[k \right] \left\{ a \right\} \tag{3.27}$$

where

$$\left\{ f_i \right\} = \left[f_{xi} \;\; f_{yi} \;\; f_{zi} \;\; M_{xi} \;\; M_{yi} \;\; M_{zi} \right]^T$$

$$\left\{ a_i \right\} = \begin{Bmatrix} a_{mi} \\ a_{bi} \\ \theta_{zi} \end{Bmatrix} \tag{3.28}$$

The element stiffness matrix is made up of the following submatrices:

$$\left[k \right]_{18X18} = \begin{bmatrix} [k_m]_{6X6} & [0] & [0] \\ [0] & [k_b]_{9X9} & [0] \\ [0] & [0] & [0]_{3X3} \end{bmatrix} \tag{3.29}$$

The terms in this matrix corresponding to θ_z direction are zero. This causes a singularity problem with the computational algorithm. The singularity is avoided by modifying the element stiffness matrix before assembly by the following equation (Zienkiewicz et al 1968)

$$\begin{Bmatrix} M_{zi} \\ M_{zj} \\ M_{zk} \end{Bmatrix} = \alpha \, E \, V \begin{bmatrix} 1 & -0.5 & -0.5 \\ -0.5 & 1 & -0.5 \\ -0.5 & -0.5 & 1 \end{bmatrix} \begin{Bmatrix} \theta_{zi} \\ \theta_{zj} \\ \theta_{zk} \end{Bmatrix} \tag{3.30}$$

where

E = the modulus of elasticity

V = element volume, and

α = small number, typically in the range of 10^{-6} to 10^{-2}

A quadrilateral element with thirty degrees-of-freedom can be obtained by combining four triangular subelements. Static condensation can then be used to exclude the degrees-of-freedom associated with the interior node to obtain an element stiffness matrix of size 24 by 24 (Fig.3.8).

3.4 Results and Discussion

A computer program based on the finite element formulation given in section 3.3 is developed for the two dimensional analysis of the tubular T-joint. The stresses are obtained at the centroid of each element. The joint parameters are given in Table 3.1. Figure 3.9 shows the schematic of the T-joint model analysed. Finite element meshes for different regions and the complete discretised model are shown in Figs. 3.10 and 3.11. The convergence of this formulation occurs when the aspect ratios of the elements are in the range of 0.6 to 1.5. For this formulation, the stresses converge with a discretization error of $O(h^2)$, where h is the element size (Zienkiewicz 1977). The total number of elements and nodes considered in this study are 416 and 464, respectively. All translational and rotational degrees-of-freedom have been restrained for the nodes at each end of the chord i.e. along lines CD and EF. The x translational, and the y and z rotational degrees-of-freedom for the nodes along the edges AB, BC, DE, FG, GH and BIG

Table 3.1 Joint parameters.

Type of Joint	D (mm)	T (mm)	$\beta = \frac{d}{D}$	$\tau = \frac{t}{T}$	$\gamma = \frac{D}{2T}$	$\alpha = \frac{2L}{D}$
Tee	850	32	0.5	0.5	13.2	8.4

D = Chord diameter
d = Brace diameter
T = Chord thickness
t = Brace thickness
L = Length of chord between supports

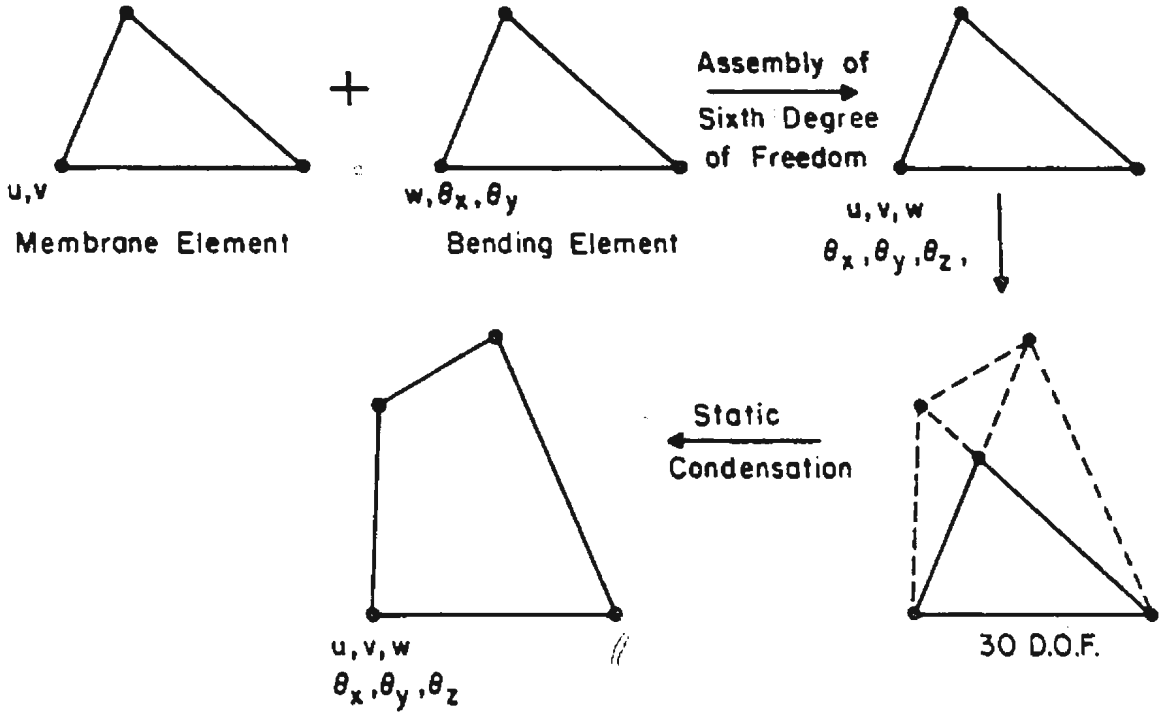

Fig. 3.8 Assembly of triangular element to form quadrilateral element.

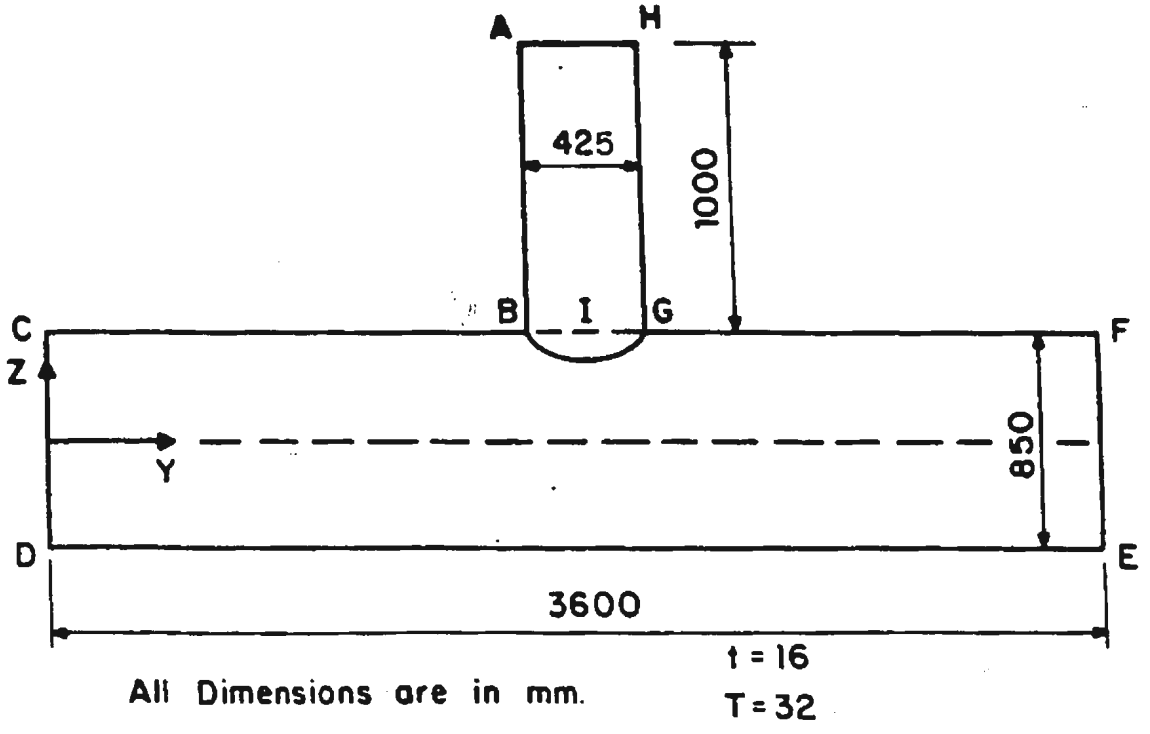

Fig. 3.9 Schematic of T-joint model.

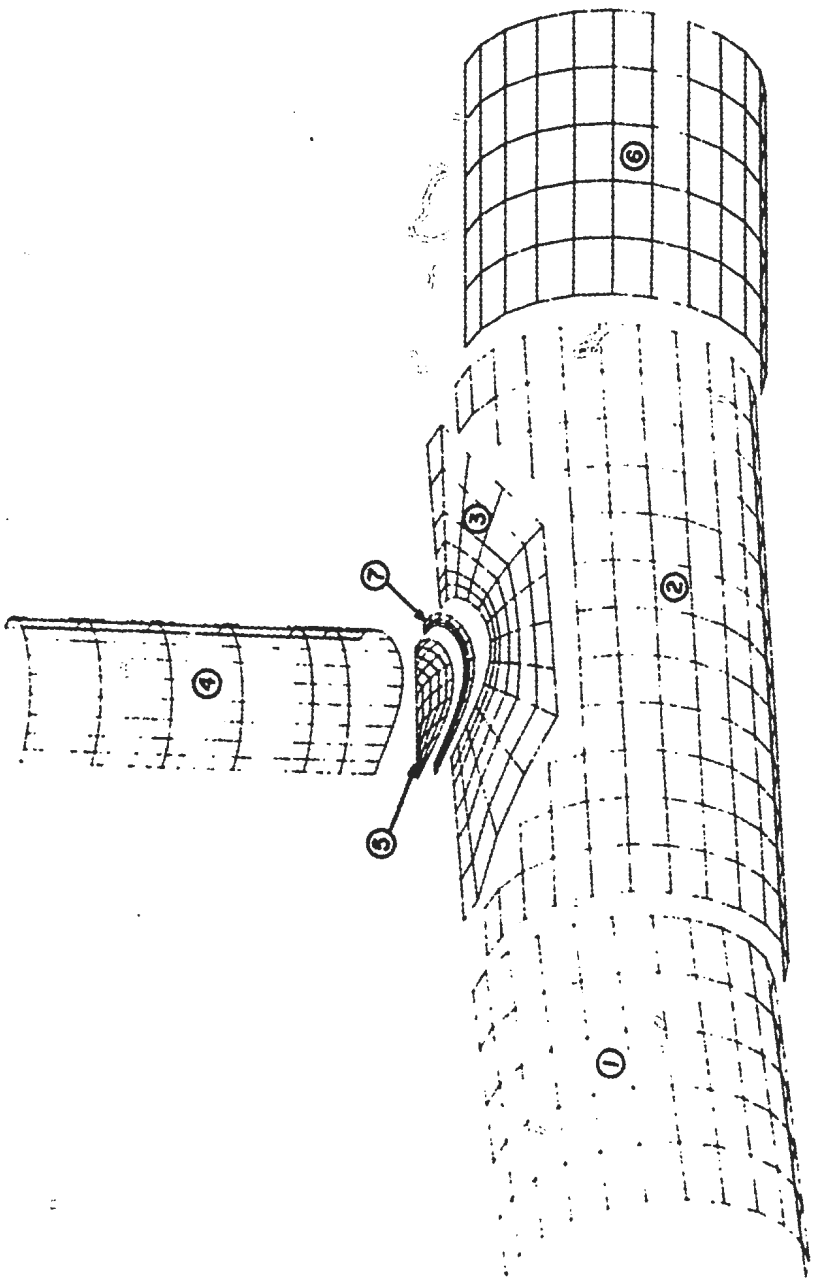

Fig. 3.10 Finite element mesh for different region.

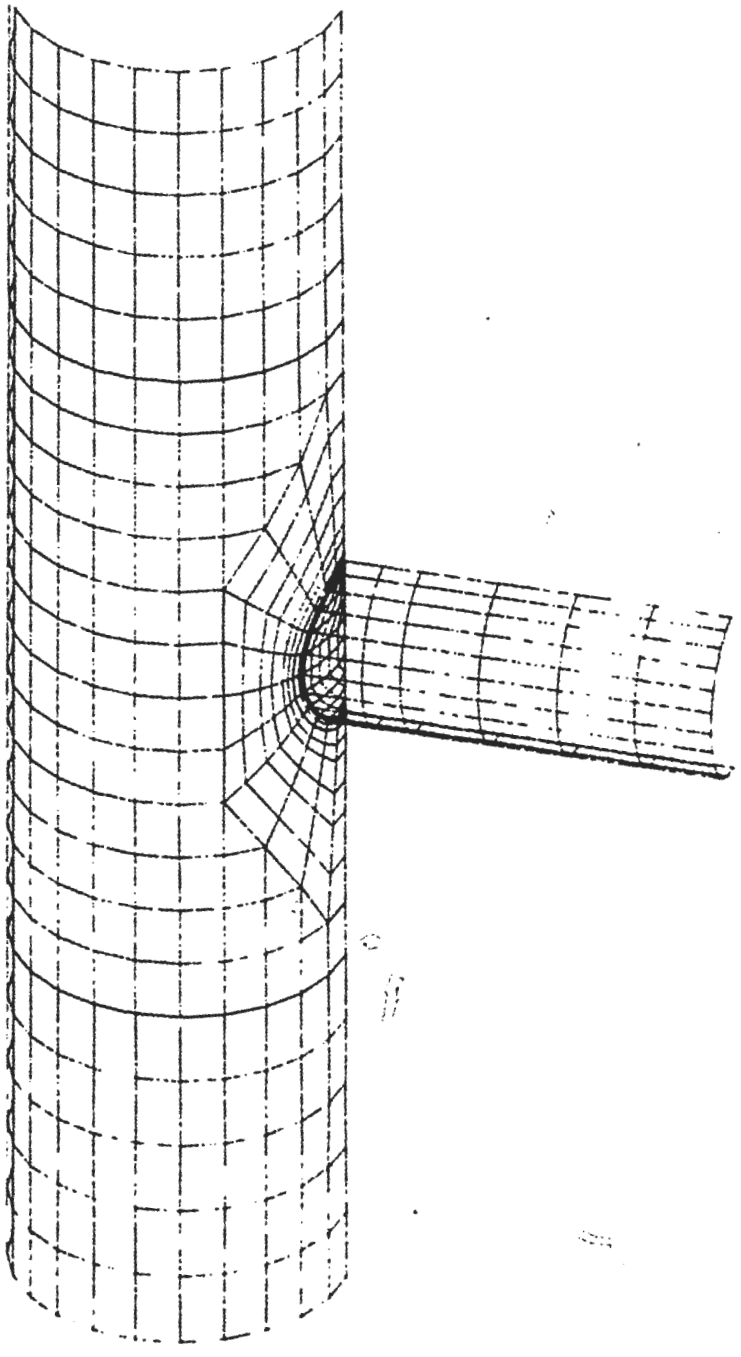

Fig. 3.11 Finite element mesh for the joint.

are restrained by the symmetric consideration. The results are for the following material properties of steel: Young's Modulus, E = 2.1 x 10^5 MN/m^2 and Poisson ratio, $\nu = 0.3$. The joint is analysed for two different loads acting on the brace - (i) axial compressive load of 1 MN and (ii) in-plane load of 0.1 MN. The normalized deformed shapes of the joint for the two cases are shown in Figs. 3.12 and 3.13. The variations of the maximum principal stresses for both cases at certain critical locations (Fig. 3.14) are shown in Figs. 3.15 - 3.22. The stress concentration factors for the chord and the brace at the crown and saddle points due to axial compressive and in-plane bending loads are shown in Table 3.2. It can be noted that the stress concentration factors for the joint due to axial compressive and tensile loads at brace are same from stress analysis point of view. The calculated stress concentration factors are compared with the published literature based on experimental work and finite element analysis (Irvine 1981b; Clayton and Martin 1980) and the parametric equations (Wordsworth and Smedly 1978; Gibstein 1978; Kuang et al 1977). The parameters of the joint analysed by Clayton and Martin are $\alpha = 13.5$, $\beta = 0.5$, $\tau = 0.5$, $\gamma = 12.1$ whereas those of the joint analysed by Irvine are $\alpha = 10.5$, $\beta = 0.53$, $\tau = 0.51$ and $\gamma = 13.4$.

3.4.1 Chord stresses

In the chord, measured and predicted stress concentration factors show good general agreement. Under an axial load, the peak stress occurs at the saddle point. There is a reversal of the principal stress along line-4 (Fig. 3.21). In the case of

Table 3.2 Stress concentration factors.

Methods	Chord Side				Brace Side			
	Axial		In-plane Bending		Axial		In-plane Bending	
	Crown Line-3	Saddle Line-4	Crown Line-3	Saddle Line-4	Crown Line-1	Saddle Line-2	Crown Line-1	Saddle Line-2
Present 2-Dimensional Finite Element Analysis (without plug)	2.968	7.004	1.35	0.977	4.18 3.96*	7.68 7.04*	3.36 2.34*	0.584 0.481*
Present 2-Dimensional Finite Element Analysis (with plug)	2.656	6.277	1.07	0.8	3.69 2.41*	6.8 6.02*	2.92 2.08*	0.497 0.427*
Analysis (Clayton & Martin 1980)	-	6.7	2.6	-	-	9.3	3.0	-
Experiment (Clayton & Martin 1980)	-	5.8	2.0	-	-	7.1	1.7	-
Experiment (Irvine 1981b)	-	7.7	1.2	-	-	-	-	-
Wordsworth & Smedly(1978)	3.097	7.439	2.38	-	2.951	5.686	2.499	-
Gibstein(1978)	-	6.7	2.2	-	-	-	2.065	-
Kuang et al (1977)	-	6.9	1.9	-	-	-	2.358	-

* With correction for brace rotation and translation

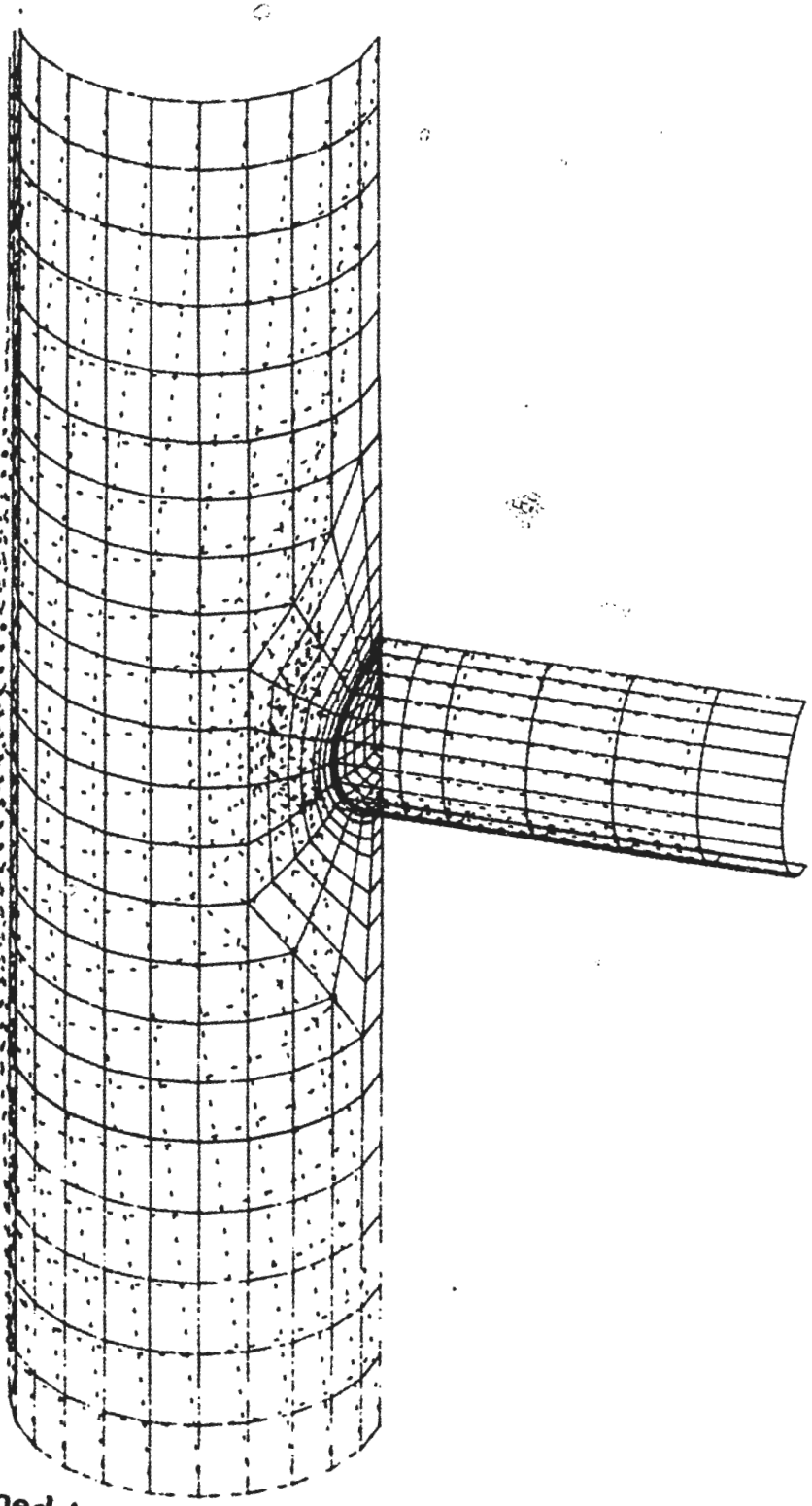

Fig. 3.12 Deformed joint due to axial compressive load.

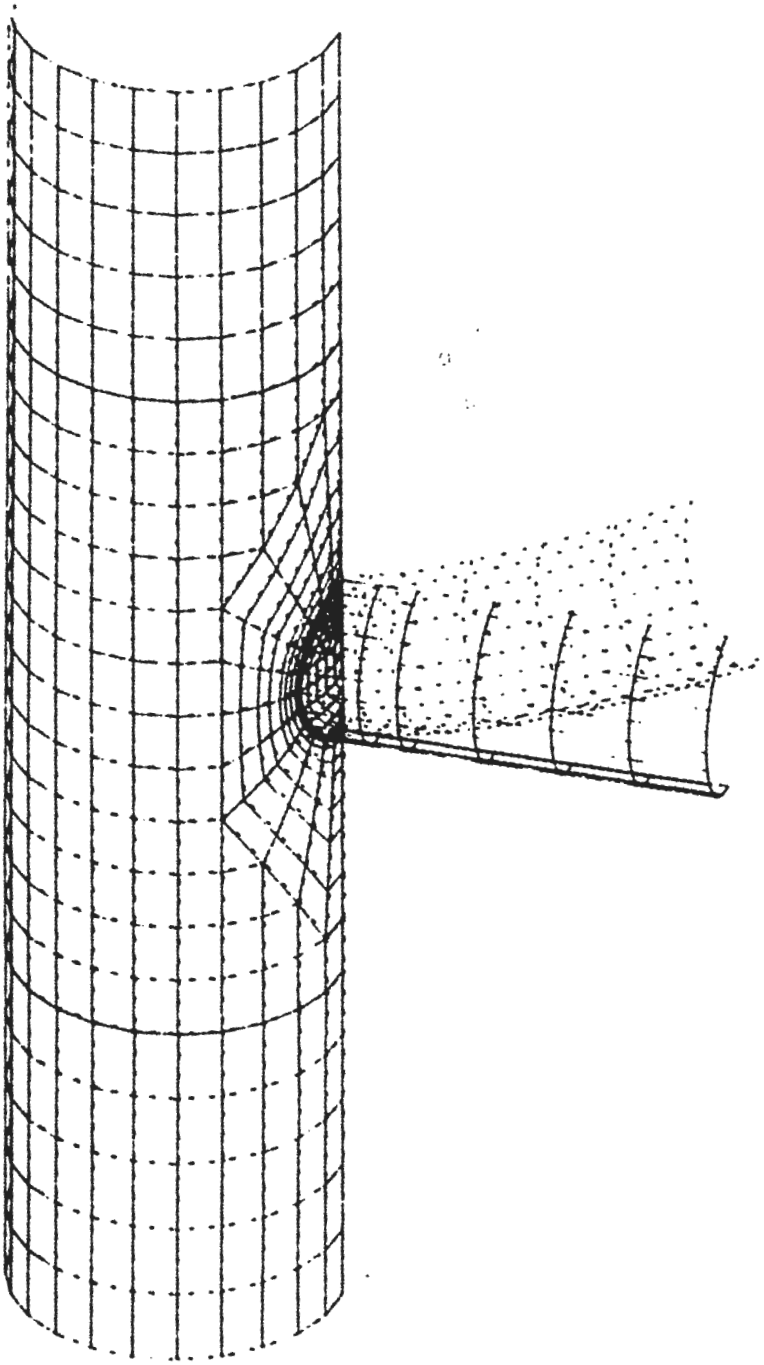

Fig. 3.13 Deformed joint due to in-plane bending load.

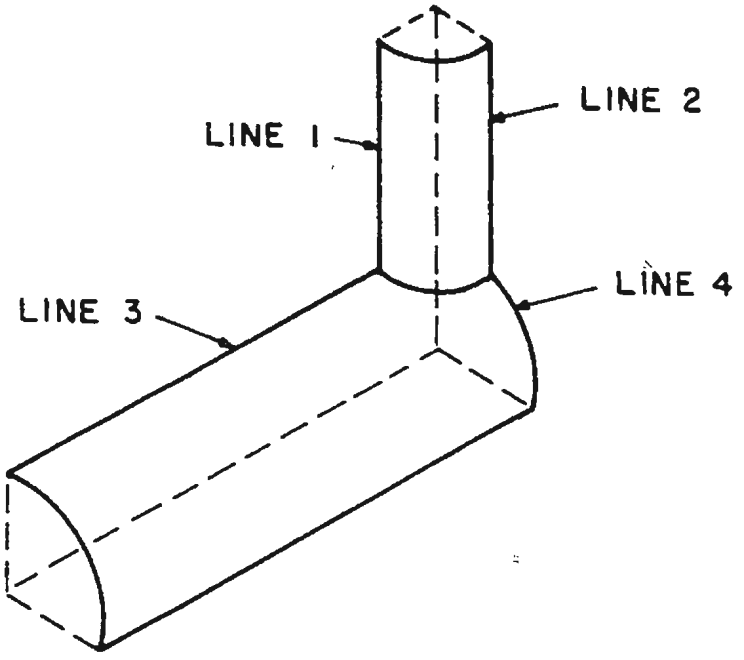

Fig. 3.14 Characteristic lines of the joint.

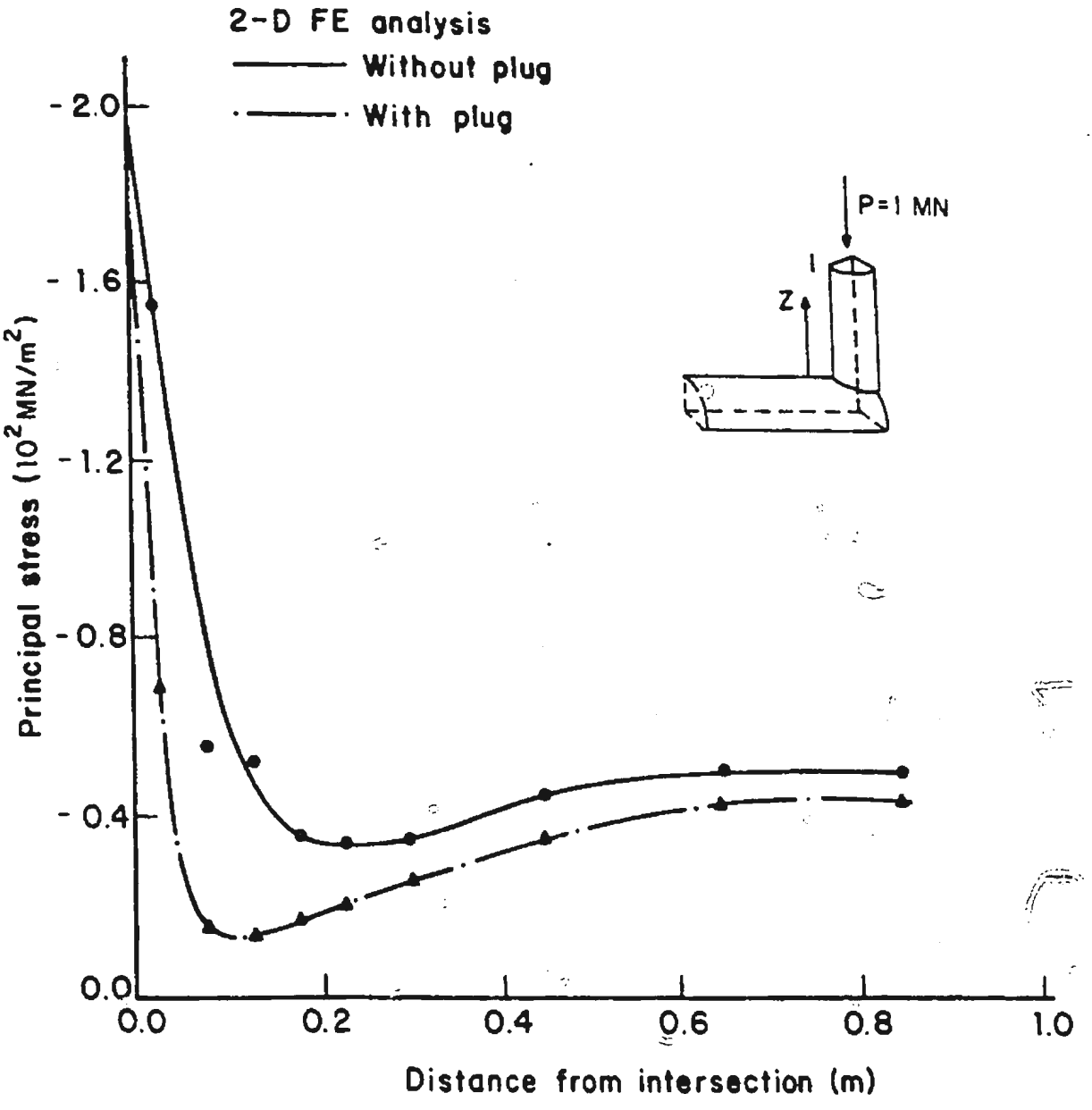

Fig. 3.15 Principal stress distribution: brace, line 1 - axial load.

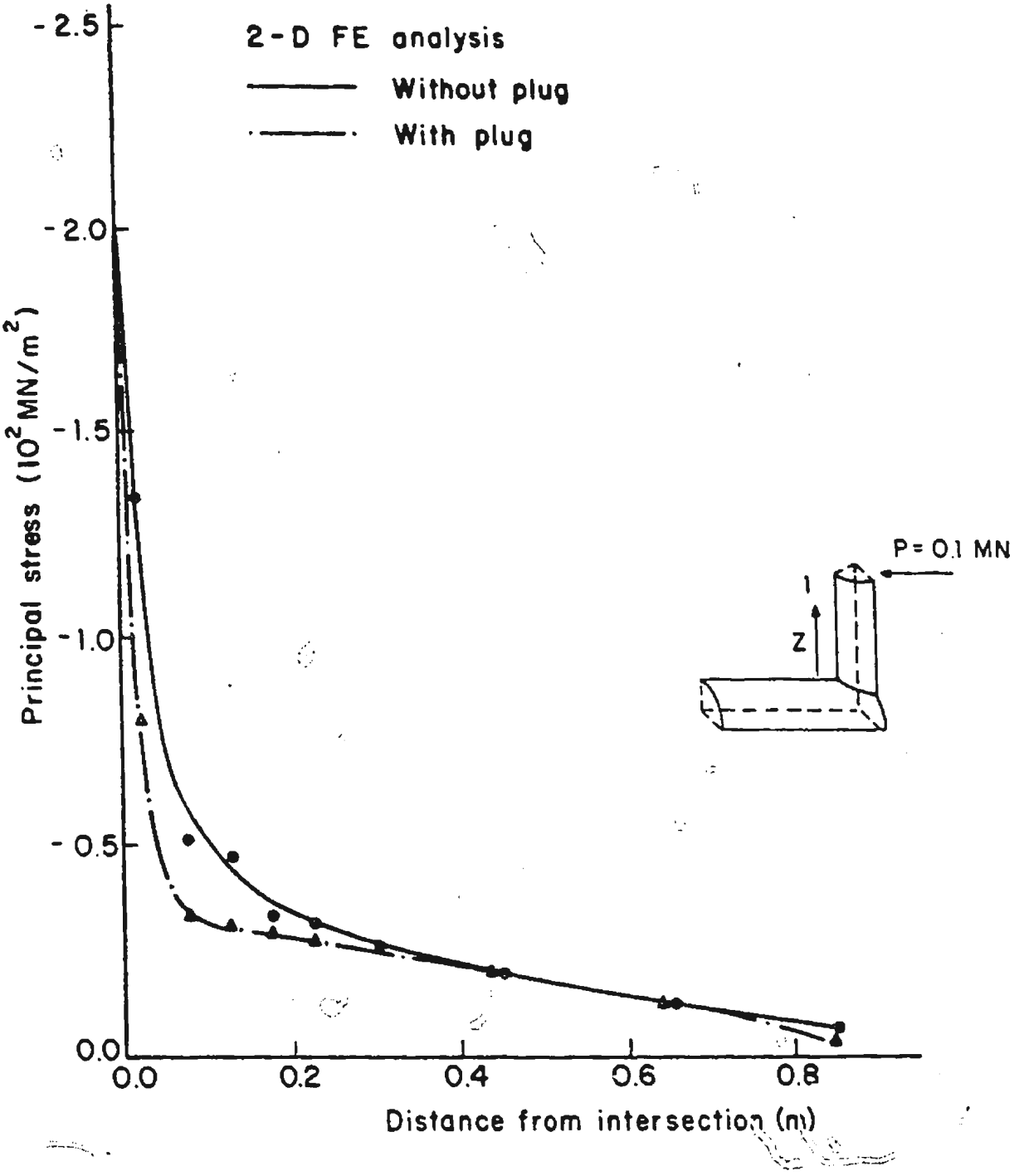

Fig. 3.16 Principal stress distribution: brace, line 1 - in-plane bending.

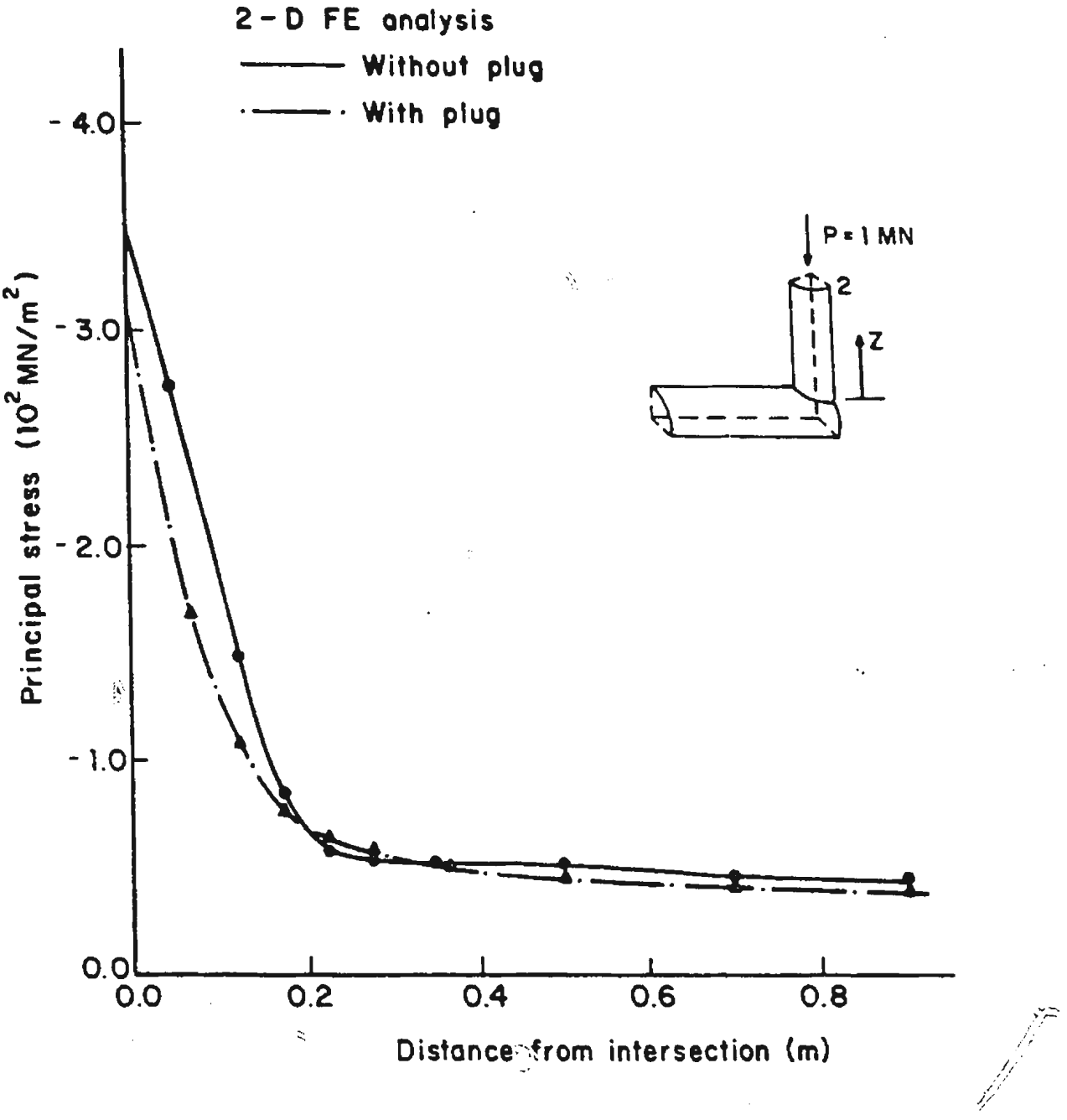

Fig. 3.17 Principal stress distribution: brace, line 2 - axial load.

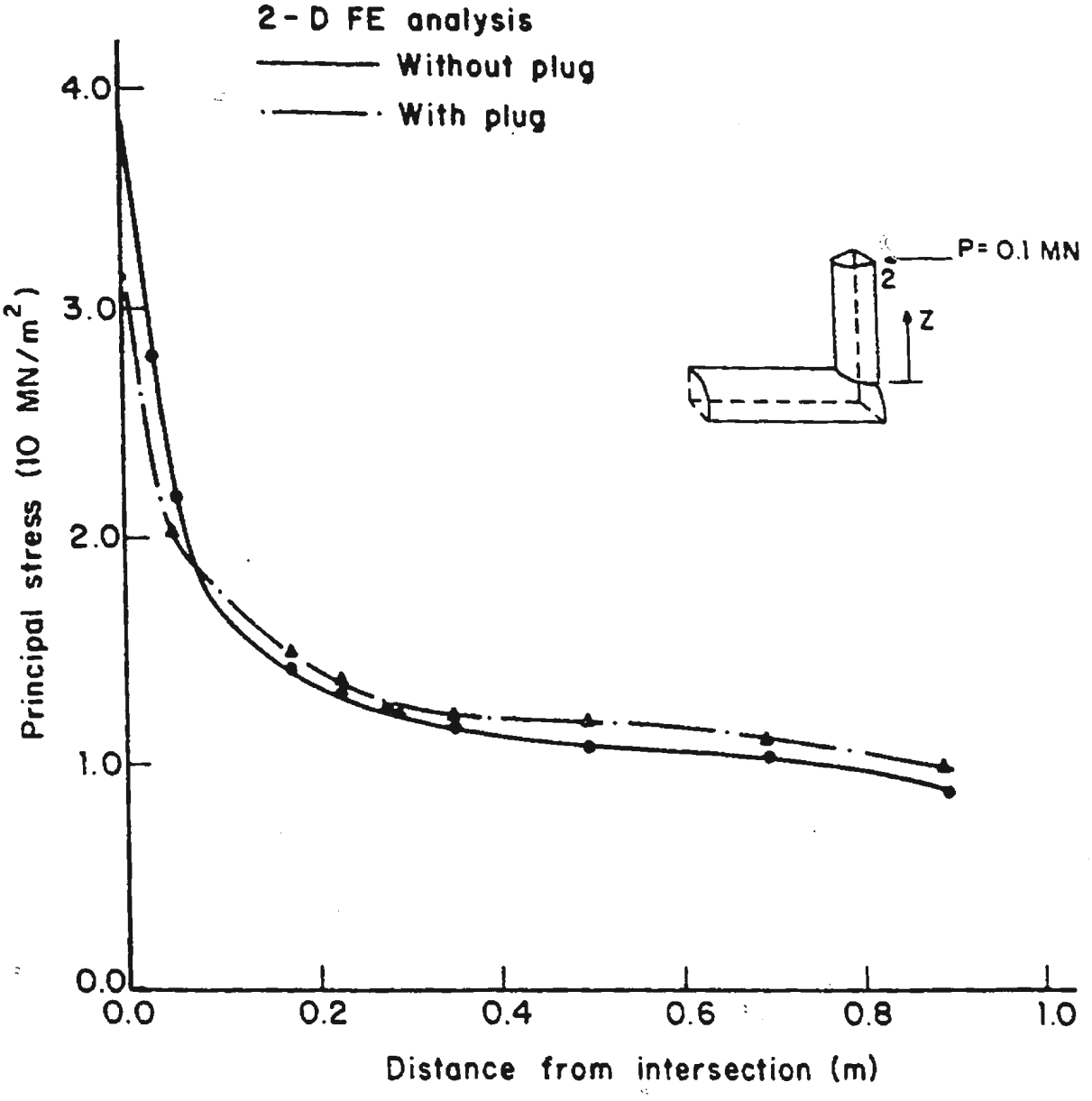

Fig. 3.18 Principal stress distribution: brace, line 2 - in-plane bending.

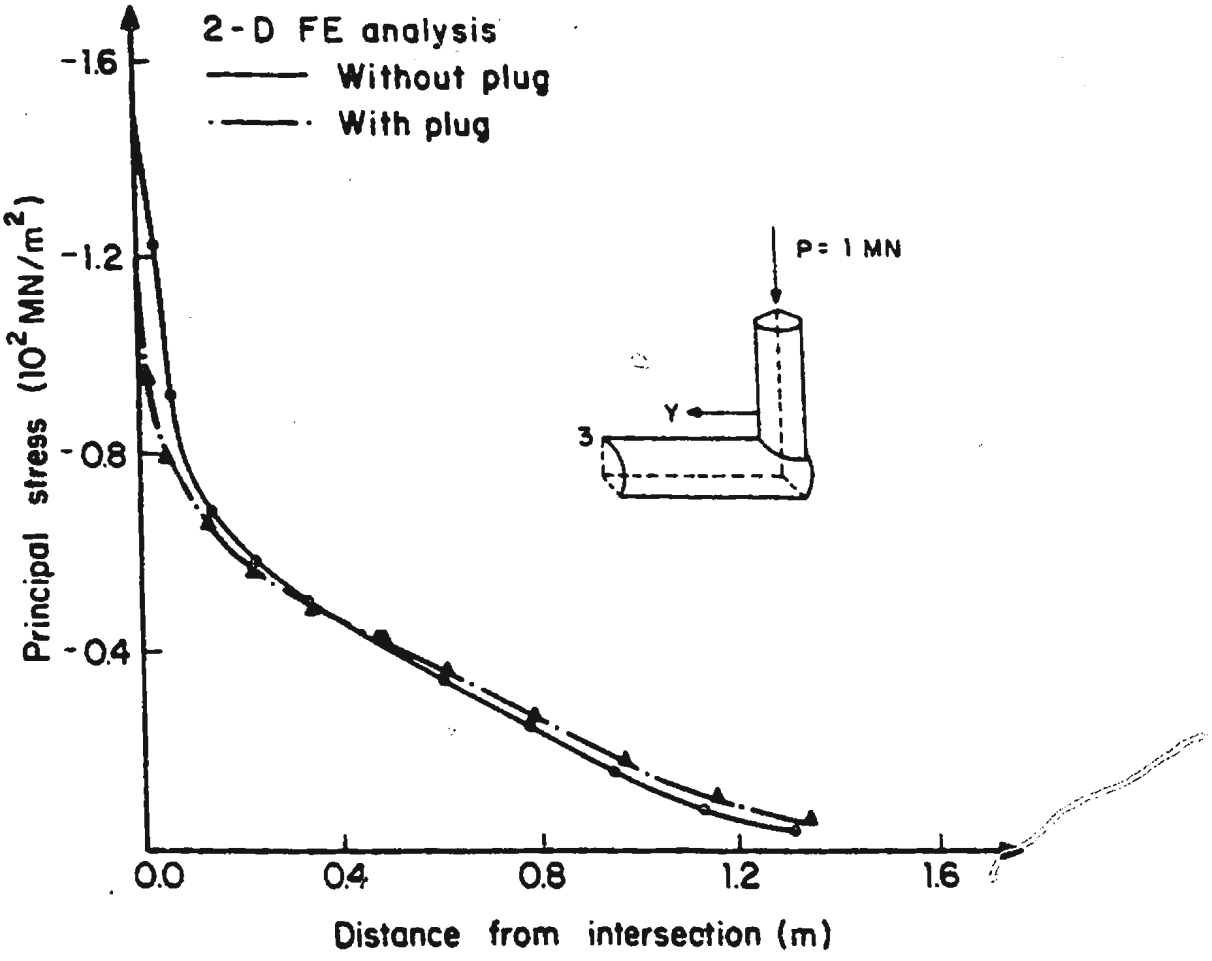

Fig. 3.19 Principal stress distribution: chord, line 3 - axial load.

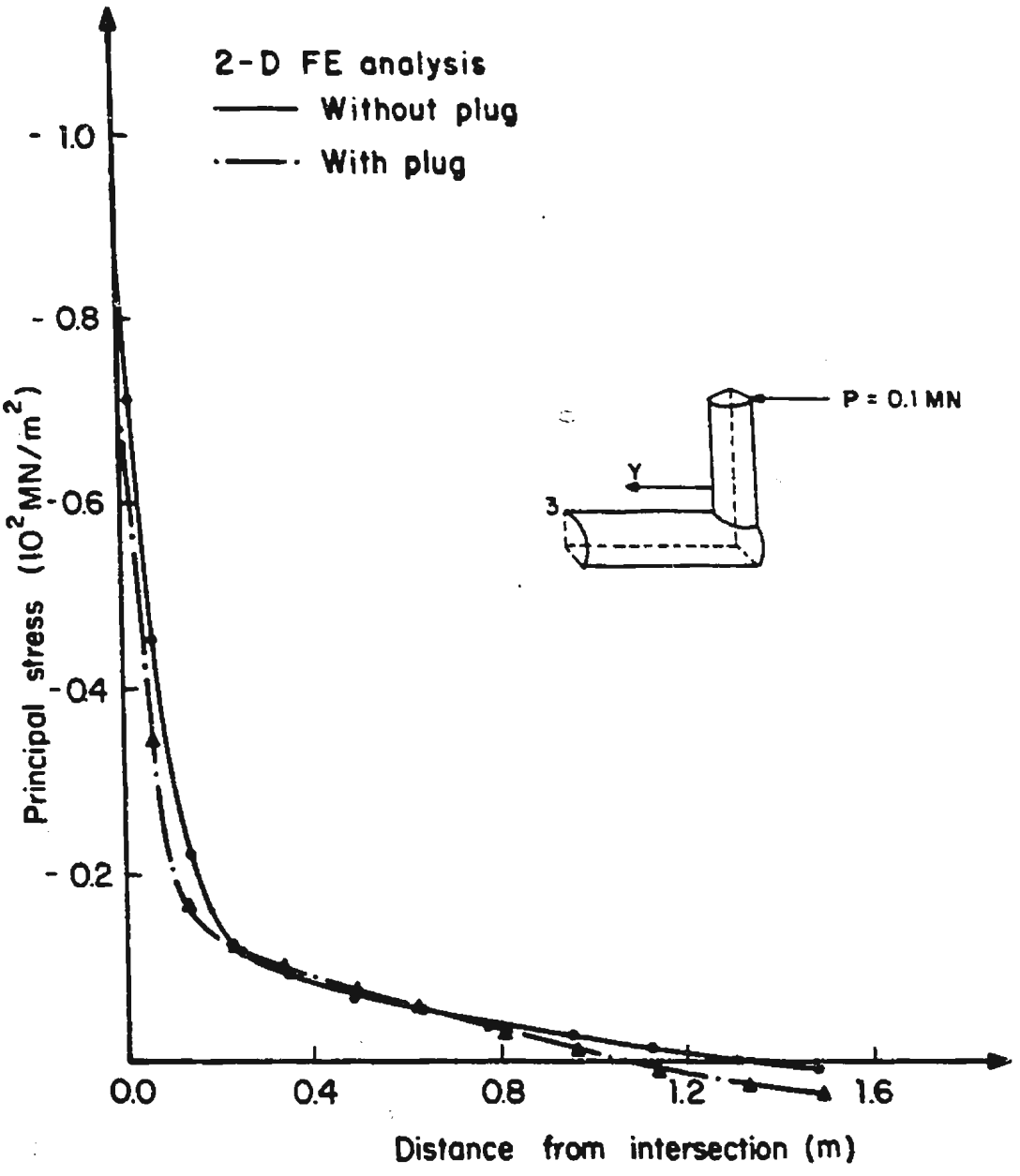

Fig. 3.20 Principal stress distribution: chord, line 3 - in-plane bending.

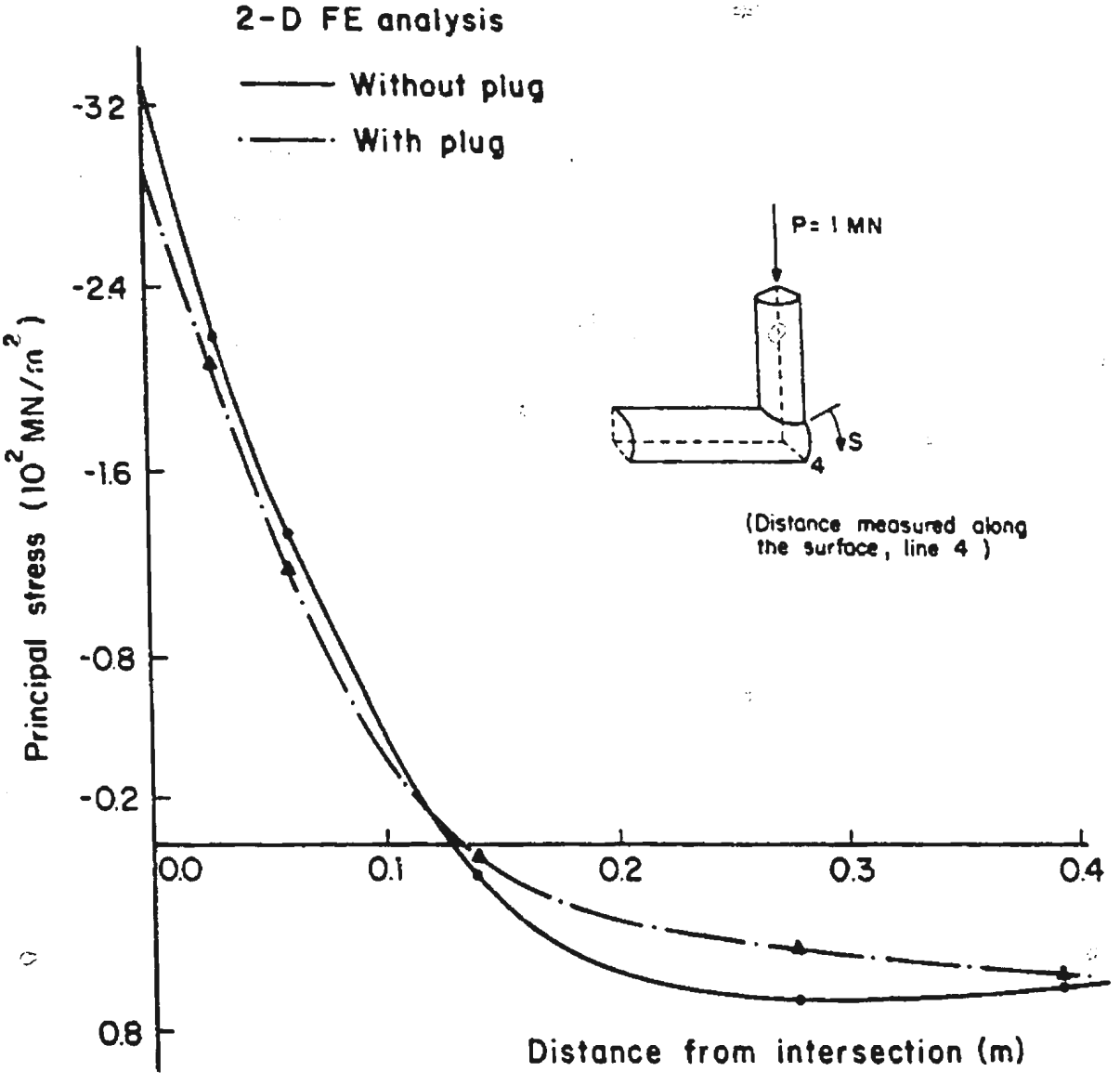

Fig. 3.21 Principal stress distribution: chord, line 4 - axial load.

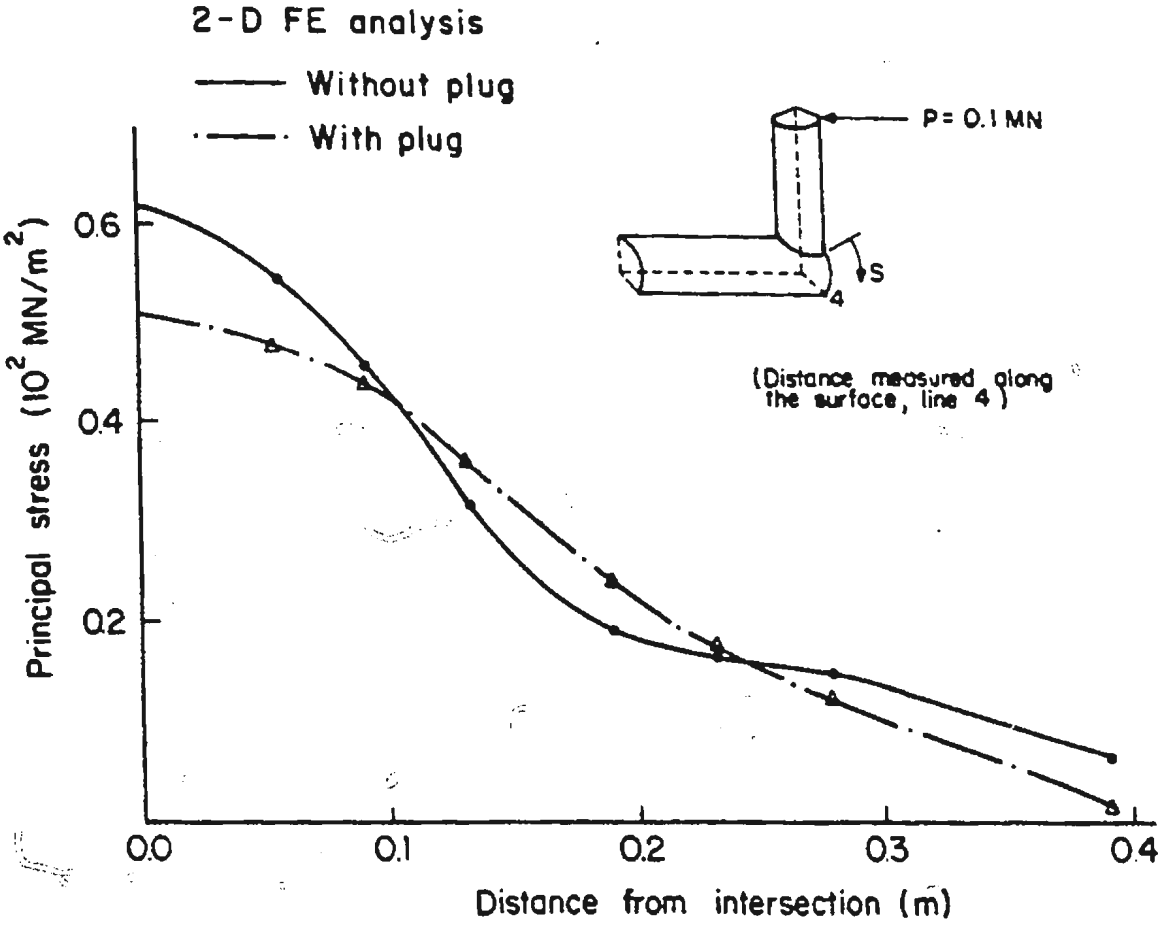

Fig. 3.22 Principal stress distribution: chord, line 4 - in-plane bending.

an in-plane bending load, the peak stress occurs at the crown (Table 3.2). The stress gradient near the intersection in line-3 is less compared to that on brace line-1.

3.4.2 Brace stresses

In the brace, measured and predicted stress concentrations factors are not in good agreement. The finite element analysis tends to overestimate the brace-side SCFs due to the displaced brace/chord intersection. Loading in the brace distorts the chord, as shown in Fig. 3.23. The degree of ovalling of the chord is influenced primarily by the brace loading and the chord stiffness. Hence, the wall rotation at the end of the brace is dictated by the chord. The thickness of the chord wall and its resistance to shear results in the brace end rotating about and translating from a point, a, within the chord in between the chord-brace mid surface intersection and the point above, b, on the chord upper surface. To interpret the finite element results in terms of the physical model stress values, the entire brace finite element representation must be translated from the mid surface intersection to the point b.

Irvine(1980) calculated this shift, Δ, and found it to be

$$\Delta = \frac{1}{2} T - p + q \qquad (3.31)$$

where T is the chord wall thickness and p is a small positive correction factor. It can be expressed in terms of the joint parameters as

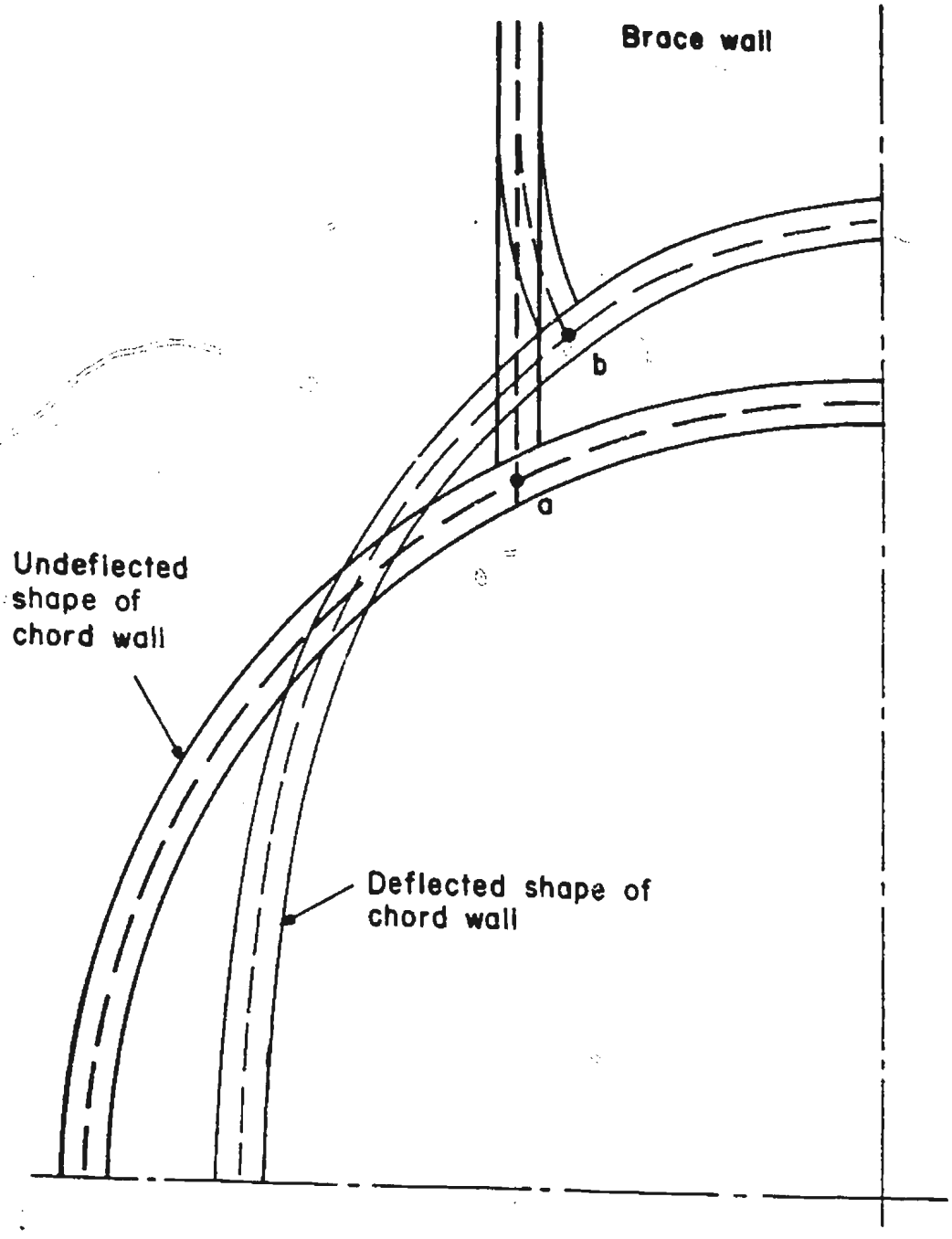

Fig. 3.23 Schematic of displacements on the plane of symmetry (Irvine 1980).

$$p = \left\{ 0.0163 \frac{\tau}{\beta} + 0.297 \frac{\tau^{\frac{3}{4}}}{\beta^{\frac{1}{4}}} \right\} T \qquad (3.32)$$

The term q in Eqn.3.31 is a small positive correction for the weld profile. For this joint, p equals 0.23 T. The most significant part of the formula for Δ is 1/2 T. Assuming $q = p$ for the joint under investigation, the value of Δ is 16 mm.

The modified stress concentration factors for the brace side are tabulated in Table 3.2. These are in good agreement with the experimental values reported in the literature. The brace stresses after axial shifting are shown in Figs. 3.24 - 3.27.

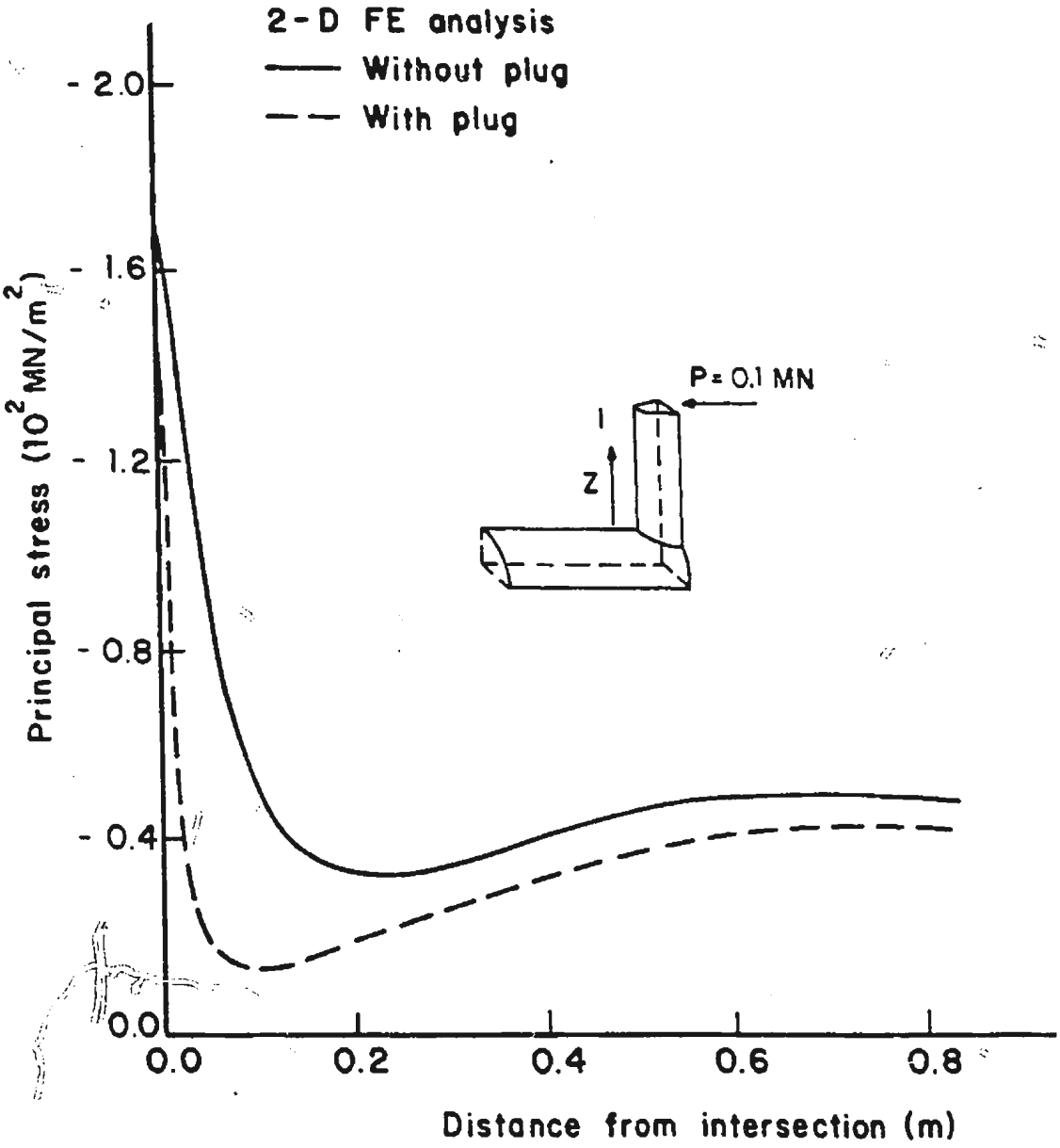

Fig. 3.24 Modified principal stress distribution after axial shifting: brace, line 1 - in-plane bending.

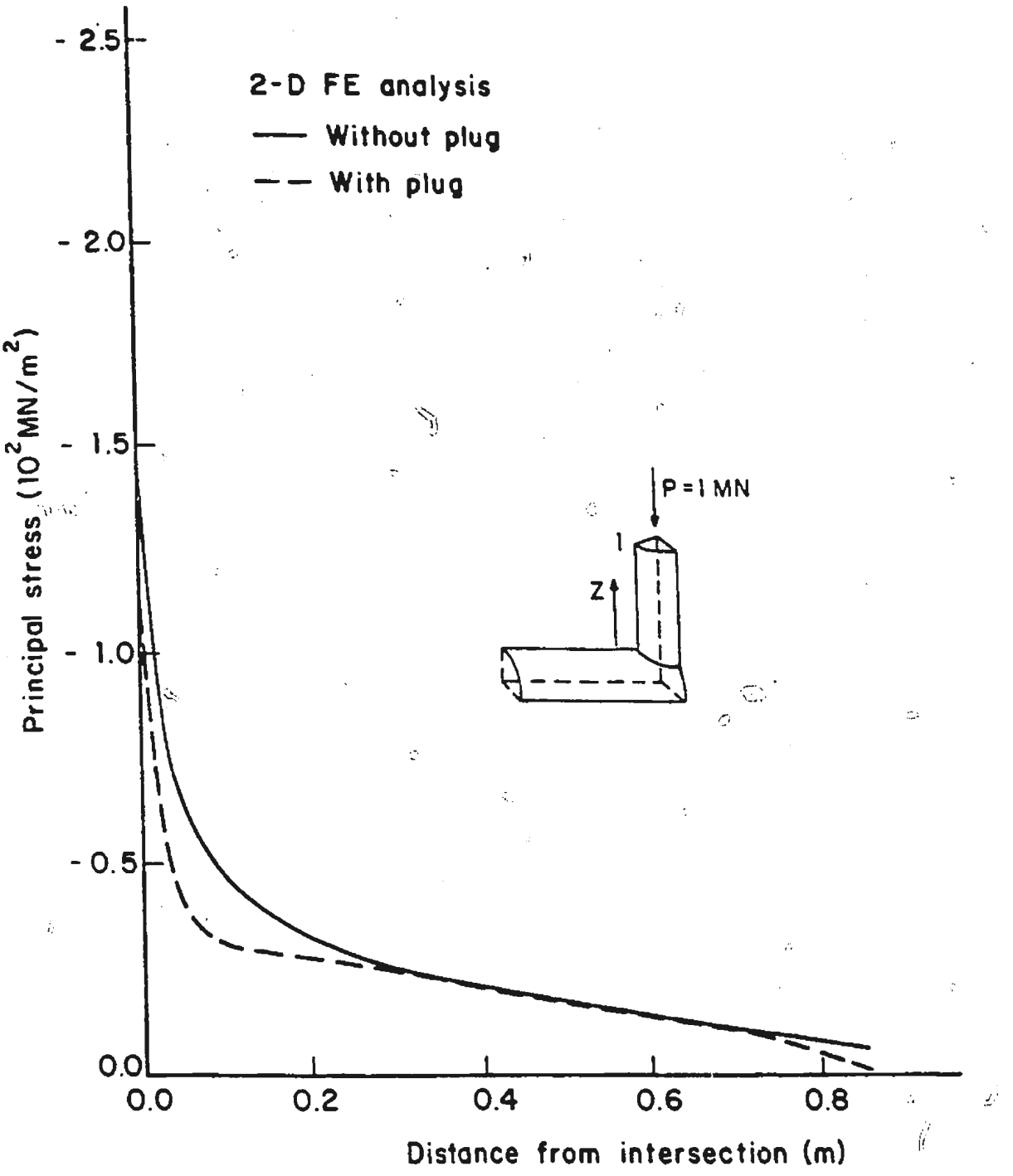

Fig. 3.25 Modified principal stress distribution after axial shifting: brace, line 1 - axial load.

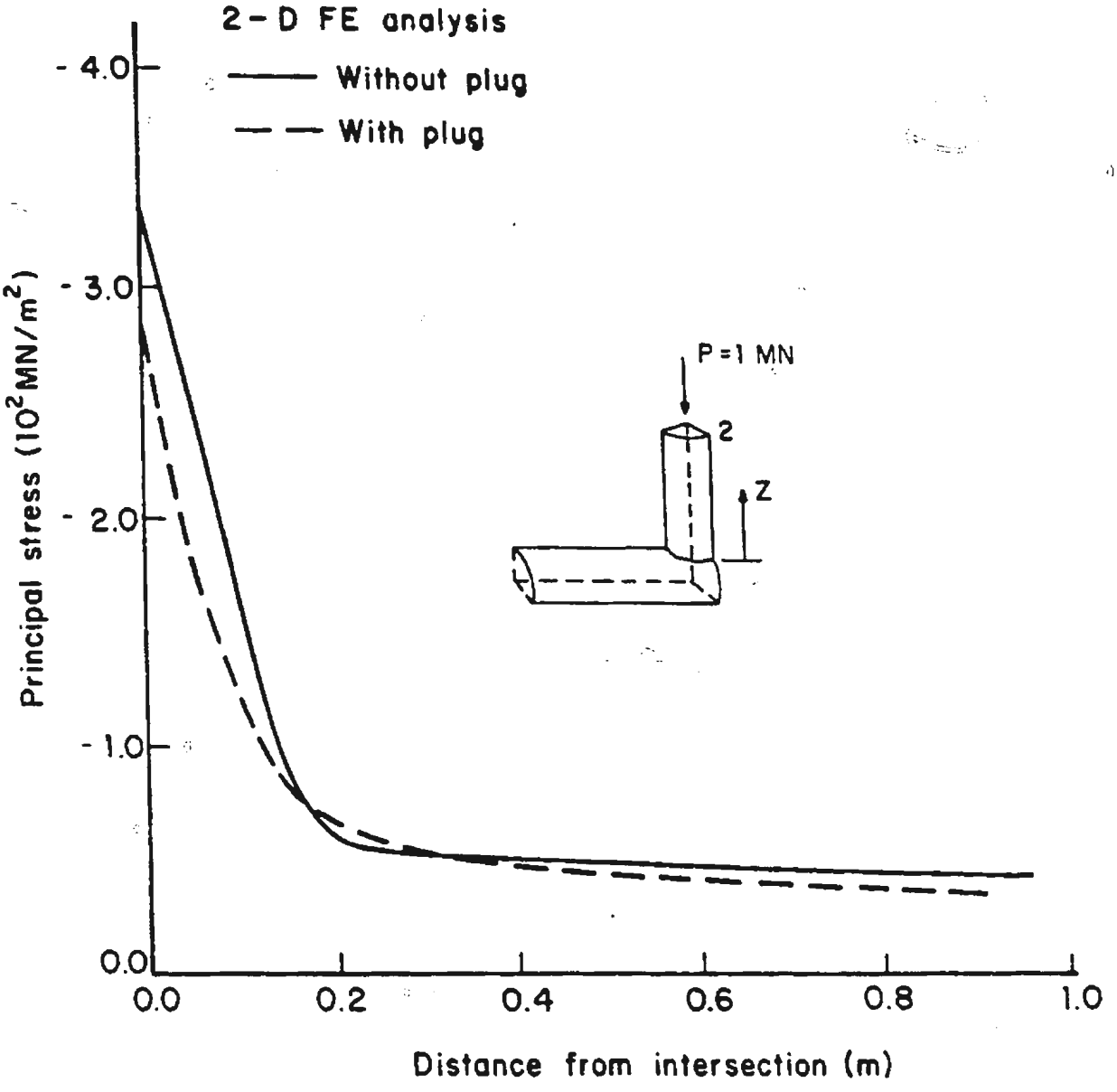

Fig. 3.26 Modified principal stress distribution after axial shifting: brace, line 2 - axial load.

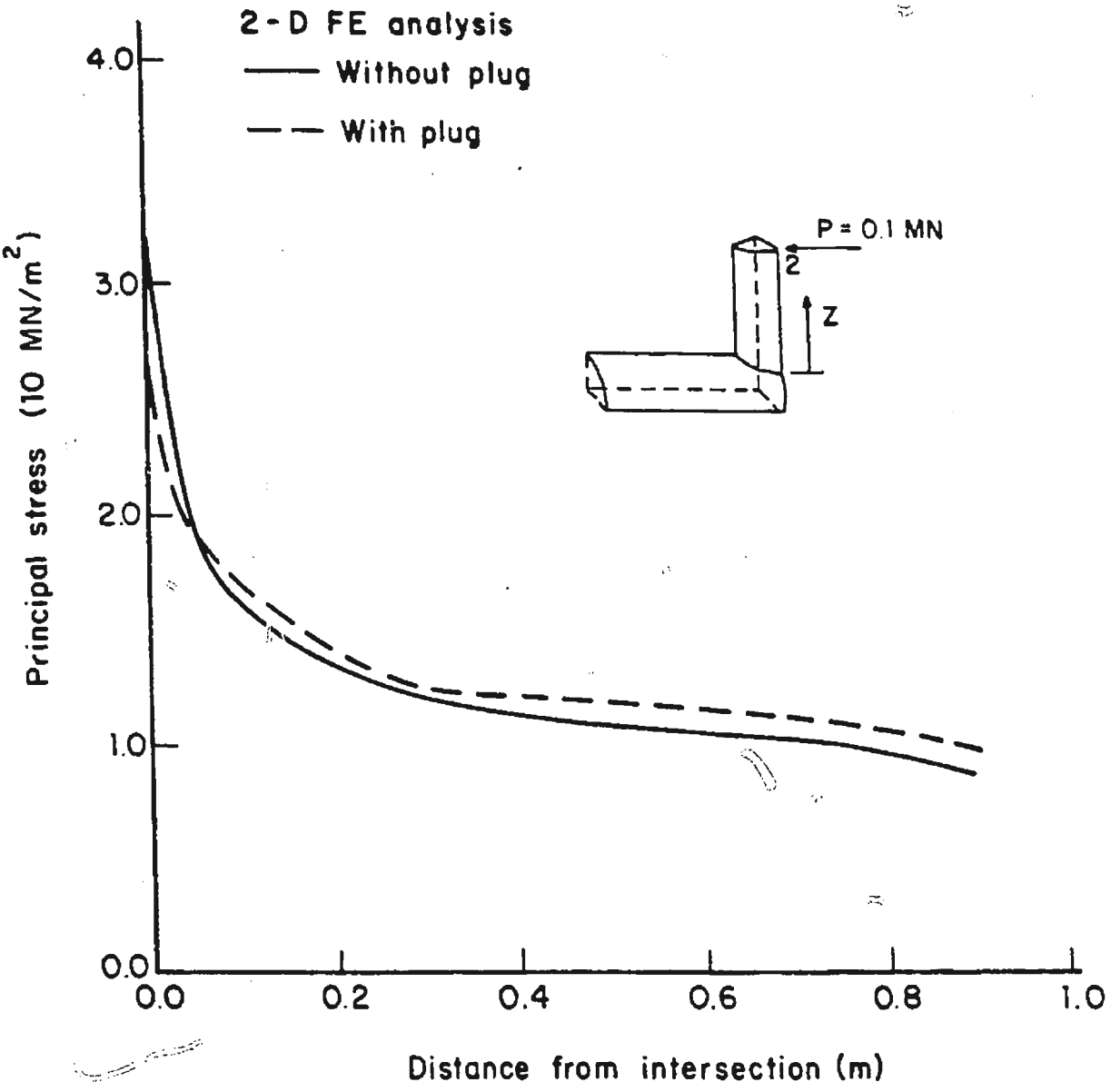

Fig. 3.27 Modified principal stress distribution after axial shifting: brace, line 2 - in-plane bending.

CHAPTER 4

THREE DIMENSIONAL ANALYSIS

4.1 Introduction

The tubular joint is analysed using the plate element in Chapter 3, in which the joint is idealized by the midsurface of the chord and the brace. The thickness of the shell is used only in the computation of the membrane and the flexural stiffnesses. It is not considered in the physical modelling of the joint and the consequent through-thickness variation of the displacements and the resulting stresses. The plate element idealisation also does not permit the consideration of the weld profile and the actual intersection. These limitations of the plate finite element modelling are overcome by three dimensional modelling of the T-joint.

This chapter presents the necessary theory and the results for the three dimensional idealisation of the joint including the weld reinforcement, based on the modelling of (i) entire T-joint and (ii) region around the hot spot using rezone technique.

4.2 Modelling of Entire Joint

The entire joint is discretized using the same mesh generation technique discussed in the previous chapter. The weld dimensions used for the modelling are shown in Fig. 4.1. The chord/brace surface and the weld regions are discretized using 8-

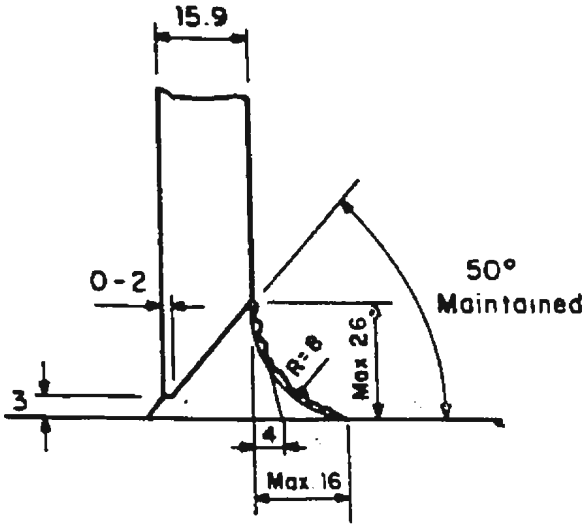

(a) Details of weld

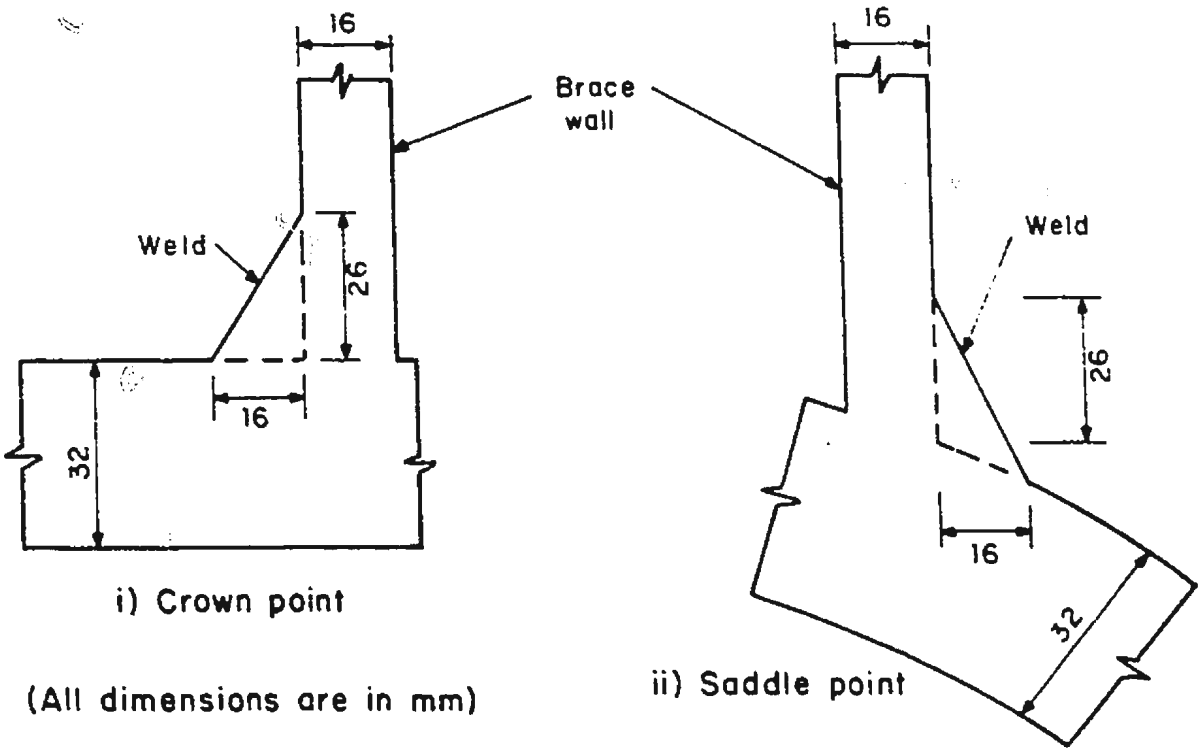

(All dimensions are in mm)

(b) Idealisation of weld

Fig. 4.1 Modelling of weld at chord/brace intersection.

node and 6-node three dimensional elements respectively. The discretized model is shown in Fig. 4.2.

4.2.1 Element stiffness formulation

The displacements u_i , v_i and w_i at each node along the x, y and z axes are taken as the nodal degrees-of-freedom. The faces of the 8-node brick element (Fig. 4.3) are defined by the local coordinates ξ , η , $\varsigma = \pm 1$. The global coordinates are defined as

$$\begin{aligned} x &= \sum_{i=1}^{8} N_i \, x_i \\ y &= \sum_{i=1}^{8} N_i \, y_i \\ z &= \sum_{i=1}^{8} N_i \, z_i \end{aligned} \tag{4.1}$$

where x_i , y_i and z_i are the element nodal point coordinates and N_i is the shape function, which is given by

$$N_i = \frac{1}{8} (1 + \xi\xi_i) (1 + \eta\eta_i) (1 + \varsigma\varsigma_i) \tag{4.2}$$

To improve the flexural characteristics of the 8-node isoparametric brick elements, three incompatible modes are introduced into the displacement interpolation functions. The global displacements u , v and w at any point within the element can be expressed as (Wilson et al 1973),

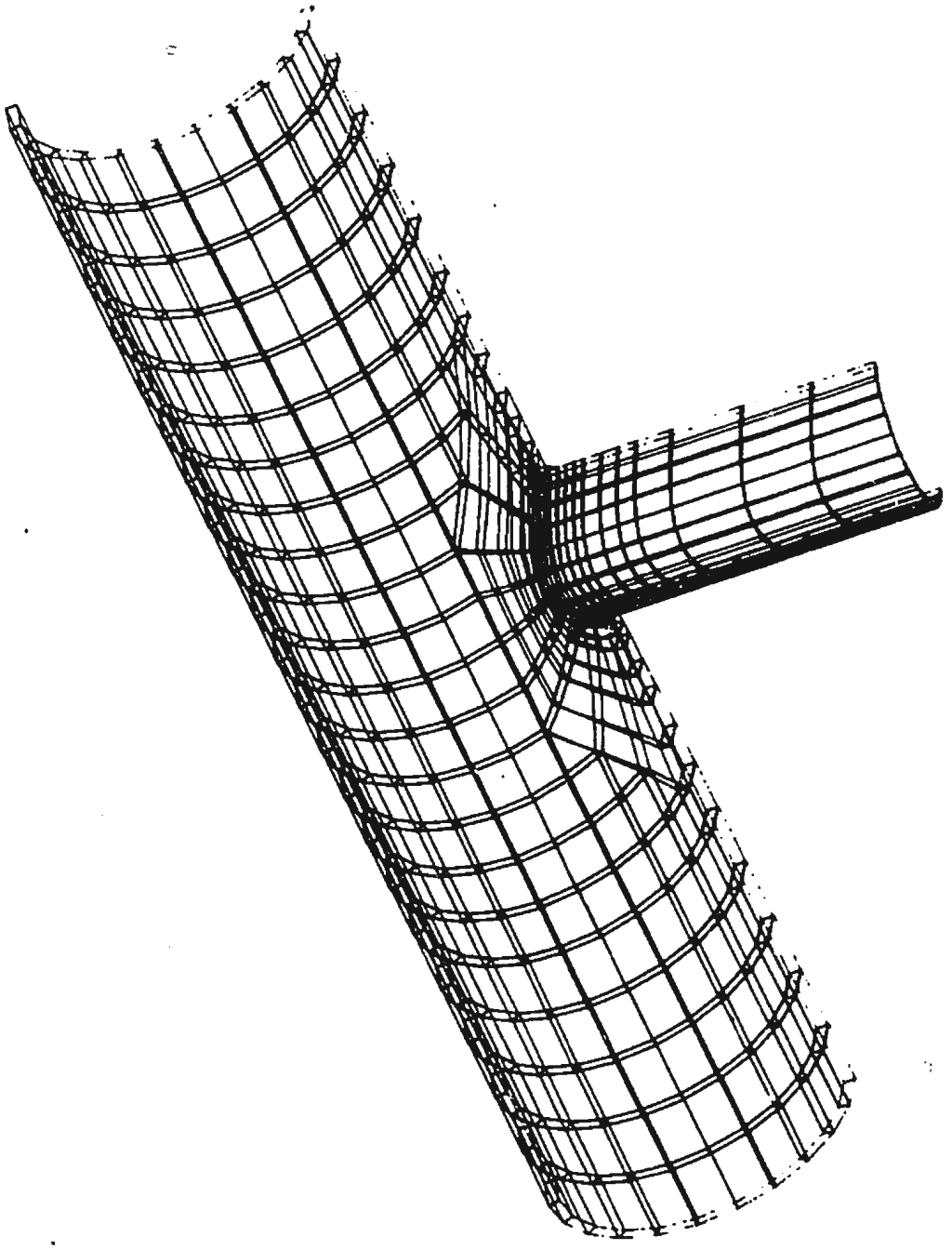

Fig. 4.2 Three dimensional finite element mesh for the joint.

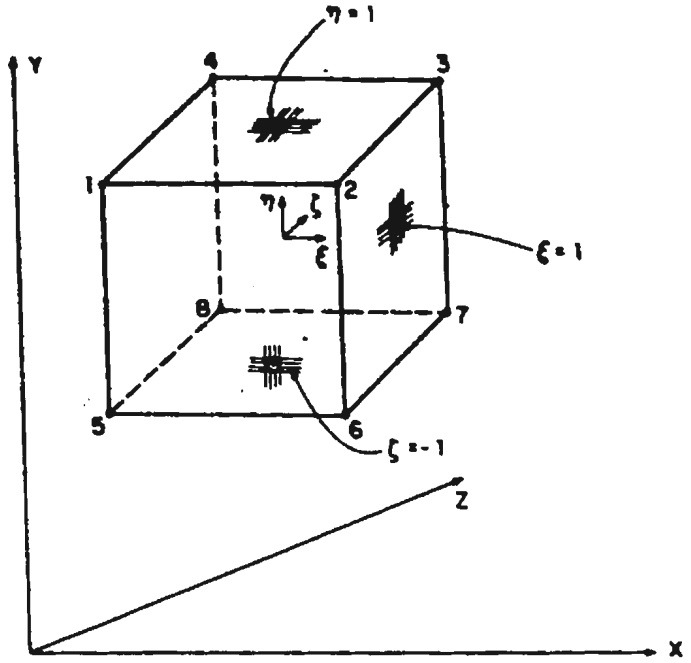

Fig. 4.3 Three dimensional 8-noded element.

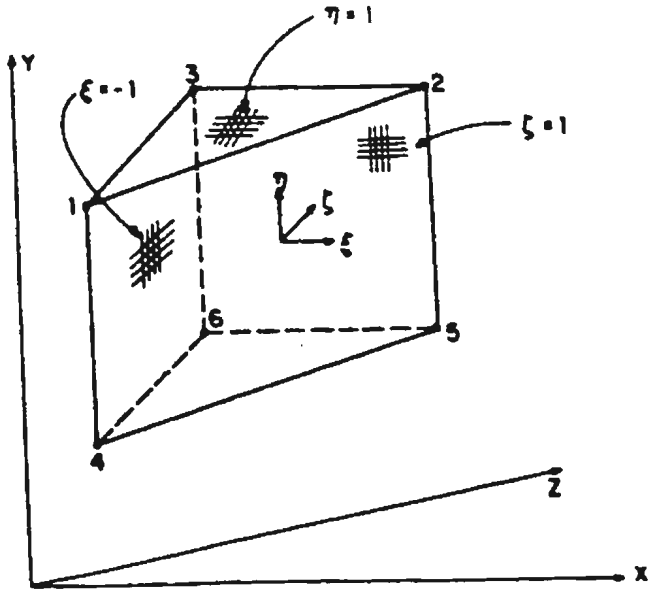

Fig. 4.4 Six-noded prism element.

$$u = \sum_{i=1}^{8} N_i u_i + \sum_{j=1}^{3} g_j \alpha_j$$

$$v = \sum_{i=1}^{8} N_i v_i + \sum_{j=1}^{3} g_j \beta_j \qquad (4.3)$$

$$w = \sum_{i=1}^{8} N_i w_i + \sum_{j=1}^{3} g_j \gamma_j$$

where $g_j (j=1, 2, 3)$ are the additional shape functions for the incompatible element and α_j , β_j and γ_j are generalized displacement coordinates. The first group of terms of the right hand side of Eqn. 4.3 represents the polynomial corresponding to the basic element. The displacements due to the terms in the polynomial of the basic element are continuous across the interface of the element, but those due to the second group of terms in Eqn. 4.3 are not necessarily continuous across the element boundaries. The incompatible shape functions g_j are given as

$$\begin{aligned} g_1 &= (1 - \xi^2) \\ g_2 &= (1 - \eta^2) \\ g_3 &= (1 - \zeta^2) \end{aligned} \qquad (4.4)$$

The stress-strain relations are

$$\begin{aligned} \left\{ \sigma \right\} &= \left[\sigma_x \, \sigma_y \, \sigma_z \, \tau_{xy} \, \tau_{yz} \, \tau_{zx} \right]^T = \left[D \right] \left\{ \epsilon \right\} \\ &= \left[D \right] \left[\epsilon_x \, \epsilon_y \, \epsilon_z \, \gamma_{xy} \, \gamma_{yz} \, \gamma_{zx} \right]^T \end{aligned} \qquad (4.5)$$

where [D] is the elasticity matrix, which is given by

$$\left[D \right] = \frac{E(1-\nu)}{(1+\nu)(1-2\nu)} \begin{bmatrix} 1 & \frac{\nu}{(1-\nu)} & \frac{\nu}{(1-\nu)} & 0 & 0 & 0 \\ & 1 & \frac{\nu}{(1-\nu)} & 0 & 0 & 0 \\ & & 1 & 0 & 0 & 0 \\ & & & \frac{(1-2\nu)}{2(1-\nu)} & 0 & 0 \\ & & & & \frac{(1-2\nu)}{2(1-\nu)} & 0 \\ & & & & & \frac{(1-2\nu)}{2(1-\nu)} \end{bmatrix} \tag{4.6}$$

The strain-displacement relation of the element can be written as

$$\left\{ \epsilon \right\} = \left[B_1 \quad B_2 \right] \left\{ \begin{matrix} a_1 \\ -- \\ a_2 \end{matrix} \right\} \tag{4.7}$$

where

$$\left\{ a_{1i} \right\} = \left[u_i \; v_i \; w_i \right]^T, \quad \text{for } i = 1, \ldots, 8 \tag{4.8}$$

are the element nodal displacements, and

$$\left\{ a_2 \right\} = \left[\alpha_1 \; \beta_1 \; \gamma_1 \; \alpha_2 \; \beta_2 \; \gamma_2 \; \alpha_3 \; \beta_3 \; \gamma_3 \right]^T \tag{4.9}$$

are the element generalized coordinates due to the incompatible modes. The submatrices $[B_1]$ and $[B_2]$ contain the derivatives of the functions, N and g, respectively. The general forms of the submatrices $[B_1]$ and $[B_2]$ are given by

$$\left[B_{1i} \right] = \begin{bmatrix} \frac{\partial N_i}{\partial x} & 0 & 0 \\ 0 & \frac{\partial N_i}{\partial y} & 0 \\ 0 & 0 & \frac{\partial N_i}{\partial z} \\ \frac{\partial N_i}{\partial y} & \frac{\partial N_i}{\partial x} & 0 \\ 0 & \frac{\partial N_i}{\partial z} & \frac{\partial N_i}{\partial y} \\ \frac{\partial N_i}{\partial z} & 0 & \frac{\partial N_i}{\partial x} \end{bmatrix} \tag{4.10}$$

and

$$\left[B_{2i} \right] = \begin{bmatrix} \frac{\partial g_i}{\partial x} & 0 & 0 \\ 0 & \frac{\partial g_i}{\partial y} & 0 \\ 0 & 0 & \frac{\partial g_i}{\partial z} \\ \frac{\partial g_i}{\partial y} & \frac{\partial g_i}{\partial x} & 0 \\ 0 & \frac{\partial g_i}{\partial z} & \frac{\partial g_i}{\partial y} \\ \frac{\partial g_i}{\partial z} & 0 & \frac{\partial g_i}{\partial x} \end{bmatrix} \tag{4.11}$$

The global and the local derivatives of the shape functions are related by the equation

$$\begin{Bmatrix} \frac{\partial N_i}{\partial x} \\ \frac{\partial N_i}{\partial y} \\ \frac{\partial N_i}{\partial z} \end{Bmatrix} = \left[J \right]^{-1} \begin{Bmatrix} \frac{\partial N_i}{\partial \xi} \\ \frac{\partial N_i}{\partial \eta} \\ \frac{\partial N_i}{\partial \zeta} \end{Bmatrix} \tag{4.12}$$

where [J] is the Jacobian matrix, which is given by

$$\left[J \right] = \begin{bmatrix} \sum \frac{\partial N_i}{\partial \xi} x_i & \sum \frac{\partial N_i}{\partial \xi} y_i & \sum \frac{\partial N_i}{\partial \xi} z_i \\ \sum \frac{\partial N_i}{\partial \eta} x_i & \sum \frac{\partial N_i}{\partial \eta} y_i & \sum \frac{\partial N_i}{\partial \eta} z_i \\ \sum \frac{\partial N_i}{\partial \varsigma} x_i & \sum \frac{\partial N_i}{\partial \varsigma} y_i & \sum \frac{\partial N_i}{\partial \varsigma} z_i \end{bmatrix} \tag{4.13}$$

The equilibrium equations for the element can be written as

$$\begin{bmatrix} \left[K_{11} \right] & \left[K_{12} \right] \\ -- & -- \\ \left[K_{21} \right] & \left[K_{22} \right] \end{bmatrix} \begin{Bmatrix} \{ a_1 \} \\ -- \\ \{ a_2 \} \end{Bmatrix} = \begin{Bmatrix} \{ F_1 \} \\ -- \\ \{ F_2 \} \end{Bmatrix} \tag{4.14}$$

where

$$[K_{ij}] = \int_{-1}^{1} \int_{-1}^{1} \int_{-1}^{1} [B_i]^T [D] [B_i] | J | \, d\xi \, d\eta \, d\varsigma \tag{4.15}$$

are the submatrices of the element stiffness matrix. $\{F_1\}$ is the element load vector containing equivalent nodal forces. $\{F_2\}$ represents the forces, in terms of the element generalized coordinates, contributed by thermal loading; in the present case $\{F_2\} = \{0\}$. Before assembling the global stiffness matrix, the incompatible degrees-of-freedom $\{a_2\}$ in Eqn. 4.14 are condensed out to get the resulting equation

$$\left[\bar{K}_{11} \right] \left\{ a_1 \right\} = \left\{ F_1 \right\} \tag{4.16}$$

where

$$\left[\bar{K}_{11}\right] = \left[K_{11}\right] - \left[K_{12}\right]\left[K_{22}\right]^{-1}\left[K_{21}\right] \tag{4.17}$$

Equation 4.16 is used to assemble the global stiffness matrix, and nodal displacements are then computed. The incompatible degrees-of-freedom $\{a_2\}$ are calculated as

$$\left\{a_2\right\} = -\left[K_{22}\right]^{-1}\left[K_{21}\right]\left\{a_1\right\} \tag{4.18}$$

Knowing the displacements $\{a_1\}$ and $\{a_2\}$, the element strains and the corresponding stresses are obtained using Eqns. 4.7 and 4.5 respectively.

The stiffness matrix of the 6-node incompatible prism element is derived from the 8-node incompatible brick element by coalescing the nodes 1, 2 and 5, 6 (Fig. 4.4).

4.3 Modelling of Hot Spot Region Using Rezone Technique

The rezone technique is used to reduce the computer storage requirements as well as the solution costs that result from the large number of degrees-of-freedom associated with 3-dimensional elements. It is used here to obtain an accurate estimate of the surface and the through-thickness stresses at the intersection of the brace and the chord and also the weld reinforcement effects. The hot spot region around the weld toe and the weld reinforcement are modelled using three dimensional incompatible 8-node and 6-node elements. Using the results of the two

dimensional analysis, the boundary nodal forces/displacements are obtained as discussed in section 4.3.1. The surface stresses at the critical location of the brace-chord intersection including the through thickness distribution are compared with those obtained from the three dimensional modelling of the entire joint.

4.3.1 Rezone section

Typical rezoned regions, around the saddle point and the crown point at the brace/chord intersection, are shown in Figs. 4.5 and 4.6. A schematic example of a typical plate-to-solid element transition is shown in Fig. 4.7, in which one inner surface and one outer surface node of the brick element are assigned to each plate element node. Therefore, the plate element's boundary solutions (the displacements or the forces) are applied entirely to the brick element nodes defined at the inner and the outer surfaces of the shell (Fig. 4.8). The shell surface normal directions for all nodal locations at the plate-to-solid transition are defined as the cylinder radius vector through the transition node. The six boundary variables are distributed between two 3-D element nodes maintaining boundary compatibility of displacement or boundary force equilibrium.

The directional cosines cos α, cos β and cos γ are defined in the xyz cartesian system as shown in Fig. 4.9. This xyz coordinate system is moved from one transition node to another along the brace as well as along the chord centre lines, so

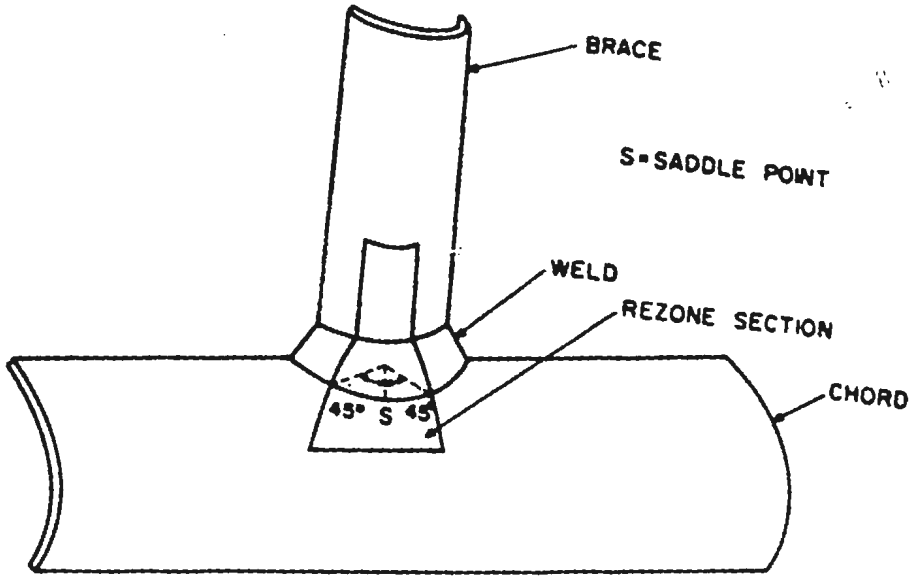

Fig. 4.5 Rezone section at saddle point.

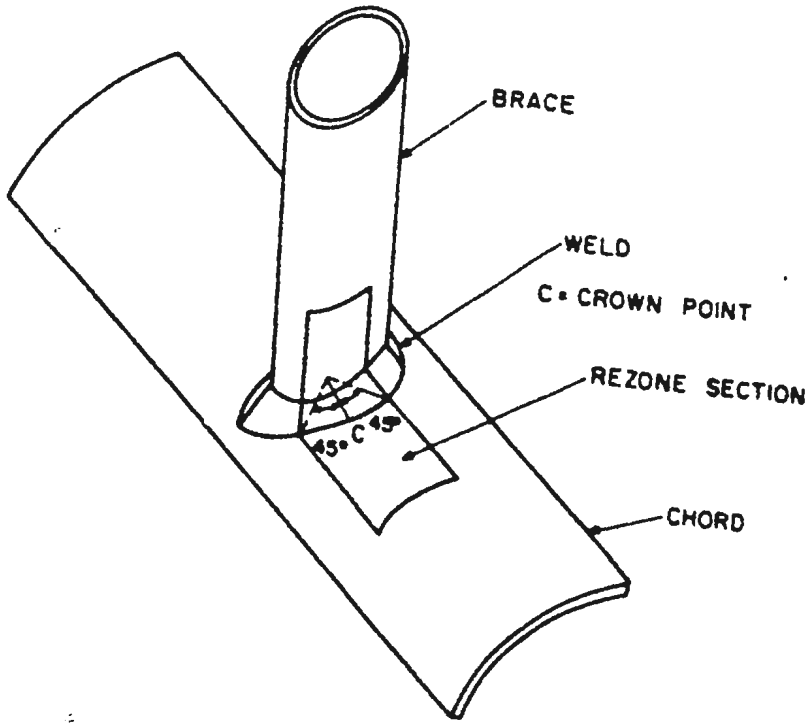

Fig. 4.6 Rezone section at crown point.

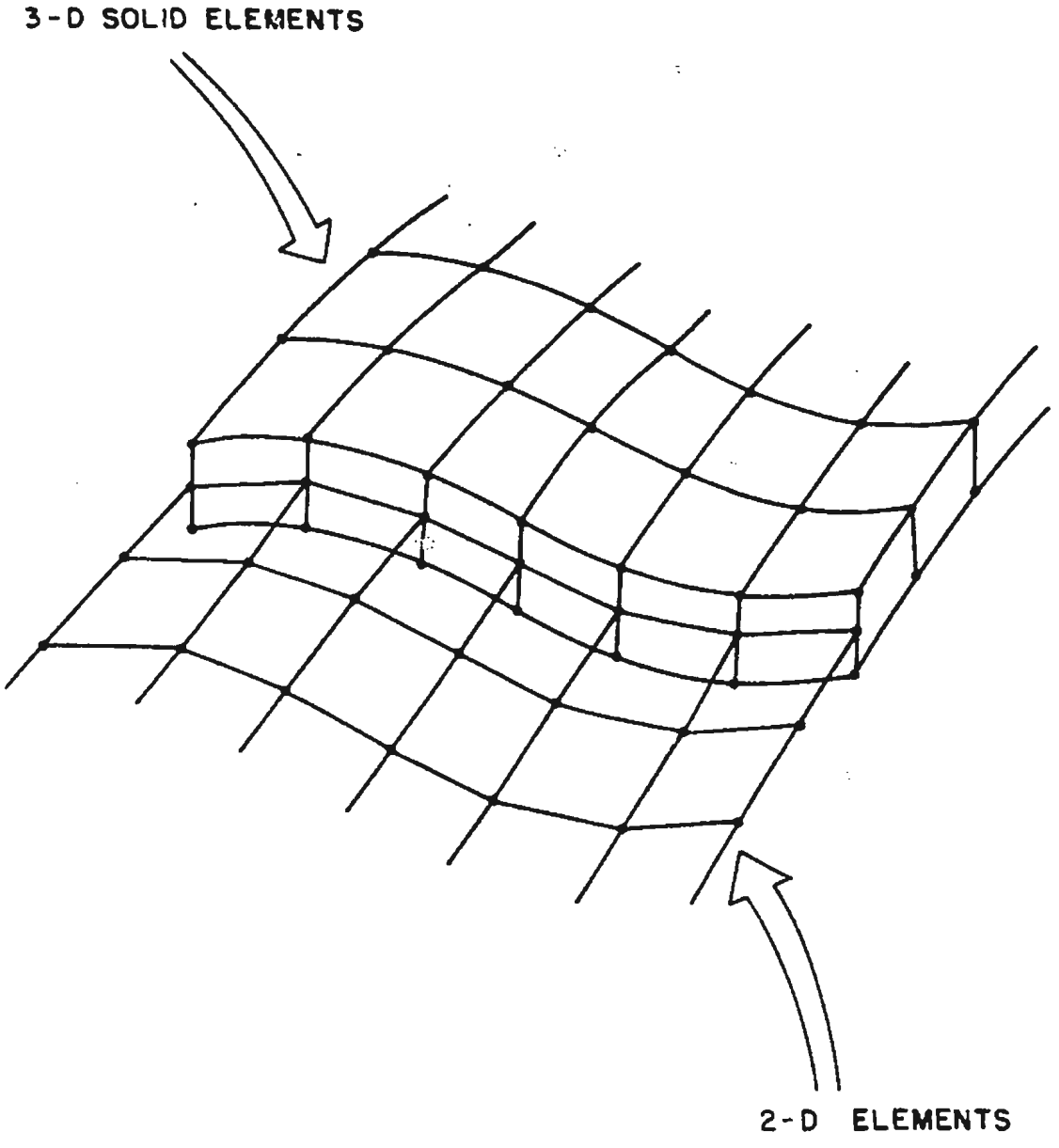

Fig. 4.7 Plate-to-solid element transition.

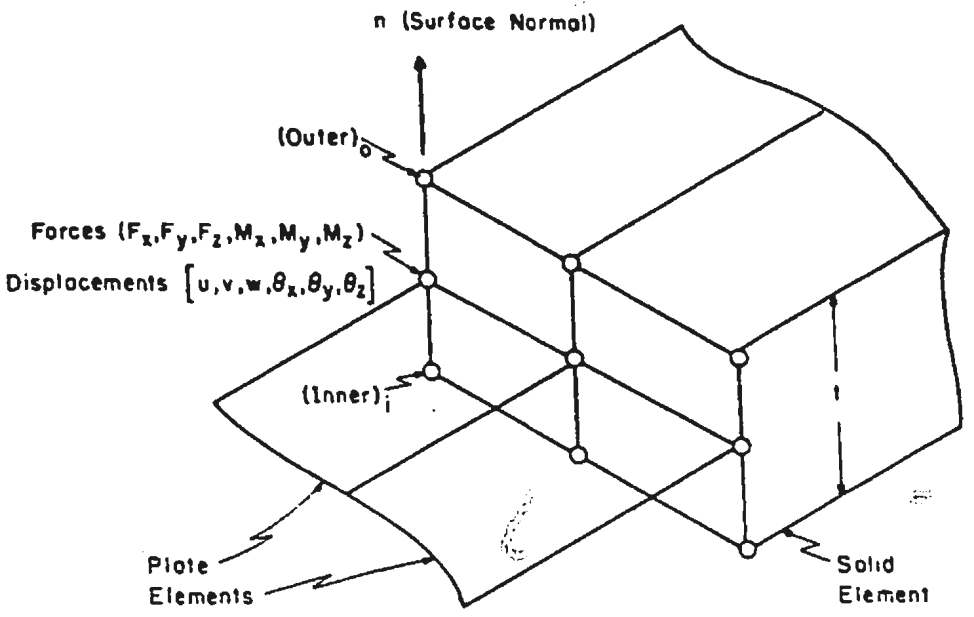

Fig. 4.8 Expanded view of plate-to-solid element transition.

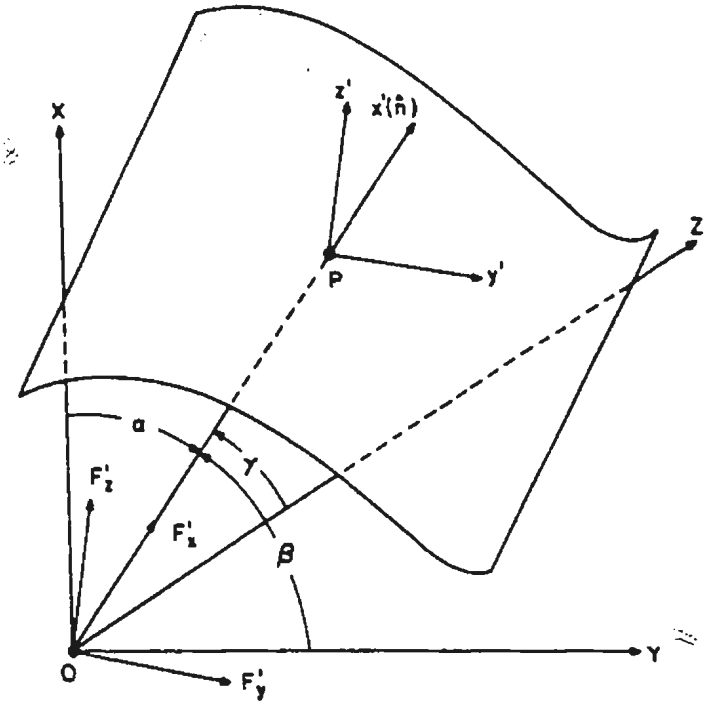

Fig. 4.9 Shell surface local coordinate system definition.

that the outward surface normal vector is the same as the radius vector. The coordinates x_o , y_o , z_o and x_i , y_i , z_i of the outer and the inner surface transition nodes, corresponding to the plate node with coordinate (x,y,z), are

$$\begin{aligned} x_o &= x + \frac{t}{2}\cos\alpha \\ y_o &= y + \frac{t}{2}\cos\beta \\ z_o &= z + \frac{t}{2}\cos\gamma \\ x_i &= x - \frac{t}{2}\cos\alpha \\ y_i &= y - \frac{t}{2}\cos\beta \\ z_i &= z - \frac{t}{2}\cos\gamma \end{aligned} \tag{4.19}$$

where t is the shell thickness and x, y, z are the plate element nodal coordinates at the transition.

4.3.2 Displacement transformation (Morgan 1979)

The boundary displacements, applied to the surface nodes of the brick element at the transition, are derived from the combined translation and rotation of the matching plate element node. The initial position vector of the surface node is defined by the outward normal vector, which connects the plate element node to the outer surface node of the solid element (Fig. 4.10). The projection of this position vector onto the x-z plane, $\hat{n}_y$, makes an inclination, λ_{yx}, with the z-axis which is given by

$$\lambda_{yx} = \sin^{-1}\left[\frac{\cos\alpha}{\sin\beta}\right] \tag{4.20}$$

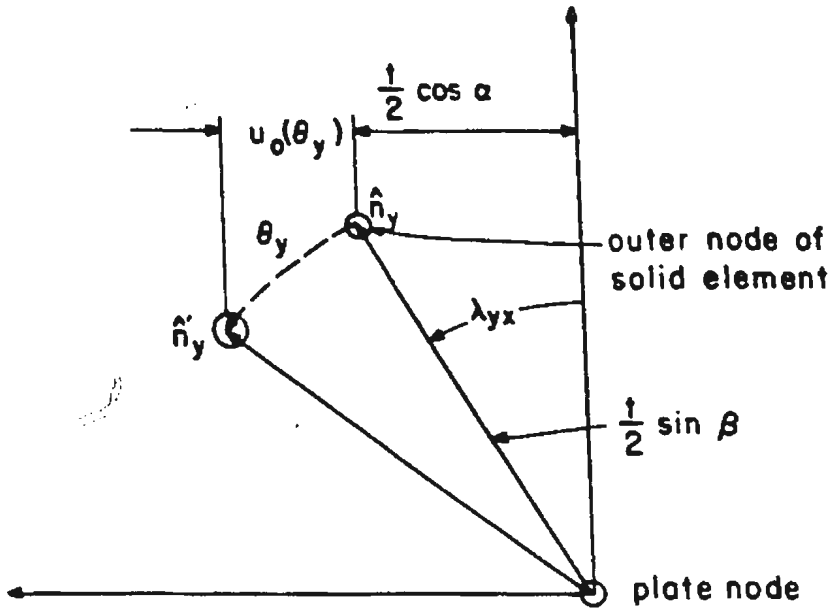

Fig. 4.10 Translation of surface node due to rotation of plate node about Y-axis.

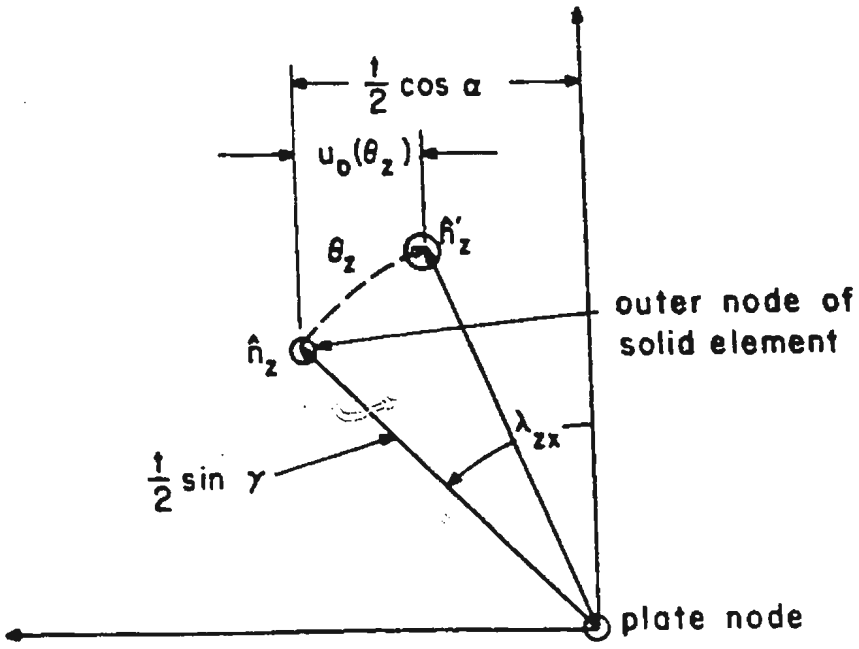

Fig. 4.11 Translation of surface node due to rotation of plate node about Z-axis.

Due to the y-axis rotation of the plate element node, θ_y , the position vector, $\hat{n}_y$, of the surface node is rotated to a new position, $\hat{n}_y'$, causing a partial translation in the x-direction, $u_o(\theta_y)$, given by

$$u_o(\theta_y) = \frac{t}{2} \sin \beta \sin (\lambda_{yx} + \theta_y) - \frac{t}{2} \cos \alpha \tag{4.21}$$

Similarly the x-direction translation due to rotation about the z-axis (Fig. 4.11), is given by

$$u_o(\theta_z) = \frac{t}{2} \sin \gamma \sin (\lambda_{zx} - \theta_z) - \frac{t}{2} \cos \alpha \tag{4.22}$$

where

$$\lambda_{zx} = \sin^{-1} \left[\frac{\cos \alpha}{\sin \gamma} \right] \tag{4.23}$$

So the total displacement in the x-direction of the outer surface node of the solid element, u_o, due to the x-translation (u), y-rotation (θ_y) and z-rotation (θ_z) of the plate node is

$$u_o = u + u_o(\theta_y) + u_o(\theta_z) \tag{4.24}$$

The total displacements, v_o and w_o, in the y and z directions can be derived in a similar manner. By assuming a rigid body movement of the solid element edge, the total x, y and z-displacements of the inner surface node, u_i , v_i and w_i, can also be obtained. The surface node displacements are

$$u_o = u + \frac{t}{2} [\sin \beta \sin (\lambda_{yx} + \theta_y) + \sin \gamma \sin (\lambda_{zx} - \theta_z) - 2 \cos \alpha]$$

$$
\begin{aligned}
v_o &= v + \frac{t}{2}\left[\sin\gamma\sin\left(\lambda_{zy}+\theta_z\right)+\sin\alpha\sin\left(\lambda_{xy}-\theta_x\right)-2\cos\beta\right] \\
w_o &= w + \frac{t}{2}\left[\sin\alpha\sin\left(\lambda_{zx}+\theta_x\right)+\sin\beta\sin\left(\lambda_{yz}-\theta_y\right)-2\cos\gamma\right] \\
u_i &= 2u - u_o \\
v_i &= 2v - v_o \\
w_i &= 2w - w_o
\end{aligned}
\tag{4.25}
$$

where

$$
\begin{aligned}
\lambda_{yx} &= \sin^{-1}\left[\frac{\cos\alpha}{\sin\beta}\right] \qquad \lambda_{zx} = \sin^{-1}\left[\frac{\cos\alpha}{\sin\gamma}\right] \\
\lambda_{zy} &= \sin^{-1}\left[\frac{\cos\beta}{\sin\gamma}\right] \qquad \lambda_{xy} = \sin^{-1}\left[\frac{\cos\beta}{\sin\alpha}\right] \\
\lambda_{xz} &= \sin^{-1}\left[\frac{\cos\gamma}{\sin\alpha}\right] \qquad \lambda_{yz} = \sin^{-1}\left[\frac{\cos\gamma}{\sin\beta}\right]
\end{aligned}
\tag{4.26}
$$

4.3.3 Force transformation (Morgan 1979)

Derivations of the force transformation relations are considerably more involved than those of the displacement transformations. There are only two orthogonal coordinate directions, which are used to balance the plate element's midplane moments with 3-D element's surface nodal forces. Forces applied to the third coordinate direction (in line with the surface normal vector) would not produce moments about the midplane, since the force line intersects that node. Since there are three moments and three forces associated with the plate element's node, a special shell coordinate system is established in order to balance the moments with the surface forces. There would be no component of moment parallel to the shell normal vector due to the fact that the plate element carries no in-plane rotational stiffness. By defining a local shell normal vector, the

surface nodal forces are determined such that equilibrium is preserved for the three components of force and the two components of moment in the plane of local shell tangent as shown in Fig. 4.9. The x'-axis of the local coordinate system is set parallel to the shell normal vector, and the z'-axis is constrained to remain in a plane parallel to the y-z cordinate plane. From the direction cosines of each of the primed directions relative to the global axis, shown in Fig. 4.12, the primed forces and moments become

$$
\begin{aligned}
F_{x'} &= F_x \cos\alpha + F_y \cos\beta + F_z \cos\gamma \\
F_{y'} &= F_x \cos\rho + F_y \cos\phi + F_z \cos\theta \\
F_{z'} &= F_y \cos\left(b + \frac{\pi}{2}\right) + F_z \cos b \\
M_{x'} &= M_x \cos\alpha + M_y \cos\beta + M_z \cos\gamma = 0 \\
M_{y'} &= -M_x \sin\alpha + M_y \cos\alpha \cos b + M_z \cos\alpha \sin b \\
M_{z'} &= M_z \cos b - M_y \sin b
\end{aligned}
\tag{4.27}
$$

The angles α, β and γ are known direction angles of the shell normal vector. The angles ρ, ϕ, θ and b are determined from the imposed constraints of the coordinate system. Since z' is parallel to the y-z plane, the y' coordinate would be in the plane defined by the x-x' axes. The direction angle ρ is given by

$$\rho = \alpha + \frac{\pi}{2} \tag{4.28}$$

The remaining direction angles are determined by reference to spherical geometry (Fig. 4.13). Using the Napier's rules for right spherical triangles, the angles b, ϕ

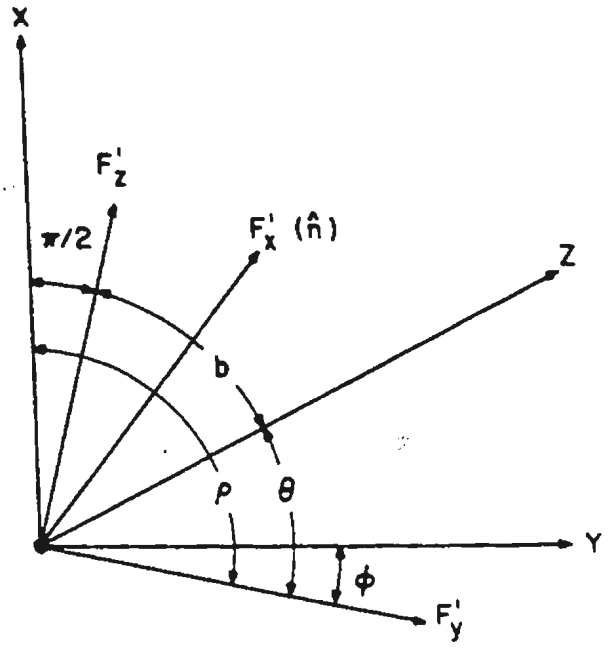

Fig. 4.12 Forces transformed to local shell surface coordinate system.

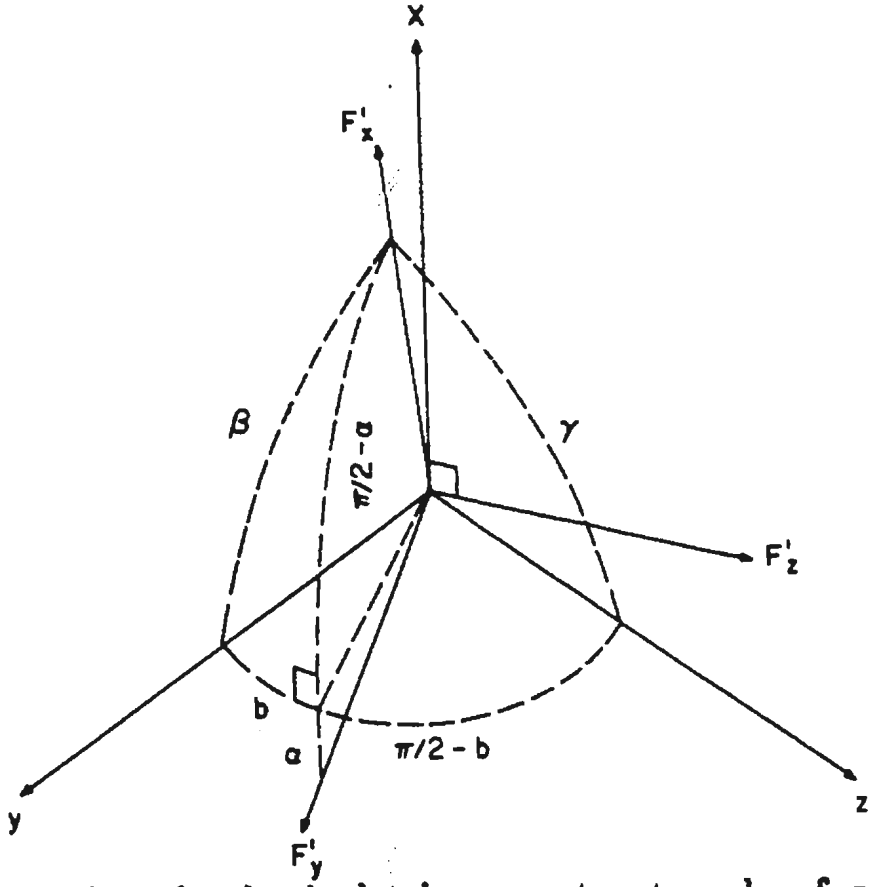

Fig. 4.13 Use of spherical trigonometry to solve for azimuth angle b.

and θ are given as

$$
\begin{aligned}
| \, b \, | &= \sin^{-1} \left(\sqrt{\sin^2 \beta - \cos^2 \beta \, \mathrm{ctn}^2 \, \alpha} \right) \\
\phi &= \cos^{-1} \left(\cos \alpha \cos b \right) \\
\theta &= \cos^{-1} \left(\cos \alpha \sin b \right)
\end{aligned}
\tag{4.29}
$$

By preserving the equilibrium of force and moment, the inner and outer surface nodal forces are

$$
\begin{aligned}
F_{x'o} &= \frac{F_{x'}}{2} & F_{x'i} &= \frac{F_{x'}}{2} \\
F_{y'o} &= \frac{F_{y'}}{2} + \frac{M_{z'}}{t} & F_{y'i} &= F_{y'} - F_{y'o} \\
F_{z'o} &= \frac{F_{z'}}{2} - \frac{M_{y'}}{t} & F_{z'i} &= F_{z'} - F_{z'o}
\end{aligned}
\tag{4.30}
$$

Finally the equilibrium forces are transferred back to the global system so that they can be used as input for the 3-D rezone model. The results of this last transformation are as follows:

$$
\begin{aligned}
F_{xo} &= F_{x'o} \cos \alpha - F_{y'o} \sin \alpha \\
F_{xi} &= F_{x'i} \cos \alpha - F_{y'o} \sin \alpha \\
F_{yo} &= F_{x'o} \cos \beta + F_{y'o} \cos \alpha \cos b - F_{z'o} \sin b \\
F_{yi} &= F_{x'i} \cos \beta + F_{y'i} \cos \alpha \cos b - F_{z'i} \sin b \\
F_{zo} &= F_{x'o} \cos \gamma + F_{y'o} \cos \alpha \sin b + F_{z'o} \cos b \\
F_{zi} &= F_{x'i} \cos \gamma + F_{y'i} \cos \alpha \sin b + F_{z'i} \cos b
\end{aligned}
\tag{4.31}
$$

Thus substituting Eqn. 4.27 into Eqn. 4.30 and then Eqn. 4.30 into Eqn. 4.31 leads to the forces which are applied to the inner and outer surface nodes of the transition boundary of the 3-D rezone model of the joint.

4.3.4 Boundary conditions

The element stiffness matrices are assembled to obtain the global stiffness of the rezoned model. The interior displacement vector for the rezoned model is determined for imposed boundary displacements/forces, obtained from the 2-D solution. For a rezoned model with n degrees-of-freedom, the force-displacement relations can be written as

$$\begin{bmatrix} K_{11} & . & K_{1n} \\ . & . & . \\ K_{n1} & . & K_{nn} \end{bmatrix} \begin{Bmatrix} \delta_1 \\ . \\ \delta_n \end{Bmatrix} = \begin{Bmatrix} f_1 \\ . \\ f_n \end{Bmatrix} \tag{4.32}$$

By imposing m boundary displacements, $\delta_1 = \beta_1$,....., $\delta_m = \beta_m$, at the transition nodes, Eqn. 4.32 becomes

$$\begin{bmatrix} 1 & . & 0 & . & 0 \\ . & . & . & . & . \\ 0 & . & K_{(m+1)(m+1)} & . & K_{(m+1)n} \\ . & . & . & . & . \\ 0 & . & K_{n(m+1)} & . & K_{nn} \end{bmatrix} \begin{Bmatrix} \delta_1 \\ . \\ \delta_{(m+1)} \\ . \\ \delta_n \end{Bmatrix} = \begin{Bmatrix} \beta_1 \\ . \\ f'_{(m+1)} \\ . \\ f'_n \end{Bmatrix} \tag{4.33}$$

where

$$\begin{aligned} f'_{(m+1)} &= f_{(m+1)} - K_{(m+1)1}\,\beta_1 - ..... - K_{(m+1)m}\,\beta_m \\ f'_n &= f_n - K_{n1}\,\beta_1 - ..... - K_{nm}\,\beta_m \end{aligned} \tag{4.34}$$

The unknown displacements, δ_{m+1} ,....., δ_n, are obtained by solving the equation

$$\begin{bmatrix} K_{(m+1)(m+1)} & \cdot & K_{(m+1)n} \\ \cdot & \cdot & \cdot \\ K_{n(m+1)} & \cdot & K_{nn} \end{bmatrix} \begin{Bmatrix} \delta_{(m+1)} \\ \cdot \\ \delta_n \end{Bmatrix} = \begin{Bmatrix} f'_{(m+1)} \\ \cdot \\ f'_n \end{Bmatrix} \tag{4.35}$$

4.4 Results and Discussion

A computer program based on the formulation presented in sections 4.2 and 4.3 is developed for the three dimensional analysis of (i) the entire joint and (ii) the rezoned section. The entire joint is first analysed for axial and in-plane bending loads. Using 3-D elements based on the above mentioned formulation, the discretization error in the stresses can be expected to converge at the same rate as the plate element formulation, i.e., of order $O(h^2)$. So the joint is discretized by keeping the aspect ratios of 3-D elements in the same range as that of the plate elements. The total number of elements, nodes and degrees-of-freedom in the discretized model are 516, 1102 and 3306 respectively. The saddle point rezoned model is analysed for an axial load in the brace, and the results are compared with those obtained from the 3-D model of the entire joint. The total number of elements, nodes and degrees-of-freedom for the rezoned analysis are 192, 416 and 1248 respectively. The discretization of the rezoned model is shown in Fig. 4.14. Since the main interest is to obtain the stress distribution at the outer surface of the shell, the stresses are computed at the nodes and are averaged between the elements that are connected at the nodes.

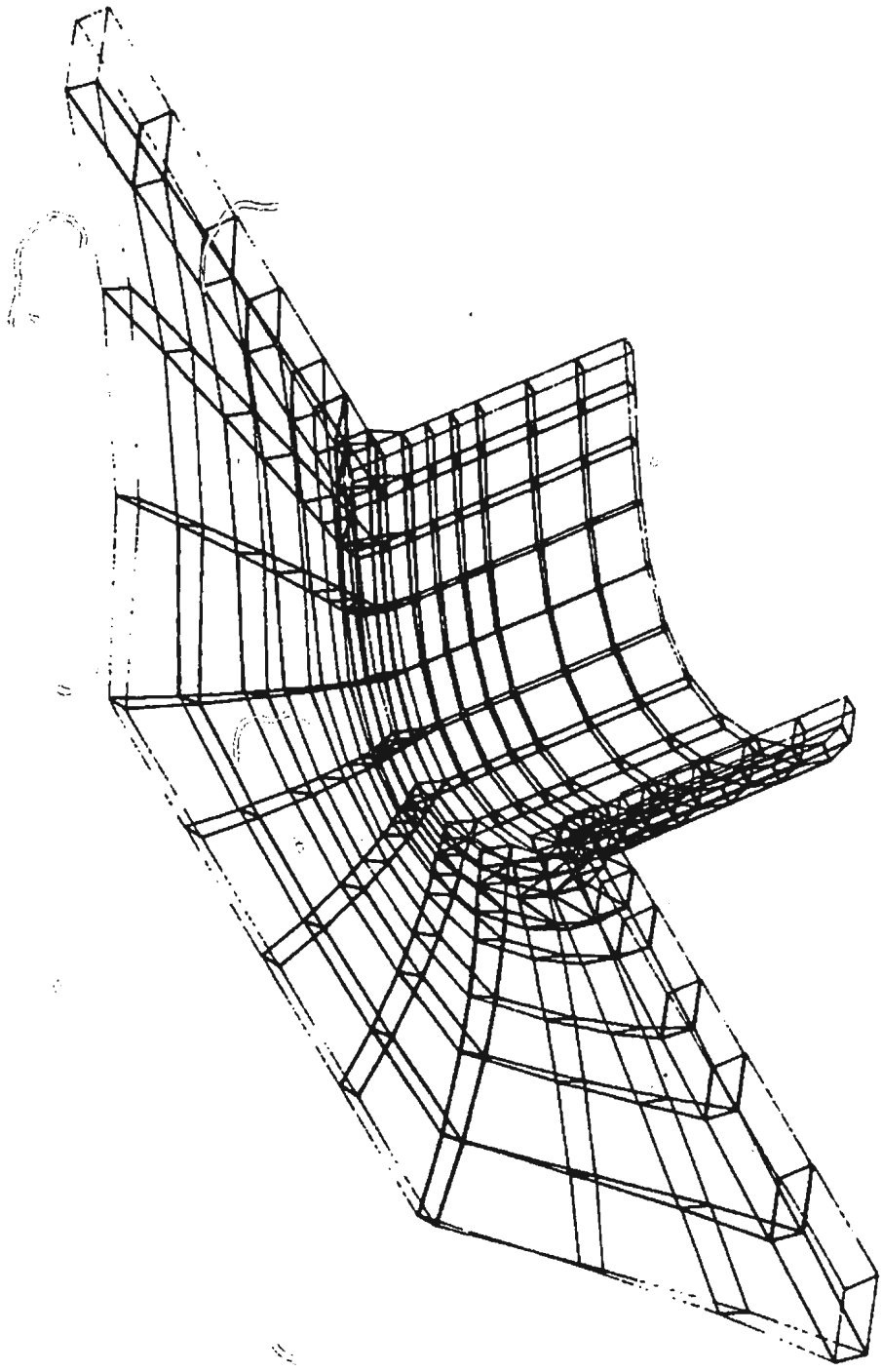

Fig. 4.14 Three dimensional finite element mesh for rezoned section of the joint at saddle point.

4.4.1 Entire joint analysis

The variation of the maximum surface stress at saddle point due to the axial load is shown in Fig. 4.15a. The results from the two dimensional analysis extend through the weld toe positions up to the intersection of the chord and the brace midsurfaces. For the chord side, both two and three dimensional analyses give similar variation of stresses (Fig. 4.15b) to that reported by Parkhouse(1981). The saddle point hot spot stress, obtained from the three dimensional analysis of the joint without plug, is 20 percent higher than that of the two dimensional analysis result. The three dimensional analysis for the no plug case gives a hot spot stress on the brace side which is only 3 percent higher than the two dimensional analysis. The stress variation agrees reasonably well with that reported by Parkhouse (Fig.4.15c). The hot spot stress concentration factors for the joint are given in Table 4.1.

The stress variation along the weld surface is shown in Fig. 4.15a. From the chord weld toe, the stress decreases up to a certain point and then starts increasing and reaches a maximum value at the brace weld toe (Fig.4.15d). This trend compares well with that reported by Morgan(1979). The variation of the stress concentration factors (SCFs) near the saddle point for the axial load 3-D case compares well with measured values reported by de Back and Vaessen (1981) (Figs. 4.15e and 4.15f). Figure 4.16 shows the stress distribution across the weld reinforcement and the brace wall at the saddle point due to axial load. A rapid decrease in stress across the weld leg is observed in contrast to the nearly

Table 4.1 Hot spot stress concentration factors.

Methods	Axial				In-plane bending			
	Chord		Brace		Chord		Brace	
	Crown	Saddle	Crown	Saddle	Crown	Saddle	Crown	Saddle
Present 3-D analysis (full model)	2.2 2.09*	6.448 4.57*	2.55 2.34*	7.08 5.41*	1.306 1.06*	- -	1.79 1.304*	- -
Present Rezoned analysis	-	7.53	-	9.83	-	-	-	-
Experiment (Clayton & Martin 1980)	-	5.8	-	7.1	2.0	-	1.7	-
Experiment (Irvine 1981b)	-	7.7	-	-	1.2	-	-	-

*In the analysis plug stiffness is included

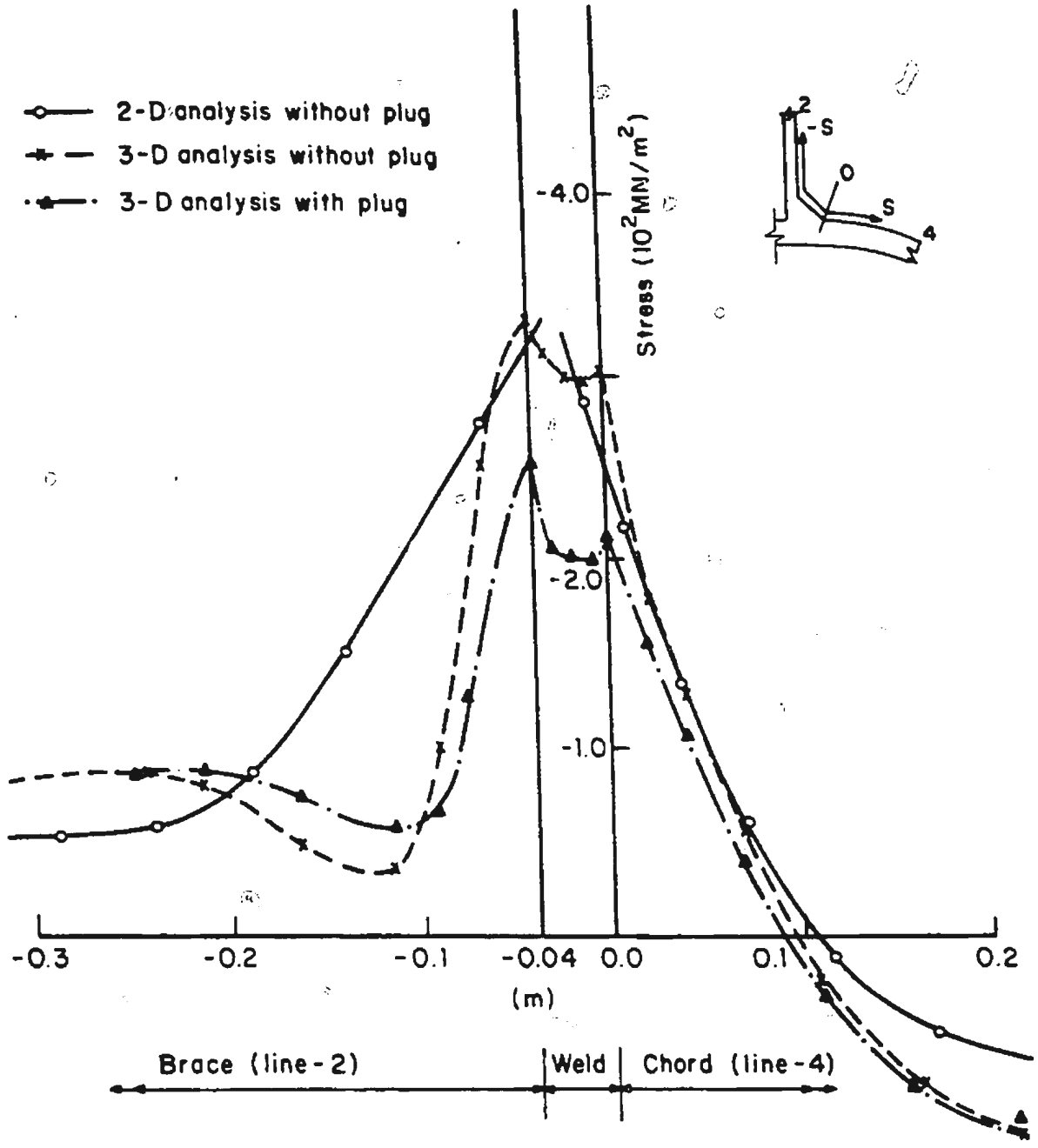

Fig. 4.15a Maximum surface stress variation at saddle point due to axial compressive load.

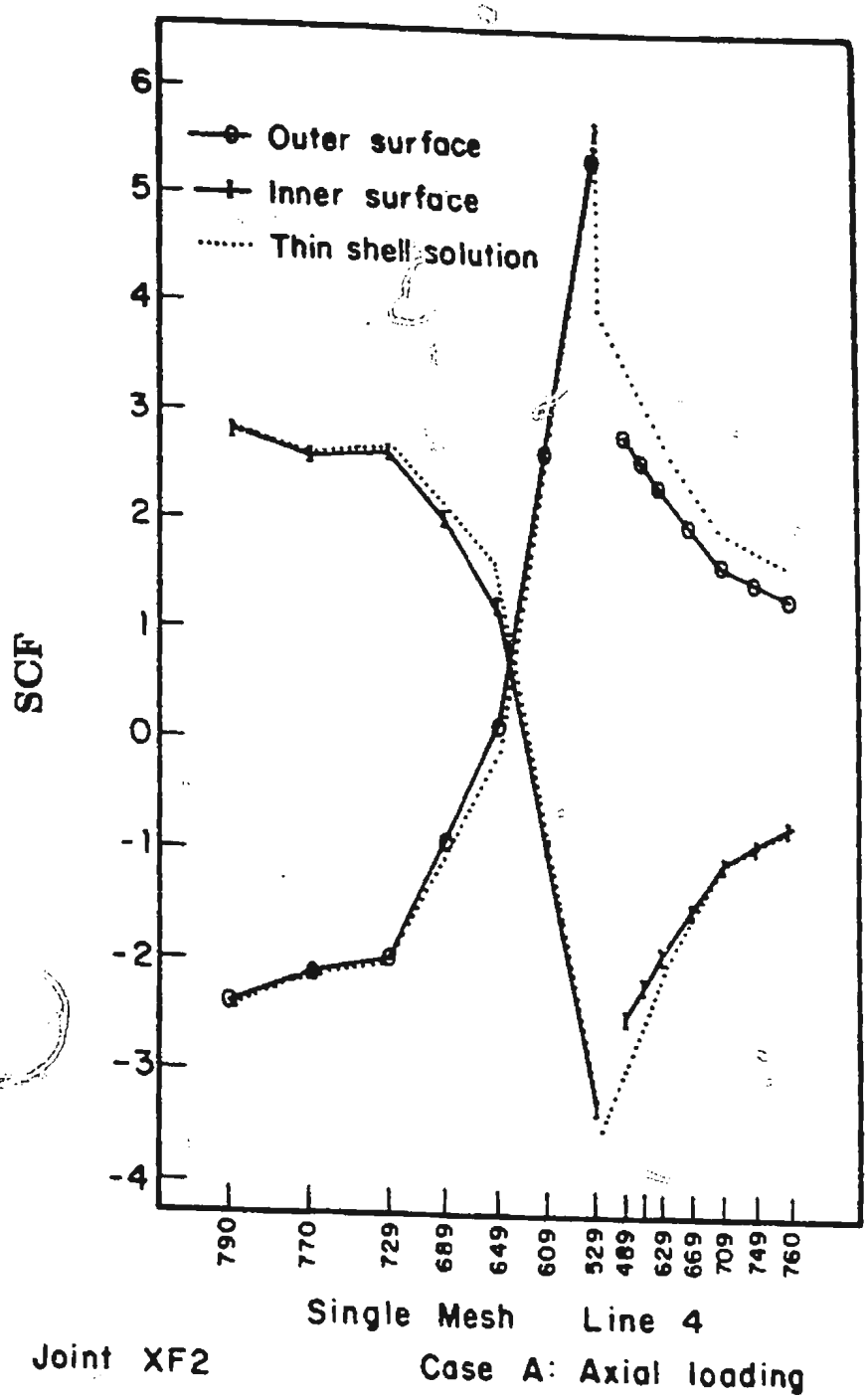

Fig. 4.15b Stresses along line-4 (Parkhouse 1981).

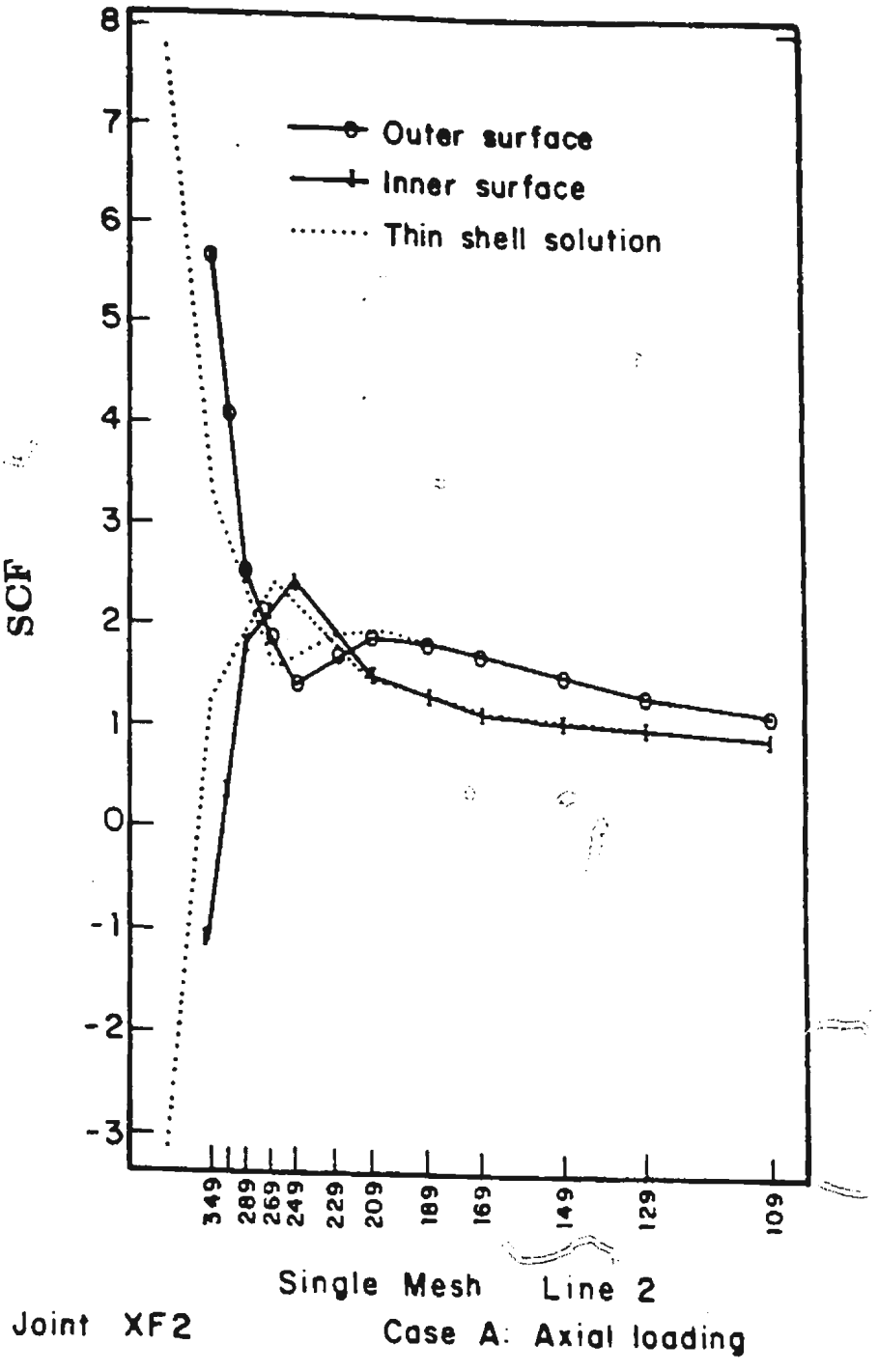

Fig. 4.15c Stresses along line-2 (Parkhouse 1981).

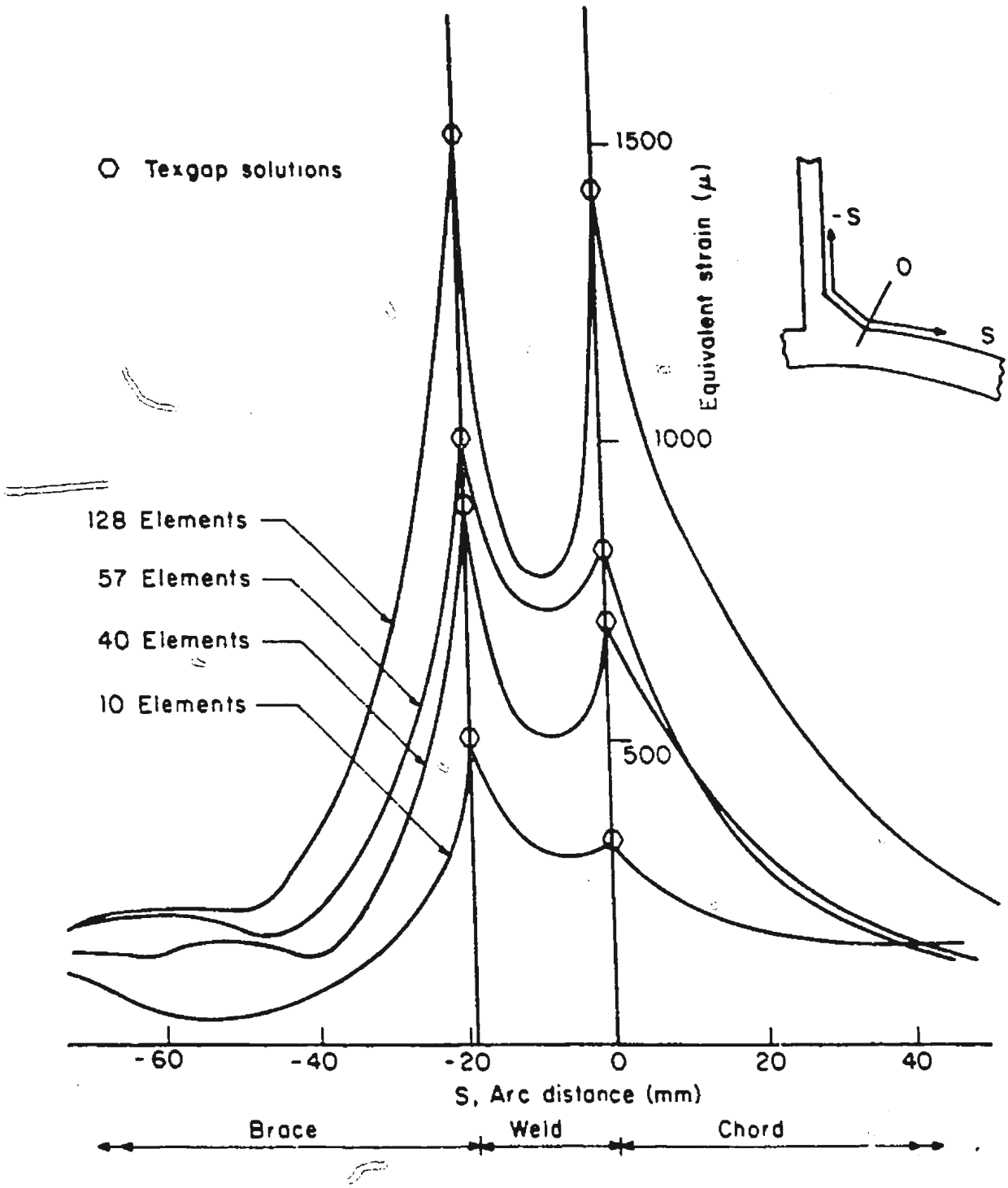

Fig. 4.15d Transverse midsection strain levels for the TEXGAP-3D solutions (Morgan 1979).

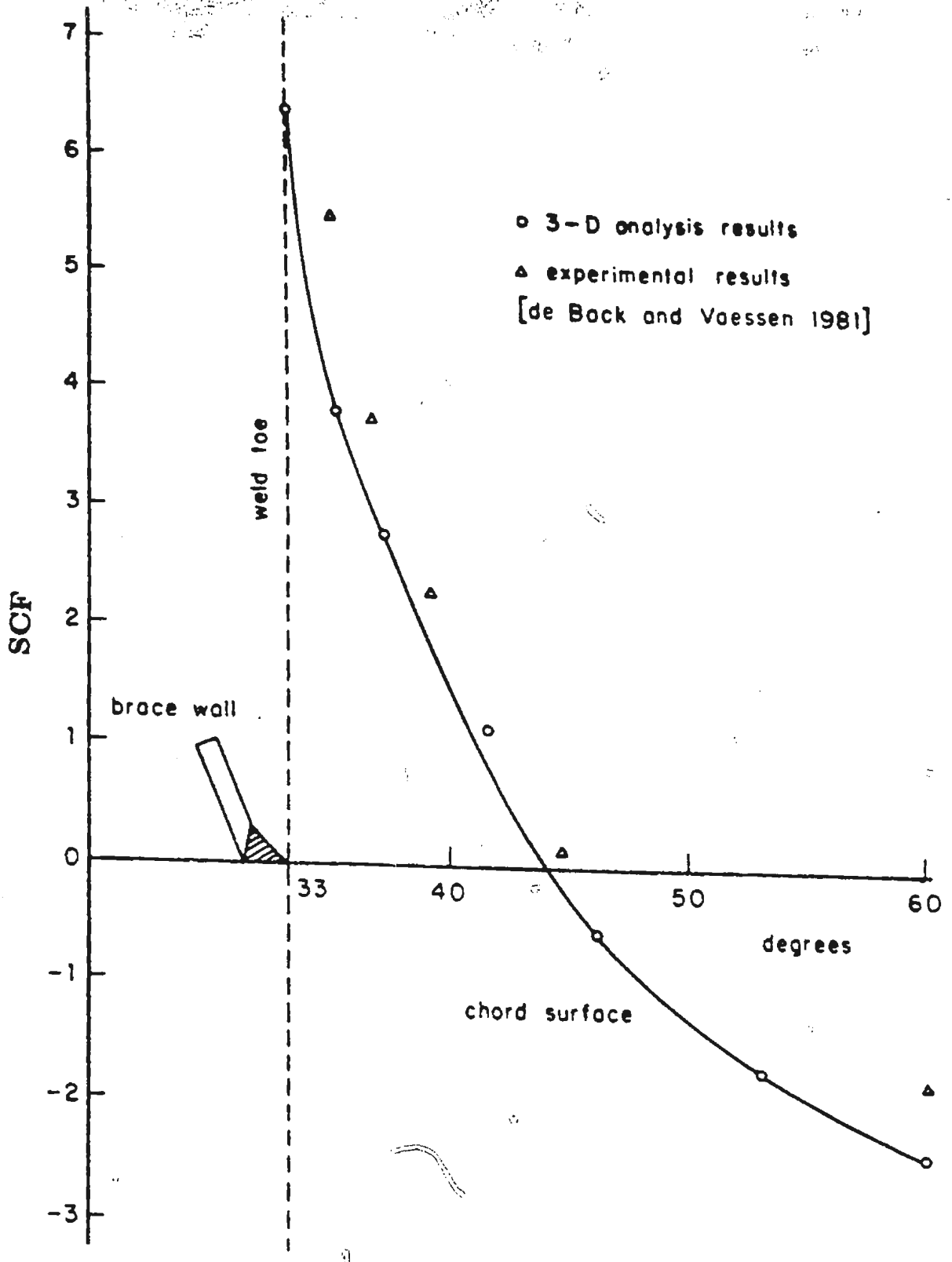

Fig. 4.15e Stress distribution along line-4 due to axial load.

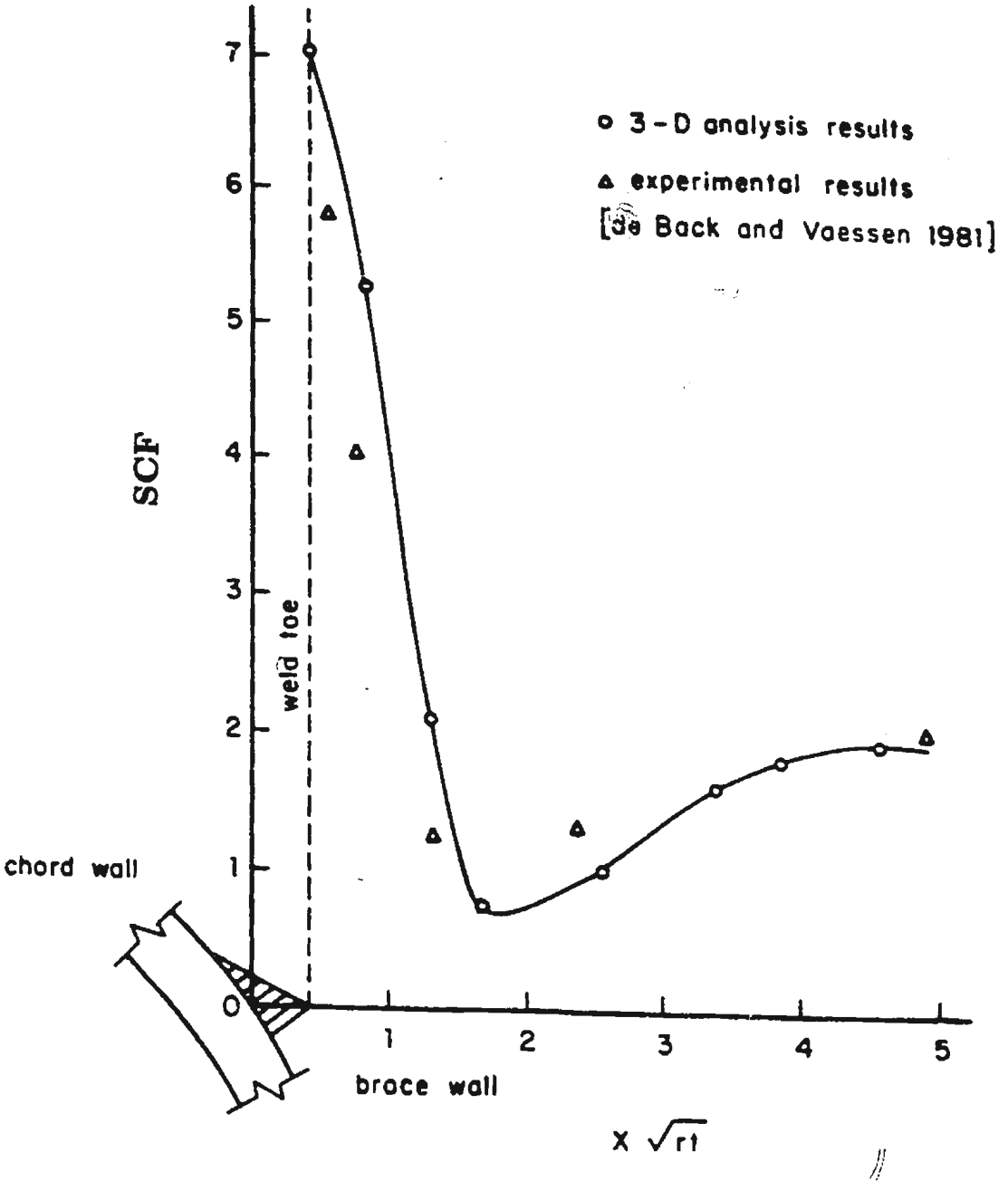

Fig. 4.15f Stress distribution along line-2 due to axial load.

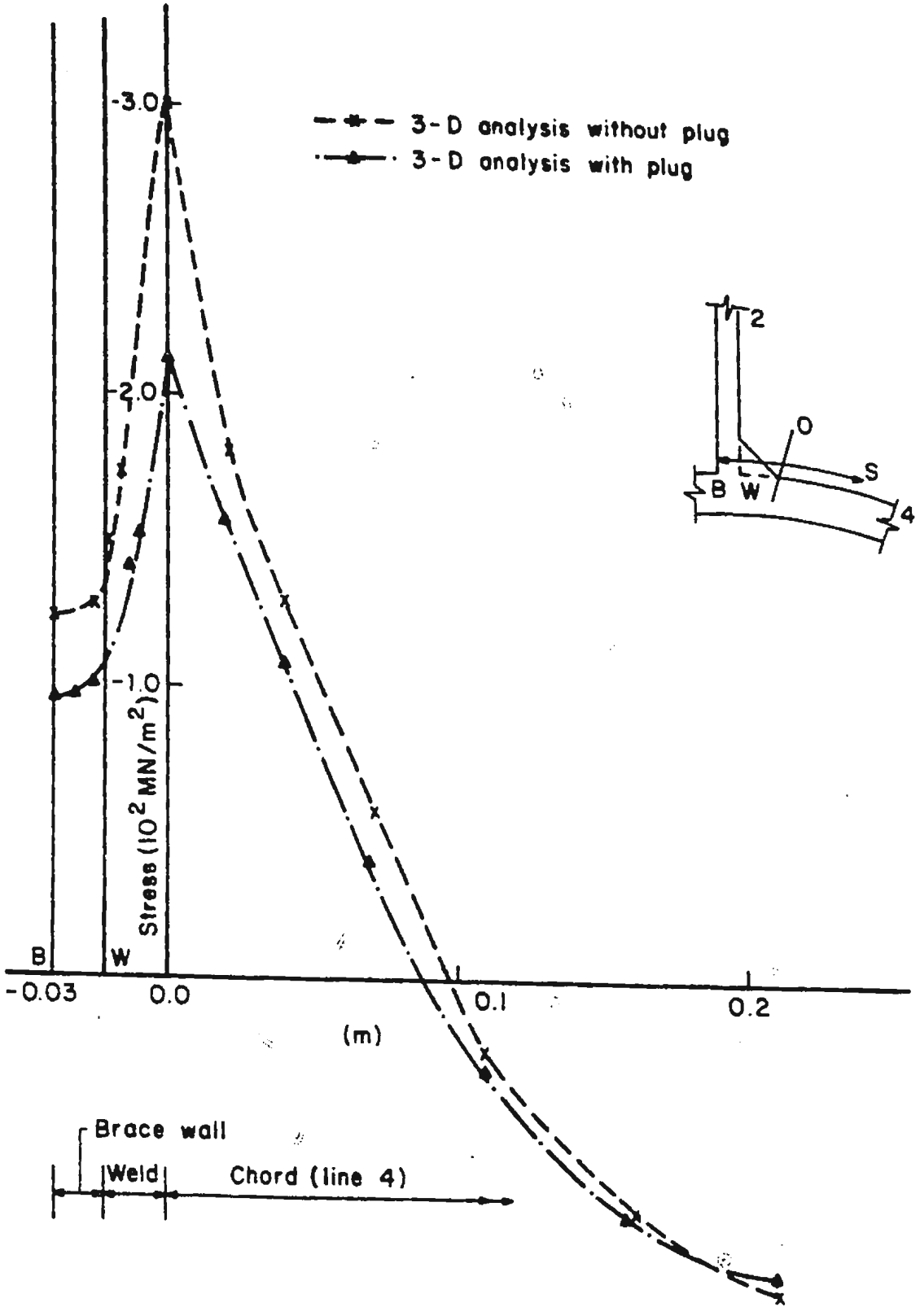

Fig. 4.16 Stress distribution across the weld and brace wall at saddle point due to axial compressive load.

constant value through the brace wall.

The stress values at the crown point obtained from the two dimensional analysis are lower than the 3-D values on the chord side but higher on the brace side (Fig. 4.17). A gradual increase in stress is observed to occur along the weld surface from the chord to the brace weld toe. The through-thickness variation of stress across the weld and the brace (Fig. 4.18) is similar to that observed at the saddle point. The hot spot stresses at the weld toe computed from the three dimensional analysis are higher than the 2-D values on both the chord and the brace sides at the crown point (Fig. 4.19). However the stress gradient obtained from the three dimensional analysis on the brace side is steeper than that given by the two dimensional analysis. The stress variations across the weld and the brace (Fig. 4.20) are similar to those obtained for the case of axial load.

4.4.2 Rezoned analysis

The forces and the displacements at the boundary nodes of the rezoned region are calculated as discussed in section 4.3.2. For an axial load case these forces/displacements are imposed at the boundary of the rezoned region. Figure 4.21 shows the stress variation in the chord along line-2. The stress variation along line-2 of the brace is shown in Fig. 4.22. From the figures, it can be seen that the stress magnitudes differ considerably from those predicted by 3-D analysis of the entire joint, especially on the brace side.

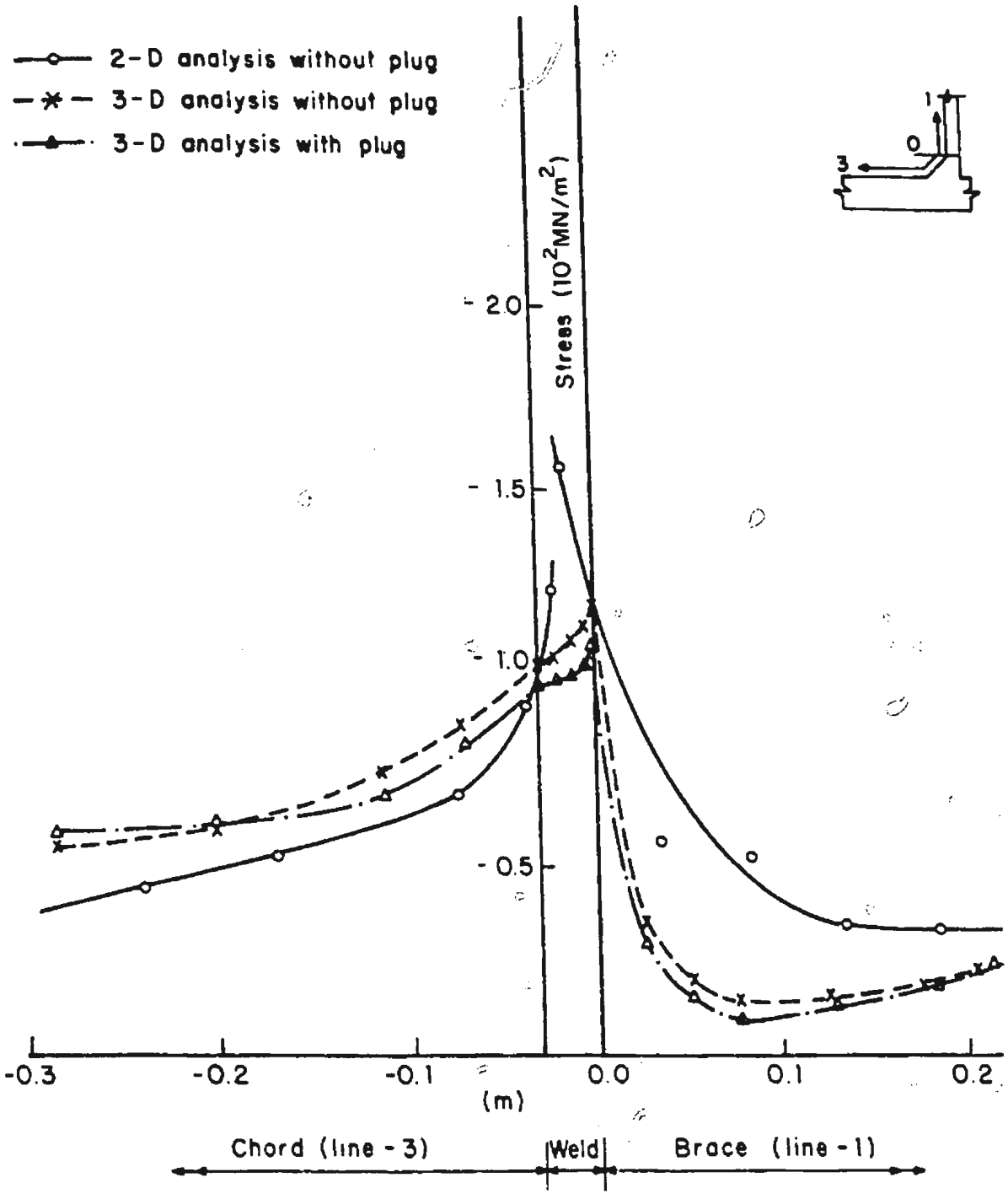

Fig. 4.17 Maximum surface stress variation at crown point due to axial compressive load.

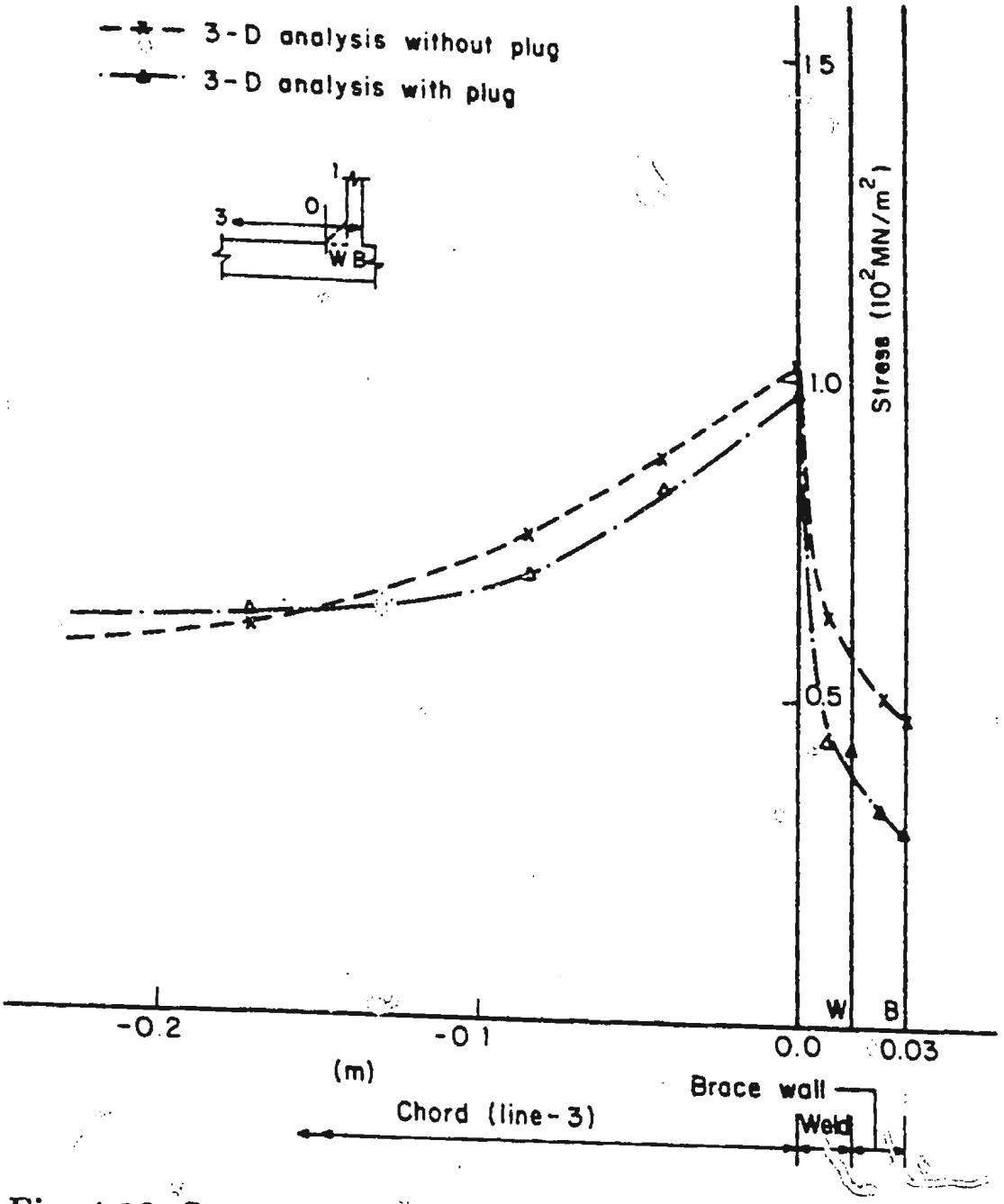

Fig. 4.18 Stress distribution across the weld and brace wall at crown point due to axial compressive load.

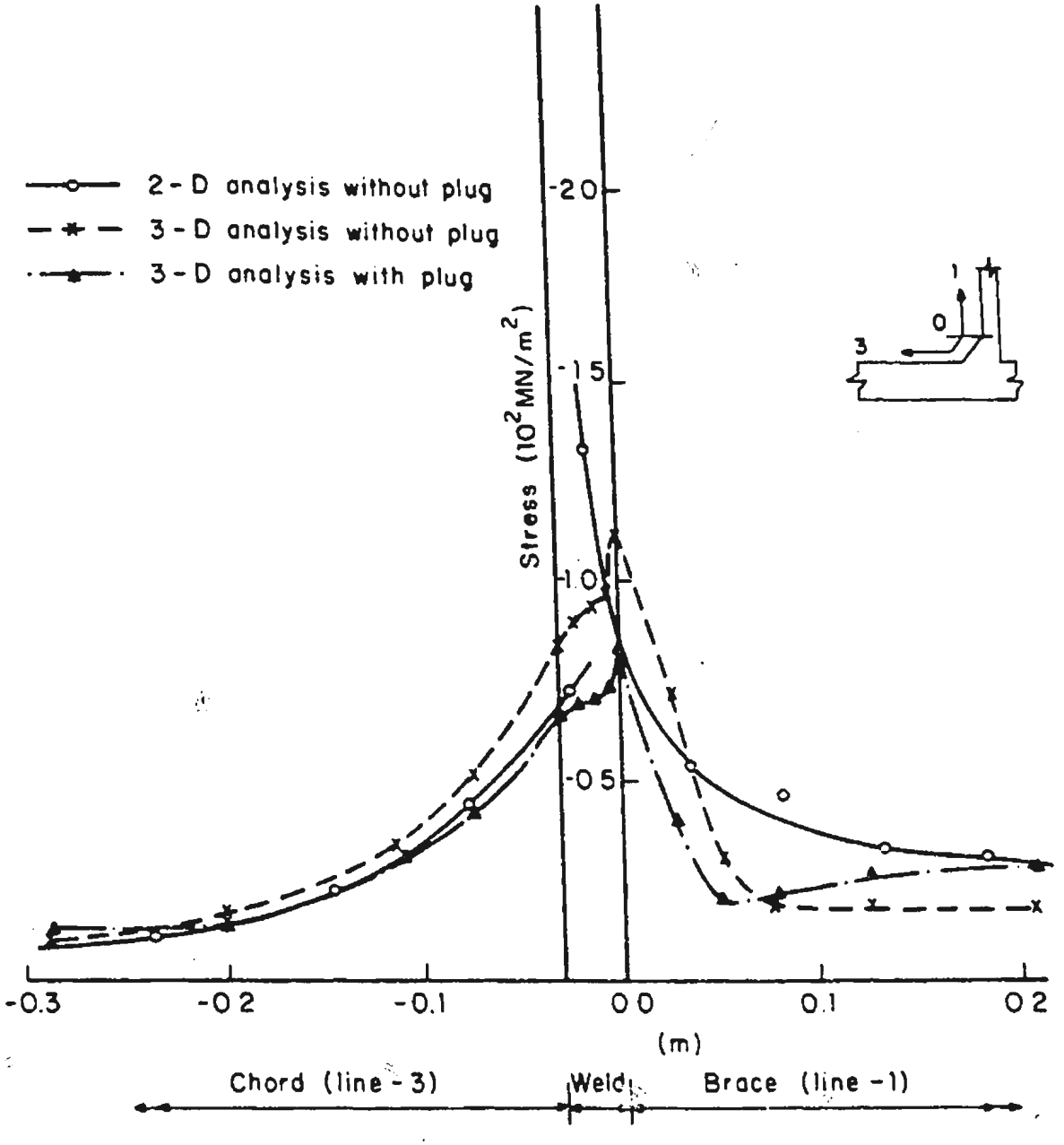

Fig. 4.19 Maximum surface stress variation at crown point due to in-plane bending load.

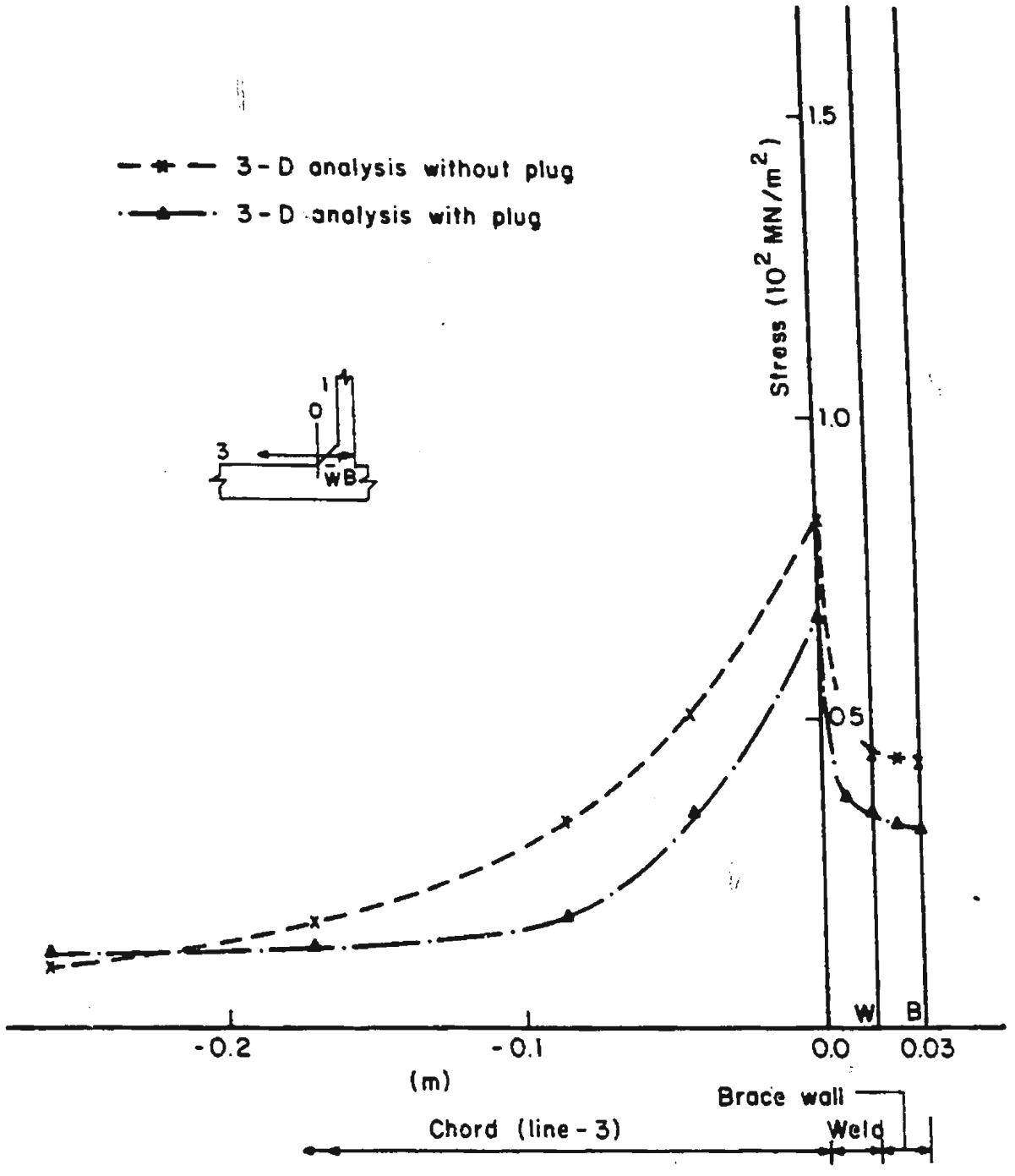

Fig. 4.20 Stress distribution across the weld and brace wall at crown point due to in-plane bending load.

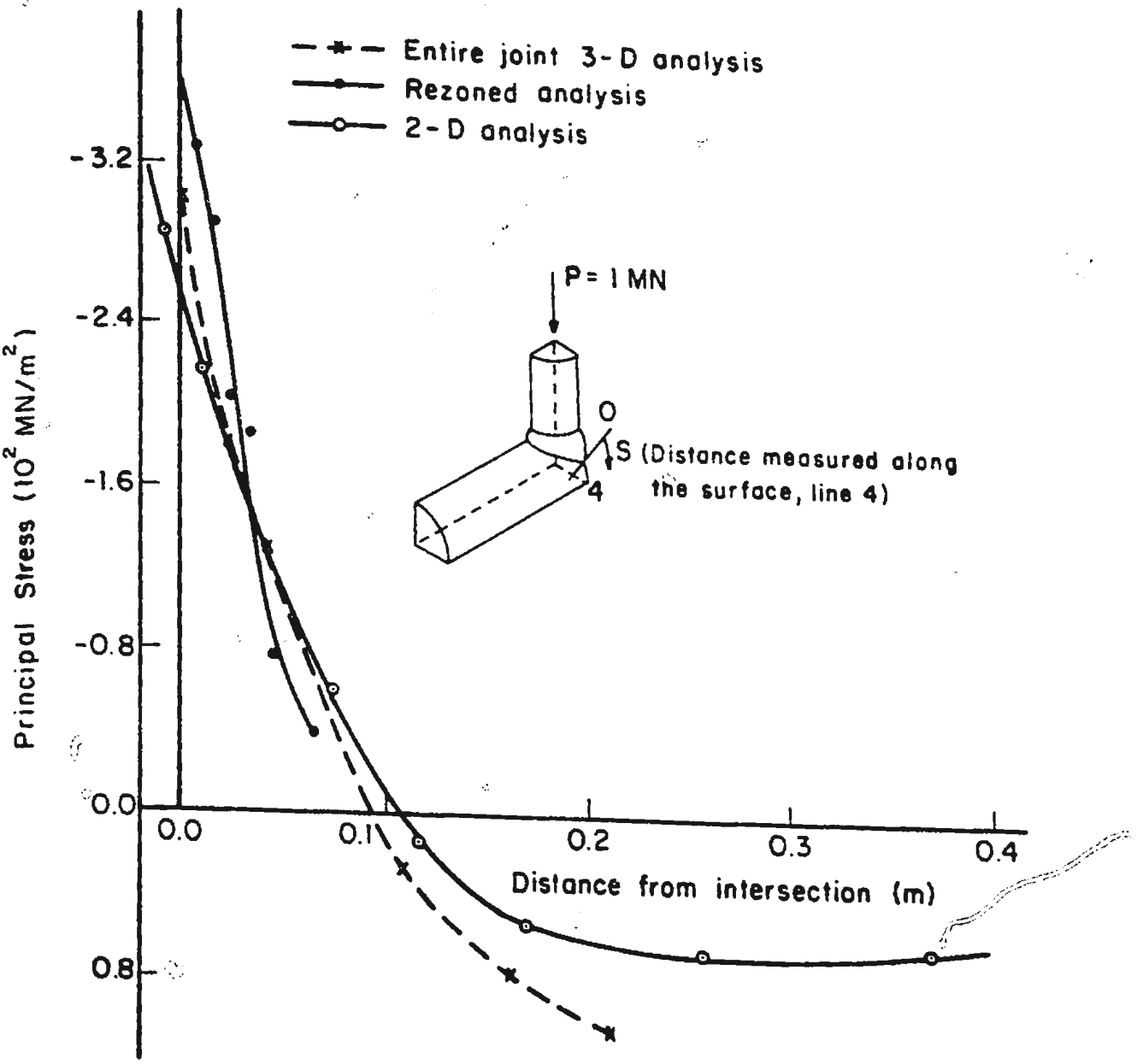

Fig. 4.21 Comparison of entire joint model and rezoned section analyses results along line-4.

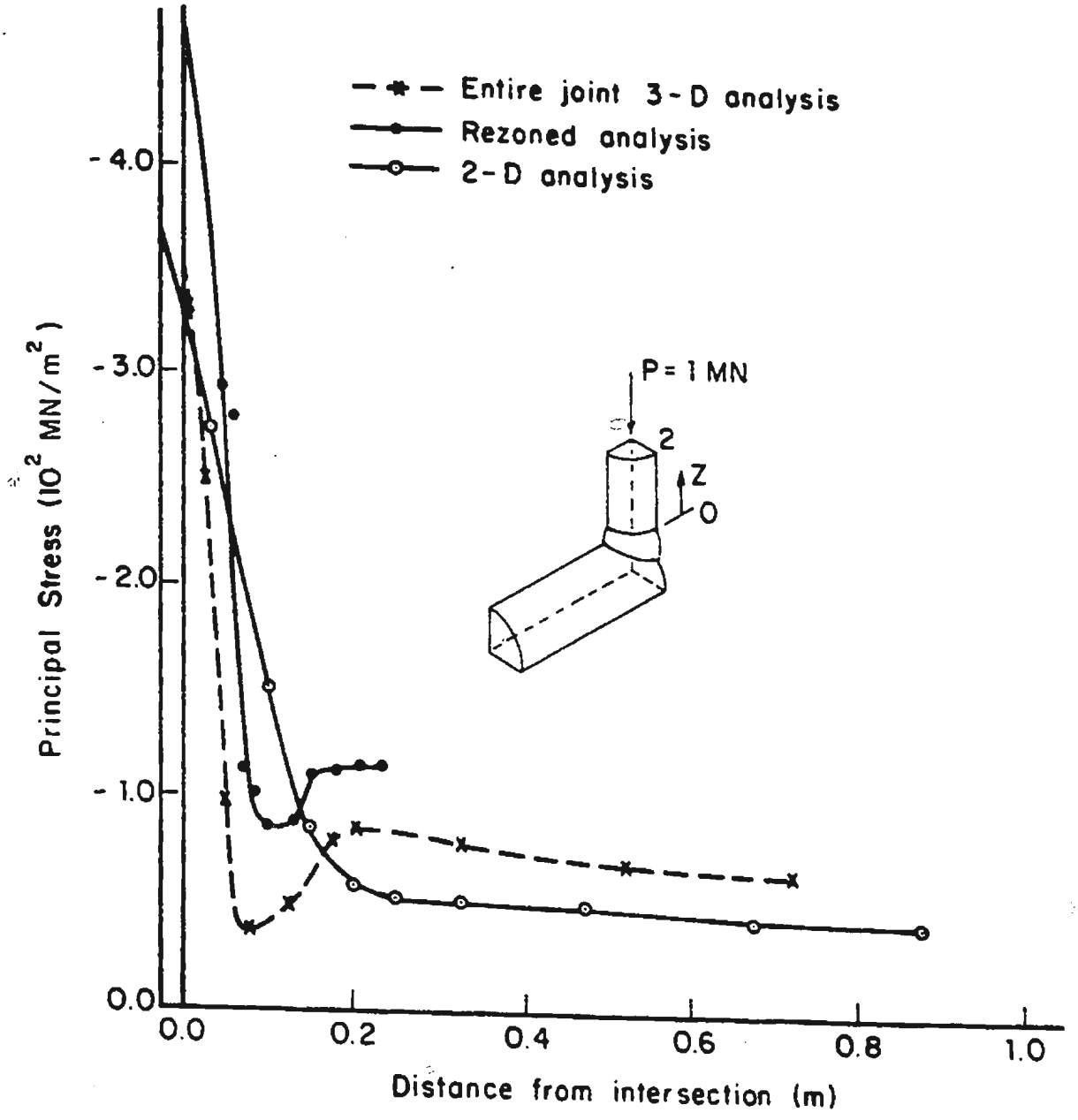

Fig. 4.22 Comparison of entire joint model and rezoned section analyses results along line-2.

CHAPTER 5

ANALYSIS OF WELD TOE CRACKS

5.1 Introduction

The fracture mechanics method has recently become an important analysis tool for offshore structural design and fabrication. All tubular joints have weld toe defects, either built in unintentionally during fabrication or initiated by the service conditions. The defects will affect the resistance of the joints against fracture or fatigue crack propagation. Surface flaws initiate at the weld toe of the tubular intersection areas and propagate under environmental loads along the thickness and surface directions. A good way to model such flaws is to represent them as cracks. A quantitative measure of the severity of such a crack is given by the stress intensity factor, K, which characterizes the intensity of the stress field in a small region surrounding the leading edge of the crack. The shape of a propagating crack is influenced by both the local stress state and the material properties near the tubular intersection area.

For an efficient treatment of such a complicated problem, it is essential that an accurate engineering model be developed based on an accurate knowledge of the local stresses and on the crack driving force. It must take into account the effects of geometry and loading conditions on these parameters. The need for an explicit consideration of surface flaw geometry in the fatigue analysis of tubular

joints using fracture mechanics requires a radically different approach from the conventional S-N curve method, which is based on a one dimensional parameter, i.e., stress concentration factor. The new approach requires an understanding of the detailed stress distribution through the chord thickness as well as along the surface near the tubular intersection in the presence of a weld toe crack.

Closed-form analytical solutions exist for idealized geometries containing cracks, but for all practical problems a numerical solution must be obtained. They are particularly difficult to achieve for cracks at geometrical discontinuities like tubular intersections, where changes in the cross-sectional dimensions of the member produce nonuniform stress fields not related to the presence of the crack. The difficulties are further compounded by the three-dimensional aspect of both the structural configuration and the crack shape.

This chapter deals with the three dimensional finite element analysis of the tubular joint with weld toe cracks and the determination of the corresponding stress intensity factors.

5.2 Modelling of the Joint

It is well known that the saddle point and crown point regions of a tubular T-joint are critical for axial and in-plane bending loads, respectively. Because of this, weld toe cracks are modelled here at the saddle point region for an axial load case and at the crown point region for an in-plane bending case. Loads are applied such that the weld toe cracks are in the opening mode in both cases. In

the literature it has been observed that the crack initiation as well as the part-through-thickness propagation in tubular joints make up a major portion of the fatigue life of the joint. During the fatigue testing of the tubular joints, the part-through-thickness crack growth rate was observed to be almost constant (Dover and Holdbrook 1979, Dover and Dharmavasan 1982, Gowda 1983).

So it will be more realistic to represent the part-through-thickness crack growth rate using the stress intensity factor corresponding to the 50 percent deep weld toe crack. In the present study, the part-through-thickness weld toe crack is modelled as a shallow crack having a maximum depth equal to one half the thickness of the chord, and the length of the crack is assumed to be 80 mm. The latter is based on the experimental results (Wylde 1984). The initial surface flaw, whose depth is very small, is modelled as a line of singularity at the weld toe and is termed herein the incipient crack.

5.3 Finite Element Idealization

The chord/brace surface away from the weld toe crack region is discretized using three dimensional incompatible elements discussed in the previous chapter. The wedge-shaped singular element developed by Tracey(1974) is used for modelling near the crack front region. This element exhibits a square root singularity (Fig. 5.1). It is obtained by collapsing one face of the 8-node brick element and by choosing appropriate displacement interpolation functions. Brick and wedge elements are considered in the parametric region $0 \leq \xi,\eta,\gamma \leq 1$. Brick nodes 1, 2, ... 8 take the $\xi\ \eta\ \gamma$ positions 000, 100, 110, 010, 001, 101, 111 and 011, respectively.

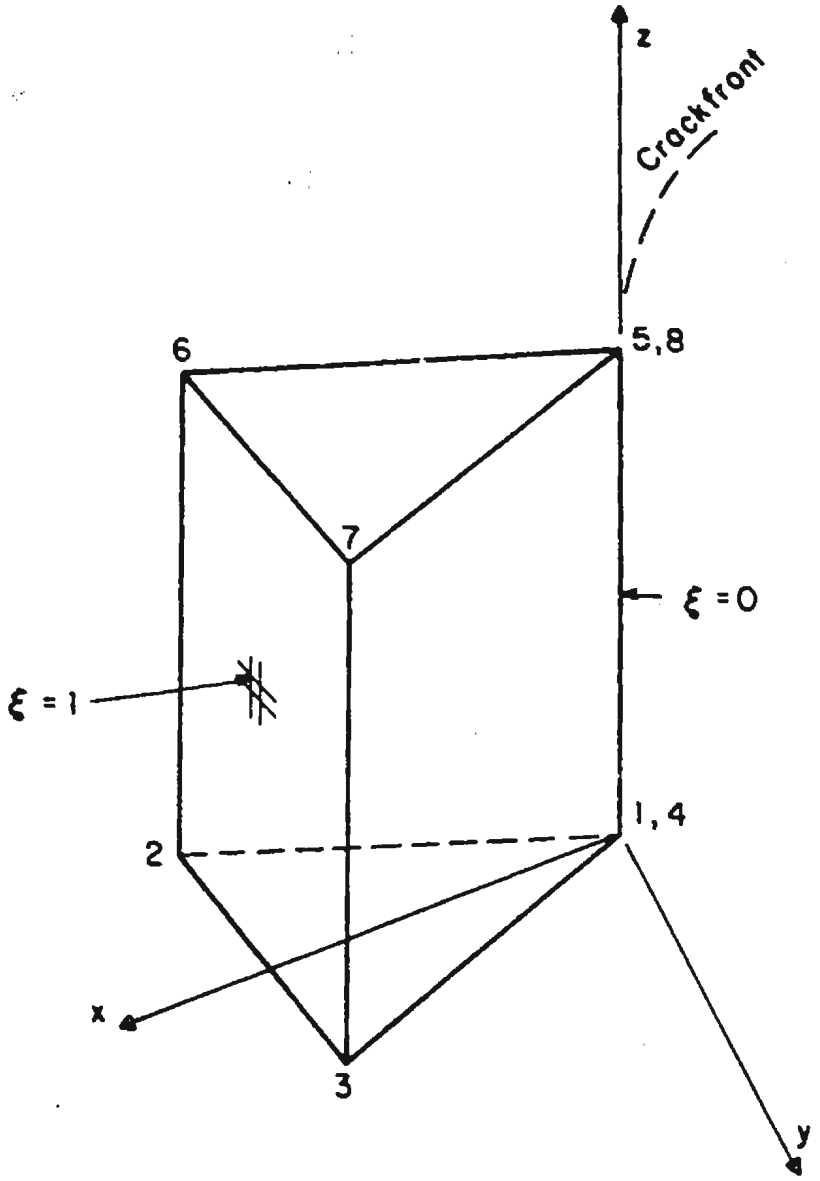

Fig. 5.1 Singular wedge element.

The mapping function for the physical global cartesian co-ordinate x is given in terms of the nodal co-ordinates as (Tracey 1974)

$$\begin{aligned} x = {} & x_1 (1 - \xi) (1 - \eta) (1 - \gamma) + x_2 \xi (1 - \eta) (1 - \gamma) \\ & + x_3 \xi \eta (1 - \gamma) + x_4 (1 - \xi) \eta (1 - \gamma) \\ & + x_5 (1 - \xi) (1 - \eta) \gamma + x_6 \xi (1 - \eta) \gamma \\ & + x_7 \xi \eta \gamma + x_8 (1 - \xi) \eta \gamma \end{aligned} \qquad (5.1)$$

where x_1 , x_2 ,...x_8 are the x-coordinates of nodes. In the same way, relationships can be written for the y and z-coordinates. The wedge element has only six nodes, but the mapping function is nonetheless valid if one makes $x_1 = x_4$ and $x_5 = x_8$. The general form of the interpolation function for the displacement component u is given as (Tracey 1974)

$$\begin{aligned} u = {} & u_1 (1 - f) (1 - \eta) (1 - \gamma) + u_2 f (1 - \eta) (1 - \gamma) \\ & + u_3 f \eta (1 - \gamma) + u_4 (1 - f) \eta (1 - \gamma) \\ & + u_5 (1 - f) (1 - \eta) \gamma + u_6 f (1 - \eta) \gamma \\ & + u_7 f \eta \gamma + u_8 (1 - f) \eta \gamma \end{aligned} \qquad (5.2)$$

where

$$\begin{aligned} f = {} & \xi^{\frac{1}{2}} \text{ for displacement components } u_x \text{ and } u_y \\ = {} & \xi \text{ for component } u_z \text{ along crack edge.} \end{aligned}$$

Equation 5.2 considers eight degrees-of-freedom, but for the wedge $u_1 = u_4$ and $u_5 = u_8$. From Eqn. 5.2 it can be seen that local u_x , u_y displacement components depend on the square root of ξ, whereas u_z depends on ξ only. This results in a $1/\sqrt{r}$ distribution for the local strain components ϵ_{xx} , ϵ_{yy} and ϵ_{xy} on a local plane perpendicular to the crack edge and non-singular variations of

ϵ_{zz} , ϵ_{zx} and ϵ_{zy} throughout the wedge, where r is the radial distance from the crack tip.

For modelling the region at the vicinity of a crack in a three dimensional structural model, one may need 5- and 4-noded singular elements. These elements can be obtained by collapsing different sides of the prism as indicated in Fig.5.2. It is observed that on any local xy plane perpendicular to the crack edge, the displacement interpolation functions satisfy singularity constraints. The embedded elliptical crack front is modelled as a number of straight line segments. Each straight crack edge is surrounded by singular elements. These in turn are surrounded by incompatible brick and prism elements. Figure 5.3 shows the schematic arrangement of elements around the crack across any cross-section at the weld toe. The three-dimensional discretization of the crack region is shown in Fig. 5.4.

5.4 Determination of Stress Intensity Factor

Due to the axial and in-plane bending loads, the fracture will be predominantly in crack opening mode or mode I. The stress distribution at a point (whose coordinate is r,θ) in the immediate vicinity of a curved crack front (Fig. 5.5) for this mode I is as follows (Fenner and Mihsein 1984):

$$\sigma_{xx} = \frac{K_I}{\sqrt{2\pi r}} \cos\frac{\theta}{2}\left(1 - \sin\frac{\theta}{2}\sin\frac{3\theta}{2}\right)$$
$$\sigma_{yy} = \frac{K_I}{\sqrt{2\pi r}} \cos\frac{\theta}{2}\left(1 + \sin\frac{\theta}{2}\sin\frac{3\theta}{2}\right)$$
$$\sigma_{zz} = \frac{2\nu K_I}{\sqrt{2\pi r}} \cos\frac{\theta}{2} \qquad (5.3)$$

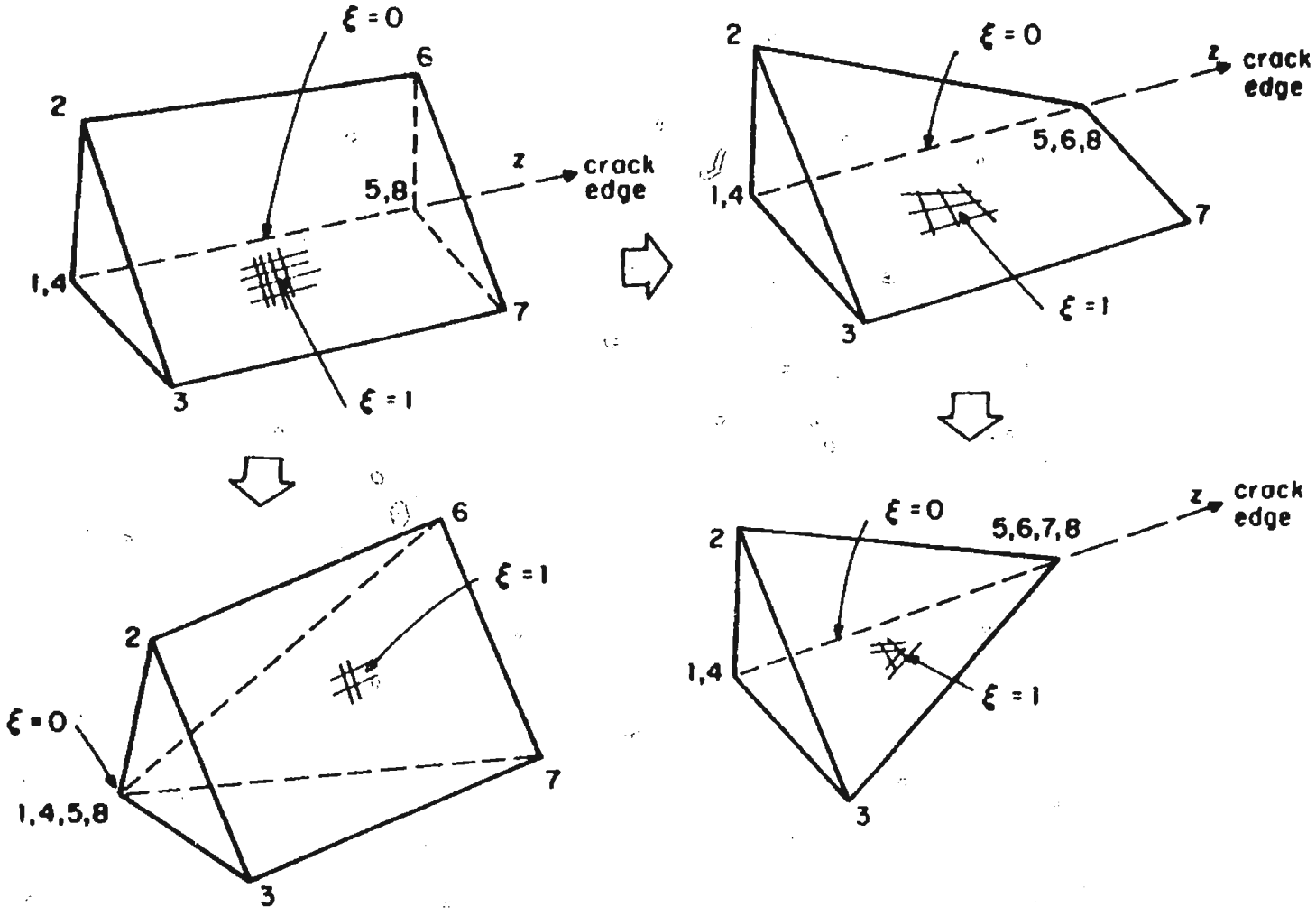

Fig. 5.2 Various singular elements developed to model crack front region.

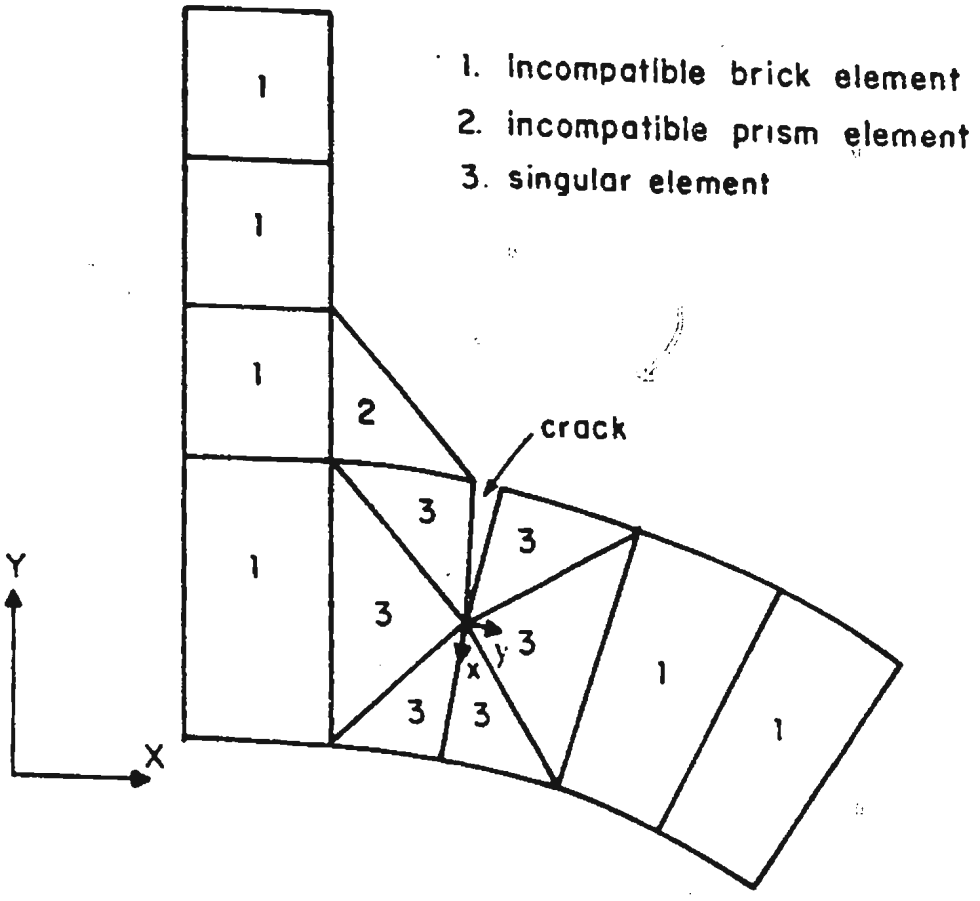

Fig. 5.3 Schematic arrangement of three types of element around crack front.

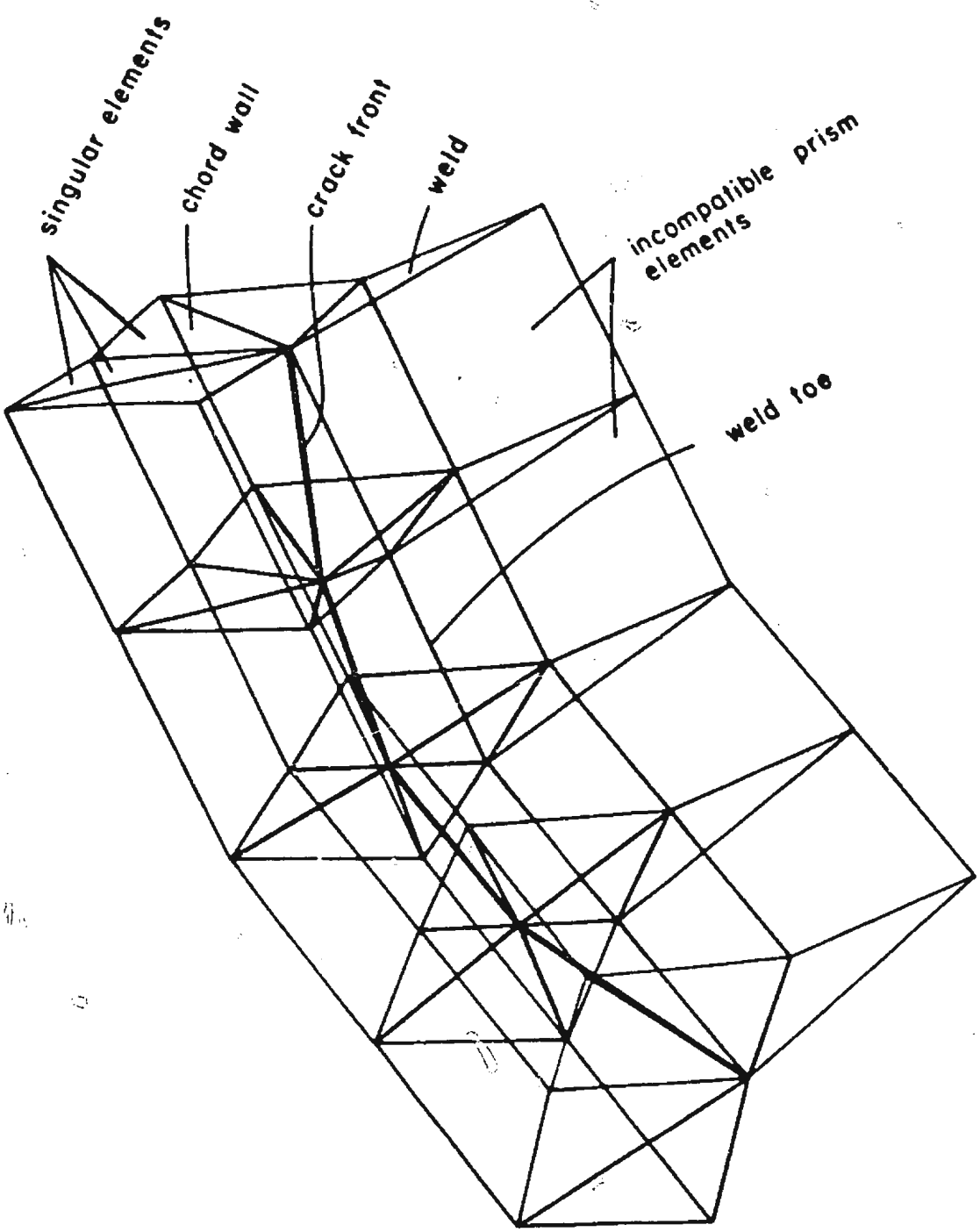

Fig. 5.4 Three-dimensional discretization of the crack region.

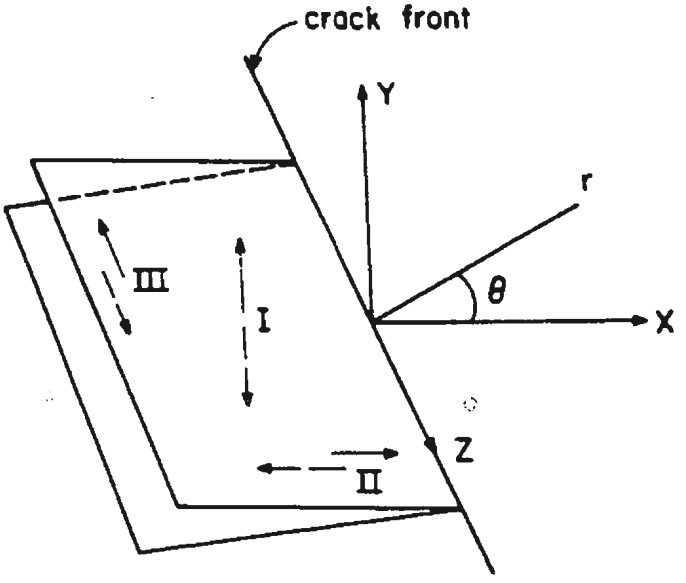

Fig. 5.5 Fracture modes.

$$\tau_{xy} = \frac{K_I}{\sqrt{2\pi r}} \cos\frac{\theta}{2} \sin\frac{\theta}{2} \cos\frac{3\theta}{2}$$

$$\tau_{yz} = \tau_{xz} = 0$$

The crack tip stress intensity factor, K_I, can be evaluated on three convenient lines i.e. in front of the crack($\theta = 0$), on the crack face($\theta = \pi$) and normal to the crack($\theta = \pi/2$). The normal stress, σ_{yy}, in front of the crack is

$$\sigma_{yy} = \frac{K_I}{(2\pi r)^{\frac{1}{2}}} \tag{5.4}$$

From the calculated stresses at two points, lying in front of the crack and very close to the front, the stress intensity factors are calculated using Eqn. 5.4. Then the crack-tip stress intensity factor, K_I, is obtained by extrapolating linearly to r $= 0$.

5.5 Results and Discussion

The variation of the maximum principal stress(σ_p) along the chord surface at the saddle and crown points is examined. Results are obtained for axial and in-plane bending loads and for the following cases: i) a joint without a crack, ii) a joint with an incipient crack and iii) a joint with a crack with depth equal to one half of the thickness of the chord at the weld toe. For the axial load case, Fig. 5.6 shows that the stresses near the weld toe region in the presence of an incipient crack at the saddle point are as much as twice those of the joint without a crack. The stress magnitude rapidly decreases away from the crack front but is always greater than that of a joint without a crack. For a joint with a finite depth

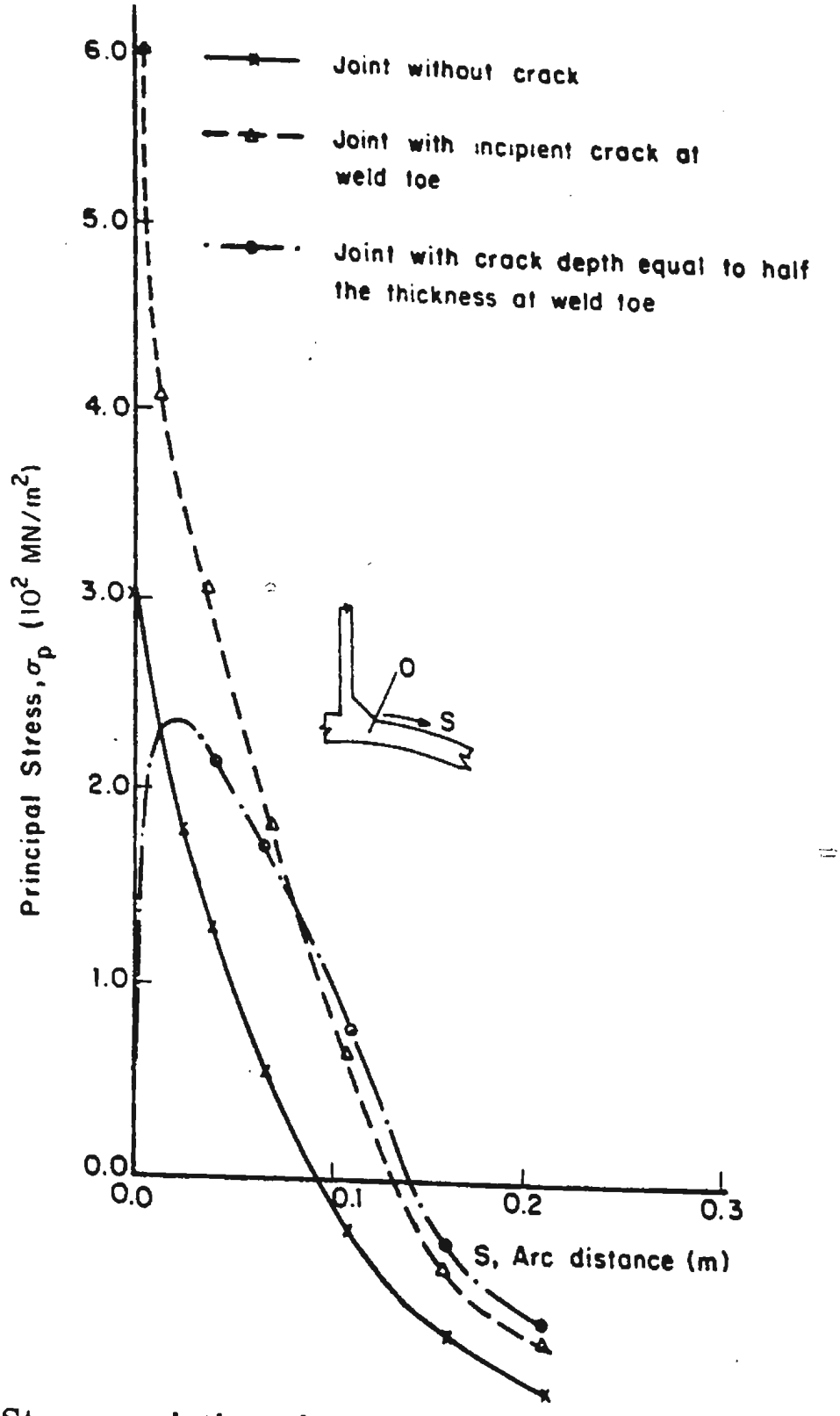

Fig. 5.6 Stress variation along chord surface at saddle point in presence of weld toe crack due to axial load.

crack, the stress distribution in the region remote from the crack almost matches that of a joint with an incipient crack. Near the crack the stress decreases considerably, which is evident from the presence of free surface of the crack face. This agrees well with the phenomenon of hot spot strain drop observed during fatigue testing of the tubular joints, reported in the literature (de Back and Vaessen 1981). For the in-plane bending case, Fig. 5.7 shows that the stresses near the weld toe region of a joint with an incipient crack at the crown point are slightly greater than those of a joint without a crack. A decrease in stress near the weld toe in the presence of a crack with a depth equal to one half of the thickness is observed similar to the axial load case. Away from the weld toe, the magnitudes of stress are almost the same for all three cases.

The normal stress (σ_Y) variations along the brace at the saddle and crown points are presented in Figs 5.8 and 5.9. At the weld toe of the brace, the stress magnitude due to an incipient crack is considerably less than that of a joint without a crack.The stress magnitude near the weld toe, for the case of finite depth, is very much less compared to the other two cases and is nearly the same in regions away from the weld toe. The stress variation along the brace surface at the crown point in the presence of an incipient crack is about 14 percent higher than that of a joint without a crack. In the case of a finite depth crack, the magnitude of stress is higher than the other two cases in the region away from the weld toe.

Figures 5.10 and 5.11 show the variation of the stress, normal to the crack front (σ_{yy}), across the thickness of the chord at the saddle and crown points. For both

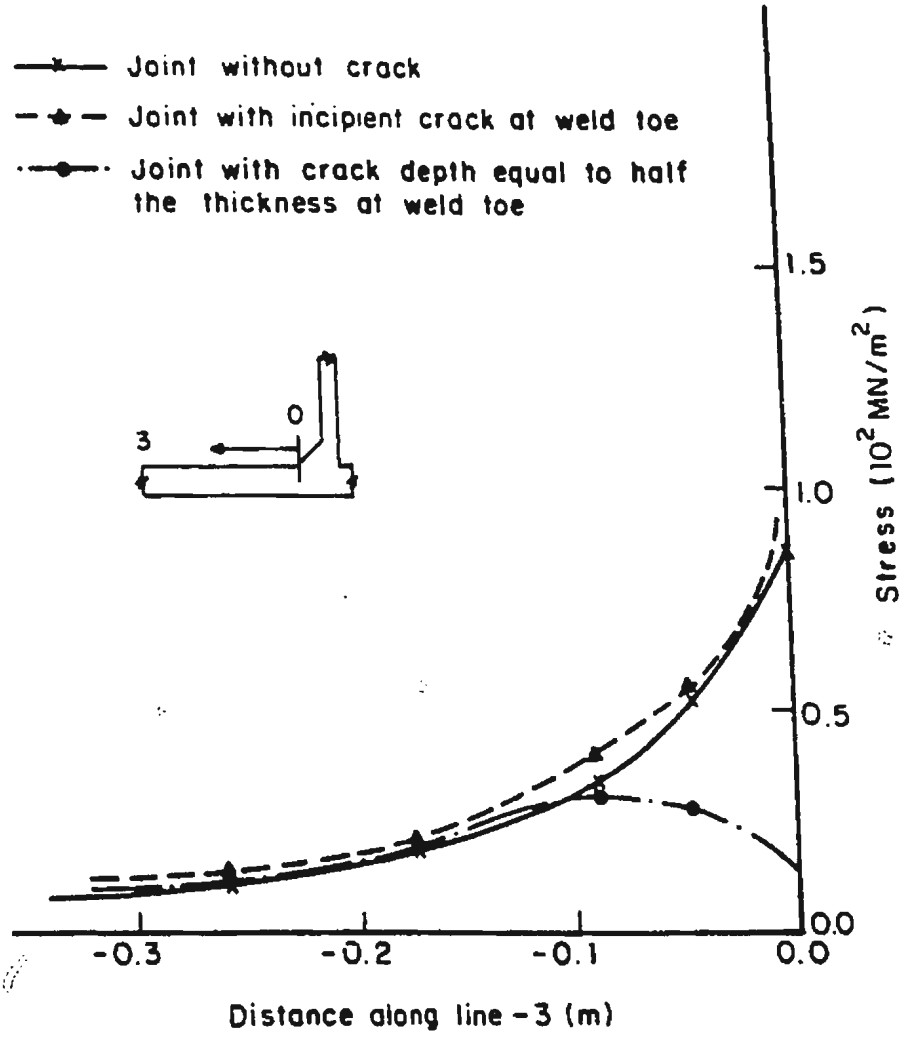

Fig. 5.7 Stress variation along chord surface at crown point in presence of weld toe crack due to in-plane bending load.

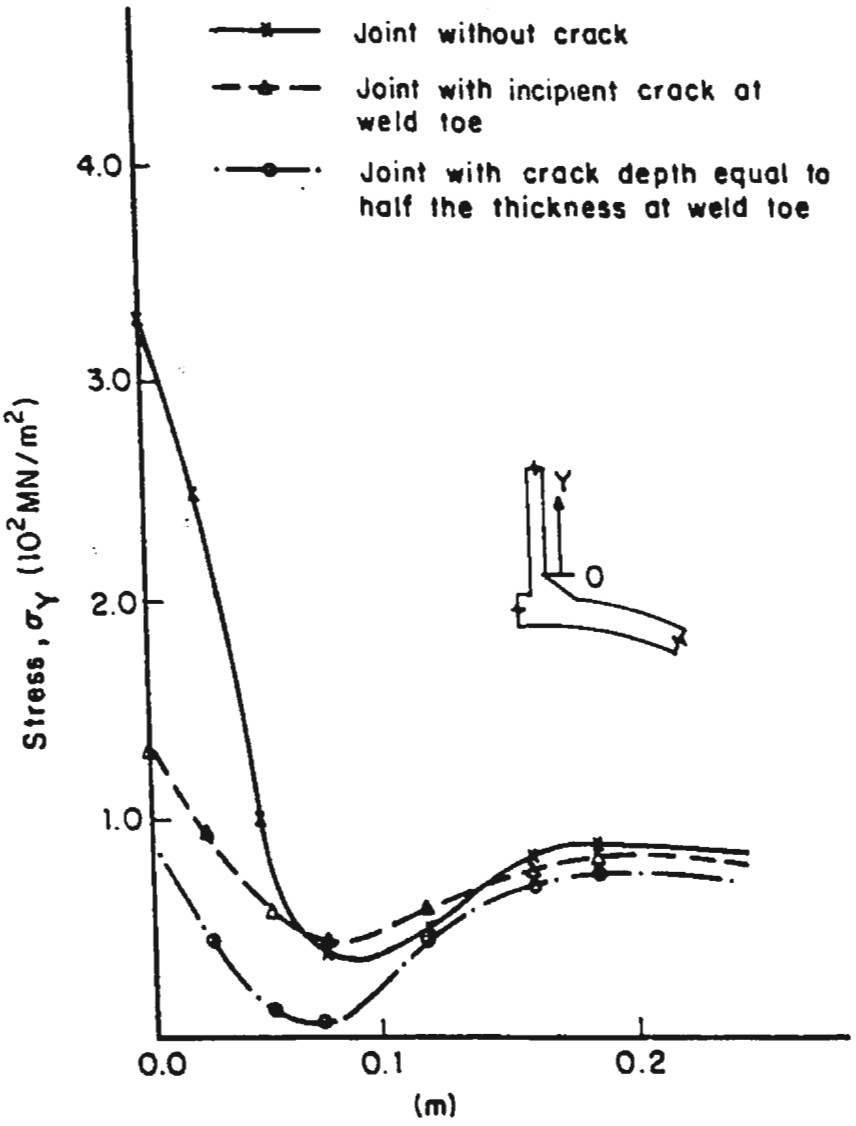

Fig. 5.8 Stress variation along brace surface at saddle point in presence of weld toe crack due to axial load.

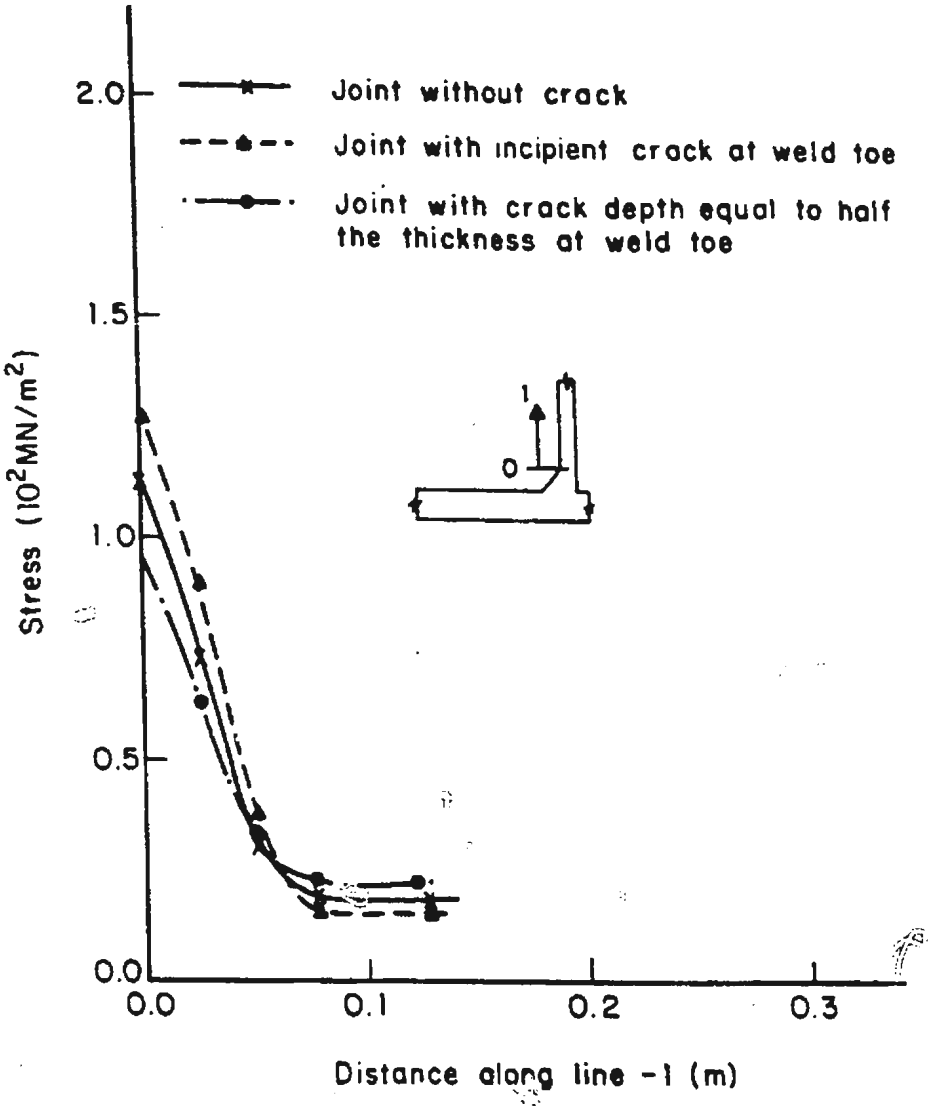

Fig. 5.9 Stress variation along brace surface at crown point in presence of weld toe crack due to in-plane bending load.

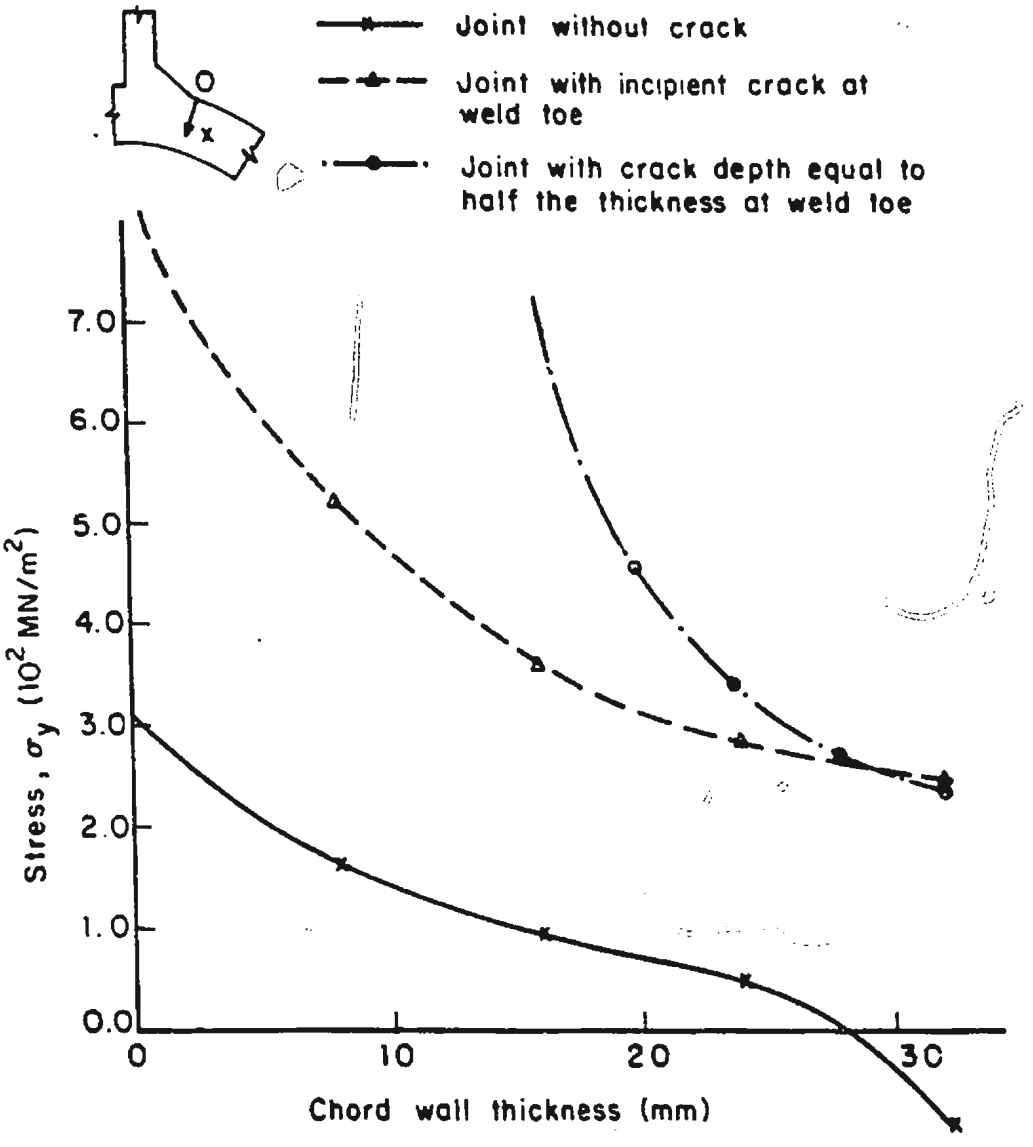

Fig. 5.10 Through-thickness stress variation in front of weld toe crack at saddle point due to axial load.

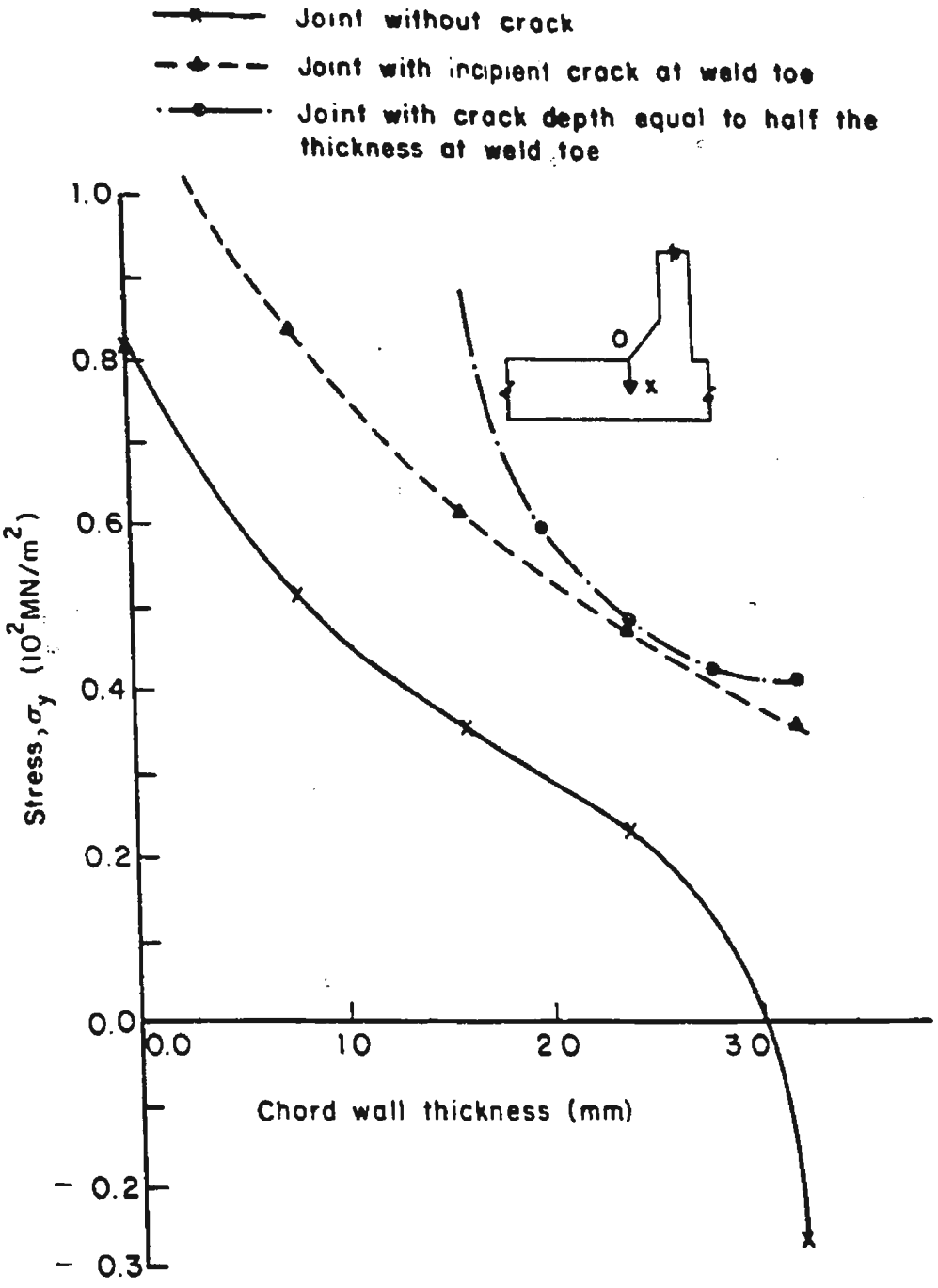

Fig. 5.11 Through-thickness stress variation in front of weld toe crack at crown point due to in-plane bending load.

axial and in-plane bending loadings, the stress is tensile at the outer surface and compressive at the inner surface of the uncracked joint. The presence of the crack changes the stress field into an entirely tensile field. The stresses across the chord wall (in front of the cracks) are much higher than those of a joint without a crack. The crack tip stress intensity factors for the incipient and the 50 percent of thickness cracks are 42.6 $MNm^{-3/2}$ and 55.6 $MNm^{-3/2}$ for axial loading and 9.31 $MNm^{-3/2}$ and 11.09 $MNm^{-3/2}$ for in-plane bending, respectively. The corresponding hot spot stresses due to axial and in-plane bending loads are 306.1 MN/m^2 and 86.4 MN/m^2. The stress intensity factors corresponding to the 50 percent of thickness cracks are compared in Fig. 5.12 with experimental results reported by Dover and Dharmavasan(1982).

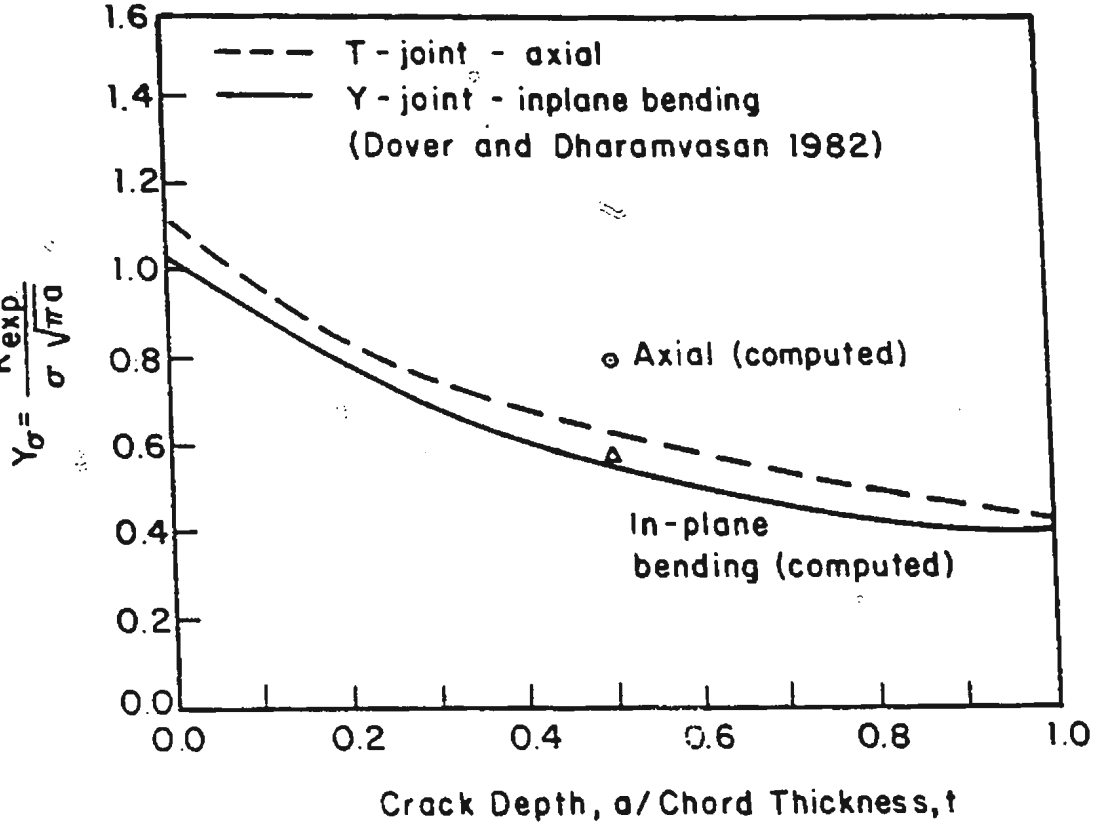

Fig. 5.12 Comparison of computed Y_σ with reported experimental variation.

CHAPTER 6

FATIGUE CRACK PROPAGATION IN BASE METAL

6.1 Introduction

A knowledge of the fatigue-crack-growth rates, in air and in seawater, and the stress intensity factors (computed) corresponding to the weld toe defects are essential to predict the fatigue life of offshore tubular structures. Factors which can influence the resistance of a material to corrosion fatigue can be separated into mechanical, environmental and metallurgical factors. Mechanical variables which govern crack-growth-rate are principally frequency, stress ratio, wave form and range of stress intensity factors. Environmental factors include temperature, degree of aggression, electro-chemical potential difference and marine fouling. The metallurgical factors arise essentially from the steel production processes, quality and production route.

Hence there is a need to generate quantitative fatigue-crack-growth information which can be used in design and in making decisions concerning fabrication, operation and protection. But the testing of large-scale and small-scale tubular joints is both costly and time consuming compared to small scale tests on CT, WOL, CCT, SET and other specimens. The small scale tests have the advantage of relative simplicity and the ability to investigate a number of variables in a reasonable time. During the past decade extensive research programmes have been

in progress, particularly in Europe, on quantifying the effects of loading and environmental parameters on fatigue-crack growth, as applied to offshore production and exploration platforms. Most of the tests were conducted at temperatures which prevail in the North Sea (5°C to 12°C), or at room temperature. The temperature of most Canadian offshore waters (0° to 5°C) is lower than that of the North Sea.

This chapter presents the results of some fatigue-crack-propagation tests on small scale specimens in air and in sea water, under constant amplitude loading. The effects of temperature, frequency, load ratio and wave form on the crack-growth-rate are studied. The Compact Tension (CT) specimen is selected for the fatigue-crack-growth-rate tests for the following reasons: ASTM E647-81 favours the CT specimen use, whose planar dimensions scale can be chosen proportional to the size. Moreover, its larger height to width ratio provides increased resistance to out-of-plane cracking and arm break off, while testing at high loads.

6.2 Experimental Procedure

Fatigue-crack-growth rates are measured for Compact Tension specimens with 24 mm thickness and 101 mm net width (Fig. 6.1). The specimens with the starter notch perpendicular to the rolling direction are prepared from 26 mm thick steel plate, manufactured to CSA G40.21 M 350 WT specification, by oxygen cutting. The specimens are notched in two steps: first by saw-cutting and then by miller cutter, specially ground to contain an included angle of 30°. The chemical composition and the mechanical properties of the plate are given in Table 6.1.

Table 6.1 Chemical composition and mechanical properties of CSA G 40.21 M 350 WT steel.

Chemical composition:				elemental weight (%)	
C	Mn	P	S	Si	others
0.22	0.8/1.5	0.03	0.04	0.15/0.4	0.1

Mechanical properties		
Yield strength	(MN/m^2)	405
Ultimate tensile strength	(MN/m^2)	513
Elongation	(%)	29

ALL DIMENSIONS ARE IN MILLIMETRES

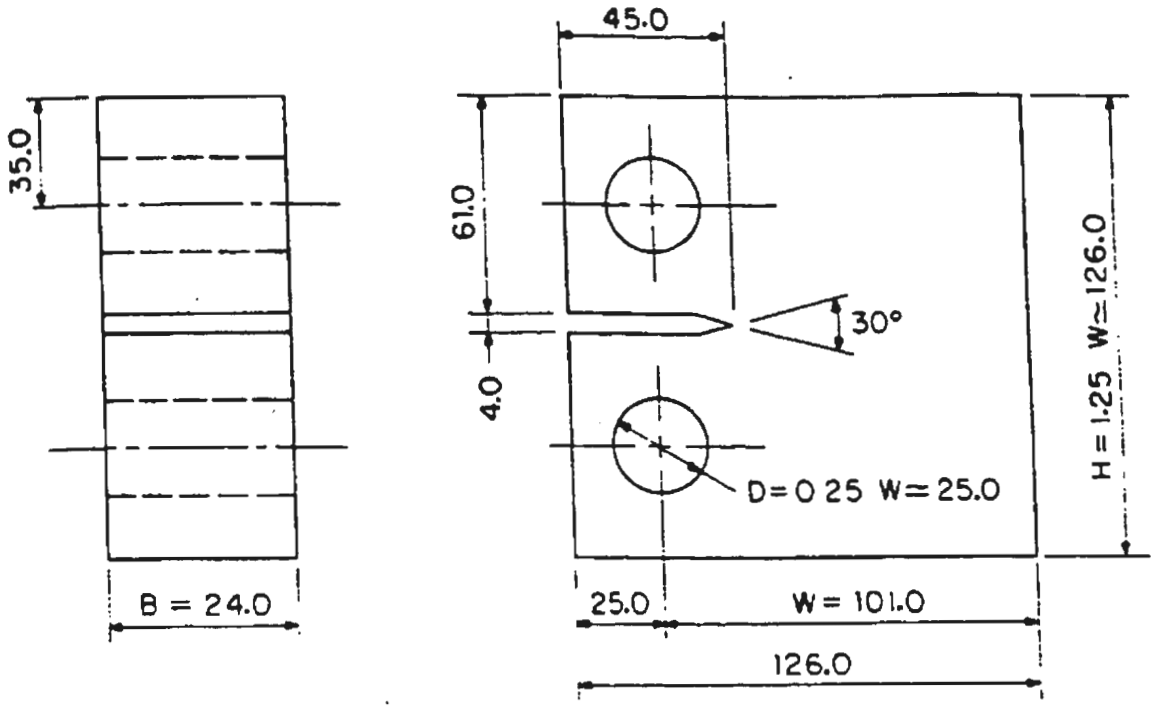

NET WIDTH = 101.0
THICKNESS B = 24.0
TOTAL WIDTH C = 1.25 W
HEIGHT H = 1.25 W

HOLE DIA D = 0.25 W = 25.0
NOTCH WIDTH N = 0.065 W MAX
EFFECTIVE NOTCH LENGTH M = 0.4 W
EFFECTIVE CRACK LENGTH a = 0.45 W

Fig. 6.1 Compact tension specimen.

Tests are carried out under constant amplitude loading on a closed-loop servohydraulic Materials Testing System (MTS) using a tension to tension loading (Fig. 6.2). Thirteen tests are carried out in air inside the laboratory cold room for various temperatures (–15°C to 4°C), load ratios (0.05 - 0.3) and frequencies (0.05 Hz - 2.0 Hz). To study the effect of sea water on crack-growth-rate, eleven specimens are tested in natural sea water. The temperature of the sea water for ten of these specimens is maintained at 0°C, using a recirculation system (Fig. 6.3). Load ratios and frequency ranges for the sea water tests are 0.05 to 0.3 and 0.05 Hz to 0.5 Hz, respectively. All tests are carried out under sinusoidal loading except one under saw tooth loading. A detailed schedule of the variables for the crack-growth-rate data generation is given in Table 6.2.

6.3 Data Analysis Procedures

Two separate computational procedures are necessary to analyze fatigue-crack growth data, so that the results can be expressed in a useful, geometry-independent form. One of these procedures is the computation of the stress intensity factor range, ΔK, from the discrete crack length measurements and the loading variables for the test specimen. The other involves computing the instantaneous fatigue-crack-growth-rate, $(da/dN)_i$, from the discrete measurements of crack length (a_i) and the elapsed fatigue cycles (N_i). Typically, both operations are conducted on 18-25 data points per test.

6.3.1 Computation of ΔK

The variation in the stress intensity factor in a fatigue cycle, ΔK, is defined using

Table 6.2 Schedule of variables for crack-growth-rate data generation.

(CT specimen, material: CSA G40.21 M 350 WT)

Sp. No.	Temp., T (°C)	Load ratio, R	Freq., f (Hz)	Envir.
1	4	0.1	0.2	A
2	4	0.1	0.5	A
3	4	0.1	2.0	A
4	4	0.1	0.1	A
5	4	0.2	0.2	A
6	4	0.3	0.2	A
7	4	0.05	0.2	A
8	4	0.1	0.05	A
9	0	0.1	0.2	A
10	-5	0.1	0.2	A
11	-10	0.1	0.2	A
12	-15	0.1	0.2	A
13	3	0.1	0.2	A
14	21	0.1	0.2	SW
15	0	0.1	0.2	SW
16	0	0.1	0.2	SW
17	0	0.2	0.2	SW
18	0	0.3	0.2	SW
19	0	0.1	0.1	SW
20	0	0.1	0.05	SW
21	0	0.1	0.5	SW
22	0	0.3	0.2	SW
23	0	0.05	0.2	SW
*24	0	0.1	0.1	SW

* saw tooth loading

A: Air

SW: Sea Water

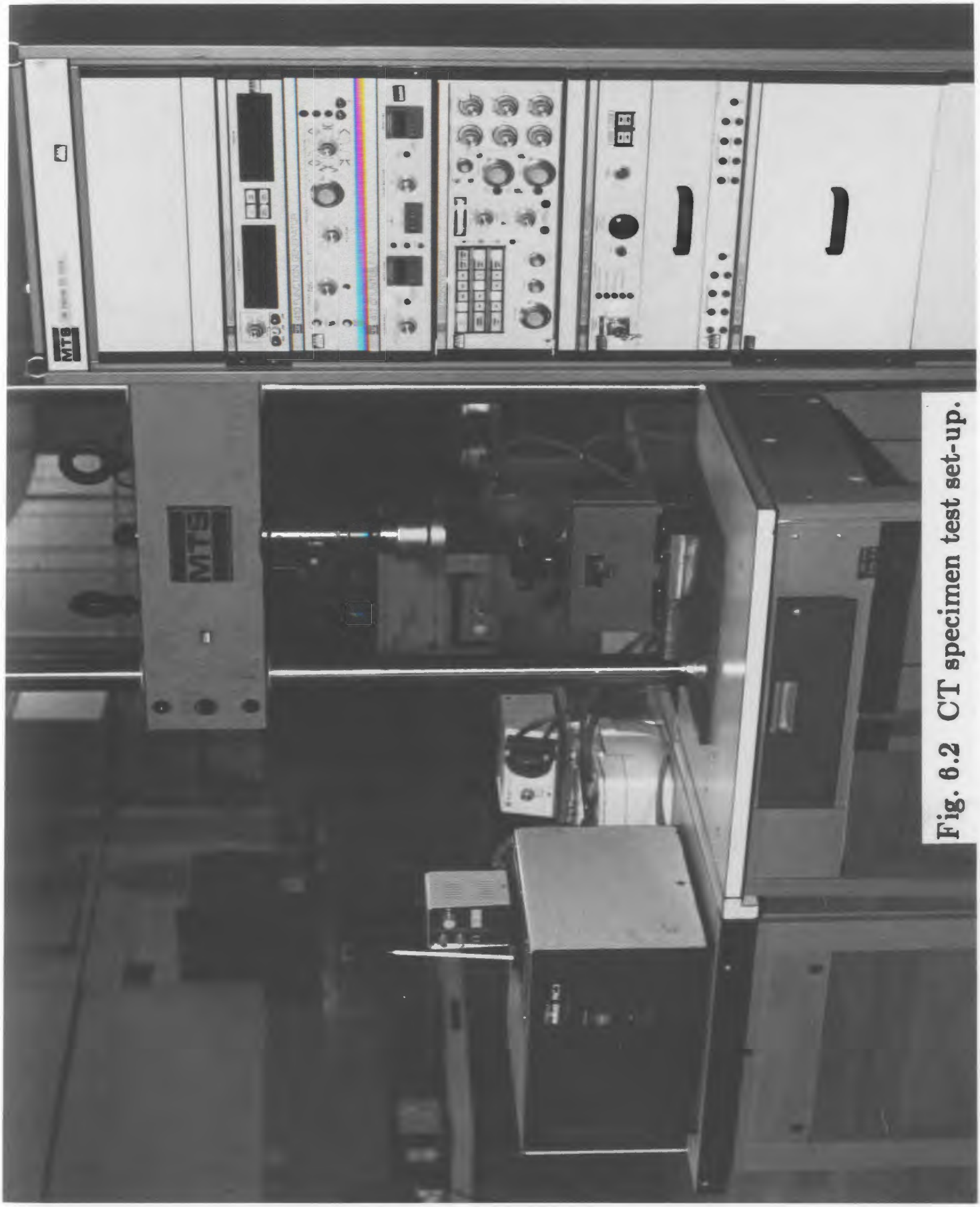

Fig. 6.2 CT specimen test set-up.

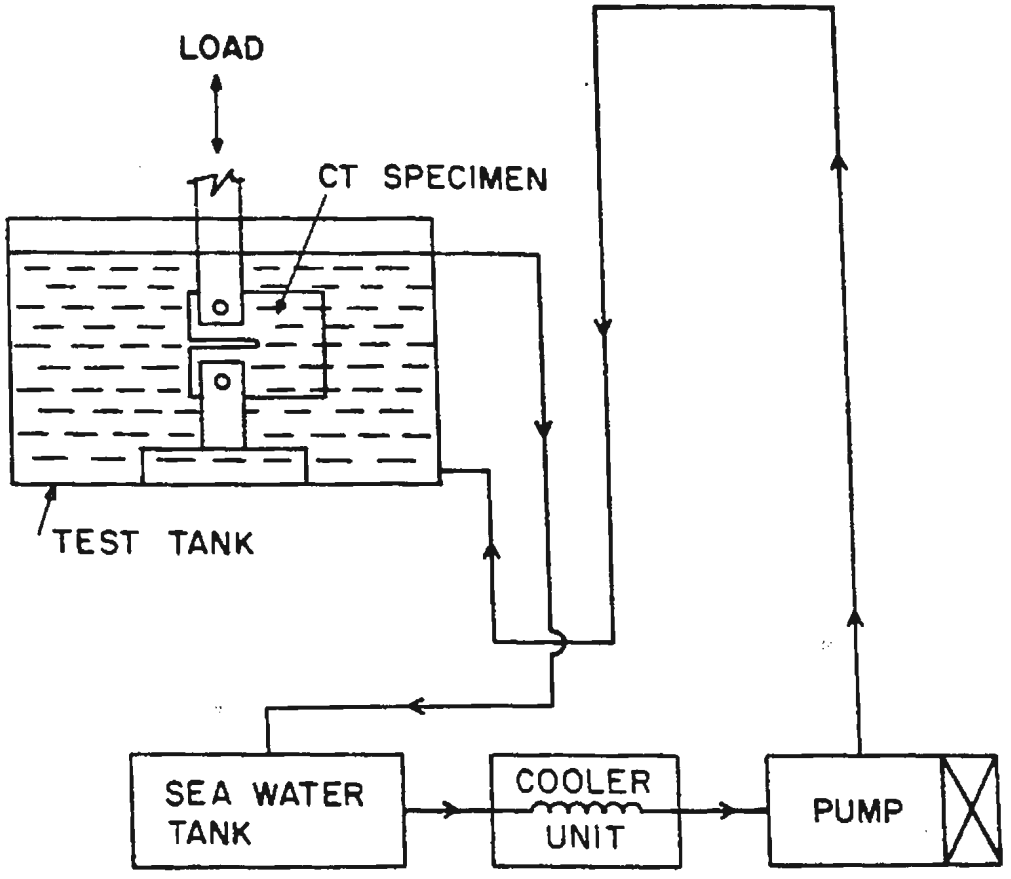

Fig. 6.3 Schematic diagram of CT specimen under test with recirculation system.

only the positive portion of the loading cycle based on the common physical concept that the stress intensity factor is equal to zero when the crack faces are closed. For the compact tension specimen, ΔK is calculated using the following expression (ASTM E647-81)

$$(\Delta K)_i = \frac{\Delta P \sqrt{a_i}}{B W} \times \left[29.60 - 185.5 \left(\frac{a_i}{W}\right) + 655.7 \left(\frac{a_i}{W}\right)^2 - 1017 \left(\frac{a_i}{W}\right)^3 + 638.9 \left(\frac{a_i}{W}\right)^4 \right] \tag{6.1}$$

where ΔP is the applied load range and a_i is the instantaneous crack length. B and W are the specimen's thickness and net width, respectively (Fig. 6.1).

6.3.2 Crack-growth-rate evaluation

The instantaneous crack-growth-rate $(da/dN)_i$ is computed by fitting a 2nd order polynomial (parabola) to sets of seven successive data points. The form of the equation for the local fit is as follows (Hudak et al 1978):

$$\hat{a}_i = b_0 + b_1 \hat{N} + b_2 \hat{N} \tag{6.2}$$

where

$$\hat{N} = \left[\frac{N_i - \frac{1}{2}(N_{i-3} + N_{i+3})}{\frac{1}{2}(N_{i+3} - N_{i-3})} \right] \tag{6.3}$$

and $\hat{a}_i$ is the fitted value of crack length at N_i. b_0, b_1 and b_2 are the regression parameters which are determined by the least squares method. The rate of crack

growth at N_i is obtained from the derivative of the above parabola, which is given by

$$(\frac{da}{dN})_{\hat{a}_i} = \frac{2b_1 + 8b_2\hat{N}}{N_{i+3} - N_{i-3}} \tag{6.4}$$

The value of ΔK associated with this da/dN value is computed using the fitted crack length, $\hat{a}_i$, corresponding to N_i.

6.4 Results and Discussion

The fatigue-crack-growth data (a vs. N) obtained from 24 tests in air and in sea water are shown in Figs. 6.5 - 6.11. Figure 6.4 shows the fractured compact tension specimens. The crack-growth-rate data are presented graphically and algebraically. The graphical method consists of log-log plots of da/dN as a function of ΔK to display wide-range data. The computed initial and final crack-growth-rates and the stress intensity factor ranges for the specimens are given in Table 6.3. A regression curve based on the least squares method is fitted to each set of experimental crack-growth-rate data (da/dN, ΔK) using Paris' equation

$$da/dN = C\,(\,\Delta K\,)^m \tag{6.5}$$

The correlation coefficients obtained from the statistical analyses of the data points are in the range of 0.98 and above for a vs. N curves and 0.85 to 0.98 for da/dN vs. ΔK curves. The lower correlation values for da/dN vs. ΔK curves are obtained for tests 1, 4 and 21; in all the other cases, it is well over 0.90. The coefficients C and m, obtained from linear regression for each specimen, are given

Table 6.3 Initial and final crack-growth-rates and stress intensity factor ranges for CT specimens.

Sp. No.	da/dN (m/cycle)		ΔK ($MNm^{-3/2}$)	
	Initial	Final	Initial	Final
1	.163E-06	.845E-06	33.08	57.57
2	.268E-06	.146E-05	33.44	64.03
3	.278E-06	.116E-05	30.42	58.88
4	.490E-06	.143E-05	43.80	67.58
5	.352E-06	.969E-06	36.54	58.11
6	.153E-06	.589E-06	25.91	47.54
7	.384E-06	.783E-06	43.59	57.01
8	.406E-06	.776E-06	39.01	50.81
9	.780E-06	.331E-05	34.68	60.33
10	.309E-06	.112E-05	35.30	61.05
11	.290E-06	.854E-06	34.09	53.69
12	.283E-06	.112E-05	33.75	56.23
13	.285E-06	.720E-06	35.28	53.56
14	.637E-06	.117E-05	36.84	55.02
15	.453E-06	.770E-06	37.52	48.58
16	.349E-06	.128E-05	34.20	60.48
17	.386E-06	.780E-06	30.79	49.91
18	.266E-06	.779E-06	26.01	47.02
19	.449E-06	.127E-05	34.31	61.62
20	.747E-06	.117E-05	34.06	49.45
21	.545E-06	.164E-05	41.99	63.08
22	.266E-06	.838E-06	26.72	43.05
23	.580E-06	.139E-05	38.26	67.38
24	.626E-06	.151E-05	36.45	62.03

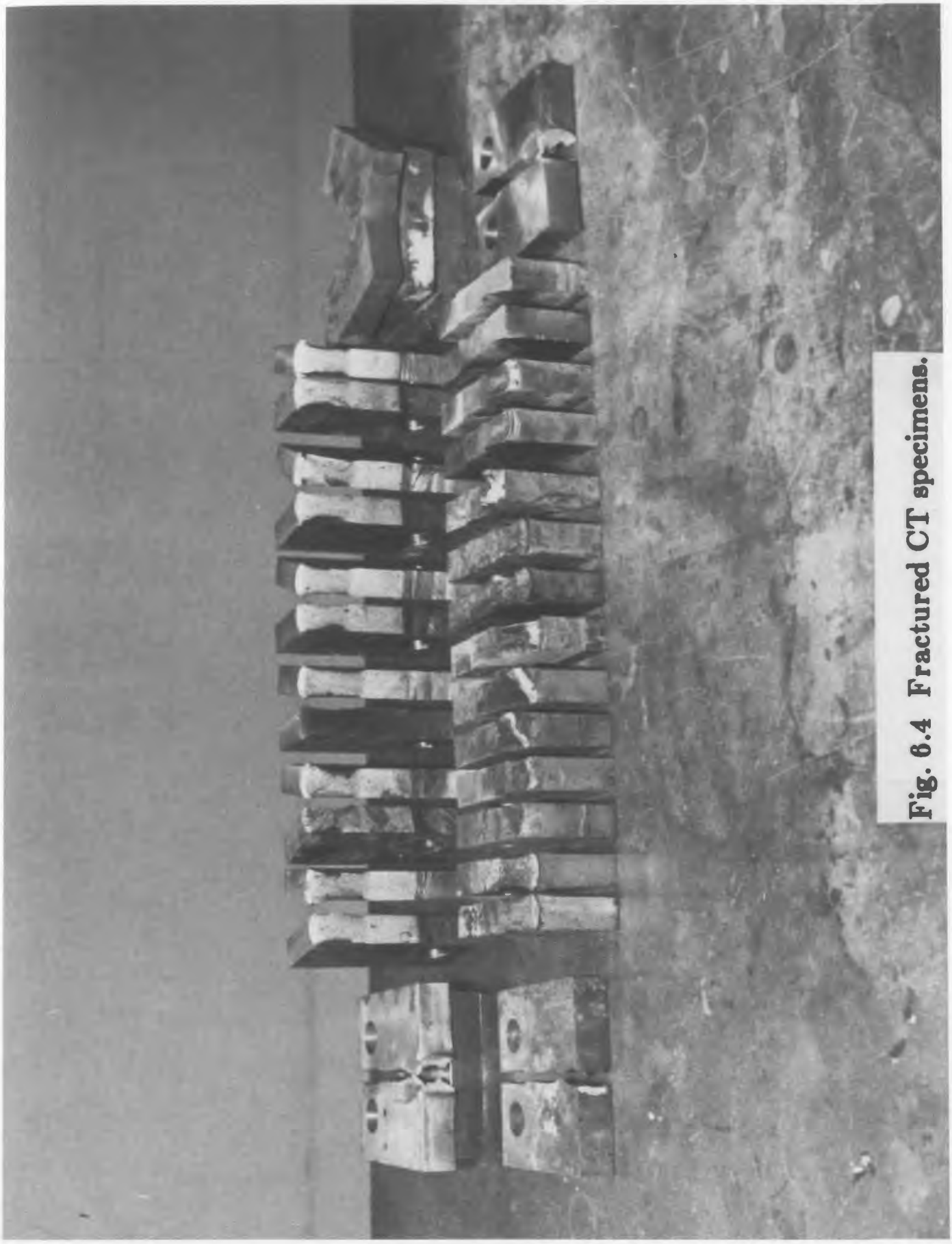

Fig. 6.4 Fractured CT specimens.

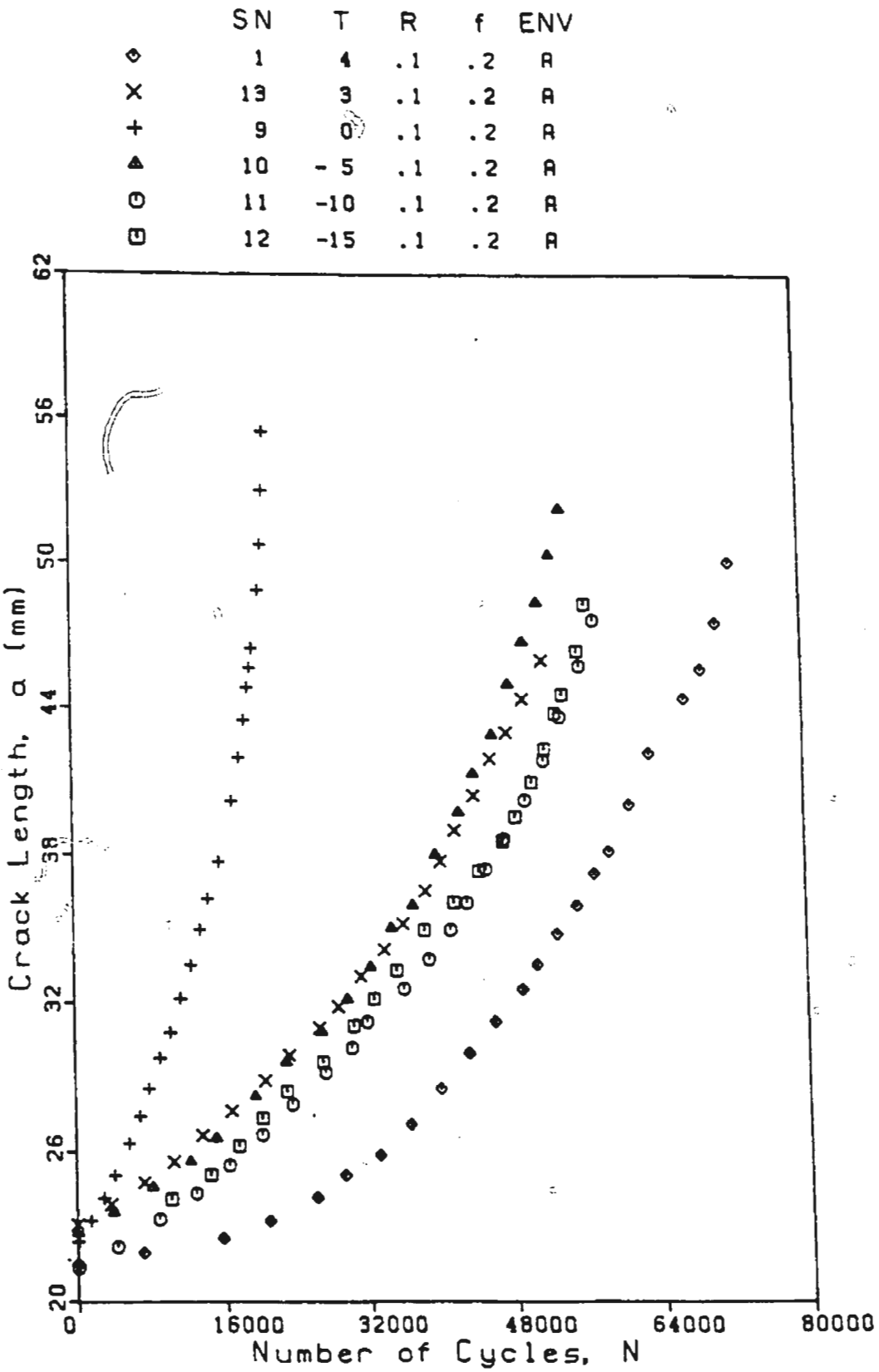

Fig. 6.5 Crack growth data in air: R = 0.1, f = 0.2 Hz and T = -15 to 4°C.

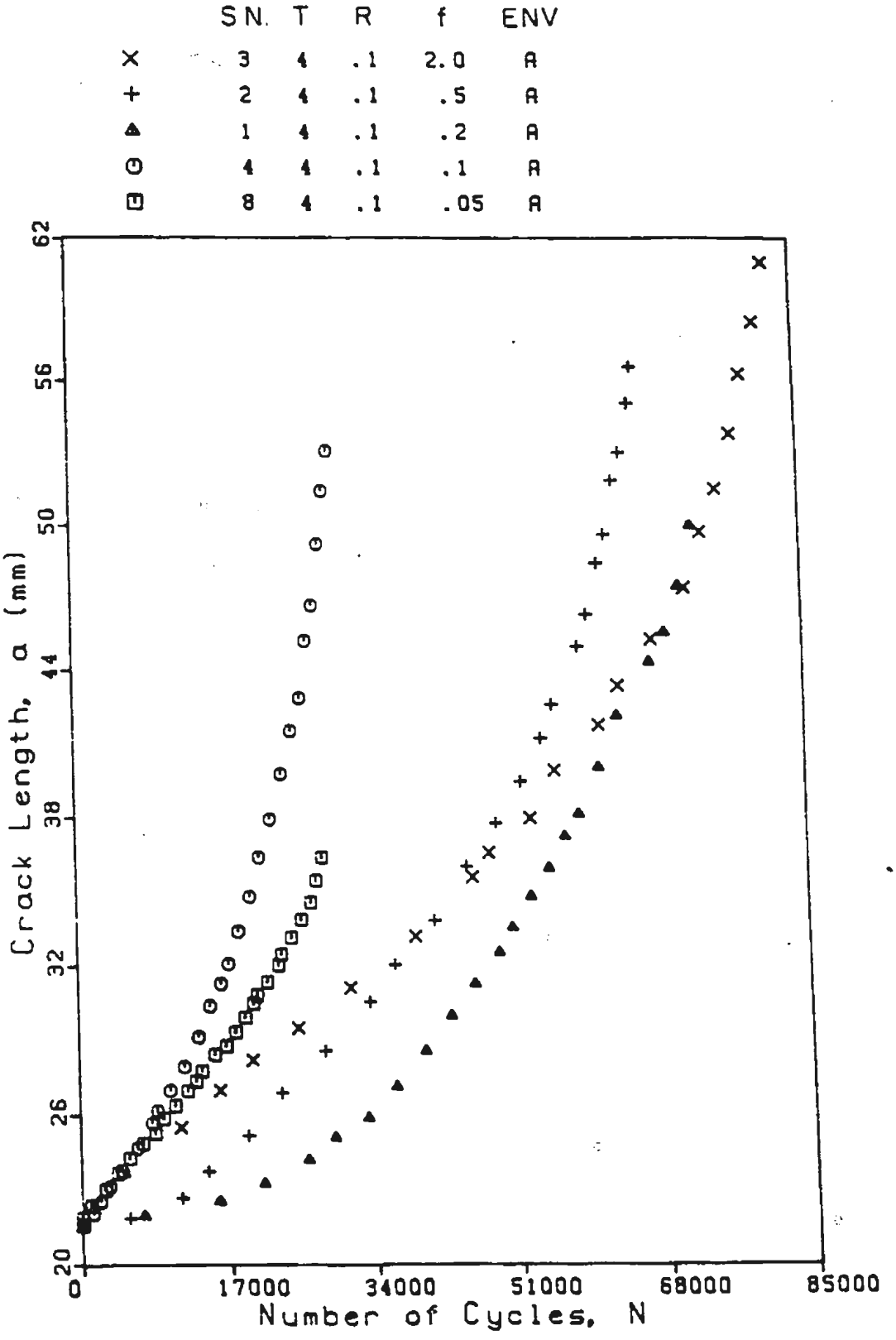

Fig. 6.6 Crack growth data in air: T = 4°C, R = 0.1 and f = 0.05 to 2.0 Hz.

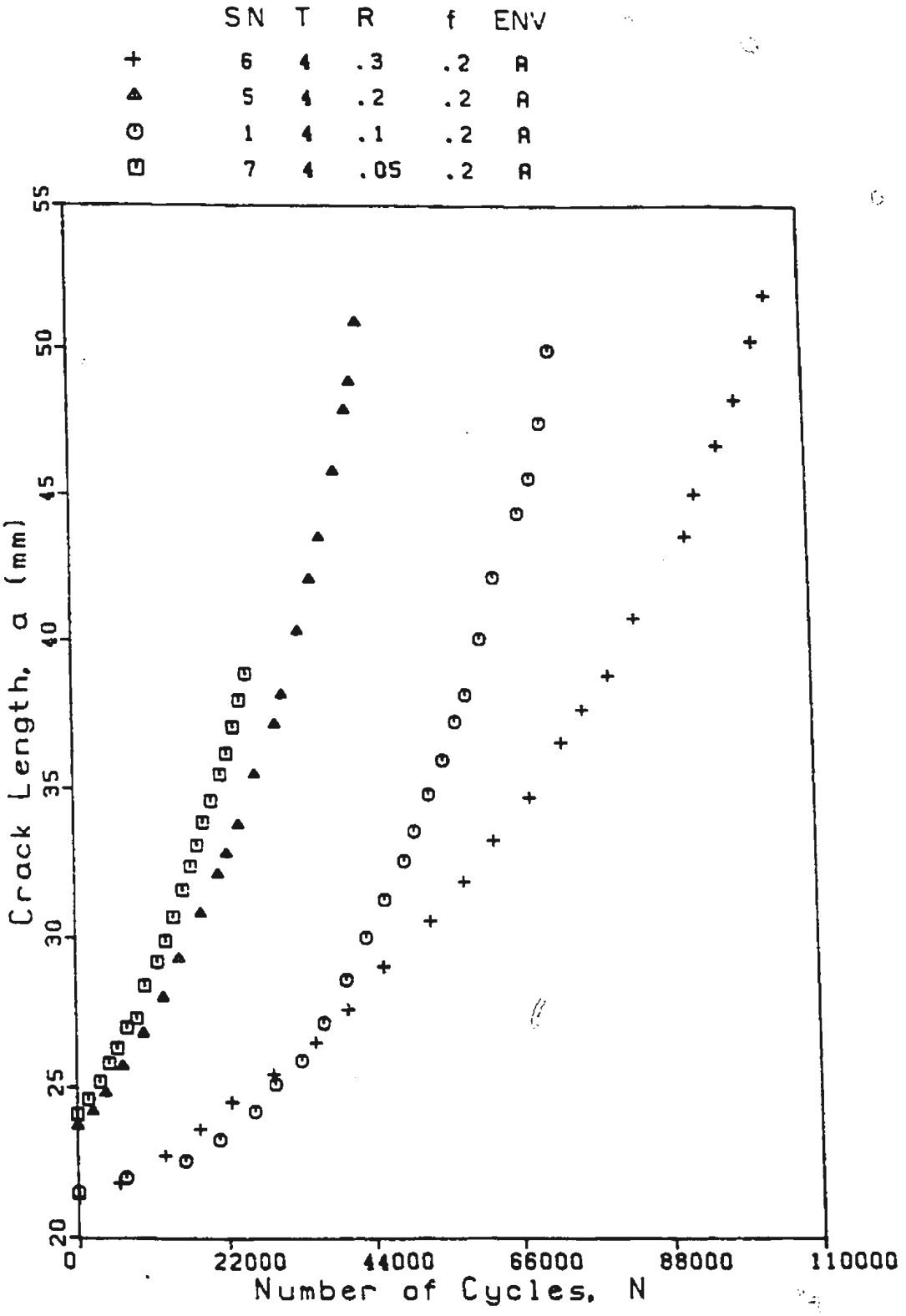

Fig. 6.7 Crack growth data in air: T = 4°C, f = 0.2 Hz and R = 0.05 to 0.3.

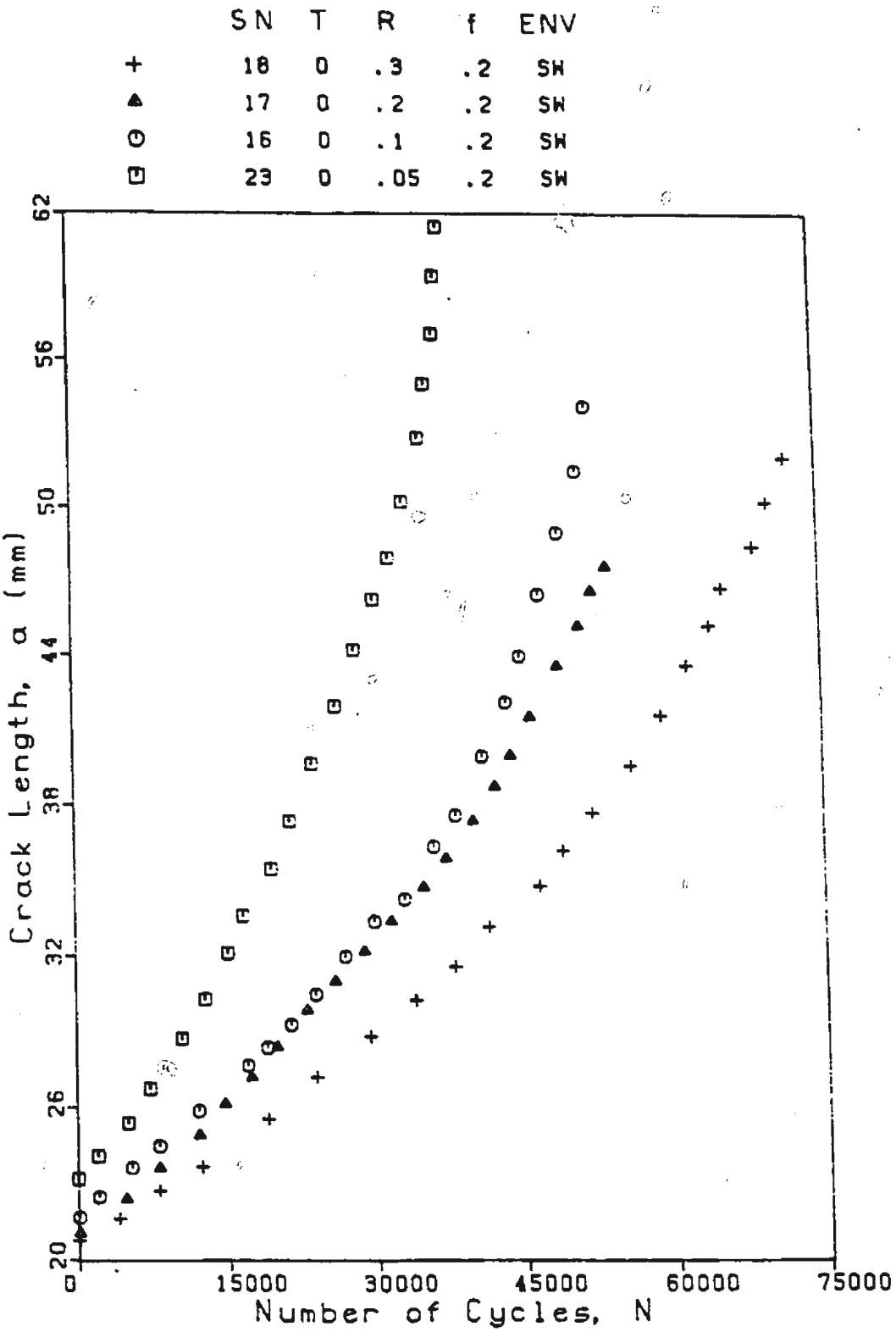

Fig. 6.8 Crack growth data in sea water: T = 0°C, f = 0.2 Hz and R = 0.05 to 0.3.

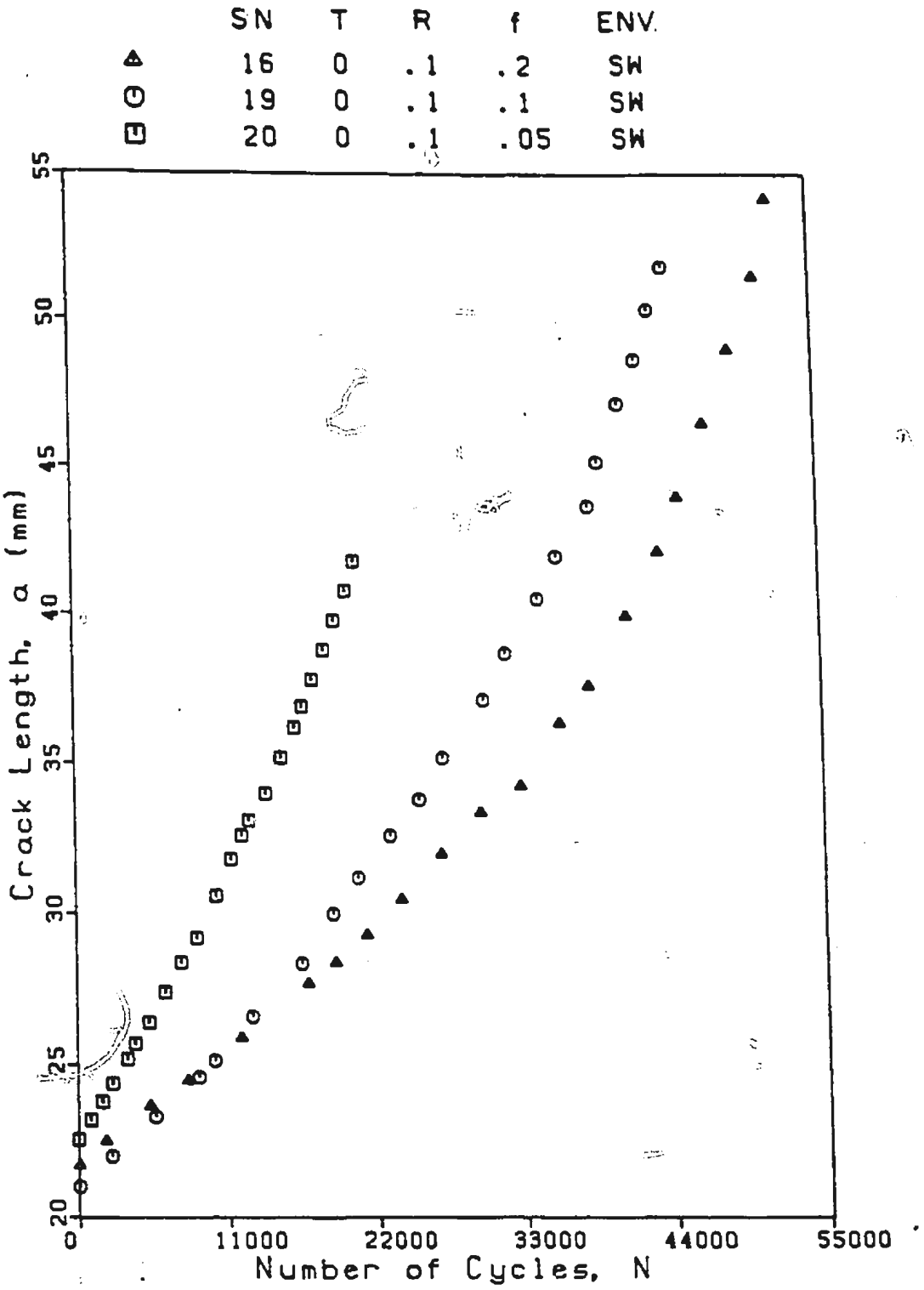

Fig. 6.9 Crack growth data in sea water: T = 0°C, R = 0.1 and f = 0.05 to 0.2 Hz.

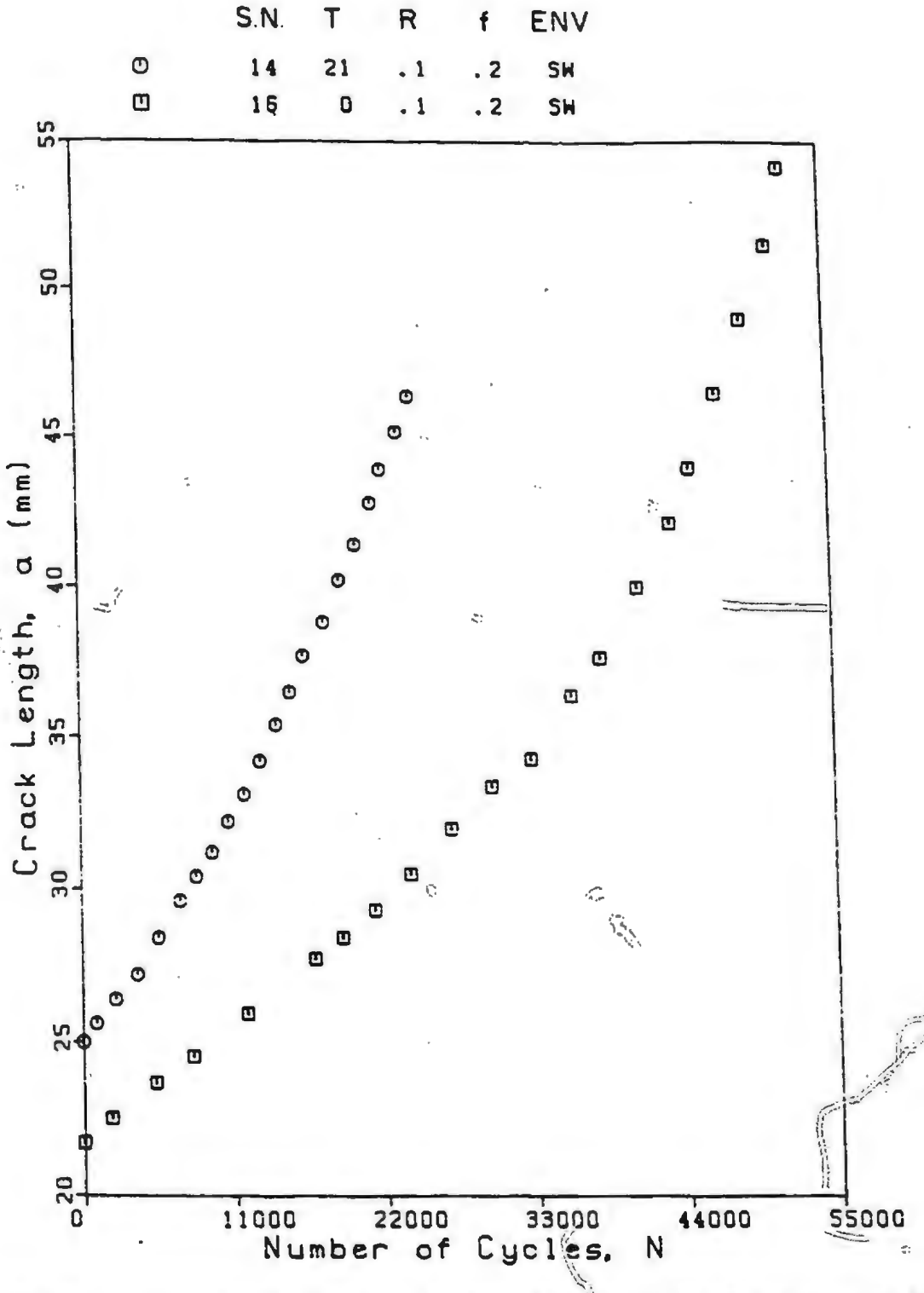

Fig. 6.10 Crack growth data in sea water: T = 0 and 21°C, R = 0.1 and f = 0.2 Hz.

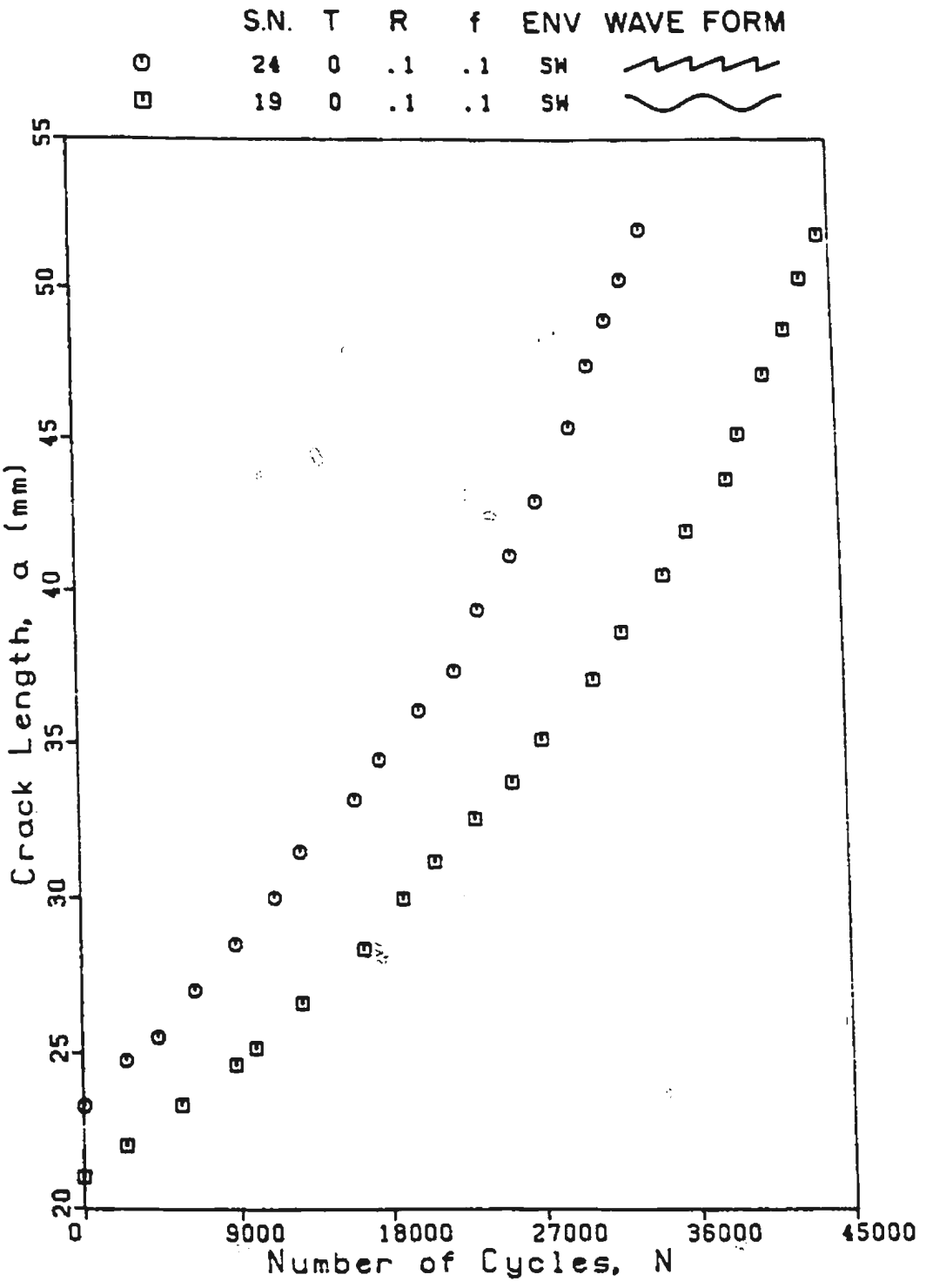

Fig. 6.11 Crack growth data in sea water under sinusoidal and saw tooth loading: T = 0°C, R = 0.1 and f = 0.1 Hz.

in Table 6.4. The data obtained from specimen no. 23 are not considered for discussion because the sea water temperature did not remain steady due to practical problems. The crack-growth-rate data are discussed below.

6.4.1 Crack-growth-rates in air

The temperature dependence of the fatigue crack-growth-rates in air on the stress intensity factor range is shown in Fig. 6.12, for a stress ratio R = 0.1 and frequency of 0.2 Hz. There is no significant decrease in the crack-growth-rate at $\Delta K = 50$ $MNm^{-3/2}$ as the temperature is lowered from 4°C to –15°C. From Fig. 6.13, it can be seen that the crack-growth-rate (growth per cycle) increases by 15 percent at $\Delta K = 45$ $MNm^{-3/2}$ as the frequency increases from 0.05 Hz to 2.0 Hz, but at the upper ΔK range the effect is not significant. The results of the tests with different R-values are presented in Fig. 6.14. Comparing these results, it can be noticed that at a stress intensity factor range of 45 $MNm^{-3/2}$ the crack-growth-rate increases by 19 percent as the load ratio increases from 0.05 to 0.2.

6.4.2 Crack-growth-rates in sea water

The fatigue-crack-growth-rates for 21°C and 0°C are shown in Fig. 6.15. A decrease in growth-rates at the lower stress intensity factor range by 43 percent is observed when the temperature is reduced from 21°C to 0°C. This is probably due to the decrease in corrosion reaction rates with decreasing temperature. In the upper ranges of ΔK, the effect of temperature is negligible. The effect of frequency on the fatigue-crack-growth-rates in sea water is shown in Fig. 6.16. From these results it can be seen that at the higher ΔK ranges, the effect of frequency

Table 6.4 Coefficients C and m for CT specimens.

Sp. No.	C (m/cycle)	m
1	.274E-10	2.598
2	.396E-10	2.507
3	.102E-09	2.263
4	.265E-10	2.598
5	.174E-09	2.131
6	.195E-09	2.074
7	.753E-10	2.296
8	.105E-09	2.223
9	.408E-10	2.757
10	.457E-10	2.475
11	.566E-10	2.407
12	.578E-10	2.402
13	.397E-10	2.490
14	.287E-08	1.509
15	.617E-10	2.419
16	.429E-10	2.513
17	.194E-08	1.524
18	.447E-09	1.947
19	.121E-08	1.675
20	.120E-07	1.166
21	.843E-11	2.959
22	.117E-09	2.300
23	.727E-09	1.822
24	.775E-09	1.826

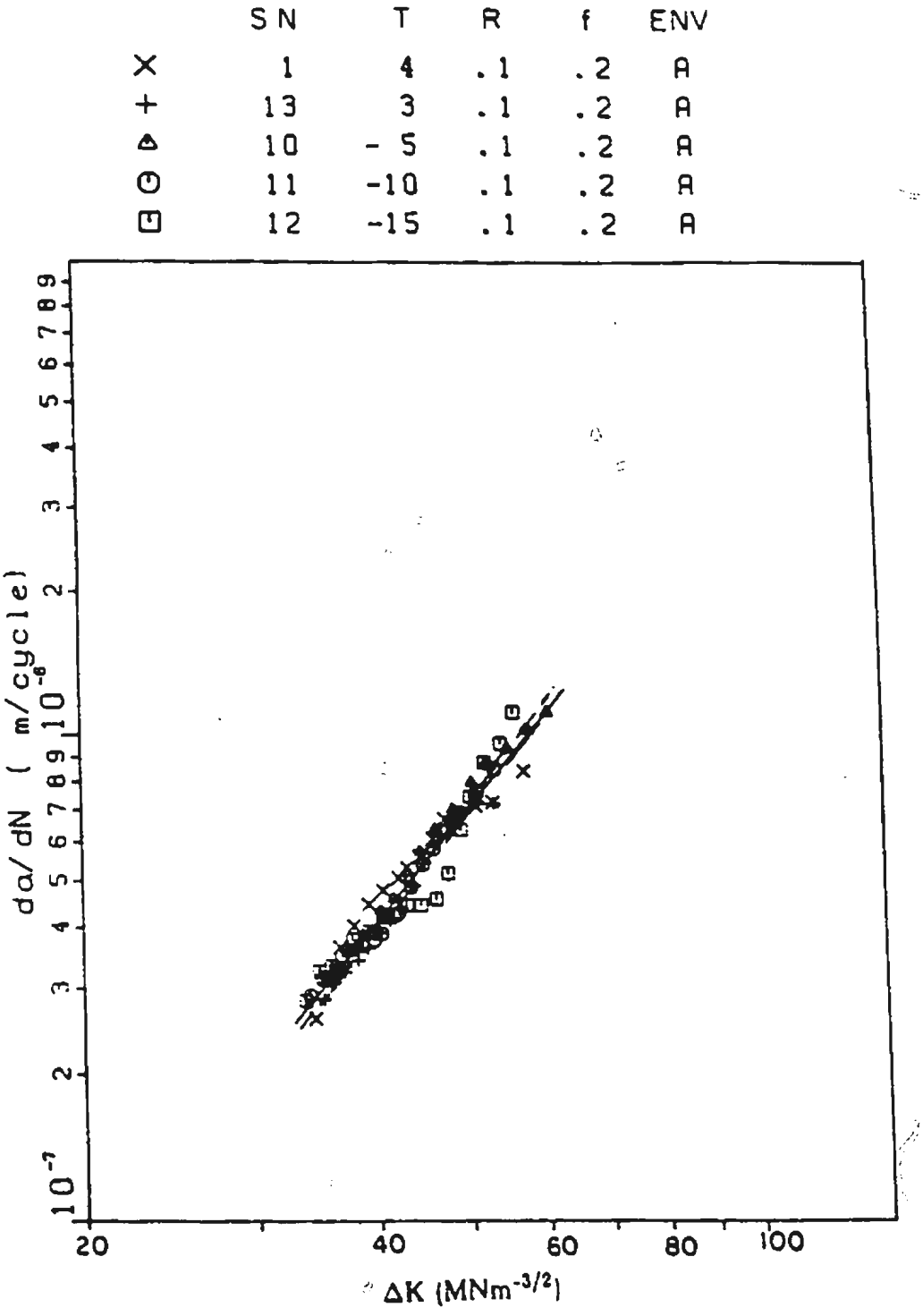

Fig. 6.12 Effect of temperature on fatigue crack-growth-rates in air: R = 0.1, f = 0.2 Hz and T = -15 to 4°C.

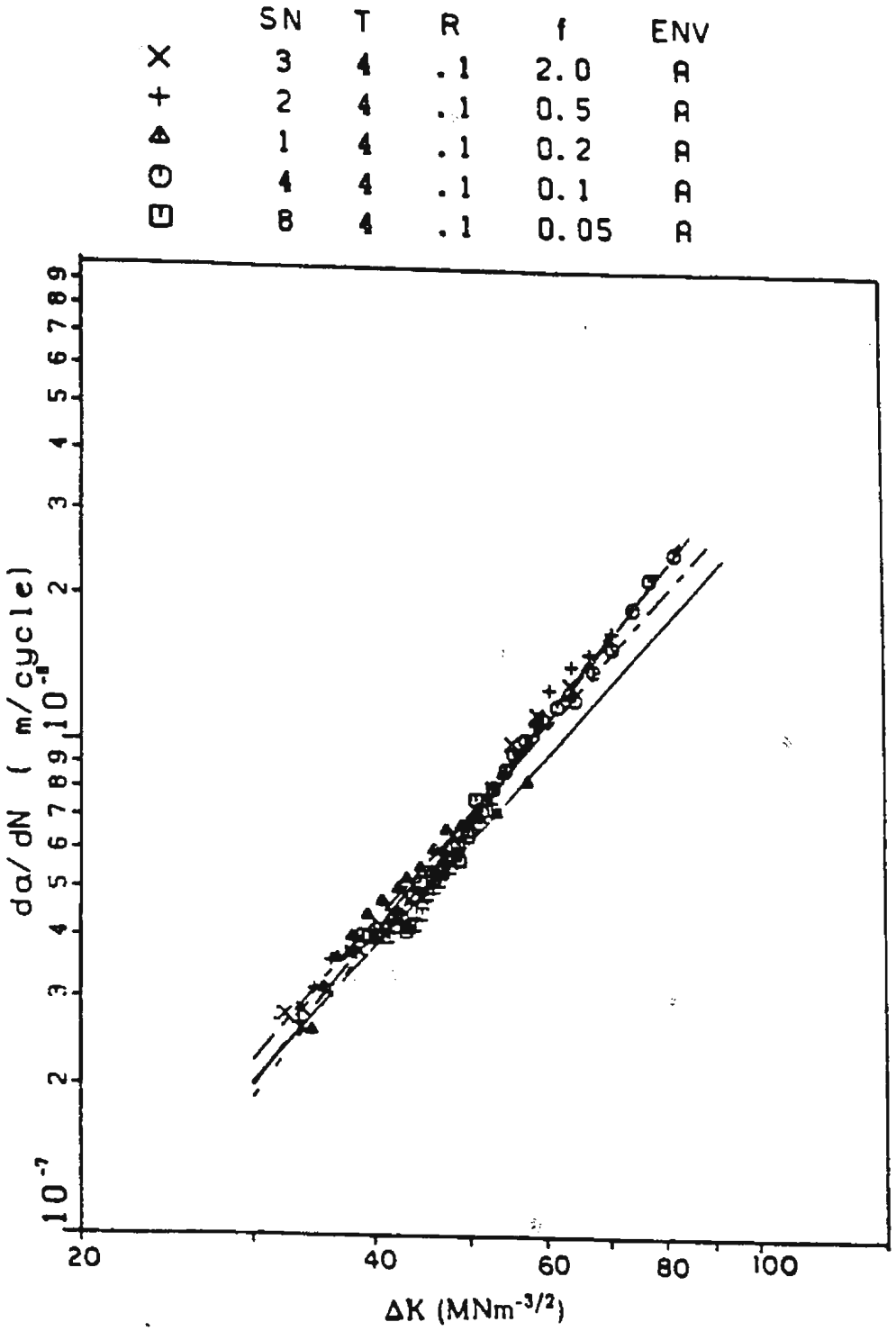

Fig. 6.13 Effect of frequency on fatigue crack-growth-rates in air: T = 4°C, R = 0.1 and f = 0.05 to 2.0 Hz.

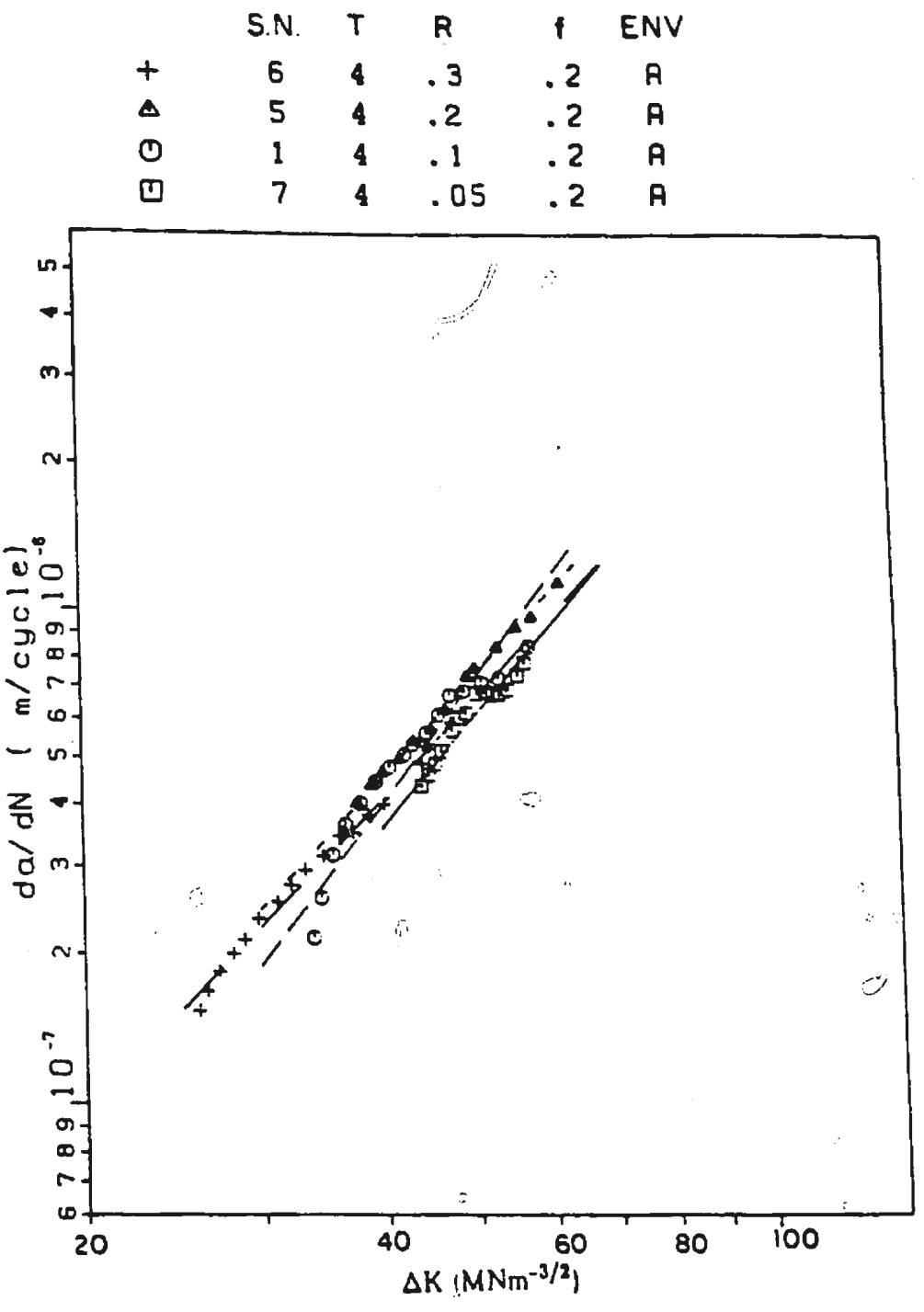

Fig. 6.14 Effect of load ratio on fatigue crack-growth-rates in air: T = 4°C, f = 0.2 Hz and R = 0.05 to 0.3.

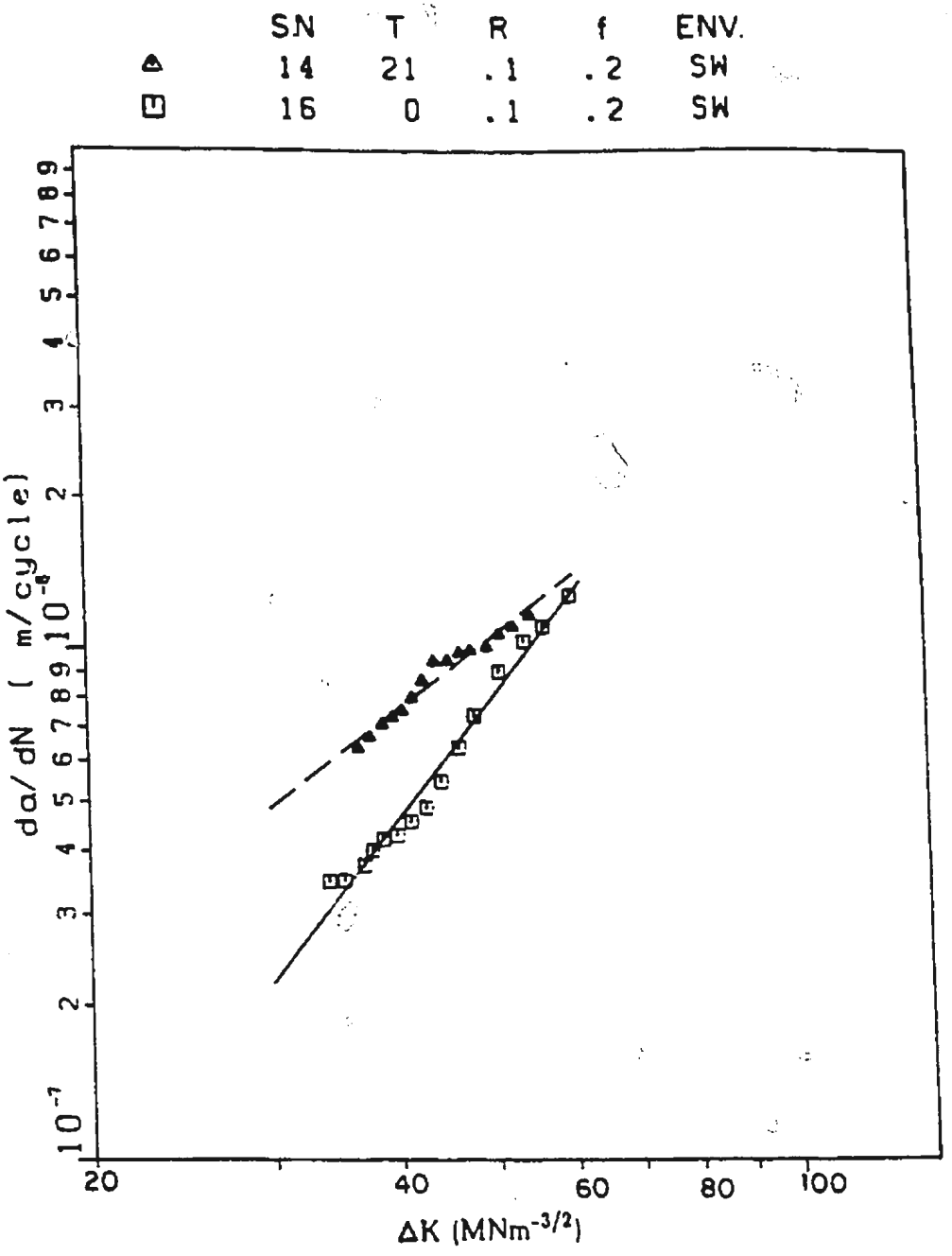

Fig. 6.15 Effect of temperature on fatigue crack-growth-rates in sea water: T = 0 and 21°C, R = 0.1 and f = 0.2 Hz.

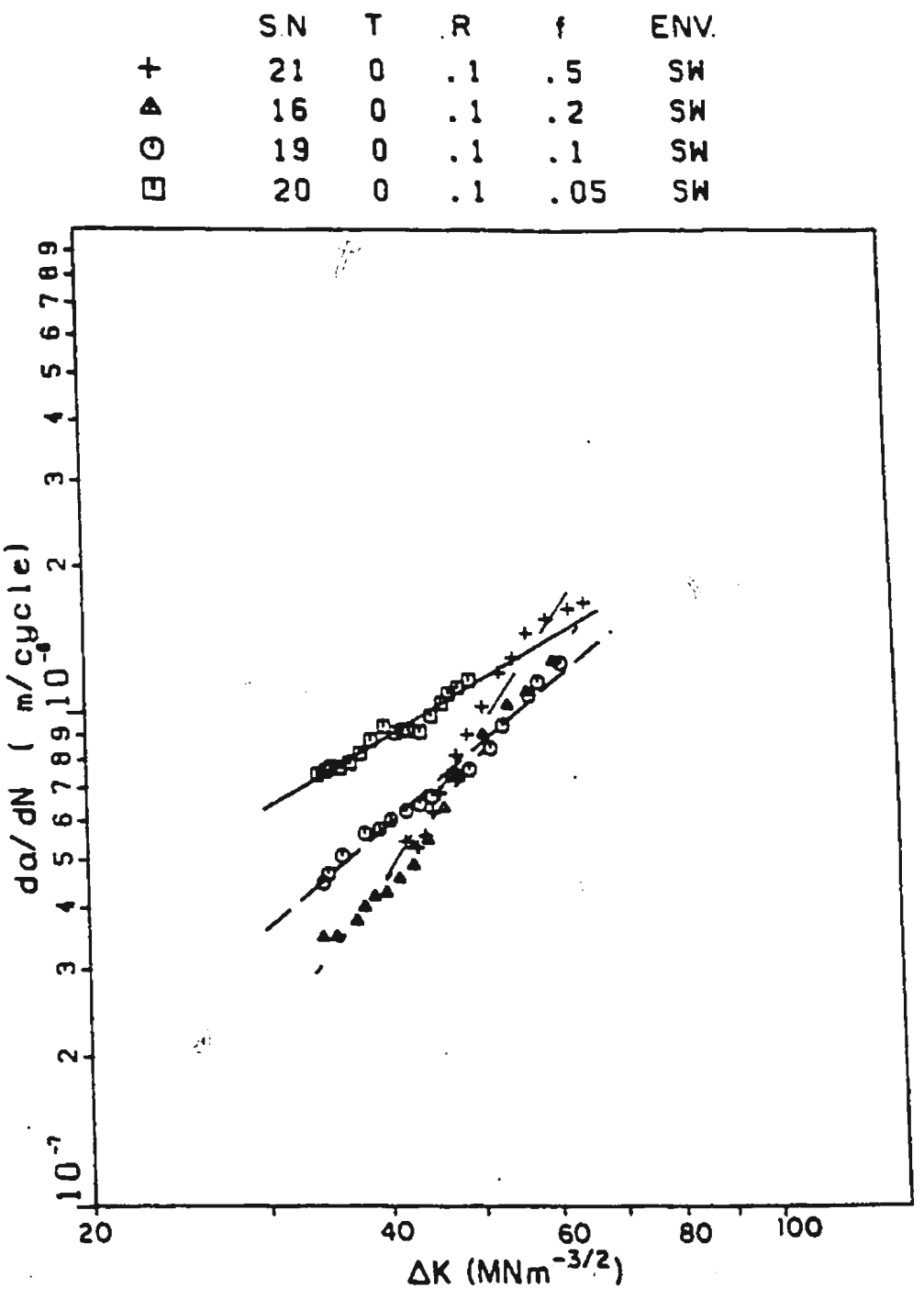

Fig. 6.16 Effect of frequency on fatigue crack-growth-rates in sea water: T = 0°C, R = 0.1 and f = 0.05 to 0.5 Hz.

is less, whereas at $\Delta K = 35$ $MNm^{-3/2}$ the growth per cycle decreases by 58 percent as the frequency increases from 0.05 Hz to 0.5 Hz, because the environmental action decreases due to shorter crack opening time. Figure 6.17 shows the effect of load ratio on the fatigue-crack-growth-rates in sea water. The effect of the loading wave form on the crack-growth-rates is shown in Fig. 6.18. The crack-growth-rates due to the saw-tooth wave form loading are about 15 percent higher than the rates due to the sinusoidal loading.

6.4.3 Influence of sea water

In Fig. 6.19 the results of the tests in sea water (at $R = 0.1$ and $f = 0.05$ Hz) are compared with the results of the tests carried out in air. This figure shows a significant influence of the environment with a crack-growth-rate in sea water up to 2.7 times as high as in air at $\Delta K = 35$ $MNm^{-3/2}$ and $T = 0$ to 4°C. This may be due to the effect of anodic dissolution as well as the hydrogen embrittlement. At high ΔK range, crack propagation rate is so fast that the mechanical cracking dominates the hydrogen embrittlement and anodic dissolution effects; hence the influence is less. As the frequency increases from 0.05 Hz to 0.5 Hz at the 0.1 load ratio, the influence of sea water on crack-growth-rates is seen to be reduced (Figs. 6.19-6.22). At $\Delta K = 35$ $MNm^{-3/2}$, the crack-growth-rates in sea water are 1.71, 1.17 and 1.06 times as high as in air for frequencies of 0.1, 0.2 and 0.5 Hz, respectively. Also, it can be seen that at a frequency of 0.2 Hz, the influence of sea water on crack-growth-rates slightly increases as the load ratio increases (Figs. 6.21, 6.23 and 6.24). Little effects of load ratio on the crack-growth-rates both in air and in sea water are observed.

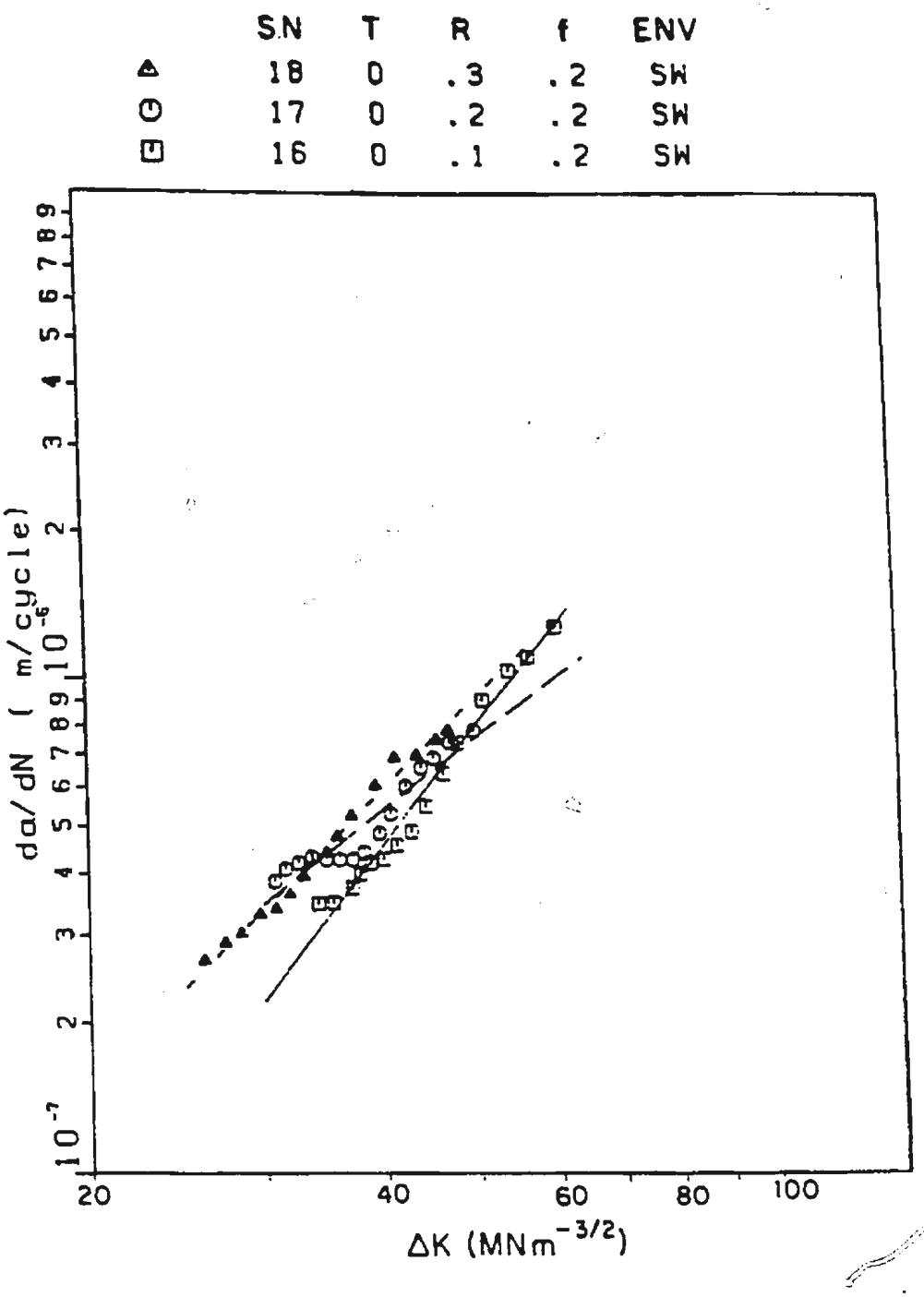

Fig. 6.17 Effect of load ratio on fatigue crack-growth-rates in sea water: T = 0°C, f = 0.2 Hz and R = 0.1 to 0.3.

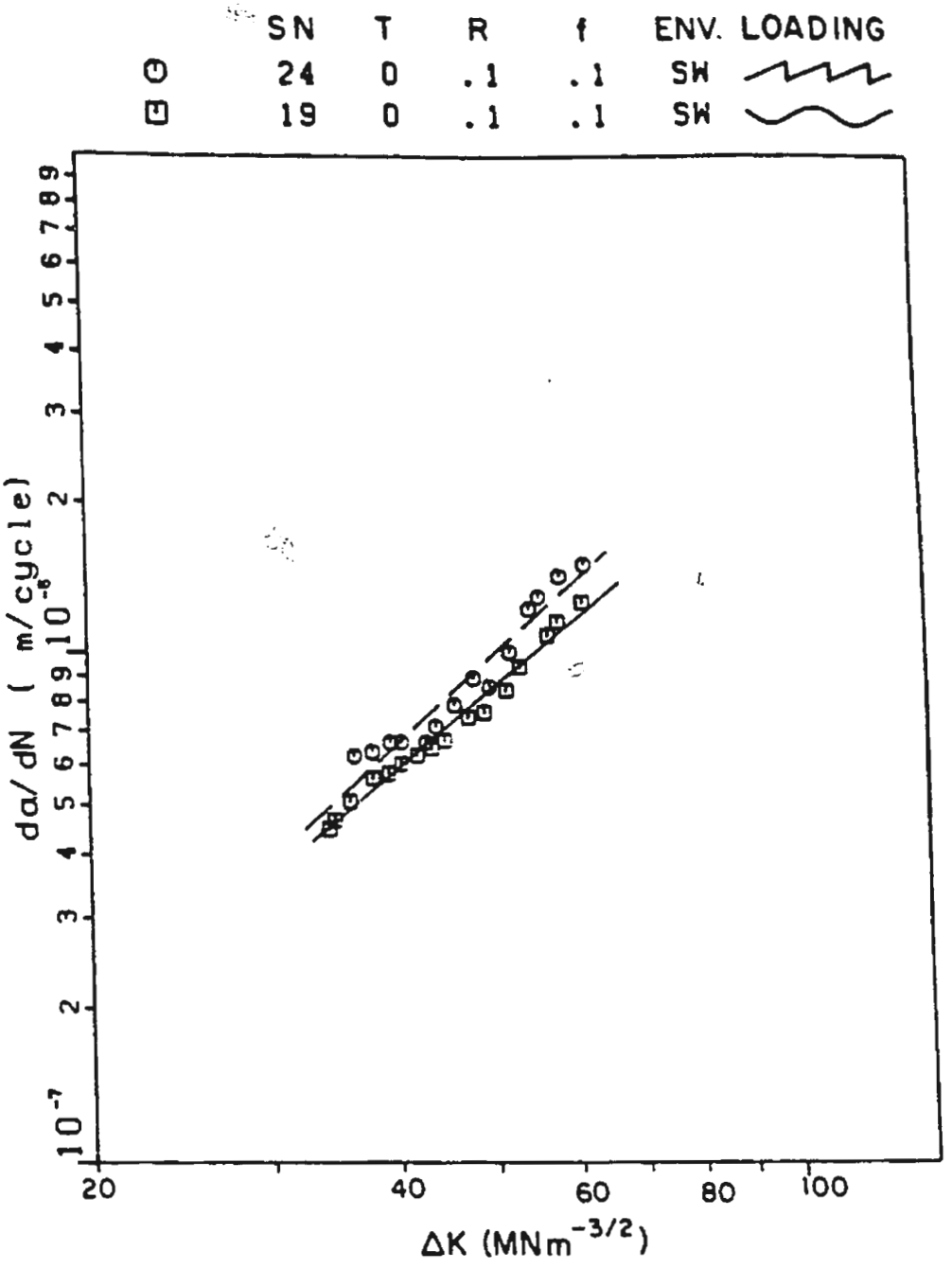

Fig. 6.18 Effect of loading wave form on fatigue crack-growth-rates in sea water: T = 0°C, R = 0.1 and f = 0.1 Hz.

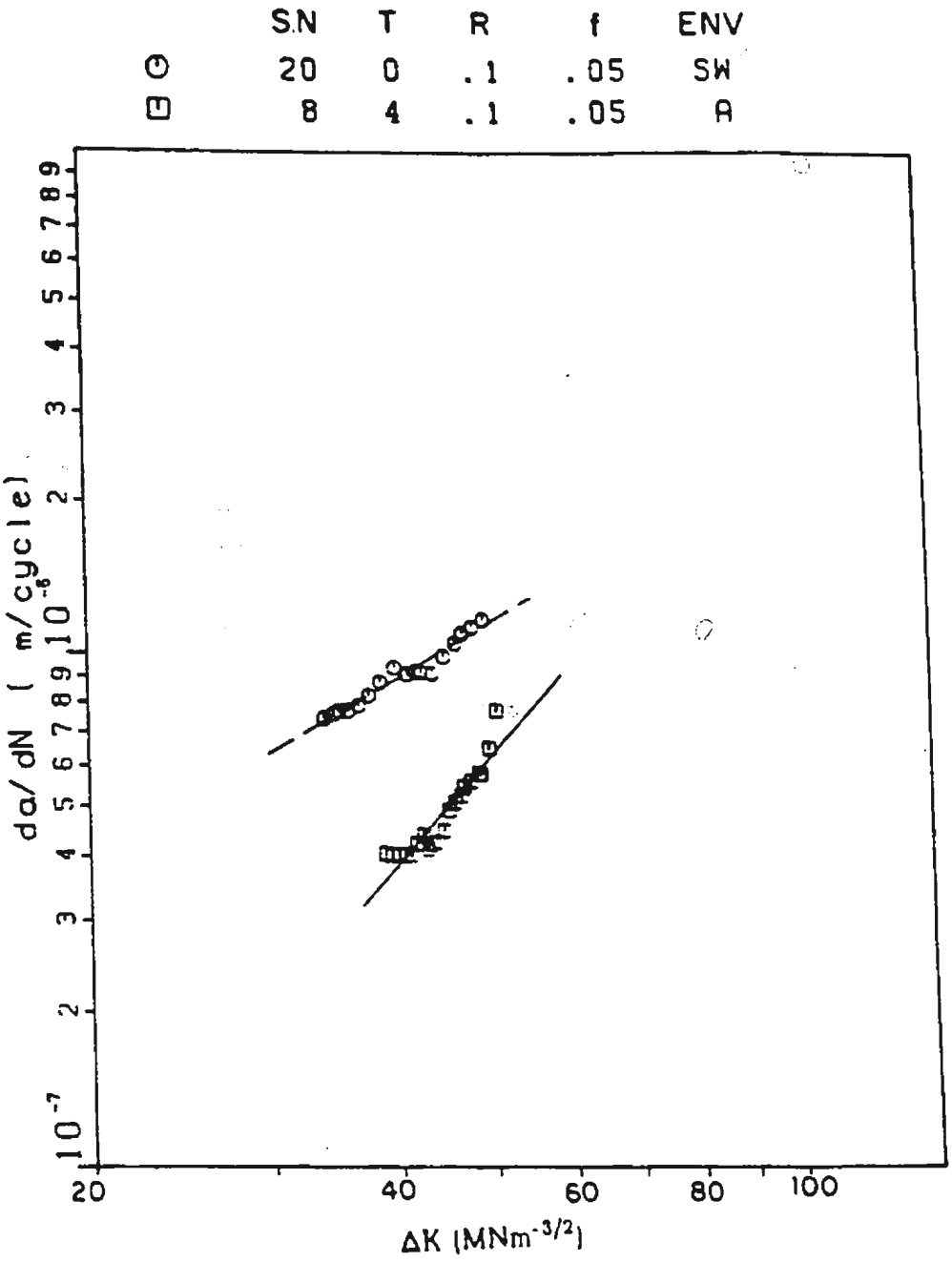

Fig. 6.19 Fatigue crack-growth-rates in air and sea water: R = 0.1 and f = 0.05 Hz.

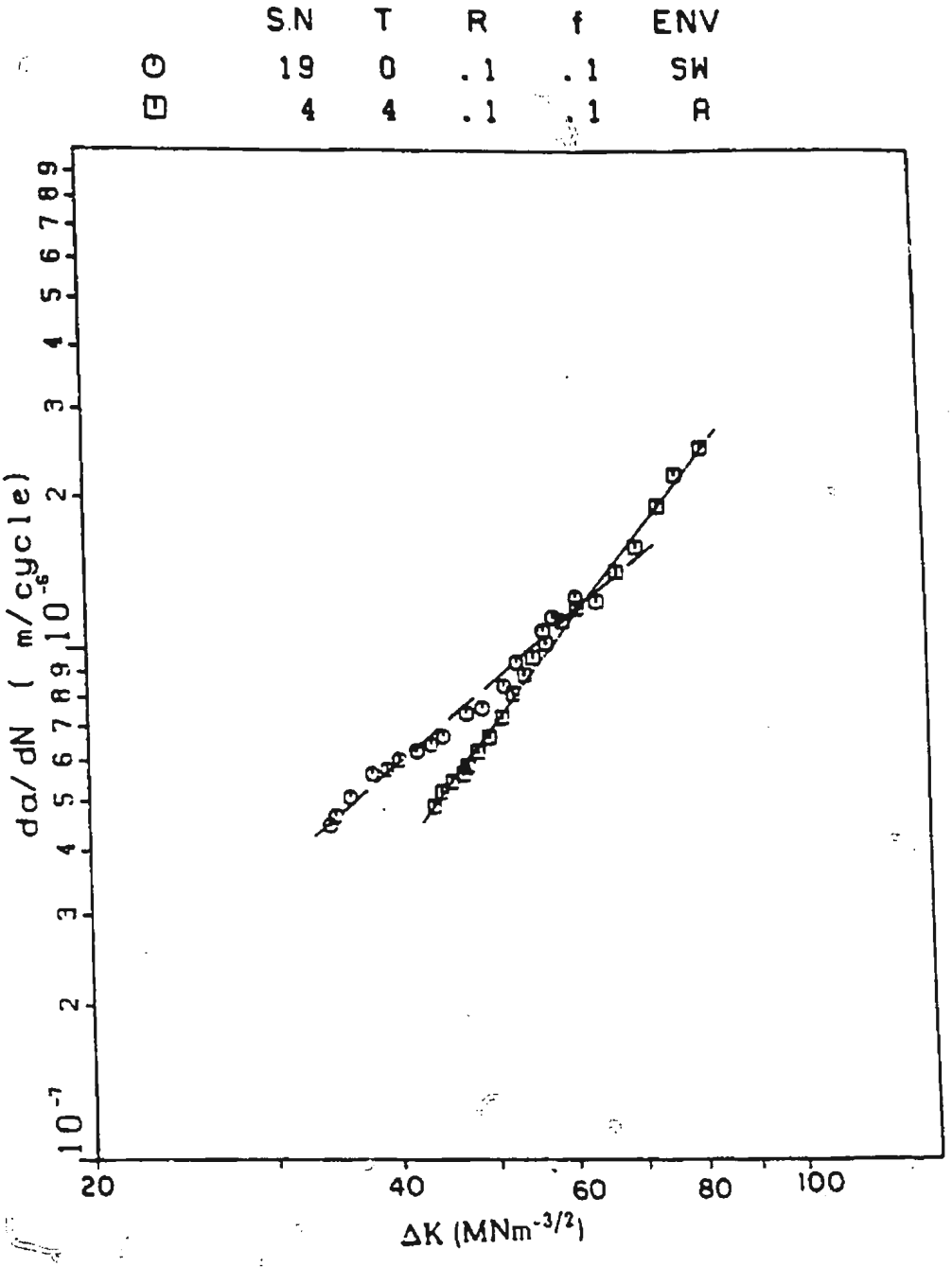

Fig. 6.20 Fatigue crack-growth-rates in air and sea water: R = 0.1 and f = 0.1 Hz.

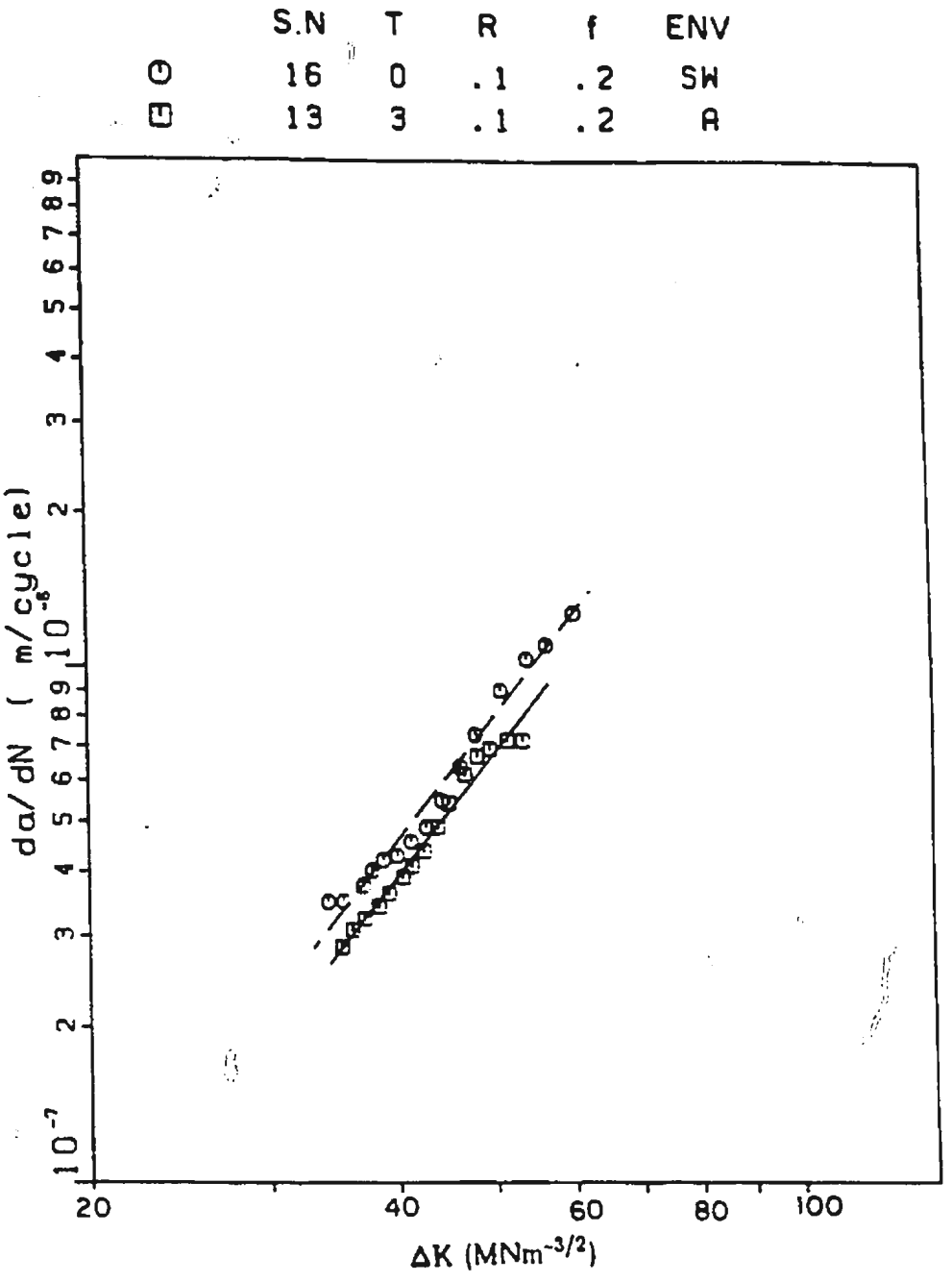

Fig. 6.21 Fatigue crack-growth-rates in air and sea water: R = 0.1 and f = 0.2 Hz.

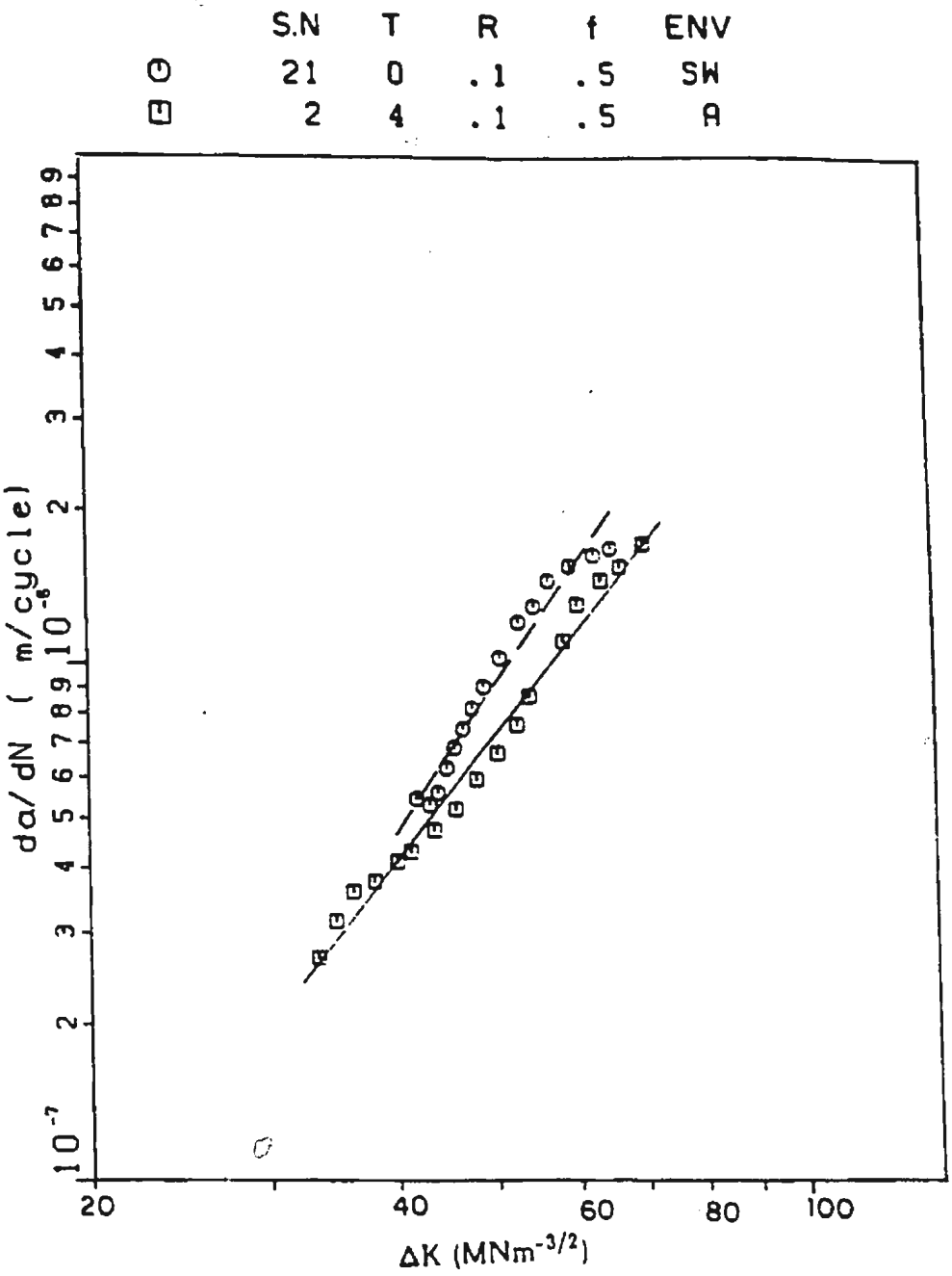

Fig. 6.22 Fatigue crack-growth-rates in air and sea water: R = 0.1 and f = 0. 5 Hz.

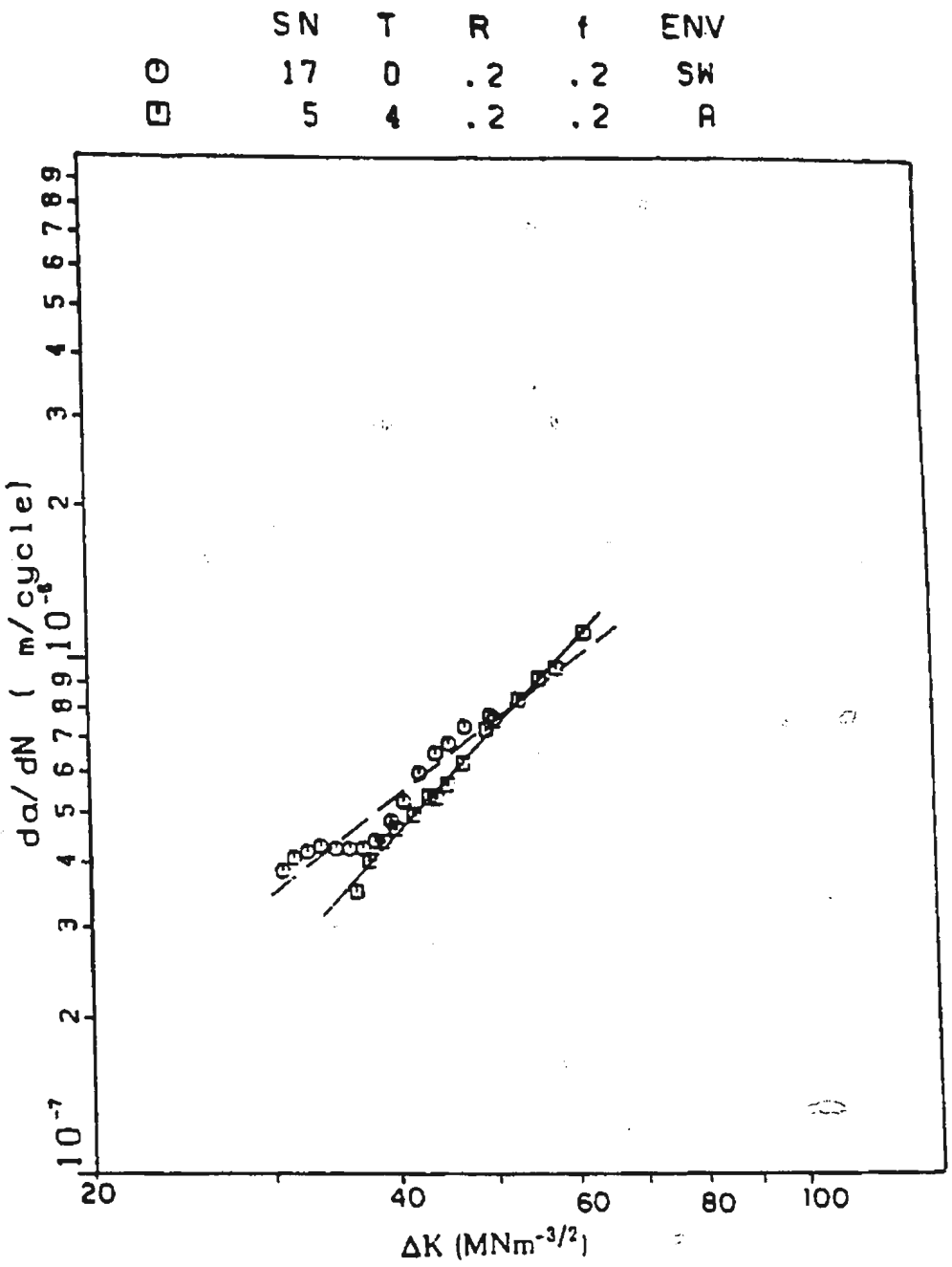

Fig. 6.23 Fatigue crack-growth-rates in air and sea water: R = 0.2 and f = 0.2 Hz.

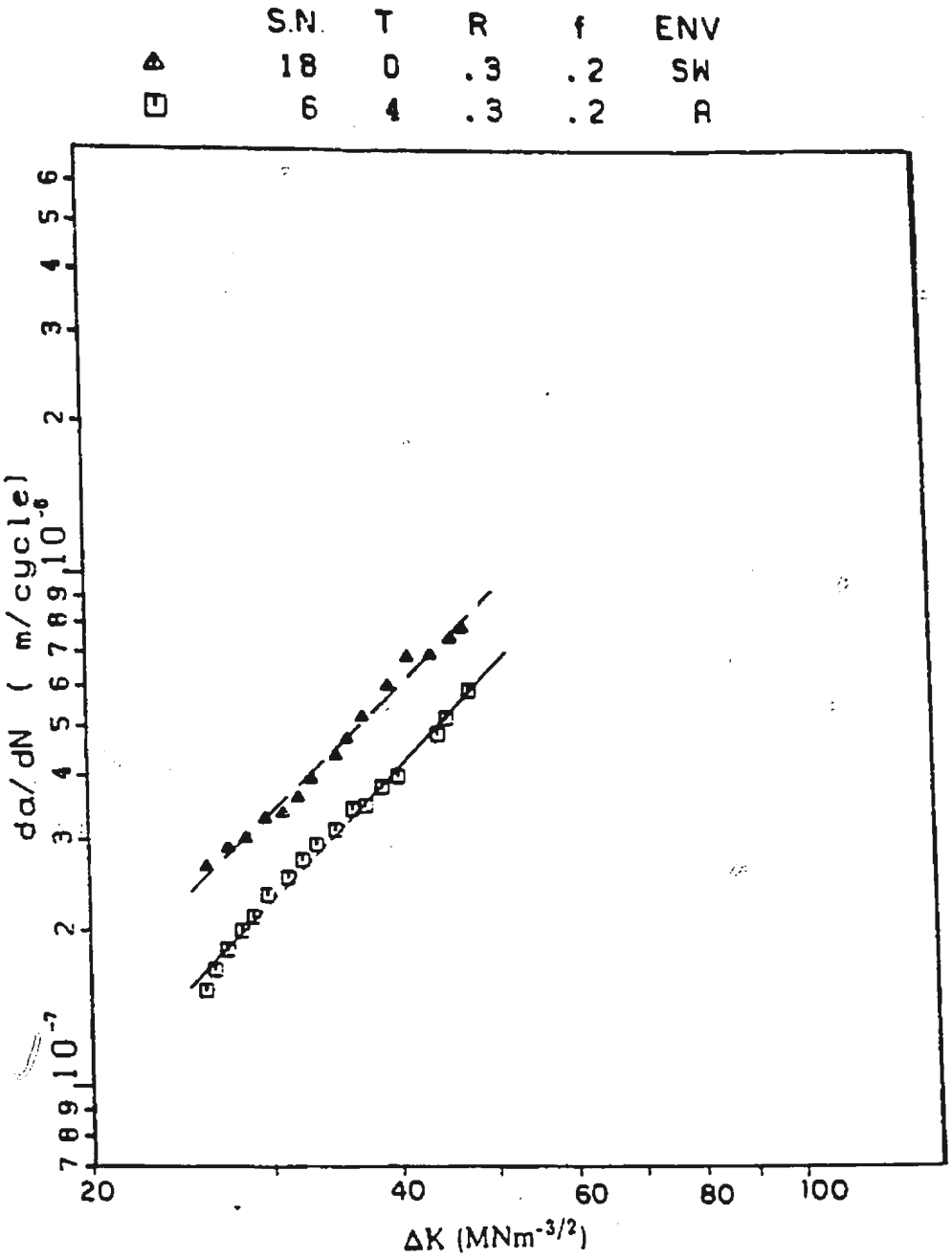

Fig. 6.24 Fatigue crack-growth-rates in air and sea water: R = 0.3 and f = 0.2 Hz.

6.4.4 Comparison with published results

In Fig. 6.25 the result of the test performed in air at R = 0.05 during the present investigation is compared with the results obtained by Vosikovsky and Rivard(1981) for X-65 pipe-line steel at R = 0.05 and by Scholte and Wildschut(1981) for Euronorm 113-72 Grade Fe E355 KT steel at R = 0.1. The figure shows there is a good agreement with the reported results. The fatigue crack-growth-rate in sea water at R = 0.05 and f = 0.2 Hz is compared with other published results (Thorpe et al 1982, Vosikovsky et al 1983) in Fig. 6.26. The difference in results is probably due to the artificial sea water as well as to the different materials used in the other two investigations. The crack-growth-rate in sea water is about a factor of 2.7 higher than in air, which shows good agreement with the results obtained by Scholte and Wildschut (1981), by Johnson et al (1978) and by Vosikovsky et al (1983). The reduction in the growth-rate in sea water by 1.7 times as the temperature is reduced from 21°C to 0°C is comparable with results reported by Vosikovsky et al (1983). During tests in sea water at R = 0.3, a slightly higher crack-growth-rate is obtained than at R = 0.1. This is in accordance with results obtained by other investigators (Johnson et al 1978, Vosikovsky 1980, Vosikovsky et al 1983). As shown in Fig. 6.27, a slight increase in 'm' with a reduction in 'C' is observed during the fatigue-crack propagation. The relation $C = 2 \times 10^{-6} / (78.029)^{m}$ is obtained from the base metal results, which is similar to the relation shown by Lieurade (1985) for E36-Z steel. This relationship appears to be a basic relationship for CSA G40.21 M 350 WT steel, except in the lower crack growth rate region.

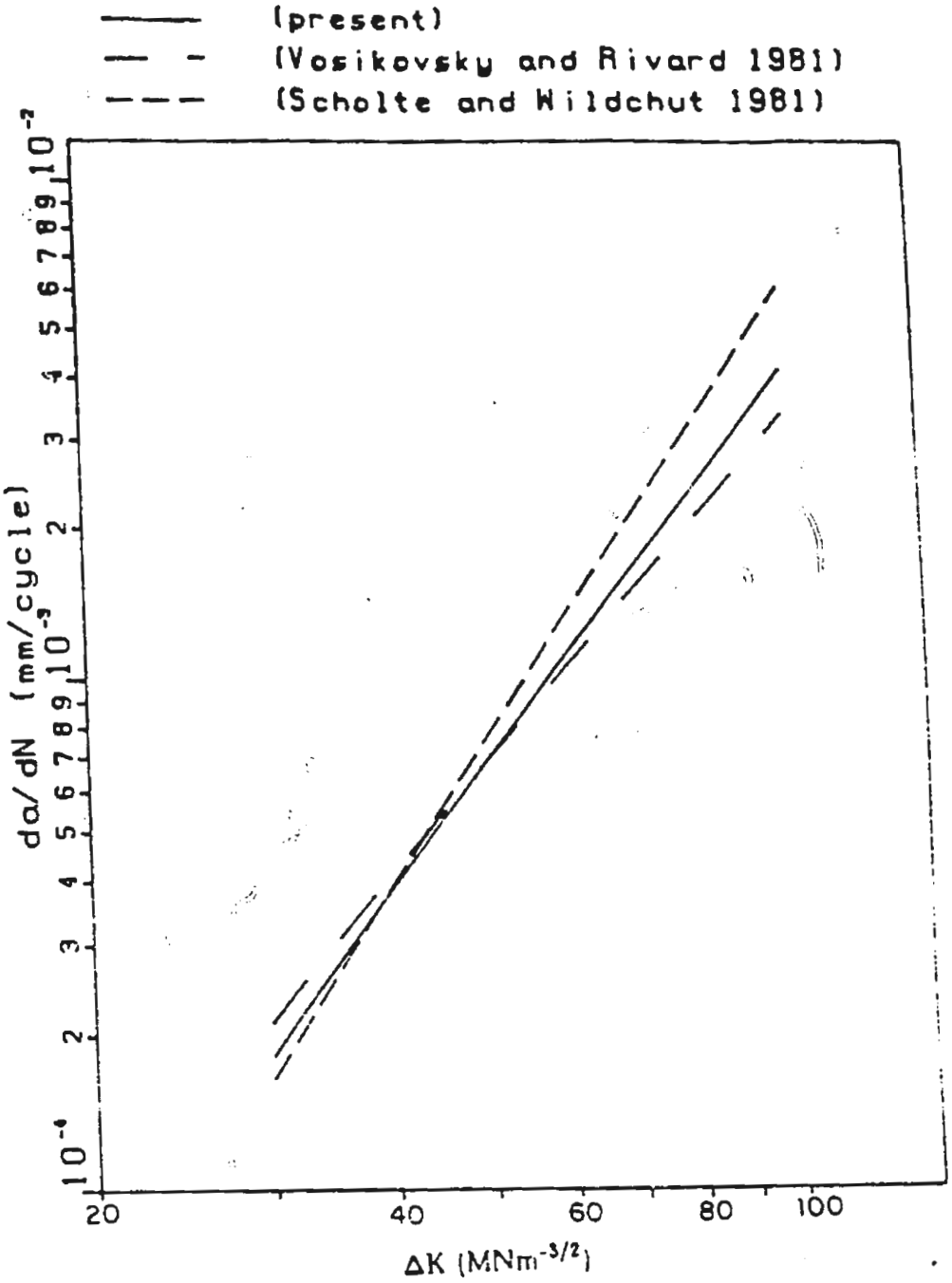

Fig. 6.25 Comparison of fatigue crack-growth-rate in air with other published results.

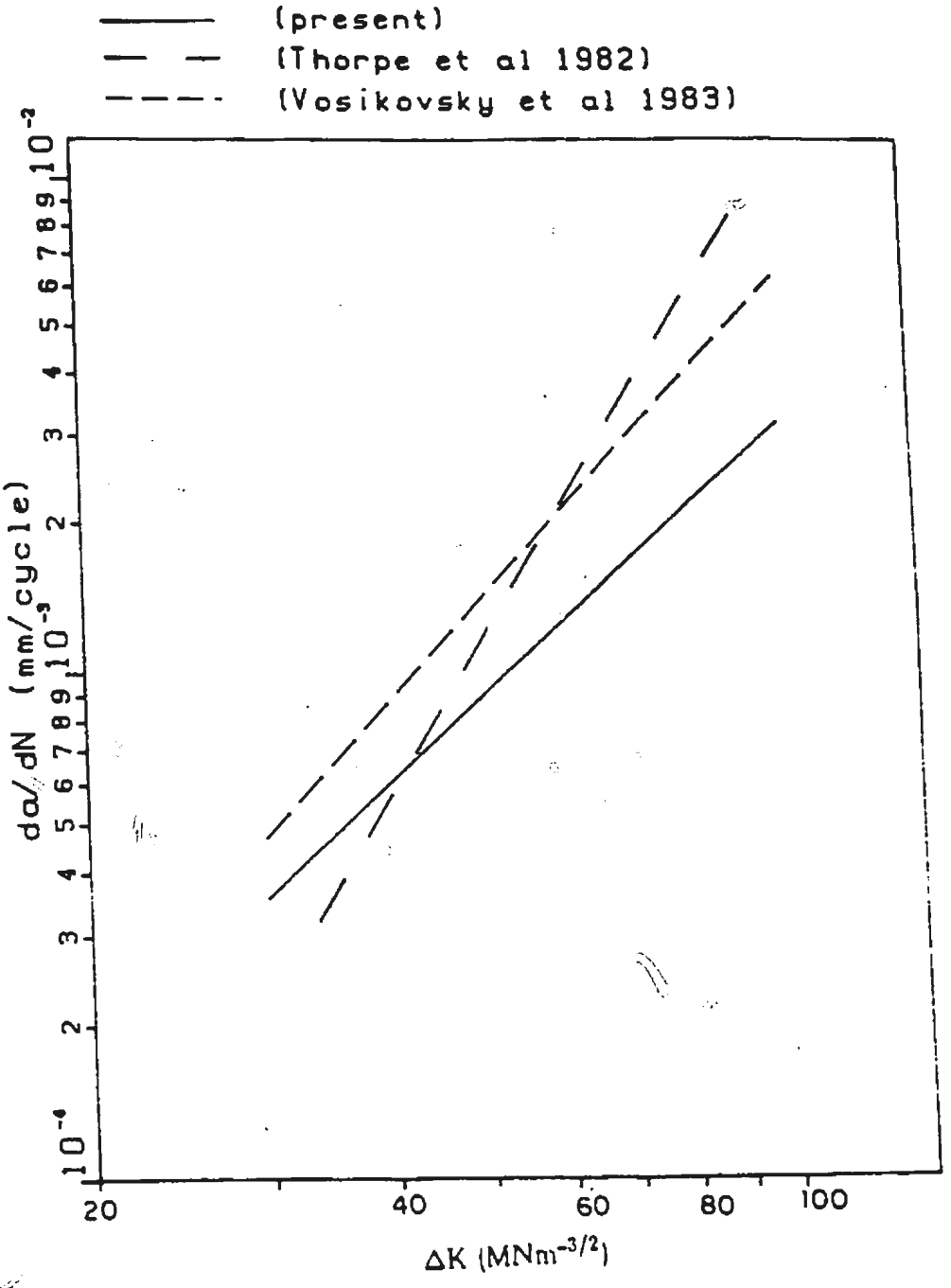

Fig. 6.26 Comparison of fatigue crack-growth-rate in sea water with other published results.

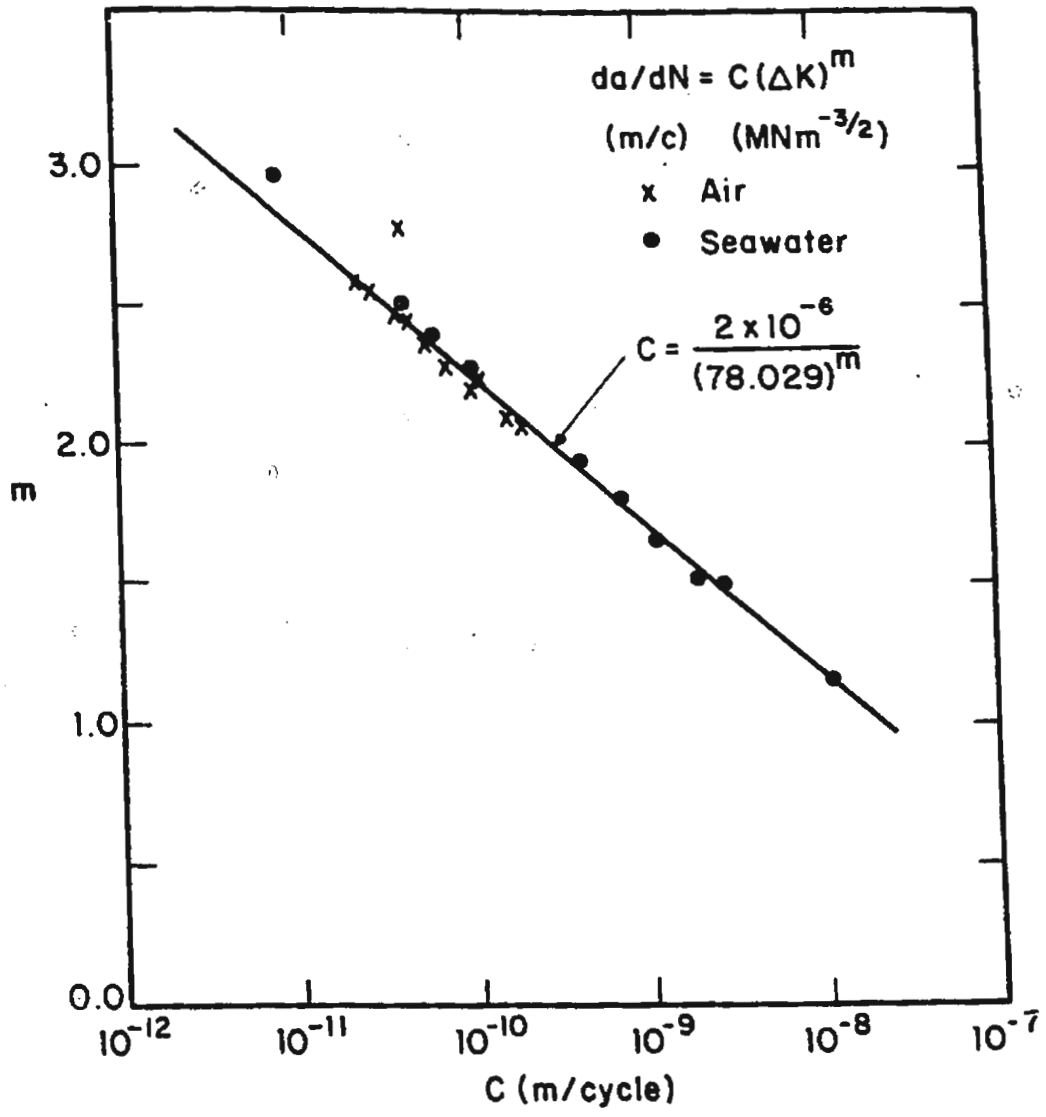

Fig. 6.27 Variation of m versus C.

CHAPTER 7

FATIGUE LIFE ESTIMATION

7.1 Introduction

Observations of marine and offshore structures during service tell us that cracks may be present as initial production cracks and/or as growing fatigue cracks. These cracks are likely to have a significant influence on the strength of tubular members; this effect is not considered in today's common design practice. The traditional approach to the design of offshore tubular structural components subjected to cyclic loading has utilized S-N (stress range, S, versus number of cycles to final failure, N) data. The method assumes that the 'hot spot stress' characterizes the tube stress field during the entire growth of a crack from start of life to failure and 'failure' has three definitions: viz., N1 corresponding to the first indication of cracking (by visual measurement or strain gauges), N2 corresponding to through tube wall cracking and N3 corresponding to the end of test (considerable reduction in stiffness).

Apart from this assumption, the S-N curve has a number of other limitations. Data have to be extrapolated to cover the very high cycle range or to allow for time dependent secondary effects, like corrosion. Moreover, the S-N approach does not separate out crack initiation and cannot be applied to the determination of the life-expectancy of a tubular joint with a crack-like defect of a known size.

So there is no clear way of calculating the fatigue life without understanding the fatigue mechanism. Hence a more comprehensive model of fatigue growth in tubular joints must be developed. This chapter presents the application of linear elastic fracture mechanics to the fatigue life estimation of a tubular joint.

7.2 Linear Elastic Fracture Mechanics (LEFM) Approach

The generalized Paris' equation (Eqn. 6.5) can be applied to any cracked body in the stable growth region. The effect of a difference in geometry can be incorporated in the solution of the stress intensity factor, K, which describes the stress environment at the crack-tip. For two different geometries of the same material, the stress distribution will be identical if the stress intensity factor, K, is the same. Therefore, once the values of the coefficients C and m in Eqn. 6.5 have been established from laboratory crack propagation tests on small scale specimens, the equation can be applied to tubular joints of the same material having the same fracture mode.

The number of cycles, N, required to propagate the weld toe crack from an initial depth, a_i to a final depth, a_f, is obtained by integrating Eqn. 6.5 as

$$N = \int_{a_i}^{a_f} \frac{da}{C\,(\Delta K)^m} \tag{7.1}$$

This equation contains five distinct parameters, i.e., (i) the initial weld toe defect size, a_i, (ii) the depth, a_f, of the crack defining failure of the joint, (iii) the variation of the stress intensity factor range, ΔK, for the joint with an embedded

moving crack front, (iv) the coefficient, C and (v) the coefficient, m, relating the crack-growth-rate to the stress intensity factor range of the material for various environmental conditions. Coefficients C and m are obtained from small scale tests and have been discussed in the previous chapter. Various factors which can influence the prediction of fatigue life based on LEFM approach are (a) magnitude of the residual stresses present at the weld toe, (b) reentrant angle of the weld, (c) size of the plastic zone and (d) initial defect size. In this study, except the initial defect size all the other effects have been neglected.

7.2.1 Initial defect size and failure depth

To date, only a moderate effort has been made to study the effect of crack initiation at welds on the fatigue life of offshore structures. Since the initial defect size is comparable with the size of the plastic zone size, the linear elastic fracture mechanics conditions will not apply until the crack has progressed some distance. Engesvik(1982) has suggested that the size of this region of plasticity is of the same order as the typical grain size, i.e., approximately 0.01 mm, and that the initial crack size, a_i should be greater than the plastic zone size. Based on the relationship between initial defect size, plate thickness and weld sizes in a fillet welded joint, reported by Burdekin(1981), the initial weld toe defect depth, a_i, can be assumed to be 1 mm for a 32 mm thick chord wall.

The choice of failure life is largely determined by the requirement. In the design of non-redundant structures, no loss of stiffness can be tolerated. This limits life

to N2. In a redundant structure N3 is frequently employed. However, for inspection, it is necessary to find a crack so that it can be repaired before reaching these failure sizes. The aim here may be to limit the crack size corresponding to a life of N1; however it is very difficult to know exactly to what extent offshore inspection could find such a crack in the large welded areas present in offshore structures. As far as crack growth analysis is concerned, it would be difficult to follow crack behaviour as break through of the chord wall occurs at the weld toe. Taking all these into account, the final depth, a_f, of the weld toe crack should be taken as the chord wall thickness, T.

7.2.2 Fatigue life

Observations suggest that fatigue cracks present in the tubular joints grow steadily through the wall thickness at a fairly constant rate (Dover and Dharmavasan 1982, Gowda 1983). Since the loading in the brace is either an axial load (tensile) or an in-plane bending load, the weld toe crack propagation will be predominantly in the opening mode. So it would be more realistic to represent the part-through-thickness crack-growth-rate for a tubular joint using the mode-I stress intensity factor range corresponding to an embedded weld toe crack having a maximum depth equal to one half of the chord wall thickness. The stress intensity factor range can be expressed in terms of the stress intensity factor of the cracked tubular joint as follows

$$\Delta K_I = (1 - R) K_I \qquad (7.2)$$

It should be noted that the above equation is valid only for positive R, i.e. when

the loading is tensile to tensile. When R is negative (loading is tensile to compressive), crack closure takes place during the compressive portion of the loading cycle and only the tensile portion is responsible for the crack propagation. So for $R < 0$, ΔK_I will be K_I only. The number of loading cycles to failure, N, is given by

$$N = \frac{T - a_i}{C\,(1 - R)^m\, K_I^m} \tag{7.3}$$

where C and m are the crack-growth parameters obtained from CT specimen tests, T is chord wall thickness, a_i is the initial defect size, R is the load ratio of the constant amplitude loading cycle and K_I is the analytically obtained opening mode stress intensity factor corresponding to the maximum fluctuating load.

7.3 Results and Discussion

The hot spot stress ranges are calculated using the peak stress obtained from the analysis as the maximum stress and the minimum stress (calculated from the peak stress using the load ratio) for each case. The hot spot stresses and the stress intensity factors for other load magnitudes for the joint can be calculated from the present linear analysis results. The estimated through-thickness-cracking lives of a tubular T-joint with 1 mm initial weld toe defect depth, due to axial as well as in-plane bending loads in both air and sea water, are tabulated in Tables 7.1 - 7.4. The life of the joint, for a particular temperature, load ratio and frequency, is calculated using the corresponding C and m values from Table 6.4.

Table 7.1 Estimated fatigue life of tubular T-joint in air due to axial load.

S.No.	Hot spot stress range (MN/m^2)	Temp., T (°C)	Freq., f (Hz)	Load ratio, R	Number of cycles, N
1	275.5	4	0.2	0.1	4.35E+04
2	275.5	4	0.5	0.1	4.29E+04
3	275.5	4	2.0	0.1	4.32E+04
4	275.5	4	0.1	0.1	4.49E+04
5	244.8	4	0.2	0.2	5.47E+04
6	214.2	4	0.2	0.3	7.96E+04
7	290.8	4	0.2	0.05	4.55E+04
8	275.5	4	0.05	0.1	4.91E+04
9	275.5	-5	0.2	0.1	4.21E+04
10	275.5	-10	0.2	0.1	4.44E+04
11	275.5	-15	0.2	0.1	4.43E+04

Table 7.2 Estimated fatigue life of tubular T-joint in air due to in-plane bending load.

S.No.	Hot spot stress range (MN/m^2)	Temp., T (°C)	Freq., f (Hz)	Load ratio, R	Number of cycles, N
1	77.7	4	0.2	0.1	2.86E+06
2	77.7	4	0.5	0.1	2.44E+06
3	77.7	4	2.0	0.1	1.66E+06
4	77.7	4	0.1	0.1	2.95E+06
5	69.1	4	0.2	0.2	1.70E+06
6	60.5	4	0.2	0.3	2.26E+06
7	82.1	4	0.2	0.05	1.84E+06
8	77.7	4	0.05	0.1	1.77E+06
9	77.7	-5	0.2	0.1	2.27E+06
10	77.7	-10	0.2	0.1	2.15E+06
11	77.7	-15	0.2	0.1	2.13E+06

Table 7.3 Estimated fatigue life of tubular T-joint in sea water due to axial load.

S.No.	Hot spot stress range (MN/m^2)	Temp., T (°C)	Freq., f (Hz)	Load ratio, R	Number of cycles, N
1	275.5	21	0.2	0.1	2.94E+04
2	275.5	0	0.2	0.1	3.87E+04
3	244.8	0	0.2	0.2	4.91E+04
4	214.2	0	0.2	0.3	5.55E+04
5	275.5	0	0.1	0.1	3.64E+04
6	275.5	0	0.05	0.1	2.69E+04
7	275.5	0	0.5	0.1	3.44E+04
8	214.2	0	0.5	0.1	5.83E+04

Table 7.4 Estimated fatigue life of tubular T-joint in sea water due to in-plane bending load.

S.No.	Hot spot stress range (MN/m^2)	Temp., T (°C)	Freq., f (Hz)	Load ratio, R	Number of cycles, N
1	77.7	21	0.2	0.1	0.33E+06
2	77.7	0	0.2	0.1	2.22E+06
3	69.1	0	0.2	0.2	0.57E+06
4	60.5	0	0.2	0.3	1.28E+06
5	77.7	0	0.1	0.1	0.54E+06
6	77.7	0	0.05	0.1	1.76E+06

The estimated lives are compared in Fig. 7.1 with the experimental data obtained from Dutch T-joint specimens with 32 mm thick chord wall, $\beta = 0.5$ and $\tau = 0.5$ (Irvine 1981c, de Back and Vaessen 1981). The mean line of experimental data reported by Irvine(1981c) was obtained from the fatigue tests on tubular T-joints with 32 mm thick chord wall with various joint parameters, whereas the lives reported by de Back and Vaessen(1981) are for the joints having approximately same parameters as of the present investigation. At higher stress range (in the present case due to axial loading), the estimated lives show good general agreement with the experimental life reported by de Back and Vaessen(1981). Slight underestimation can be justified due to the fact that the initiation life, which is about 30 percent of the crack-through life for this particular joint (de Back and Vaessen 1981) is not taken into account in the life calculation using LEFM.

The estimated lives at lower stress range, induced by in-plane bending load at brace, are not in good agreement with the reported experimental data. The inconsistancy in the results can be explained due to the use of inappropriate coefficients C and m in the life calculation. Because these lives correspond to the lower range of stress intensity factor range, the coefficients C and m should be obtained from the CT specimen's crack-growth-rate data at lower stress intensity factor ranges. Moreover, at lower stress intensity factor ranges, the crack-growth-rate in base metal is higher than that in heat affected zone (Lieurade 1985). As the stress intensity factor range increases, the difference between the base metal and the as-welded condition crack-growth-rates reduces. So the fatigue lives at lower stress intensity factor ranges are underestimated.

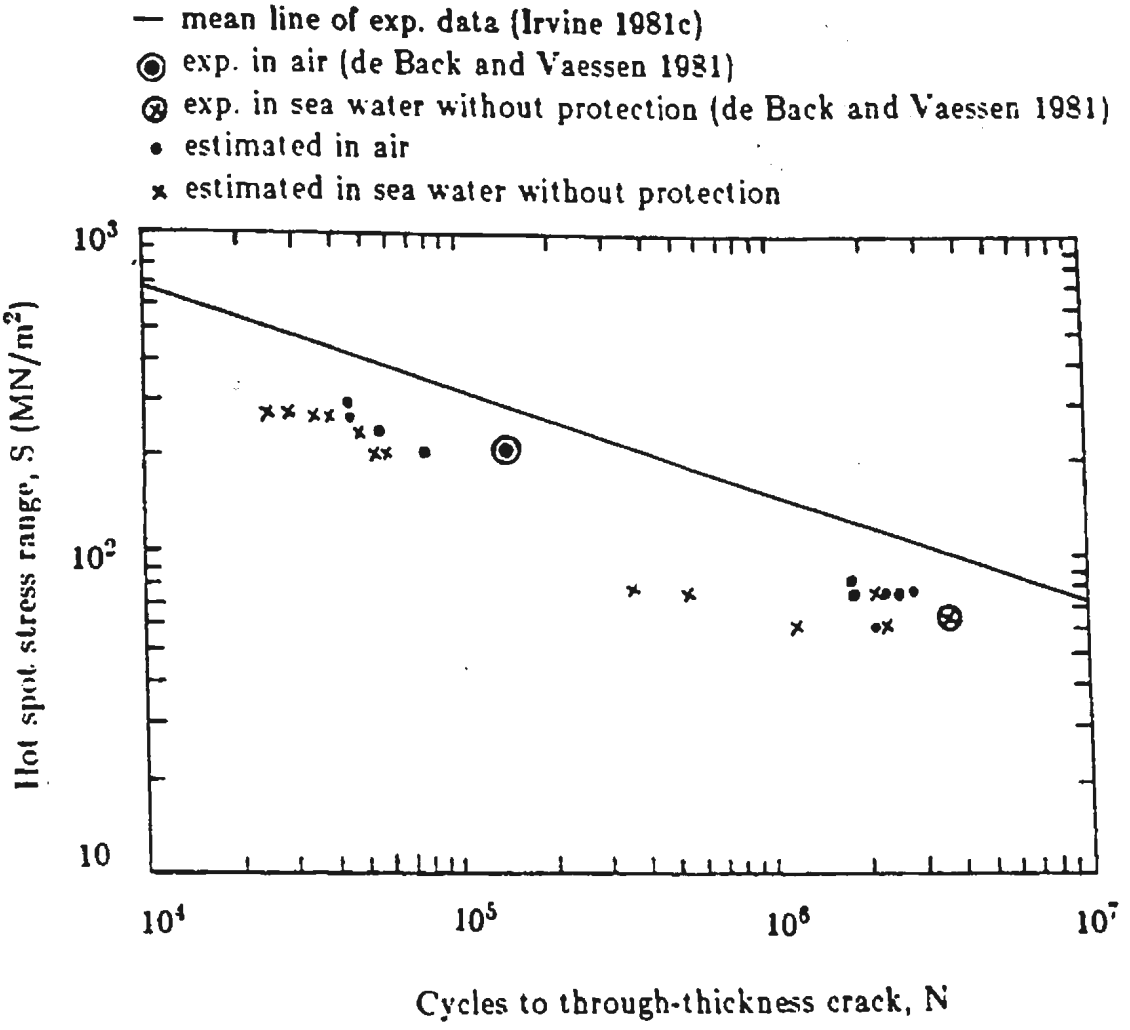

Fig. 7.1 Comparison of estimated fatigue life of tubular T-joint with reported experimental S-N data.

CHAPTER 8

EXPERIMENTAL VERIFICATION

8.1 Introduction

In order to check the stress analysis results generated by the developed computer program as well as the proposed model for predicting the fatigue life of a tubular joint through analytical procedures using crack-growth data from CTS tests, a prototype test is carried out on a large scale tubular T-joint. Joint parameters are given in Table 8.1. The material selected for the fabrication is CSA G 40.21 M 350 WT steel.

For loading purposes, a horizontal self-straining frame is built (Fig. 8.1). The load is applied by a servohydraulic actuator of capacity 3000 KN. The specimen is connected to a load cell by a swivel joint, in order to minimize the load eccentricity. The actuator is supported from the top of the loading frame by a free floating support consisting of springs and rods. The specimen is supported by a saddle assembly at both ends of the chord. Both ends of the chord are bolted on to end plates, which are connected to the loading frame through pin supports.

8.2 Instrumentation

In order to study the strain distribution at the critical regions of the joint during both the static and the fatigue tests, the specimen is extensively strain-gauged, both outside and inside using delta gauges. The exact positions for the strain

Table 8.1 Joint parameters of the specimen tested.

Type of Joint	D (mm)	T (mm)	$\beta = \frac{d}{D}$	$\tau = \frac{t}{T}$	$\gamma = \frac{D}{2T}$	$\alpha = \frac{2L}{D}$
Tee	914	19	0.5	1.0	24.05	6.33

D = Chord diameter
d = Brace diameter
T = Chord thickness
t = Brace thickness
L = Length of chord between supports

Fig. 8.1 Test frame.

gauges on the inner surface of the chord are determined using the ultrasound method. One quarter of the chord surface near to the intersection is instrumented with three rows of strain rosette. Moreover, saddle and crown point regions are instrumented for both the chord and the brace sides. The schematic arrangement of the strain gauges on the outer and inner surfaces of the chord is given in Fig. 8.2. Altogether, the specimen is instrumented with 276 strain gauges. The weld toe crack-depth profile is monitored during the fatigue test using a multiple AC potential technique. The spacing of the probes (each consisting of one active pair and reference pair) is varied from 6 mm to 24 mm. Near to the saddle point, a closer spacing of the probes is adopted to ensure that crack initiation is detected and monitored properly. Each active or reference pair consists of two spot-welded copper-coated steel wires. The schematic arrangement of the ACPD probes on the specimen is shown in Fig. 8.3.

8.3 Data Acquisition

Strains (due to static and fatigue loads) and AC potentials (for monitoring the crack depth during the fatigue test) are measured using an automatic data acquisition system, consisting of a MINC 11 computer, a crack micro gauge, Keithley scanners and a strain gauge signal indicator. Strain gauges from the specimen are connected to the strain gauge signal indicator unit via the scanner. The analog signals from the conditioners are transmitted to the computer through A/D convertors. A low current with a high frequency AC field from the crack microgauge is impressed on the specimen at a distance of 400 mm from the weld. The AC probes are connected to the crack microgauge through the

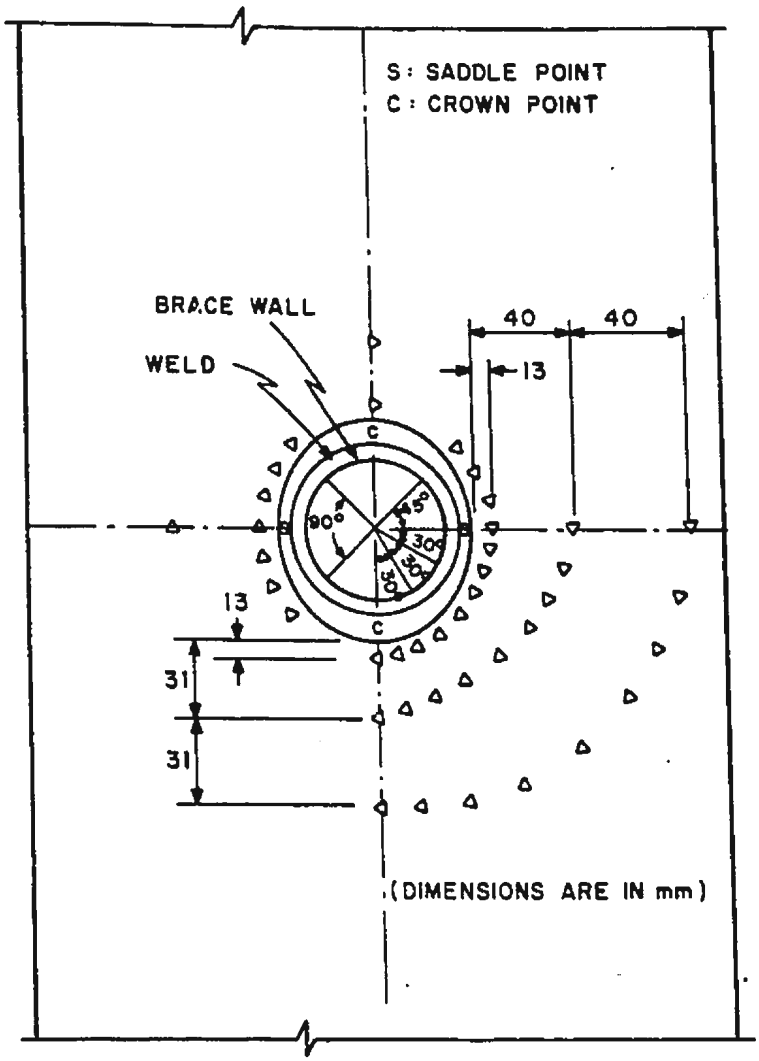

Fig. 8.2 Schematic arrangement of strain gauges on outer and inner surfaces of chord.

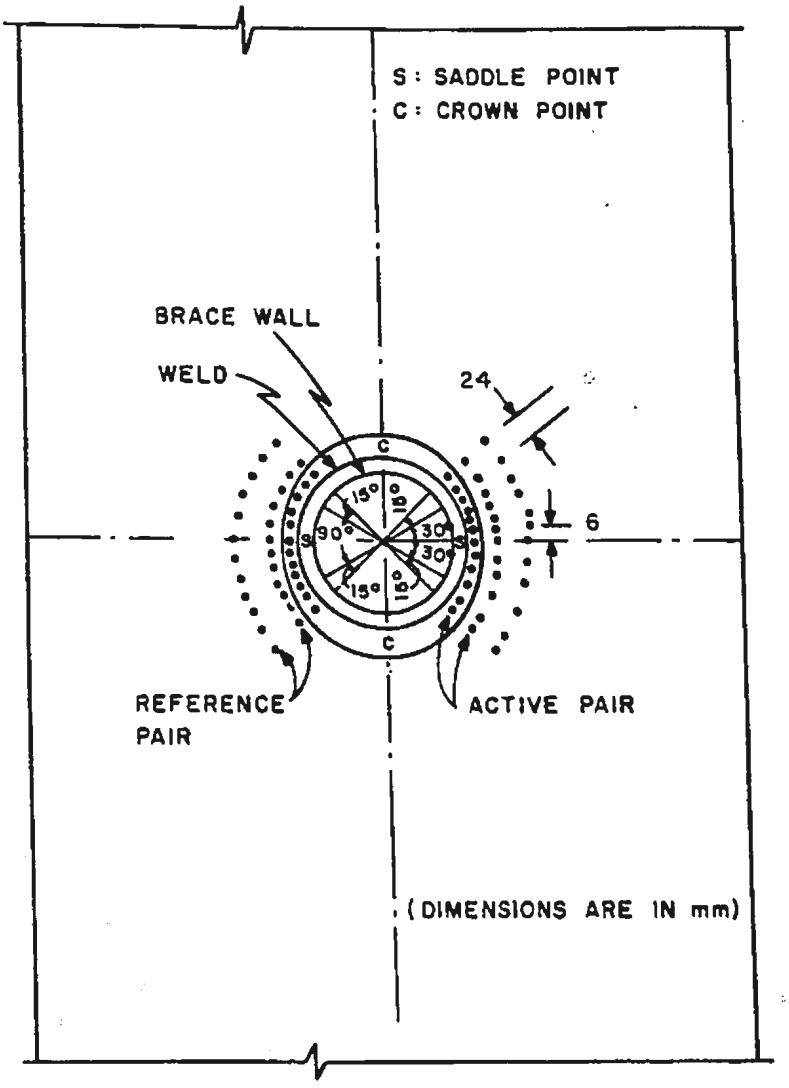

Fig. 8.3 Schematic arrangement of ACPD probes on the specimen.

scanner. The distribution of the AC field along the weld toe is scanned periodically to determine the crack depth growth. The analog signal from the crack microgauge is transmitted to the computer through the A/D converters. The block diagram for the entire data acquisition system is shown in Fig. 8.4.

8.4 Test Procedure

The specimen is loaded in a static test up to a load of 315 KN to determine the stress distribution and the stress concentration factors. The fatigue test is commenced after completion of the static test. The maximum and minimum cyclic loads are selected to obtain a desired hot spot stress range of 250 MN/m^2. The joint is tested under constant amplitude loading at a load ratio, $R = 0.16$, and frequency, $f = 3$ Hz. During the fatigue test, strains and AC fields along the weld are measured periodically in order to monitor the crack growth and the stress redistribution. The entire measurements and the testing procedure are controlled by the computer.

8.5 Results and Discussion

Before the static test, the thickness of the brace wall is measured at three locations, and the wall thickness is found to be non-uniform. The maximum and minimum thicknesses of the brace wall are found to be 20.55 mm and 17.02 mm, respectively. The average thickness is found to be 18.86 mm. The uniaxial strain gauges are mounted on a location at 8 equidistant points around the brace circumference, away from the weld. The variation of uniaxial strain along the brace circumference for two static loads is shown in Fig. 8.5. From the figure, it can be

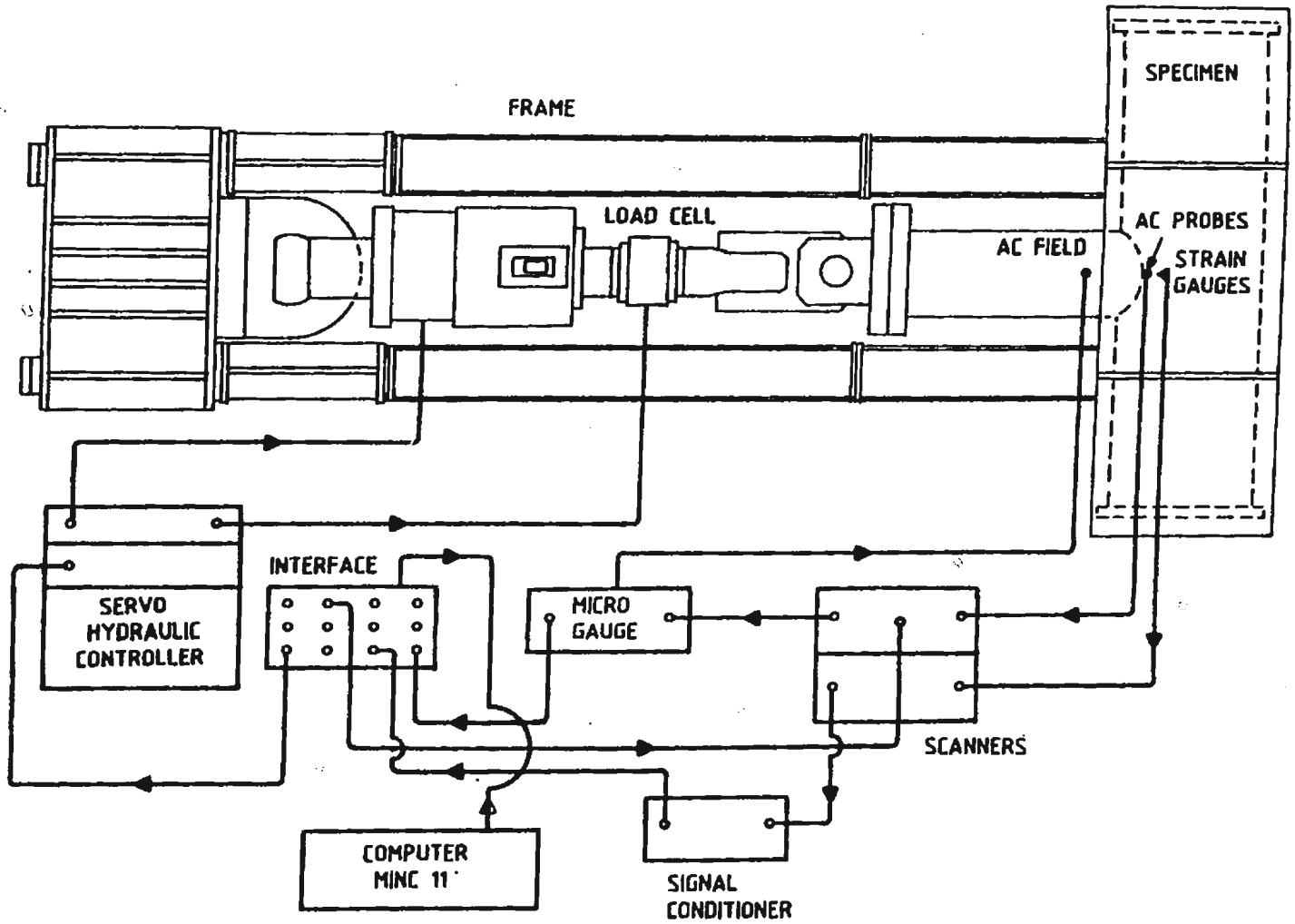

Fig. 8.4 Block diagram for data acquisition system.

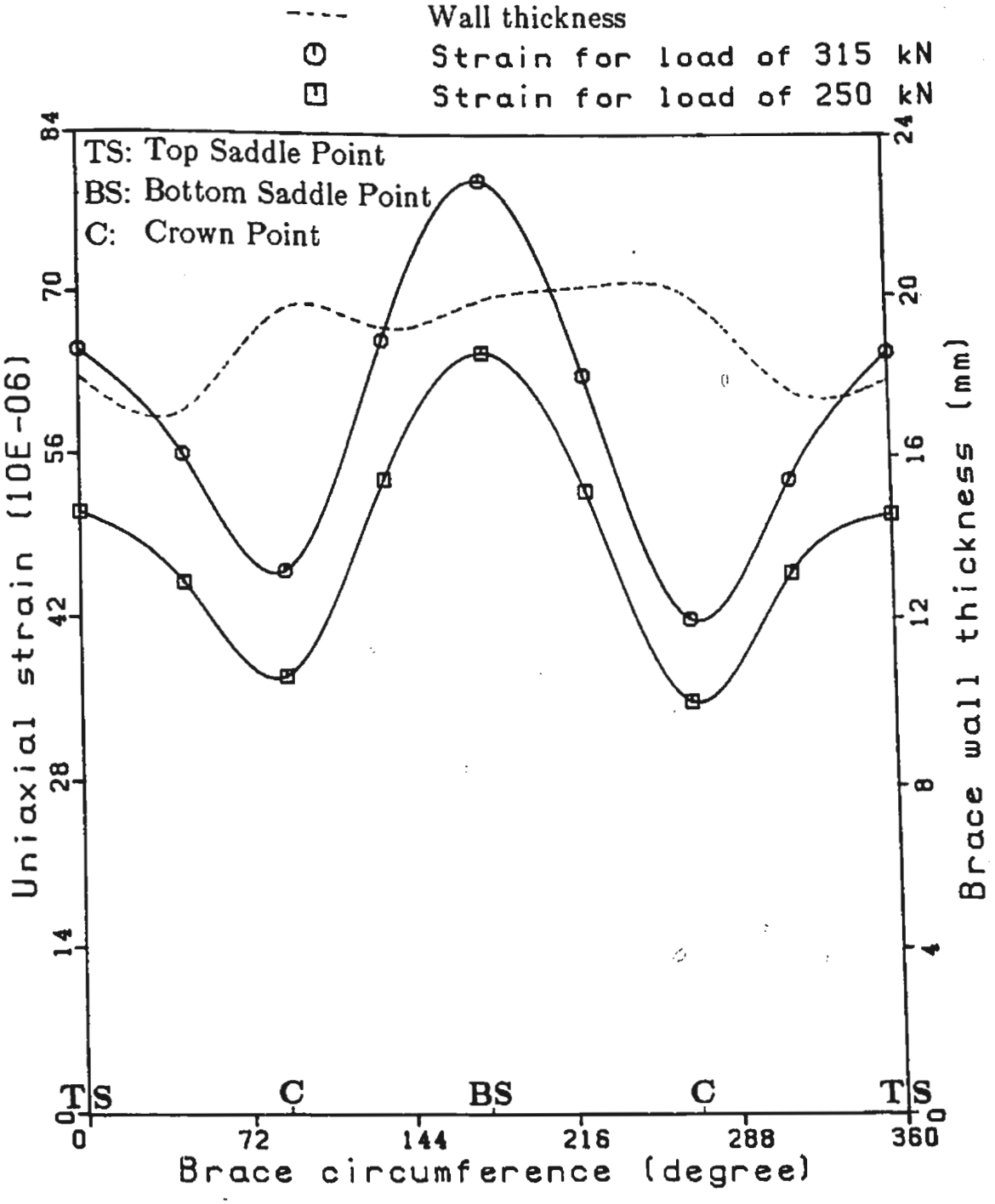

Fig. 8.5 Variation of uniaxial strain and brace wall thickness.

seen that the ratio of maximum to minimum uniaxial strains along the brace surface is about 2. The figure also shows the variation of wall thickness along the brace circumference.

Since the load acting on the joint is axial, only quarter of the joint is modelled for analysis from symmetry consideration. The joint is discretized using 3-D elements. In order to find out the mode I crack-tip stress intensity factor, corresponding to a part-through-thickness weld toe crack, the joint with a shallow crack at the saddle point is analysed. The maximum depth of the crack equals to quarter of the chord thickness. The length of the crack is assumed to be 20 mm.

The experimental hot spot stresses are obtained by extrapolating stresses linearly to the weld toe. The variation of hot spot stress concentration factors along brace/chord intersection is shown in Fig. 8.6. From the experiment, a higher hot spot stress concentration factor value of 25.23 at the bottom saddle point (corresponding to the thinner brace wall position) is obtained, compared to a value of 22.17 at the top saddle point (corresponding to the thicker brace wall position). Whereas, a value of 16.34 for the hot spot stress concentration factor is obtained from the analysis. But the experimentally obtained hot spot stress concentration factors based on the approximate nominal stress computed from the uniaxial strain measurements are 17.45 and 24.56 for bottom and top saddle points, respectively. The variation of stress concentration factor (SCF) along the chord and brace surface at the saddle point is shown in Fig. 8.7. Away from the

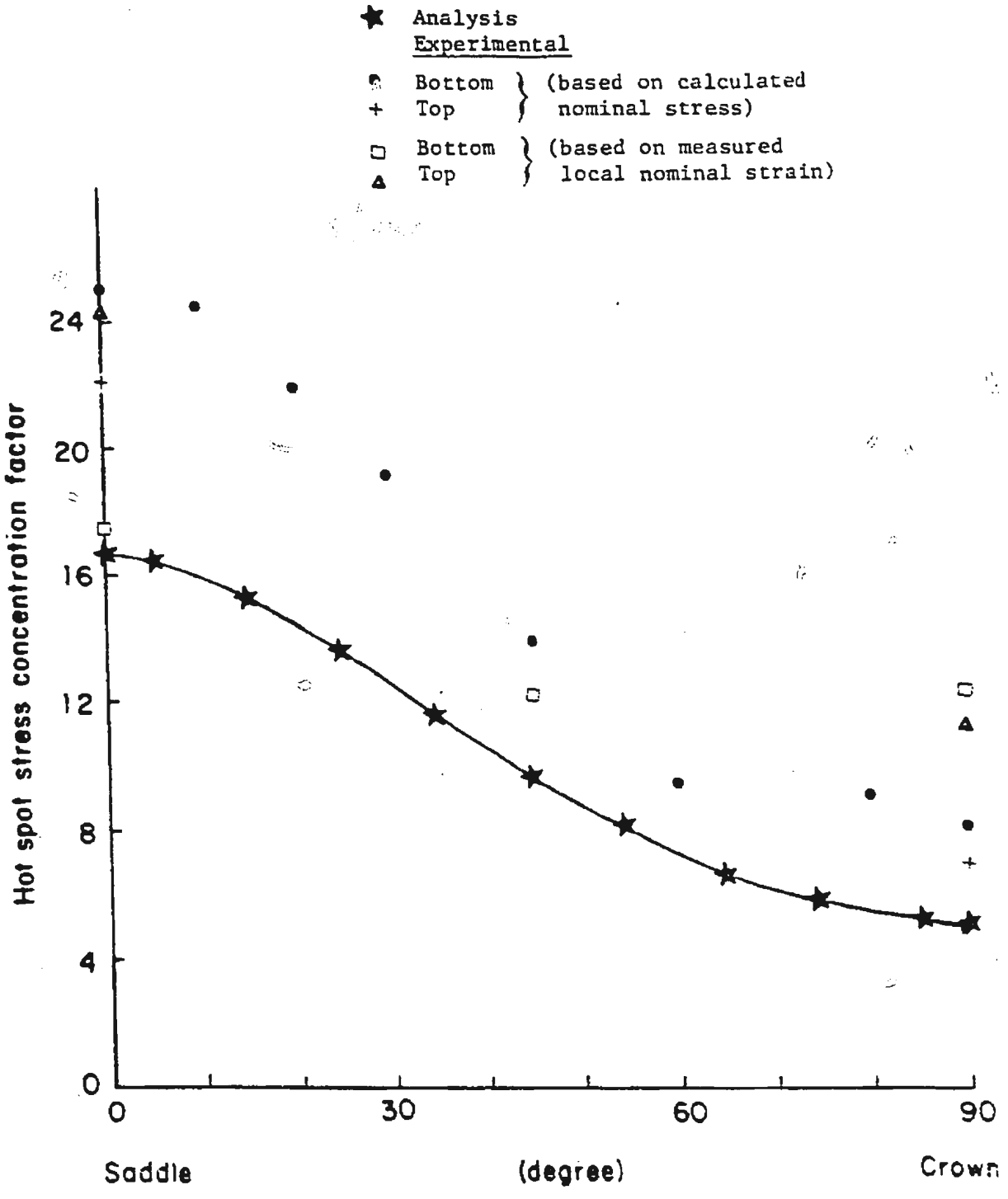

Fig. 8.6 Variation of hot spot stress concentration factor along the intersection.

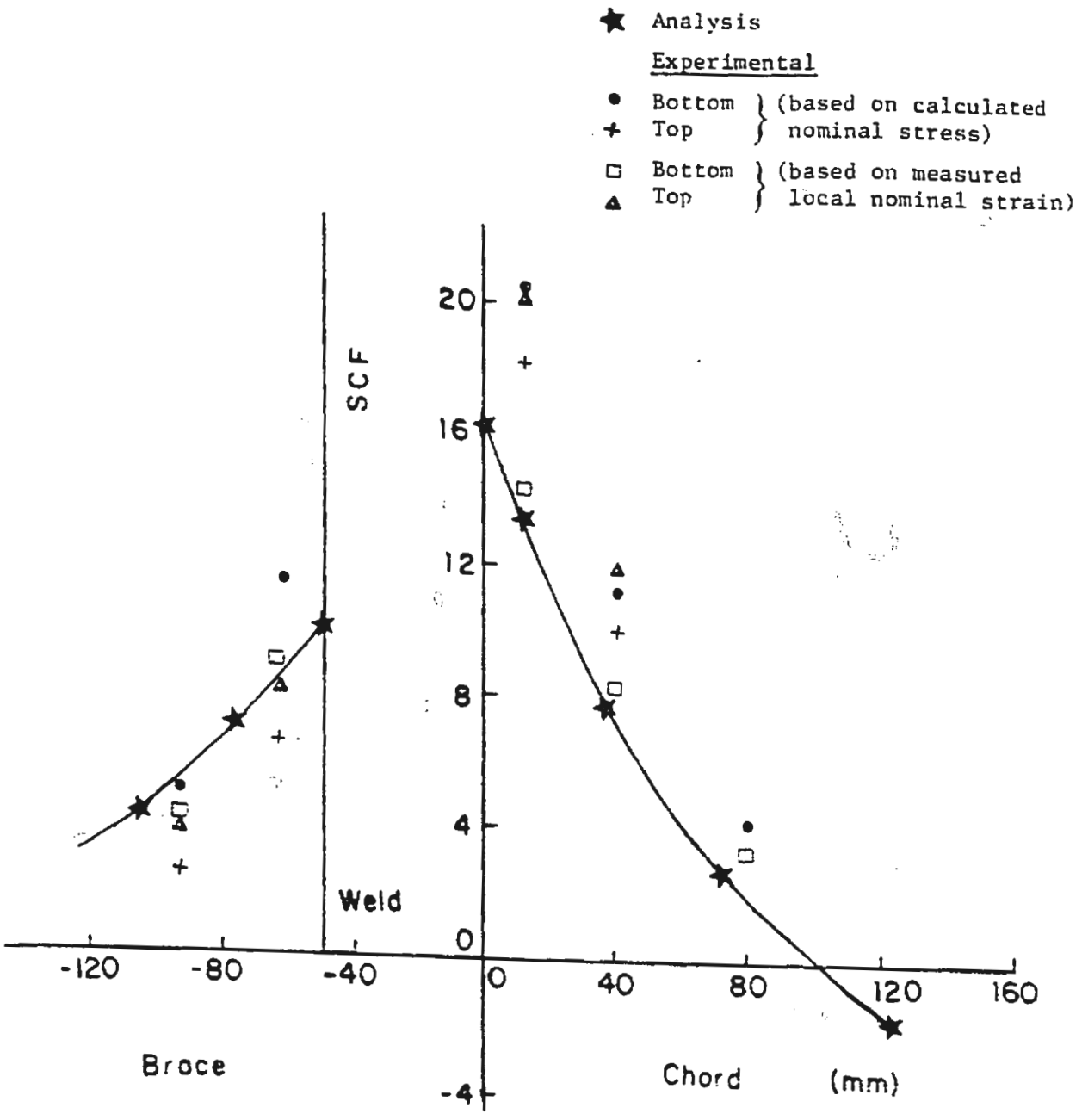

Fig. 8.7 Variation of stress concentration factor along chord/brace surface at saddle point.

weld, the SCFs obtained from both analysis and experiment are comparable.

The crack-tip stress intensity factor, calculated from the displacements in front of the crack is 18.21 $MNm^{-3/2}$. Corresponding saddle point hot spot stress is 298 MN/m^2, which is the maximum hot spot stress obtained from the fatigue test. The through-thickness cracking life of the joint is estimated using Eqn. 7.3. The values of C and m are used as 0.102×10^{-9} m/cycle and 2.263, obtained from the small scale specimen measurements at a temperature of 4°C and a load ratio of 0.1 (refer Chap. 6). The estimated through-thickness-cracking life of the joint, with an initial weld toe defect depth of 0.5 mm, is 3.79×10^5 cycles for a hot spot stress range of 250 MN/m^2.

The first weld toe crack is detected near the top saddle point of the joint after 1.0×10^5 cycles. The drop in uniaxial strain (on the chord surface at the saddle point) is observed to be 13 percent at this stage. The second weld toe crack is detected afterwards near the bottom saddle point of the joint after a total number of 1.8×10^5 cycles. The top-side crack is observed to propagate at a substantially faster rate than the bottom-side crack, untill it reaches a depth of 17.07 mm at the saddle point. Corresponding number of elapsed cycle is 4.12×10^5 cycles. After this stage, the top-side crack is observed to propagate predominantly along the weld toe, whereas bottom-side crack propagates both across the chord wall and along the weld toe.

The number of cycles, required for a weld toe crack to grow from an initial depth of 0.5 mm to a final depth of 17.07 mm, is predicted to be 3.39×10^5 cycles for

this joint with same hot spot stress range. Considering the initiation life of the joint as 1.0×10^5 cycles, the error in prediction is 6.5 percent. Underestimation of the stress concentration factor and overestimation of the stress intensity factor may be the possible reason for such a close life prediction.

CHAPTER 9

GENERAL DISCUSSION AND CONCLUSIONS

9.1 Contribution to the Field of Research

The contribution of the present study to the fatigue analysis of offshore tubular joints is as discussed below.

A computer software based on the finite element formulations, discussed in Chapters 3, 4 and 5, has been developed to investigate the stress fields in the hot spot regions of tubular joints (with or without weld toe cracks). Though various authors have analysed general crack problems using special finite elements in the past, no attempts were made to analyse welded tubular joints, containing weld toe cracks. The analyses of the joint discussed in Chapter 5 are the first of their kind.

In Chapter 6, the quantitative fatigue-crack-growth information and the material coefficients, C and m, for CSA G40.21 M 350 WT steel, proposed for the Canadian offshore region, have been obtained. The effects of environmental and mechanical variables on fatigue-crack-growth-rates in this base metal have been studied.

In the past, some researchers have discussed the fracture mechanics approach to fatigue life estimation of tubular joints. But no attempts were made to illustrate the applicability of the approach using analytically obtained crack-tip stress

intensity factors. The fatigue life of tubular joint has been predicted (discussed in Chapter 7), for the first time, based on the fatigue-crack-growth pattern in the base metal and on the analytically obtained stress intensity factor. The prediction has been checked by the experimental results on a large tubular T-joint.

9.2 Conclusions

A comprehensive study of the fatigue behaviour of tubular T-joints using the linear fracture mechanics approach is presented. A computer software is developed for the finite element analysis of tubular joints. Results are presented for axial and in-plane bending load cases. The stress concentration factors in the chord side, obtained from the two dimensional analysis, show good agreement with the measured values reported in the literature. Some difference is observed between the brace side SCFs and the measured values reported in the literature. This is probably due to the displaced brace/chord intersection. Modified SCFs on brace side, based on Irvine's recommendation, are comparable with the reported values.

The brace/chord intersection region including the weld at the saddle point is analysed for an axial load case using the rezone technique. The imposed boundary values at the plate-to-solid element transition are obtained from the two dimensional analysis. The stresses obtained from the rezoned analysis differ from the three dimensional analysis of the entire joint by 5 - 38 percent for various points of interest. The deviation in the stresses is probably due to a plate-to-solid transi

tion boundary effect.

Three dimensional stress analysis of the entire joint is done having assumed an idealized shape of the weld reinforcement. For the chord side, both the two and the three dimensional analyses give a variation of stress which resembles that reported in the literature. In the case of a joint without a plug, the hot spot stress concentration factor at saddle point on the chord side is 20 percent higher than that obtained from the two dimensional analysis. But on the brace side it is only 3 percent higher than the two dimensional analysis results. In the case of a joint with a plug, the stresses near the weld toe are smaller than those of the joint without a plug. Because of the extra stiffness contribution from the plug, the magnitude of the stress concentration is smaller than that of the joint without a plug.

Three dimensional finite element analysis results are presented for the joints, containing incipient and shallow weld toe cracks. In the case of a shallow crack, the stresses away from the weld toe on the chord surface are slightly greater than those of a joint with an incipient crack. But near the weld toe, the stresses decrease considerably due to the presence of the free surface of the crack face and are less than those of the uncracked joint. For a joint with cracks the trend of surface stress variation along the chord at the crown point, due to in-plane bending, is similar to that at the saddle point due to axial loading.

The stresses across the chord wall, in front of the cracks, are much higher than those of a joint without a crack, at both saddle and crown points. At the vicinity

of cracks, the stressses are high and approximately of the same magnitude. The crack-tip stress intensity factors obtained from the analyses are slightly higher than the reported experimental results.

The effects of sea water, temperature, frequency, load ratio and wave form on the fatigue crack-growth-rate in CSA G 40.21 M 350 WT steel are studied over a ΔK range of 35 to 70 $MNm^{-3/2}$. Maximum increase in crack-growth-rate by a factor of 2.7 is observed in sea water at $\Delta K = 35$ $MNm^{-3/2}$, $f = 0.05$ Hz and $R = 0.1$, compared to air at a temperature of 0 to 4°C. With frequency increase to 0.5 Hz the difference in growth-rate almost disappears. The crack-growth-rate at $\Delta K = 35$ $MNm^{-3/2}$ is reduced by 1.7 times, when temperature of sea water decreases from 21°C to 0°C. In air, no significant effect of temperature in the range of -15 to 4°C is observed. Strong effect of frequency is observed in sea water at low ΔK. At $\Delta K = 35$ $MNm^{-3/2}$, an increase in growth-rate by a factor of 2.3 results when frequency drops from 0.5 to 0.05 Hz. In air, the effect of frequency is negligible. The stress ratio in the range from 0.05 to 0.3 has no significant influence on the growth-rate either in sea water or in air.

The fatigue life of a tubular T-joint is predicted using the linear fracture mechanics approach. The fatigue crack-growth-rates for tubular joints are determined using the stress intensity factors corresponding to a 50 percent of thickness weld toe crack and the material coefficients C and m obtained from the small scale specimen tests. At the higher hot spot stress range, the estimated lives show good general agreement with the experimental results available in the literature as well as with the test reported in Chapter 8.

A prototype tubular T-joint is tested in order to check the stress analysis results and to verify the proposed method for predicting the fatigue life.

9.3 Scope for Further Research

Useful extensions of the present study are as follows:

(a) The analysis can be extended to the direct calculation of the stress intensity factor, by taking it as a basic unknown along with the nodal degrees-of-freedom at the element level.

(b) To investigate the effect of a weld toe crack on stress redistribution, as the crack front moves ahead, the substructuring capability can be incorporated into the computer program, so as to assist in determining the proper SIFs and the direction of crack front propagation.

(c) Crack-growth-rates in the weld metal can be studied using compact tension specimens.

(d) Crack-growth-rate data can be generated at the lower stress intensity factor range level.

(e) Crack-growth retardation due to overloading can be investigated using standard specimens.

BIBLIOGRAPHY AND LIST OF REFERENCES

Adamek, J.R., (1973), An Automatic Mesh Generator Using Two and Three Dimensional Isoparametric Finite Elements. M.Eng. Thesis, Naval Postgraduate School, California, U.S.A.

Ahamad, S., Irons, B.M. and Zienkiewicz, O.C., (1970), Analysis of Thick and Thin Shells Structures by Curved Finite Elements. Int. J. Numer. Methods Eng., 2, 419-415.

Albrecht, P. and Yamada, K., (1977), Rapid Calculation of Stress Intensity Factors. ASCE Structural Div. Journal, 103, ST2, 377-383.

Alwar, R.S. and Ramachandran, D.N., (1983), Three-Dimensional Finite Element Analysis of Cracked Thick Plates in Bending. Int. J. Numer. Methods Eng., 19, 293-303.

Arockiasamy, M., Bhuyan, G.S. and Munaswamy, K., (1984), Finite Element Analysis of Stress Concentration in Tubular T-joints. CANMET, Ottawa, Report No. OSU 83-00033, 129p.

ASTM E647-81, (1981), Standard Test Method for Constant-load-amplitude Fatigue Crack Growth Rates Above 10^{-8} m/cycle.

Austen, I.M., Rudd, W.J. and Walker, E.F., (1981), Factors Affecting Corrosion Fatigue and Stress Corrosion Crack Growth in Offshore Steels. Proc. of Int. Conf. on Steel in Marine Structures, Paper 5.4, Paris, 20p.

Barsoum, R.S., (1976), On the Use of Isoparametric Finite Elements in Linear Fracture Mechanics. Int. J. Numer. Methods Eng., 10-1, 25-37.

Bathe, K.J., (1982), Finite Element Procedures in Engineering Analysis. Prentice-Hall, Inc., New Jersey.

Bathe, K.J. and Wilson, E.L., (1976), Numerical Methods in Finite Element Analysis. Prentice-Hall, Inc., New Jersey.

Bazely, G.P., Cheung, T.K., Irons, B.M. and Zienkiewicz, O.C., (1965), Triangular Elements in Bending - Conforming and Non-conforming Solutions. Proc. Conf. Matrix Methods in Structural Mechanics, Air Force Inst. of Tech., Wright & Patterson A.F. Base, Ohio.

Beale, L.A. and Toprac, A.A., (1967), Analysis of In-plane T, Y and K Welded Tubular Connections. Welding Research Council Journal, Vol.125.

Bell, R. and Kirkhope, J., (1984), Determination of Stress Intensity Factor for Weld Toe Defects. Final Report, D.S.S. 14SU. 23440-2-9083, CANMET, Ottawa.

Bell, R., Kirkhope, J. and Vosikovsky, O., (1984), Stress Intensity Factors at Weld Toe Cracks. Proc. of Speciality Conf. on Computer Methods in Offshore Engineering, Halifax.

Bergan, P.G. and Aamodt, B., (1974), Finite Element Analysis of Crack Propagation in Three Dimensional Solids Under Cyclic Loading. Nuclear Engineering and Design, 29, 180-188.

Berge, S. and Engesvik, K., (1981), Effect of Plate Thickness in Fatigue of Transverse Fillet Welds. Proc. of Int. Conf. in Steel on Marine Structures, Paper 2.5, Paris, 28p.

Berge, S., (1985), On the Effect of Plate Thickness in Fatigue of Welds. Engg. Fracture Mechanics, 21-2, 423-435.

Blackburn, W.S. and Hellen, T.K., (1977), Calculation of Stress Intensity Factors in Three Dimensions by Finite Element Methods. Int. J. Numer. Methods Eng., 11, 211-229.

Blackburn, W.S., (1973), Calculation of Stress Intensity Factors at Crack Tips Using Special Finite Elements. The Mathematics of Finite Elements, Academic Press, London, 327-336.

Booth, G.S., (1978), Constant Amplitude Fatigue Tests on Welded Steel Joints Performed in Air. European Offshore Steel Research Seminar, Cambridge.

Bousquet, R.D. and Yates, D.N., (1973), A Low Cost Interactive Graphics System for Large Scale Finite Element Analysis. Computers and Structures, 3, 1321-1330.

Bouwkamp, J.G., (1966), Tubular Joints Under Static and Alternating Loads-Phase I. Report 66-15, Struct. and Mat. Res., Struct. Eng. Lab., Univ. of California.

Brandi, R., (1981), Behaviour of Unstiffened and Stiffened Tubular Joints. Proc. of Int. Conf. on Steel in Marine Structures, paper 6.1, Paris, 13p.

Bristoll, P., (1978), A Review of the Fracture Mechanics Approach to the Problems of Design, Quality Assurance, Maintenance and Repair of Offshore Structures. European Offshore Steel Research Seminar, Paper 24, Cambridge.

Broek, D., (1982), Elementary Engineering Fracture Mechanics. Martinus Nijhoff Publishers, The Hague, The Netherlands.

Burdekin, F.M., (1981), Practical Aspects of Fracture Mechanics in Engineering Design. Proc. Institution of Mechanical Engineers, 195, 73-86.

Claude, J.P., Michel, L. and Quoc, S.N., (1980), Use of Fracture Mechanics in Tubular Connections Fatigue Crack Growth. Proc. Offshore Tech. Conf., Paper 3701, Houston, 1, 231-236.

Clayton, A.M. and Martin, T., (1980), Comparison of Stress Levels Obtained on Some Early Welded T-joints Tests. Interim Technical Report, 2/07, UKOSRP.

Clayton, A.M., (1981), Prediction of Crack Growth in Tubular Joints - An Alternative Approach. Fatigue in Offshore Structural Steels, Paper 11, London.

Clough, R.W. and Johnson, C.P., (1968), A Finite Element Approximation for the Analysis of Thin Shells. Int. J. of Solids and Structures, 4, 43-60.

Clough, R.W. and Tocher, J.L., (1965), Finite Element Stiffness Matrices for Analysis of Plate Bending. Conf. on Matrix Methods in Structural Mechanics, Wright-Patterson Air Force Base, Ohio, U.S.A., 515-545.

Damilano, G.F., Camisetti, C. and Negri, A., (1981), Fatigue Behaviour of Unstiffened and Stiffened Y Tubular Joints. Proc. of Int. Conf. on Steel in Marine Structures, Paper 10.1, Paris, 16p.

Dawe, D.J., (1975), High-Order Triangular Finite Element for Shell Analysis. Int. J. Solids Struct., 11, 1097.

de Back, J. and Vaessen, G.H.G., (1981), Fatigue and Corrosion Fatigue Behaviour of Offshore Steel Structures. ECSC Convention, 7210-KB/6/602, Delft.

Dept. of Energy, (1985), Offshore Installations: Guidance on Design and Construction. Her Majesty's Stationary Office, London, England.

Dharmavasan, S. and Dover, W.D., (1984), Stress Distribution Formulae and Comparison of Three Stress Analysis Techniques for Tubular Joints. Proc. of third Int. Offshore Mech. and Arctic Engg. Symposium, Louisiana, U.S.A., 424-432.

Dijkstra, O.D. and de Back, J., (1980), Fatigue Strength of Tubular T and X-joints. Proc. of Offshore Tech. Conf., Paper 3696, Houston, 1, 177-186.

Dijkstra, O.D., (1981), Comparison of Strain Distribution in Three X-joints Determined by Strain Gauge Measurements and Finite Element Calculations. Proc. of Int. Conf. on Steel in Marine Structures, Paper 6.2, Paris, 12p.

DNV, (1982), Rules for the Design Construction and Inspection of Offshore Structures, Appendix C, Norway.

Donald, A.M.C., Brown, G. and Kerr, J., (1981), The Influence of Geometrical and Loading Parameters on the Fatigue Life of Tubular Joints. Proc. of Int. Conf. on Steel in Marine Structures, paper 10.2, Paris, 14p.

Dover, W.D. and Dharmavasan, S., (1982), Fatigue Fracture Mechanics Analysis of T and Y Joints. Proc. of Offshore Tech. Conf., Paper 4404, Houston, 4, 315-326.

Dover, W.D. and Holdbrook, M.S.J., (1979), Fatigue Crack Growth in Tubular Welded Connections. Proc. of Second Int. Conf. on Behaviour of Offshore Structures, Paper 40, London, 1, 507-522.

Dover, W.D., Holdbrook, M.S.J., Hibberd, R.D. and Charlesworth, F.D.W., (1978), Fatigue Crack Growth in T-joints: Out-of-plane Bending. Proc. of Offshore Tech. Conf., Paper 3252, Houston, 3, 1729-1736.

Durelli, A.J., (1981), Stress Concentrations, in: Mechanics of Fracture, Vol.7 (G.C. Sih, editor). Martinus Nijhoff Publishers, The Hauge, The Netherlands, Chap.1, 1-155.

Durocher, L.L., (1979), A Versatile Two-Dimensional Mesh Generator with Automatic Bandwidth Reduction. Computers and Structures, 10, 561-575.

Edwards, C.D. and Fessler, H., (1985), Stress Concentrations in Cast Corner Joints of Tubular Structures. Proc. of Fourth Int. Conf. on Behaviour of Offshore Structures, Delft, 465-473.

Efthymiou, M. and Durkin, S., (1985), Stress Concentrations in T/Y and Gap/overlap K-Joints. Proc. of Fourth Int. Conf. on Behaviour of Offshore Structures, Delft, 429-440.

Engesvik, K.M., (1982), Analysis of Uncertainties in Fatigue Capacity of Welded Joints. Dept. of Marine Technology, Univ. of Trondheim, Report UR-82-17, Norway.

Felippa, C.A., (1972), An Alphanumeric Finite Element Mesh Plotter. Int. J. Numer. Methods Eng., 5, 217-236.

Fenner, D.N. and Mihsein, M.J.A., (1984), Crack Front Elastic Stress State for Three-dimensional Crack Problems. Int. J. of Fracture, 25, 121-131.

Gallagher, R.H., (1975), Finite Element Analysis - Fundamentals. Prentice-Hall, Inc., New Jersey.

Gibstein, M.B. and Moe, E.T., (1981), Numerical and Experimental Stress Analysis of Tubular Joints with Inclined Braces. Proc. of Int. Conf. on Steel in Marine Structures, Paper 6.3, Paris, 18p.

Gibstein, M.B., (1978), Parametric Stress Analysis of T Joints. European Offshore Steel Research Seminar, Paper 26, Cambridge.

Gibstein, M.B., (1981), Fatigue Strength of Welded Tubular Joints at Det Norske Veritas Laboratories. Proc. of Int. Conf. on Steel in Marine Structures, Paper 8.5, Paris, 19p.

Gifford, L.N. Jr. and Hilton, P.D., (1978), Stress Intensity Factors by Enriched Finite Elements. Engg. Fracture Mechanics, 10-3, 485-496.

Gowda, S.S., (1983), Analytical and Experimental Investigation on the Fatigue Behaviour of Tubular Joints for Offshore Monopod Structures. Ph.D. Thesis, Memorial University of Newfoundland, Canada, 249p.

Greimann, L.F., DeHart, R.C. and Blackstone, W.R., (1973), Finite Element Analysis of Complex Joints. Proc. Offshore Tech. Conf., Paper 1823, Houston, 1, 877-888.

Gurney, T.R., (1979), The Influence of Thickness on the Fatigue Strength of Welded Joints. Proc. of Int. Conf. on Behaviour of Offshore Structures, Paper 41, London, 1, 523-534.

Gurney, T.R., (1982), The Basis of the Revised Fatigue Design Rules in the Dept. of Energy Offshore Guidance Notes. Proc. of Second Int. Conf. on Offshore Welded Structures, London.

Gurney, T.R., (1983), Revised Fatigue Design Rules. Metal Construction, 15(1), 37-44.

Haagensen, P.J., Orjasaeter, O. and Draagen, A., (1981), Load Interaction Effects During Fatigue Crack Growth. Proc. of Int. Conf. on Steel in Marine Structures, Paper 7.4, Paris, 17p.

Haagensen, P.J. and Dagestad, V., (1978), Random Load Crack Propagation in Sea Water Under Realistic Load Sequences. European Offshore Steels Research Conf., Cambridge.

Hans, D., Visser, W. and Zunderdorp, H., (1973), The Stress Analysis of Tubular Joints for Offshore Structures. Second Annual Meeting of the Petroleum Engineers of AIME, SPE 4342, London.

Hartranft, R.J. and Sih, G.C., (1969), The Use of Eigen Function Expansions in the General Solution of Three-Dimensional Crack Problems. J. of Math. and Mech., 19-2, 123-138.

Hibbered, R.D. and Dover, W.D., (1977), Random Load Fatigue Crack Growth in T-joints. Proc. of Offshore Tech. Conf., Paper 2853, Houston, 2, 365-372.

Hoffman, R.E., (1983), Interactive Graphics Finite Element Mesh Generation. Computing in Civil Engineering, 700-713.

Hoffman, R.E. and Sharifi, P., (1980), On the Accuracy of Different Finite Element Types of the Analysis of Complex Welded Tubular Joints. Proc. Offshore Tech. Conf., Paper 3691, Houston, 1, 127-140.

Holmes, R. and Booth, G.S., (1981), Fatigue and Corrosion Fatigue of Welded Joints Under Narrow Band Random Loading. Proc. of Int. Conf. on Steel in Marine Structures, Paper 7.2, Paris, 16p.

Hudak, S.J., Saxena, A., Bucci, R.J. and Malcolm, R.C., (1978), Development of Standard Methods of Testing and Analysing Fatigue Crack Growth Data. Technical Report AFML-TR-78-40, Air Force Material Lab., Wright-Patterson Air Force Base, Ohio, 221p.

Irons, B.M., (1976), The Semiloof Shell Element. Finite Elements for Thin Shells and Curved Members, Chap.11, Eds. D.G. Ashwell and R.H. Gallagher, Wiley, 197-222.

Irvine, N.M., (1980), Comparison of Stress Analysis Methods in the Region of Chord/Brace Intersection. Interim Technical Report, 2/08, UKOSRP.

Irvine, N.M., (1981a), Comparison of Tubular Joint Stress Analysis Methods in the Near Weld Region. Proc. of Int. Conf. on Steel in Marine Structures, Paper 1.2, Paris, 15p.

Irvine, N.M., (1981b), Comparison of the Performance of Modern Semi-empirical Parametric Equations for Tubular Joint Stress Concentration Factors. Proc. of Int. Conf. on Steel in Marine Structures, Paper 6.5, Paris, 17p.

Irvine, N.M., (1981c), Interpretation of S-N Tubular Joint Data. Proc. of Int. Conf. on Steel in Marine Structures, Paper 10.3, Paris, 15p.

Iwasaki, T., Kawahara, M. and Asano, K., (1979), Fatigue Crack Growth Behaviour in Welded Tubular Joints in T, TY and K. Proc. of Offshore Tech. Conf., Paper 3423, Houston, 1, 575-582.

Johnson, R., Bretherton, I., Tomkins, B. and Scott, P.M., (1978), The Effect of Sea Water Corrosion in Fatigue Crack Propagation in Structural Steel. Seminar on European Offshore Steels Research, Paper 15, The Welding Institute, Cambridge, U.K.

Kassir, M.K. and Sih, G.C., (1966), Three Dimensional Stress Distribution Around an Elliptical Crack Under Arbritary Loadings. J. of Applied Mechanics, 33-3, 601-611.

Kikukswa, M., Jono, M. and Tanaka, K., (1976), Fatigue Crack Closure Behavior of Low Stress Intensity Level. Proc. of Second Int. Conf. on Mech. Behavior of Materials, Boston.

Kuang, J.G., Potvin, A.B., Leick, R.D. and Kahlich, J.L., (1977), Stress Concentration in Tubular Joints. Pet. Eng. Journal, 287-299.

Kuo-Kuang, H., Chen-Ming, J.H. and Stuart, E.S., (1983), Finite Element Model to Determine K_I. J. of Engg. Mech., 109-4.

Kurobane, Y., (1969), Effects of Low-cycle Alternating Loads on Tubular K-joints. IIW Doc. XV-271-69.

Lereim, J., (1983), Significance of Fracture Mechanics on Design of Offshore Structures. Fracture Prevention in Energy and Transport Systems, Brazil, 1, 135-147.

Liaw, C.Y., Litton, R.W. and Reimer, R.B., (1976), Improved Finite Elements for Analysis of Welded Tubular Joints. Proc. Offshore Tech. Conf., Paper 2642, Houston, 3, 267-282.

Liaw, P.K. and Logsdon. W.A., (1985), The Influence of Load Ratio and Temperature on the Near-threshold Fatigue Crack Growth Rate Properties of Pressure Vessel Steels. J. Engineering Materials and Technology, ASME, 107, 26-33.

Lieurade, H.P., (1985), Fatigue in Welded Constructions. Bulletin Technique de Bureau Veritas, 281-302.

Lloyd's Register of Shipping, (1983), Complex Joints and Loading Fatigue Study. Report No OSG/TR/83004, London.

Maeda, T., Uchino, K. and Sakurai, H., (1969), Experimental Study on the Fatigue Strength of Welded Tubular K-joints. International Institute of Welding, Doc. No. XV-269-69.

Marshall, P.W., (1974), General Consideration for Tubular Joint Design. Welding in Offshore Construction, Welding Institute Conf., Newcastle.

Miller, C.D. and Trammell, J.H., (1974), An Analytical and Experimenta Study of Stiffened Tubular Joints with Multiple Branches. Proc. Offshore Tech. Conf., Paper 2101, Vol.2, Houston.

Mitsui, Y., Kurobane, Y. and Nishimura, M., (1984), Fatigue Resistance of Stiffened Tubular Joints. Proc. of Second Int. Conf. on Welding of Tubular Structures, Boston, 501-508.

Morgan, E.F., (1979), Use of High Order Isoparametric Solid Finite Elements for the Stress Analysis of Welded Tubular Joints. Southwest Research Institute, Project 03-9217-001, Texas.

Morgan, H.G., Thorpe, T.W., Sylvester, D.R.V. and Scott, P.M., (1981), An Investigation of the Corrosion Fatigue Crack Growth Behaviour of Structural Steels in Seawater. Proc. of Int. Conf. on Steel in Marine Structures, Paper 5.1, Paris, 25p.

Morris, S. and Becker, E.B., (1978), A Conforming Crack Tip Element with Quadratic Variation in the Singular Fields. Int. J. Numer. Methods Eng., 12, 279-288.

Natarajan, M. and Toprac, A.A., (1968), The Fatigue Strength of Tubular T-joints. S.F.R.L. Report, University of Texas, Austin, Texas.

Oberparleiter, W. and Schutz, W., (1981), Fatigue Life Prediction in a Corrosive Environment. Proc. of Second Int. Symposium on Integrity of Offshore Structures, Glasgow, Scotland.

Parker, A.P., (1981), The Mechanics of Fracture and Fatigue. E. & F.N. Spon Ltd., London.

Parkhouse, J.C., (1981), Improved Modelling of Tube Wall Intersections Using Brick Elements. Proc. of Int. Conf. on Steel in Marine Structures, Paper 1.3, Paris, 14p.

Polak, J. and Knesl, Z., (1975), On the Fatigue Crack Growth Rate Evaluation from Experimental Data. Int. J. of Fracture, 11, 693-696.

Radenkovic, D., (1981), Stress Analysis in Tubular Joints. Proc. of Int. Conf. on Steel in Marine Structures, Special and Plenary Sessions, Paris, 53-96.

Raju, I.S. and Newman, J.C. Jr., (1977), Three Dimensional Finite Element Analysis of Finite-Thickness Fracture Specimens. NASA Technical Note, TN D-8414.

Rolfe, S.T. and Barsom, J.M., (1977), Fracture and Fatigue Control in Structures. Prentice-Hall, Inc., New Jersey.

Ryan, I., Recho, N., Regnier, L. and Lieurade, H.P., (1984), Fatigue Life of Welded Circular Tubular Joints in Offshore Structures. Proc. of Second Int. Conf. on Welding of Tubular Structures, Boston, 535-542.

Sasski, K., Ohta, A. and Kosugs, M., (1977), Fatigue Crack Propagation Rate and Stress Intensity Threshold Level of Several Structural Materials of Varying Stress Ratios. Report of National Research Institute for Metals, Tokyo.

Scholte, H.G. and Wildschut, H., (1981), Fatigue Crack Propagation Tests on Welded Specimens in Air and Seawater. Proc. of Int. Conf. on Steel in Marine Structures, Paper 5.2, Paris, 17p.

Scordelis, A.C. and Lo, K.S., (1964), Computer Analysis of Cylindrical Shells. J. Am. Concr. Inst., 61.

Shiyekar, M.R., Kalani, M. and Belkune, R.M., (1982), Stresses in Stiffened Tubular T-joint of an Offshore Structure. Proc. of first Offshore Mechanics/ Arctic Engineering/ Deepsea Systems Symposium, Vol.1, New Orleans, 258-266.

Sih, G.C., (1971), A Review of the Three-Dimensional Stress Problem for a Cracked Plate. Int. J. Fracture Mech., 7-1, 39-61.

Stephens, R.I., Chung, J.H. and Glinka, G., (1980), Low Temperature Fatigue Behavior of Steels - A Review. Society of Automative Engineers, Inc., 1892-1904.

Thomas, G.R. and Gallagher, R.H., (1974), A Triangular Element Based on Generalized Potential Energy Concepts. Proc. of Conf. on Finite Element Applied to Thin Shells and Curved Members, Wales, 155-170.

Thorpe, T.W., Scott, P.M., Rance, A. and Silvester, D., (1982), Corrosion-fatigue of BS 4360:50D Structural Steel in Sea Water. Report AERE Harwell - R 10679.

Tracey, D.M., (1971), Finite Elements for Determination of Crack Tip Elastic Stress Intensity Factors. Engg. Fracture Mech., 3, 255-265.

Tracey, D.M., (1974), Finite Elements for Three Dimensional Elastic Crack Analysis. Nuclear Engineering & Design, 26, 282-290.

Van Delft, D.R.V., Noordhoek, C. and Back, de J., (1985), Evaluation of the European Fatigue Test Data on Large-size Welded Tubular Joints for Offshore Structures. Proc. of Offshore Tech. Conf., Paper 4999, Houston, 3, 351-360.

Visser, W., (1974), On the Structural Design of Tubular Joints. Proc. Offshore Tech. Conf., Paper 2117, Houston, 2, 881-894.

Vosikovsky, O. and Rivard, A., (1984), Fatigue Crack Propagation in Welded Plate T-Joints. Interim Report, ERP/PMRL, CANMET, Ottawa.

Vosikovsky, O. and Rivard, A., (1981), Growth of Surface Fatigue Cracks in a Steel Plate. Int. J. Fatigue, 111-115.

Vosikovsky, O., (1980), Effects of Stress Ratio on Fatigue Crack Growth Rates in X-70 Pipeline Steel in Air and Sea Water. J. of Testing and Evaluation. 8-2, 68-73.

Vosikovsky, O., (1975), Fatigue-crack Growth in an X-65 Line-pipe Steel at Low Cyclic Frequencies in Aqueous Environments. J. of Engg. Materials & Technology, 97-4, 298-302.

Vosikovsky, O., Bell, R., Burns, D.J. and Mohaupt, U.H., (1985), Fracture Mechanics Assessment of Fatigue Life of Welded Plate T-joints, Including Thickness Effect. Proc. of Fourth Int. Conf. on Behaviour of Offshore Structures, Delft, 453-464.

Vosikovsky, O., Neill, W.R., Carlyle, D.A. and Rivard, A., (1983), The Effect of Sea Water Temperature on Corrosion Fatigue Crack Growth in Structural Steels. Div. Report, ERP/PMRL 83-27(OP-J), CANMET, Ottawa.

Walker, E.F., (1981), Effects of Marine Environments. Proc. of Int. Conf. on Steel in Marine Structures, Plenary Sessions, Paris, 195-252.

Wildschut, H., de Back, J., Dortland, W. and Van Leeuwen, J.L., (1978), Fatigue Behaviour of Welded Joints in Air and Seawater. European Offshore Steels Research Seminar, Cambridge.

Wilson, E.L., Taylor, R.L., Doherty, W. and Ghaboussi, J., (1973), Incompatible Displacement Model. Numerical and Computer Methods in Structural Mechanics, Academic Press, Inc., New York, 43-57.

Wordsworth, A.C. and Smedly, G.P., (1978), Stress Concentrations at Unstiffened Tubular Joints. European Offshore Steel Research Seminar, Paper 31, Cambridge.

Wylde, J.G. and McDonald, A., (1979), The Influence of Joint Dimensions on the Fatigue Strength of Welded Tubular Joints. Proc. of Second Int. Conf. on Behaviour of Offshore Structures, Paper 42, London, 1, 535-550.

Wylde, J.G., (1981), The Fatigue Performance of Tubular K and KT Joints. Proc. of Int. Conf. on Steel in Marine Structures, Paper 8.2, Paris, 12p.

Wylde, J.G., (1984), Fatigue Crack Growth in Welded Tubular Joints. Proc. of Int. Conf. on Welding of Tubular Structures, Boston, 561-571.

Zienkiewicz, O.C., (1977), The Finite Element Method. Third Edition, McGraw-Hill Book Company, London.

Zienkiewicz, O.C., Parekh, C.J. and King, I.P., (1968), Arch Dams Analysed by a Linear Finite Element Shell Solution Program. Proc. Symp. Arch Dams, Inst. Civil Eng., London.

Zwaans, M.H.J.M., Jonkers, P.A.M. and Overbeeke, J.L., (1981), The Endurance of a Welded Joint Under Two Types of Random Loading in Air and Seawater. Proc. of Int. Conf. on Steel in Marine Structures, Paper 7.3, Paris, 15p.

CENTRE FOR NFLD. STUDIES
JUL 18 1978
MEMORIAL UNIVERSITY
OF NEWFOUNDLAND